Double-resonant Raman scattering in graphene, few-layer graphene, and carbon nanotubes

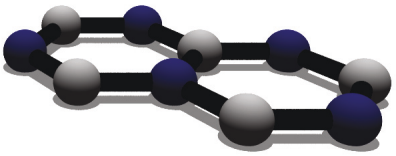

by Felix Herziger

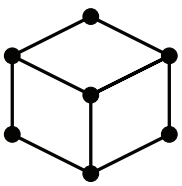

Technische Universität Berlin
Institut für Festkörperphysik
Berlin, Oktober 2015

Double-resonant Raman scattering in graphene, few-layer graphene, and carbon nanotubes

vorgelegt von
Master of Science (M.Sc.)
Felix Herziger
aus Rostock

von der Fakultät II - Mathematik und Naturwissenschaften
der Technischen Universität Berlin
zur Erlangung des akademischen Grades

Doktor der Naturwissenschaften
– Dr. rer. nat. –

genehmigte Dissertation

Promotionsausschuss:

Vorsitzender:	Prof. Dr. Thomas Möller
Berichterin:	Prof. Dr. Janina Maultzsch
Berichter:	Prof. Dr. Stéphane Berciaud

Tag der wissenschaftlichen Aussprache: 22. Oktober 2015

Berlin 2015

Zusammenfassung

In dieser Arbeit werden verschiedene doppelresonante Raman-Moden in Graphen, mehrlagigem Graphen und Kohlenstoff-Nanoröhren analysiert, wobei hier Phonon-Phonon als auch Phonon-Defekt Streuprozesse untersucht werden sollen. Als Graphen bezeichnet man eine atomare Schicht aus sp^2-hybridisiertem Kohlenstoff, welcher in einem hexagonalen Gitter angeordnet ist. Dieses Material ist einer der Forschungsschwerpunkte moderner Festkörperphysik und hat seit seiner erstmaligen Präparation im Jahr 2004 enormes wissenschaftliches Interesse auf sich gezogen. Kohlenstoff-Nanoröhren hingegen sind schon länger bekannt und können, bildlich gesprochen, durch das "Aufrollen" von Graphen erzeugt werden. Bei der Untersuchung dieser Materialsysteme hat sich vor allem die Raman-Spektroskopie als eine sehr umfassende und vielseitige Methode zur Charakterisierung der elektronischen und vibronischen Eigenschaften etabliert. Konsequenterweise wird deshalb auch in der vorliegenden Arbeit Raman-Spektroskopie und vor allem doppelresonante Raman-Spektroskopie als experimentelle Methode zur Untersuchung der Materialeigenschaften angewendet. Obwohl die theoretischen Grundlagen der doppelresonanten Raman-Streuung schon vor mehr als einem Jahrzehnt etabliert wurden, stellen sich bis heute Fragen bezüglich der exakten Streuprozesse, welche bestimmten Raman-Moden zu Grunde liegen. Im Folgenden sollen diese Fragestellungen nun beantwortet werden.
Im ersten Teil der vorliegenden Arbeit werden wir die doppelresonante $2D$-Mode in zweilagigem Graphen untersuchen. Im Gegensatz zu einer Lage Graphen, besitzt die $2D$-Mode in zweilagigem Graphen eine komplexe Linienform mit mehreren Beiträgen, welche Anlass für zahlreiche theoretische und experimentelle Arbeiten waren. Jedoch konnte bis heute keine eindeutige und schlüssige Zuordnung der verschiedenen Beiträge zu den einzelnen Streuprozessen präsentiert werden. Im Rahmen dieser Arbeit werden wir zeigen, dass die $2D$-Mode aus drei Hauptbeiträgen besteht, was im Gegensatz zu allen früheren Arbeiten auf diesem Gebiet steht. Des Weiteren werden wir nachweisen, dass die dominanten Beiträge im Raman-Streuquerschnitt von Phononen aus der $\mathbf{K} - \mathbf{\Gamma}$ Richtung der Brillouin-Zone stammen. Im Folgenden werden wir auf den quantenmechanischen Charakter von doppelresonanter Raman-Streuung eingehen, welcher sich vor allem in den verschiedenen Intensitäten der einzelnen Beiträge manifestiert. Wir werden demonstrieren, dass die destruktive und konstruktive Interferenz der einzelnen Beiträge mittels externer Parameter gezielt manipuliert werden kann, was sich direkt in einer Veränderung der Linienform widerspiegelt. Für eine exakte Analyse der Linienform der $2D$-Mode ist weiterhin die Berücksichtigung der Aufspaltung zwischen den beiden transversal optischen Phononenzweigen entlang der $\mathbf{K} - \mathbf{\Gamma}$ Richtung von großer Bedeutung. Wir werden eine Methode vorstellen, mit deren Hilfe diese Aufspaltung direkt aus den experimentellen Raman-Spektren ermittelt werden kann. Ebenso erlaubt unsere Methode die Berechnung der energetischen Aufspaltung zwischen den elektronischen Bändern. Abschließend diskutieren wir noch die Polarisationsabhängigkeit der $2D$-Mode und zeigen, dass sogenannte innere und äussere Prozesse teilweise gezielt unter-

drückt werden können. Die Ergebnisse dieser Arbeit führen schließlich zu einem umfassenden Verständnis der komplexen $2D$-Moden Linienform in zweilagigem Graphen.
Der zweite Teil dieser Arbeit befasst sich mit der doppelresonanten Raman-Streuung an Phononen und Defekten. Nach einer einführenden allgemeinen Diskussion zu Defekten in Graphen werden wir speziell die D-Mode in Kohlenstoff-Nanoröhren untersuchen. Wir werden zunächst ein allgemeingültiges Modell zur Beschreibung von doppelresonanten Streuprozessen in Kohlenstoff-Nanoröhren präsentieren und anschließend auf die Durchmesserabhängigkeit der D-Moden Frequenz eingehen. Betrachtet man diese Frequenz am resonanten optischen Übergang der Kohlenstoff-Nanoröhre, so lassen sich zwei verschiedene Abhängigkeiten beobachten: Kleinere Kohlenstoff-Nanoröhren haben generell eine höhere D-Moden Frequenz; ebenso steigt diese Frequenz für höhere optische Übergänge. Die zuvor experimentell beobachteten Diskontinuitäten zwischen D-Moden Frequenzen von verschiedenen optischen Übergängen können als eine Konsequenz von Durchmessereffekten auf die Dispersion der Phononen mit A_{1g} Symmetrie am **K**-Punkt erklärt werden. Die vorgestellten Ergebnisse dieses Kapitels bringen schließlich alle vorherigen experimentellen Arbeiten in Einklang und liefern ein konsistentes Model zur Beschreibung von doppelresonanten Streuprozessen in Kohlenstoff-Nanoröhren.
Im Gegensatz zu den intensiven defektinduzierten D- und D'-Moden, existieren in Graphen und Kohlenstoff-Nanoröhren weitere Defektmoden mit niedriger Intensität. Ein Beispiel hierfür ist die D''-Mode, welche wir in Abhängigkeit der Lagenanzahl, der Laserenergie und des Nanoröhrendurchmessers untersuchen. Wir weisen nach, dass diese Raman-Mode aus der Streuung von longitudinal akustischen Phononen mit Defekten resultiert und in einlagigem Graphen eine Dispersion von $-80\,\mathrm{cm}^{-1}/\mathrm{eV}$ hat. Die charakteristische Linienform, welche eine asymmetrische Flanke zu höheren Frequenzen aufweißt, kann durch die Beiträge verschiedener Phononen erklärt werden. Wir werden zeigen, dass der Hauptbeitrag von Phononen aus der $\mathbf{K}-\mathbf{\Gamma}$ Richtung stammt, wohingegen die zusätzlichen Beiträge von Phononen nahe dieser Hochsymmetrierichtung resultieren. Die Linienform der D''-Mode für mehrlagiges Graphen spiegelt die Entwicklung der elektronischen Bänder am **K**-Punkt wider. Bei unseren Messungen an Kohlenstoff-Nanoröhren kann die charakteristische asymmetrische Linienform nicht beobachtet werden, viel mehr stellt sich die D''-Mode stark verbreitert dar, was aus den diversen Beiträgen von Nanoröhren in oder nahe der Resonanz mit der Laserenergie resultiert. Unser zuvor entwickeltes Model zur Beschreibung von doppelresonanten Streuprozessen in Kohlenstoff-Nanoröhren kann ebenfalls erfolgreich auf die D''-Mode angewendet werden und liefert eine sehr gute Übereinstimmung mit unseren experimentellen Daten.
Im letzten Teil der vorliegenden Arbeit werden wir eine *in-situ* Untersuchung des laserinduzierten Oxidierungsprozesses in Graphen präsentieren. Die Oxidierung kann hierbei gezielt und selektiv durch das Bestrahlen von Graphen mit einem leistungsstarken Laser hervorgerufen werden. Die zeitliche Entwicklung der D-, G- und $2D$-Moden liefert dabei entscheidende Hinweise auf die verschiedenen physikalischen Prozesse während der Oxidierung. Im Wesentlichen können wir die Oxidierung in zwei aufeinanderfolgende Prozesse reduzieren: Erstens, tensile Verspannung der Graphen-Schicht durch laserinduziertes Heizen und, zweitens, p-Dotierung durch Bindung von Sauerstoff an die Graphen-Schicht. Weiterhin beobachten wir das unerwartete Absinken des D/G-Verhältnisses mit zunehmender Bestrahlungszeit, was vor allem durch die Dotierungsabhängigkeit des D/G-Verhältnisses erklärt werden kann. Abschließend diskutieren wir AFM-Aufnahmen der oxidierten Graphen-Schichten. Unsere vorgestellte Methode stellt einen Ansatz zur gezielten Manipulation der Eigenschaften von Graphen auf der sub-μm Skala dar.

Abstract

In this work, we present an analysis of double-resonant two-phonon and phonon-defect Raman modes in graphene, few-layer graphene and carbon nanotubes. Graphene is a single-layer of sp^2-hybridized carbon atoms that arrange in a hexagonal lattice and has attracted tremendous scientific interest since its first experimental preparation in 2004. Carbon nanotubes can be considered as a rolled-up piece of graphene with periodic boundary conditions along its circumference. The study of both systems is largely based on optical spectroscopy, namely Raman spectroscopy, since this approach enables a thorough characterization of their electronic and vibrational properties. Raman scattering and especially double-resonant Raman scattering are also the experimental methods of choice for the analyses presented here. Although the concept of double-resonant Raman scattering has been introduced more than a decade ago, the precise scattering processes of certain Raman modes are still controversially discussed and thus need clarification.

The present work can be separated into two main parts. The first part will, both theoretically and experimentally, investigate the double-resonant $2D$ mode in Bernal-stacked bilayer graphene. The $2D$ mode is a two-phonon process, in which two transverse optical (TO) phonons with opposite momentum from the edges of the Brillouin zone ($\mathbf{K}$ points) are scattered. In contrast to single-layer graphene, this Raman mode presents a complex lineshape in bilayer graphene and was subject of many theoretical and experimental works. However, a consistent explanation of the different contributions to the characteristic peak shape is still lacking. By calculating the two-dimensional double-resonant scattering cross-section of this Raman mode completely from first principles, we will unravel the dominant contributions and provide a precise analysis of the different scattering processes. In fact, by proving that the $2D$ mode in bilayer graphene is composed of three dominant contributions, we contradict all previous works on this topic. Moreover, we show that the dominant contribution to the Raman scattering cross-section stems from so-called inner scattering processes with phonons from the $\mathbf{K}-\mathbf{\Gamma}$ high-symmetry direction. A very important, but often neglected, key feature of double-resonant Raman scattering is quantum interference between different scattering paths. We will demonstrate that the characteristic lineshape of the $2D$ mode in bilayer graphene is dictated by interference effects. In fact, the observed $2D$-mode lineshape strongly depends on the electronic broadening, *i.e.*, the inverse lifetime of the electronic states, and can be manipulated by external parameters, such as doping, defects, strain, or the laser excitation energy. We furthermore demonstrate that the splitting between both TO phonon branches in bilayer graphene along $\mathbf{K}-\mathbf{\Gamma}$ is of great importance for a correct analysis of the $2D$-mode lineshape. Using our correct assignment of the different peaks in the $2D$-mode spectrum, we present an approach to directly extract the TO phonon splitting from experimentally measured Raman spectra. Furthermore, we show that the splitting of the electronic bands can be also obtained using the presented analysis. Finally, we discuss the po-

larization dependence of the $2D$ mode and demonstrate that inner and outer processes can be partially selectively suppressed. Our results finally clarify the origin of the complex $2D$-mode lineshape in bilayer graphene.

The second part of this thesis is devoted to the analysis of double-resonant phonon-defect Raman modes. First, we will start with a general discussion of defects in graphene. Afterwards, we will present an analysis of the D mode in carbon nanotubes. In this context, different models were proposed concerning the dependence of the D-mode frequency on the tube diameter. In the present work, we attempt a harmonization all previous experimental results. As a starting point, we will introduce a universal geometrical model to describe the diameter and energy dependence of the resonant phonon wave-vector in the double-resonance process in carbon nanotubes. In the following, this model is applied to investigate the defect-induced D mode in chiral carbon nanotubes in order to calculate the D-mode frequency of CNTs at their resonant optical transitions. We will show that small-diameter tubes exhibit a higher D-mode frequency in general and that higher resonant optical transitions exhibit a systematically higher D-mode frequency. The experimentally observed discontinuities between different transition branches of the D-mode frequency is shown to be a consequence of curvature effects that alter the TO phonon dispersion around the **K** point. Furthermore, we show that the D-mode frequencies arrange in branches and families, in analogy to other Raman modes in carbon nanotubes, such as the RBM or the G mode. Our results finally harmonize the different previous experimental observations regarding the diameter dependence of the D mode in carbon nanotubes.

Subsequently, we present an analysis of the defect-induced D'' mode in graphene, few-layer graphene, and carbon nanotubes. We demonstrate that this mode results from a double-resonant intervalley scattering process of longitudinal acoustic (LA) phonons and defects. The experimentally observed peak dispersion with laser excitation energy has a value of $-80\,\mathrm{cm}^{-1}/\mathrm{eV}$ in single-layer graphene. We explain the characteristic asymmetric lineshape with a high-frequency tail by the dominant contribution of inner scattering processes with additional contributions from phonons next to the high-symmetry direction. Furthermore, the lineshape is shown to depend on the number of graphene layers and reflects the evolution of the electronic bands around the **K** point. In carbon nanotubes, the lineshape of the D'' mode is significantly broadened due to contributions from different tubes in or close to resonance with the excitation laser. Using our previously developed model, we observe very good agreement between our experimental data and the theoretically predicted frequencies.

In the last section of this chapter, we will present an *in-situ* analysis of the laser-induced oxidation process in single-layer graphene. As we will demonstrate, the oxidation process can be selectively initiated by high-power laser irradiation of graphene. We will investigate the laser-induced oxidation as a function of the irradiation time and discuss the different temporal evolution of the D, G, and $2D$ modes. This analysis demonstrates that basal-plane oxidation in graphene can be divided into two different stages, namely, tensile strain due to laser-induced heating and subsequent p-type doping due to oxidation. During the oxidation process, we observe an unexpected decrease of the D/G-mode ratio with increasing irradiation time and progressing oxidation, which we explain with laser-induced annealing, as well as by the doping dependence of the double-resonant D-mode scattering process. Finally, we present AFM measurements of the laser-irradiated single-layer graphene samples and demonstrate the possibility of tailoring graphene's properties selectively at the sub-μm scale using a fully optical method.

List of publications

1. Layer-number determination in graphene by out-of-plane phonons
   Felix Herziger, Patrick May, and Janina Maultzsch
   Physical Review B **85**, 235 447 (2012)

2. Molecular beam growth of micrometer-size graphene on mica
   Gunther Lippert, Jarek Dabrowski, Yuji Yamamotoa, Felix Herziger, Janina Maultzsch, Max C. Lemme, Wolfgang Mehr, and Grzegorz Lupina
   Carbon **52**, 40 – 48 (2012)

3. Molecular beam epitaxy of graphene on mica
   Gunther Lippert, Jarek Dabrowski, Yuji Yamamoto, Felix Herziger, Janina Maultzsch, Jens Baringhaus, Christoph Tegenkamp, Max C. Lemme, Wolfgang Mehr, and Grzegorz Lupina
   physica status solidi (b) **249**, 2507 – 2510 (2012)

4. Signature of the two-dimensional phonon dispersion in graphene probed by double-resonant Raman scattering
   Patrick May, Michele Lazzeri, Pedro Venezuela, Felix Herziger, Gordon Callsen, Juan S. Reparaz, Axel Hoffmann, Francesco Mauri, and Janina Maultzsch
   Physical Review B **87**, 075 402 (2013)

5. Influence of the layer number and stacking order on out-of-plane phonons in few-layer graphene
   Felix Herziger and Janina Maultzsch
   physica status solidi (b) **250**, 2697 – 2701 (2013)

6. Graphene Grown on Ge(001) from Atomic Source
   Gunther Lippert, Jarek Dabrowski, Thomas Schroeder, Markus Andreas Schubert, Yuji Yamamoto, Felix Herziger, Janina Maultzsch, Jens Baringhaus, Christoph Tegenkamp, Maria Carmen Asensio, Jose Avila, and Grzegorz Lupina
   Carbon **75**, 104 – 112 (2014)

7. Two-dimensional analysis of the double-resonant $2D$ Raman mode in bilayer graphene
   Felix Herziger, Matteo Calandra, Paola Gava, Patrick May, Michele Lazzeri, Francesco Mauri, and Janina Maultzsch
   Physical Review Letters **113**, 187 401 (2014)

8. Double-resonant LA phonon scattering in defective graphene and carbon nanotubes
   Felix Herziger, Christoph Tyborski, Oliver Ochedowski, Marika Schleberger, and Janina Maultzsch
   Physical Review B **90**, 245 431 (2014)

9. Beyond double-resonant Raman scattering: UV Raman spectroscopy on graphene, graphite and carbon nanotubes
   Christoph Tyborski, Felix Herziger, Roland Gillen, and Janina Maultzsch
   Physical Review B **92**, 041 401(R) (2015)

10. *In-situ* Raman study of laser-induced graphene oxidation
    Felix Herziger, Rasim Mirzayev, Emanuele Poliani, and Janina Maultzsch
    physica status solidi (b) **252**, 2451 – 2455 (2015)

11. Raman spectroscopy of nondispersive intermediate frequency modes and their overtones in carbon nanotubes
    Christoph Tyborski, Felix Herziger, and Janina Maultzsch
    physica status solidi (b) **252**, 2551 – 2557 (2015)

12. Understanding double-resonant Raman scattering in chiral carbon nanotubes: Diameter and energy dependence of the *D* mode
    Felix Herziger, Asmus Vierck, Jan Laudenbach, and Janina Maultzsch
    accepted for publication in Physical Review B

13. Diameter dependence of the defect-induced Raman modes in functionalized carbon nanotubes
    Jan Laudenbach, Daniel Schmid, Felix Herziger, Frank Hennrich, Manfred Kappes, Matthias Muoth, Miroslav Haluska, Christofer Hierold, Ferdinand Hof, Claudia Backes, Frank Hauke, Andreas Hirsch, and Janina Maultzsch
    in preparation

14. Tuning quantum interference in bilayer graphene: The effect of the electronic broadening on the double-resonant *2D* Raman mode
    Felix Herziger, Markus Schleuning, and Janina Maultzsch
    in preparation, based on Chapter 4.7

Contents

1 Introduction

The first successful isolation of two-dimensional layered materials, such as graphene, a single layer of sp^2-hybridized carbon atoms, or transition-metal dichalcogenides (TMDs), is today not much longer than ten years ago [1]. Despite their young history, both fundamental and application-oriented research on these materials is the fastest evolving field in solid-state physics [2–6]. This enormous scientific interest is usually motivated by quoting the extraordinary properties of these materials, such as high charge-carrier mobilities in graphene of up to $350000\,\mathrm{cm}^2/\mathrm{Vs}$ [7, 8], high mechanical robustness with breaking strengths of $42\,\mathrm{N/m}$ [9], and superior thermal conductivity of more than $5000\,\mathrm{W/mK}$ [10]. Consequently, Geim and Novoselov were awarded with the Nobel Prize in physics in 2010 for their 'groundbreaking experiments regarding the two-dimensional material graphene' [11]. The relative young history of two-dimensional materials can be understood from the fact that their existence was questioned for many decades. Due to fundamental theorems from Landau [12], Mermin, and Wagner [13, 14], a long-range order cannot exist in perfectly two-dimensional systems. Therefore, graphene was thought to be destroyed at finite temperatures by thermal fluctuations. However, the existence of graphene is explained with out-of-plane deformations of the graphene sheet [15], considering it as quasi two-dimensional.

Graphene can be regarded as the building block for all other carbon allotropes with reduced or higher dimensionality. Owing to the flexibility of the bonds between the carbon atoms, this element appears in a variety of different structures [2]. It can be folded into zero-dimensional fullerenes [16], reeled into one-dimensional carbon nanotubes (CNTs) [17] or layered into three-dimensional graphite [18]. Thus, graphene bridges the gap between the low-dimensional fullerenes and nanotubes and the bulk graphite. Ergo, graphene plays an important role in understanding the electronic and vibrational properties of all other carbon allotropes.

Among all two-dimensional materials, graphene has experienced the most scientific interest during the last decade. On the one hand, this might be explained with the easy availability of high-quality samples by the simple 'Scotch tape' method. On the other hand, this has certainly to do with the unique electronic bandstructure of graphene, which exhibits a linear dispersion of the π bands around the six edges of the hexagonal Brillouin zone. Directly connected to this linear dispersion are several interesting physical phenomena, such as the half-integer Quantum Hall effect at room temperature [19]. Furthermore, the outstanding electronic and mechanical

properties favor graphene for future applications in microelectronic devices, such as sensors [20, 21], high-frequency transistors [22, 23], or highly-efficient batteries [24]. However, the lack of an intrinsic bandgap prevents graphene from integration in digital logic devices in order to replace silicon technologies. In fact, one should not try to mimic "old" applications with new materials, but should rather find new applications for these materials. Nevertheless, there is still a broad range of possible applications of two-dimensional materials in future industries [25], *e.g.*, highly-sensitive, all-surface sensors [26, 27] or artificially engineered heterostructures for light harvesting and photocurrent generation [28].

Besides their high potential in future applications, graphene and related two-dimensional materials are very interesting from a fundamental point of view. For instance, molybdenum disulfide (MoS_2) observes a transition from an indirect to a direct semiconductor for less than two layers of MoS_2 [29]. Graphene in turn is a zero-gap semimetal with a linear electronic dispersion and allows the observation of fundamental physics such as the Hofstadter butterfly [30]. Fundamental research on graphene and TMDs often involves optical spectroscopy in order to probe various material characteristics. In this context, especially Raman spectroscopy has presented itself as a versatile experimental technique that allows the investigation of graphene's properties [31]. In fact, Raman scattering can give insights to the influences of defects [32, 33], doping [34, 35], strain [36–38] or the interaction with the substrate [39]. Furthermore, fundamental physical properties like the electron-phonon coupling or the mechanical strength can be probed [40–44].

In contrast to Raman scattering in conventional semiconductors, the Raman spectrum of graphene is dominated by so-called double-resonant Raman modes [45]. Double-resonant Raman scattering is a second-order process that combines two phonons with opposite momenta in order to satisfy momentum conservation. The concept of double-resonant Raman scattering has enabled a detailed analysis of the interplay between the electronic and vibrational structure in graphene. In fact, the measured peak shifts as a function of the laser energy are a convolution of the electronic and phonon dispersion. Thus, by tuning the laser excitation energy, we can probe the phonon dispersion if the electronic bandstructure is known or vice versa. In this context, the double-resonant $2D$ mode has been the most discussed and investigated peaks in the Raman spectrum of single- and few-layer graphene and is routinely used for graphene characterization [46]. For instance, a single-Lorentzian and symmetric lineshape of the $2D$ mode is usually considered as a benchmark for single-layer graphene [46], although this assumption oversimplifies the physics behind this scattering process [47–49]. Since the electronic bandstructure is uniquely captured in the lineshape of a double-resonant Raman mode, the situation gets even more complex when the $2D$ mode is analyzed in bi- and few-layer graphene. Here, the $2D$ mode is composed of multiple peaks with changing intensity as a function of the laser energy. The origin of these different contributions and the corresponding scattering processes in bilayer graphene were controversially discussed for many years [50–54]. However, the absence of a profound understanding of the double-resonant Raman scattering processes in bilayer graphene inhibits a more detailed analysis of experimental data.

Besides two-phonon scattering, momentum conservation in a double-resonant second-order Ra-

man process can be also satisfied by scattering of a phonon and a defect. This results in the so-called defect-induced D, D', and D'' modes. These Raman modes are frequently used to quantize defect densities in defective graphene and derive geometrical parameters of the defects [32]. Especially the D mode in carbon nanotubes was controversially discussed regarding the diameter dependence of its frequency [55–58]. In fact, different dependences of the D-mode frequency on the chiral index were suggested by various authors.

In this work, we will analyze various aspects of double-resonant Raman scattering in graphene, few-layer graphene and carbon nanotubes. Special attention will be paid to the analysis of the different double-resonant scattering processes in bilayer graphene and their assignment to the different spectral features that are observed experimentally. We present a consistent interpretation of the $2D$-mode spectrum in bilayer graphene and demonstrate that the lineshape can be externally manipulated, *e.g.*, by tuning the laser excitation energy or the defect density in the sample. Double-resonant Raman scattering processes are also observed in carbon nanotubes, however, due to multiple possibilities of phonon scattering in the electronic bandstructure, their detailed analysis remains often futile. Here, we develop a geometrical model to analyze these scattering processes in arbitrary carbon nanotubes and subsequently employ this new approach to investigate the dependence of the D-mode frequency on the CNT diameter and the laser excitation energy. In the following, we analyze a defect-induced double-resonant Raman mode that results from scattering of LA phonons with defects. The origin of this Raman mode can be traced to processes along the $\Gamma - K$ direction with additonal contributions away from this high-symmetry line, explaining the experimentally observed asymmetric lineshape. Our analysis of double-resonant Raman processes in sp^2-hybridized carbons is finalized by a discussion of the laser-induced oxidation process in graphene. By carefully analyzing the temporal evolution of the frequency, intensity, and width of the main Raman features in the spectrum of graphene, we demonstrate that the oxidation process is composed of two subsequent steps, namely, tensile strain and p-type doping.

The work is organized as follows: First, we will introduce the basic structural and electronic properties of graphene and carbon nanotubes in Chapter 2. The fundamental concepts of first-order and double-resonant Raman scattering will be explained in Chapter 3 together with a brief introduction to the vibrational properties of the investigated systems. In the following, we present a thorough analysis of the $2D$ mode in Bernal-stacked bilayer graphene in Chapter 4. We will clarify the dominant scattering processes for this Raman mode and disprove all previous works on this topic. Using our findings, we will present a simple approach to derive quantities such as the splitting between the two transverse optical phonon branches or the splitting between the electronic bands from experimental Raman spectra. Considering the quantum-mechanical character of double-resonant Raman scattering, we demonstrate a consistent interpretation of the $2D$-mode lineshape and discuss its dependence on the electronic broadening. This chapter is finalized by a discussion of the polarization dependence of the $2D$ mode in bilayer graphene. Chapter 5 is devoted to the analysis of defect-induced double-resonant Raman modes in graphene and carbon nanotubes. In Section 5.3, the double-resonant D-mode process in carbon nanotubes

is analyzed. We will present a harmonization of all previous experimental results on this topic and establish a simple geometric approach in order to model the double-resonance process in an arbitrary carbon nanotube. We will emphasize the importance of curvature-dependent corrections of the D-mode frequency and will show that the D-modes arrange in families and branches. In the following, we will analyze the D'' mode in graphene and carbon nanotubes in Section 5.4. We discuss the origin of the asymmetric lineshape of this Raman mode and analyze its layer-number dependence in graphene. The D'' mode in carbon nanotubes is analyzed within the framework of the previously developed model and we obtain good agreement between the calculated frequencies and our experimental data. The last Section 5.5 of this Chapter will present an *in-situ* analysis of the laser-induced graphene oxidation. We demonstrate that the oxidation process in graphene can be selectively initiated. The temporal evolution of the G and $2D$ mode is analyzed and reveals two different subsequent processes upon laser irradiation, *i.e.*, tensile strain due to laser-induced heating and subsequent p-type doping due to oxidation. Our results demonstrate the possibility of sub-μm patterning of graphene by an all-optical method.

2 Basic electronic properties of graphene and carbon nanotubes

In this chapter, we will briefly recapitulate the basic electronic and vibrational properties of graphene and carbon nanotubes. Since the electronic band structure and phonon dispersion of carbon nanotubes can be, to a certain extent, derived from graphene's properties within the zone-folding approach, we will start with the description of graphene.

2.1 Tight-binding approach for graphene

Graphene is a single layer of sp^2-hybridized carbon atoms arranged in a hexagonal lattice. The unit cell contains two atoms A and B, which each belong to a different sublattice [compare Fig. 2.1 (a)]. The in-plane bonds between atom A and the three neighboring B atoms are formed by σ bonds. The formation of strong σ bonds is responsible for the robustness of all sp^2-hybridized carbon allotropes [2]. Perpendicular to these in-plane bonds, the fourth valence electrons form $2p_z$ orbitals which can bind covalently to neighboring atoms, leading to the formation of π-bands [2]. Electrons from this electronic band are usually referred to as π-electrons. In contrast to the filled σ states, the π orbitals are half-filled and thus give rise to electronic states in the visible energy range [2]. The distance between neighboring carbon atoms is [59]

$$a_{\mathrm{CC}} \approx 1.422\,\text{Å},$$

resulting in a lattice constant of

$$a_0 = \sqrt{3}\, a_{\mathrm{CC}} \approx 2.463\,\text{Å}.$$

The lattice vectors in Fig. 2.1 in real and reciprocal space are given by

$$\mathbf{a}_1 = \frac{a_{\mathrm{CC}}}{2}\,(3,\,\sqrt{3}) \qquad \mathbf{a}_2 = \frac{a_{\mathrm{CC}}}{2}\,(3,\,-\sqrt{3}) \qquad \text{and} \tag{2.1}$$

$$\mathbf{k}_1 = \frac{2\,\pi}{\sqrt{3}\,a_0}\,(-\sqrt{3},1) \qquad \mathbf{k}_2 = \frac{2\,\pi}{\sqrt{3}\,a_0}\,(\sqrt{3},1), \tag{2.2}$$

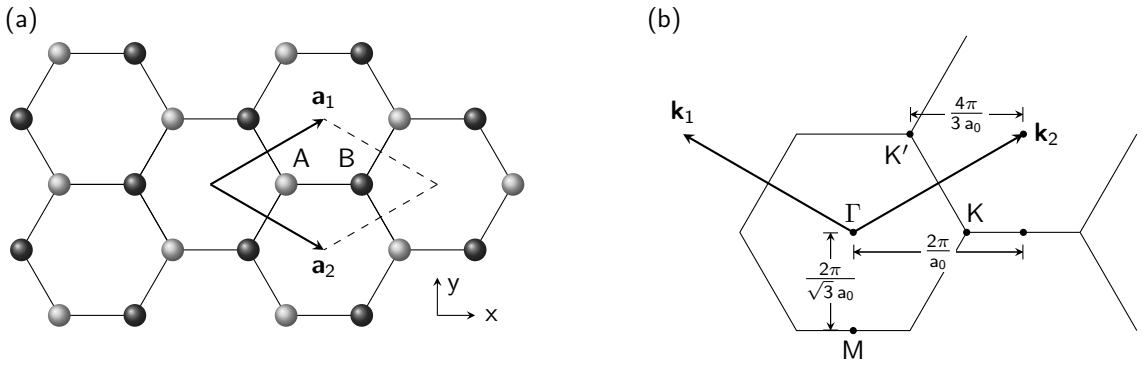

Figure 2.1: (a) Lattice structure of graphene in real space. The atoms belonging to the two interpenetrating sublattices are shown in gray and lightgray. $\mathbf{a_1}$ and $\mathbf{a_2}$ represent the lattice unit vectors, the unit cell is indicated with dashed lines. (b) Brillouin zone of graphene in reciprocal space with the high-symmetry points $\mathbf{\Gamma}$, $\mathbf{K}$, $\mathbf{K'}$, and $\mathbf{M}$. Important distances between high-symmetry points are indicated.

respectively. The Fourier transformation of graphene's real-space lattice is again a hexagonal lattice, which is shown in Fig. 2.1(b). With respect to real space, the unit cell in reciprocal space is rotated by 90° inside the graphene plane. The edges of the Brillouin zone are labeled as $\mathbf{K}$ and $\mathbf{K'}$, the center between them is named $\mathbf{M}$, and the zone center is referred to as $\mathbf{\Gamma}$.
Graphene can be easily prepared by the so-called 'Scotch tape' method. This technique relies on the weak van-der-Waals forces between adjacent graphene layers compared to the strong in-plane σ bonds between neighboring carbon atoms. In brief, natural graphite crystals are placed on the sticky side of an adhesive tape and subsequently peeled apart several times. Finally, the adhesive tape is gently pressed on a target substrate and slowly removed at an angle of 90° to the substrate surface. Using this method, large-area and single-crystal graphene samples can be prepared with sizes of up to $200 \times 50\,\mu\mathrm{m}^2$. All graphene samples in this work were prepared by mechanical exfolilation on SiO_2/Si substrates. The silicon dioxide thickness was carefully chosen to be 100 nm, in order to increase the optical contrast of the graphene samples on the substrates [60]. Freestanding graphene samples were prepared by exfoliation on SiO_2/Si substrates with 8 μm deep holes. These structured substrates were produced in the Fraunhofer IZM by reactive ion etching (RIE), also known as Bosch process, using sulfur hexafluoride (SF_6) and octafluorocyclobutane (C_4F_8). We used natural graphite crystals from NGS Naturgraphit GmbH, Germany.
The electronic bandstructure of graphene can be calculated within the tight-binding approximation, which was first demonstrated by Wallace in 1947 [61]. This method involves the interaction with a certain number of nearest neighbors to an atom and uses Bloch functions as linear combinations of the atomic wave functions. In the original work by Wallace [61], the overlap between p_z orbitals centered at different atoms was neglected. This assumption can reproduce the low-energy region close to the $\mathbf{K}$ point. However, for a better agreement between calculation and experiment on a larger energy range, the overlap between different p_z orbitals and the interaction

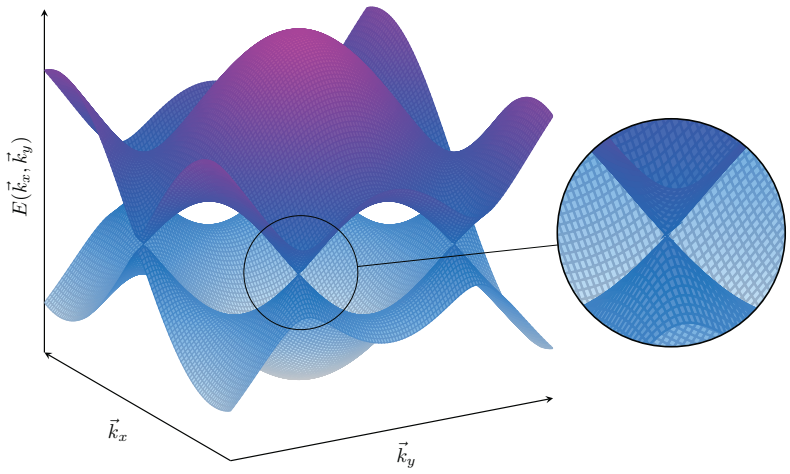

Figure 2.2: Electronic bandstructure of graphene from a third-nearest neighbor tight-binding approach. The inset shows a magnified view of the electronic bands around a **K** point. The linear dispersion of the electronic bands can be clearly seen.

with a larger number of neighboring atoms has to be considered.

By including third-nearest-neighbors, the band structure for the π valence and the π^* conduction band is given by

$$E^{\pm}(\mathbf{k}) = \frac{-(-2\,E_0 + E_1) \mp \sqrt{(-2\,E_0 + E_1)^2 - 4\,E_2\,E_3}}{2\,E_3}, \tag{2.3}$$

where the E_i refer to different combinations of the overlaps and matrix elements of wave functions from atoms A and B and are explicitly given in Ref. [62]. We therefore refer the reader to this work or the more detailed derivation by Reich *et al.* in Ref. [63]. The expression in Eq. (2.3) contains various parameters, which are usually chosen to reproduce *ab-initio* calculated bandstructures for optical transitions below 4 eV. This set of parameters is usually referred to as the 'Optical' fit and yields a deviation of less than 5 meV with *ab-initio* results [63]. The resulting electronic bandstructure is shown in Figure 2.2. The crossing of the bands at the six edges of the first Brillouin zone and the linearity of the electronic dispersion around these points can be clearly seen. Since the valence and conduction bands touch at the **K** points, graphene is said to be a semimetal.

In physics, a linear energy dispersion is otherwise only known from Dirac physics for massless particles like photons. Therefore, electrons in graphene are referred to as 'massless Dirac particles' [19]. This analogy only holds for the region next to the edges of the first Brillouin zone, where the electronic bands can be considered linear. However, recent works showed that the absence of screening effects in suspended graphene reshapes the linear dispersion due to increased electron-electron interaction [64–66]. In fact, the electronic dispersion close to the **K**

points can be described by a logarithmic divergence, as predicted by perturbation theory [66]. Nevertheless, charge carriers are commonly still considered as massless Dirac fermions.
Due to the linear dispersion of the electron and hole states around the **K** points, interesting physical phenomena such as the anomalous half-integer Quantum Hall effect at room temperature arise [19, 67]. Furthermore, charge carriers, both electrons and holes, exhibit mobilities in excess of $15\,000\,\mathrm{cm}^2/(\mathrm{Vs})$ at room temperature [18]. Moreover, even higher electron mobilities of $200\,000\,\mathrm{cm}^2/(\mathrm{Vs})$ has been observed in suspended ultra-clean graphene at low temperatures of 5 K [7]. Only recently, mobilities of up to $350\,000\,\mathrm{cm}^2/(\mathrm{Vs})$ have been realized in CVD-grown graphene on hexagonal boron-nitride at $T = 1.6\,\mathrm{K}$ [8]. For comparison, charge carrier mobilities for electrons and holes in silicon are 1 400 and $450\,\mathrm{cm}^2/(\mathrm{Vs})$ at 300 K temperature [68], respectively. Despite these high mobilities compared to conventional semiconductors, graphene's potential for applications in transitors and logic devices is rather limited. This can be understood from the lack of a bandgap in single-layer graphene that inhibit a controllable switching between On and Off states. There are several approaches to overcome this problem, *e.g.*, by functionalization of graphene with hydrogen for instance [69, 70] or by spatial confinement to graphene quantum dots [71]. Another route to obtain a bandgap in graphene structures is the usage of bilayer graphene. In these systems, a bandgap as large as 250 meV can be tuned by breaking the inversion symmetry between the both layers [72], *e.g.*, by applying an external electric field in out-of-plane direction. However, bilayer graphene does not present the same electronic structure as single-layer graphene. In fact, the linear electronic bands from single-layer graphene are replaced by two set of parabolic valence and conduction bands, as in usual semiconductors. Therefore, electrons in bilayer graphene cannot be considered as massless, relativistic particles but are said to be massive Dirac fermions. In principle, the electronic band structure of N-layer graphene can be understood from zone-folding of the bulk graphite electronic dispersion along the $\mathbf{K} - \mathbf{H}$ high-symmetry direction (out-of-plane direction) [73]. Therefore, for layer numbers $N > 2$, the electronic band structure is a superposition of contributions from massless and massive Dirac particles, depending whether n is even or odd. A more detailed introduction to the electronic properties of bilayer graphene will be given in Chapter 4.1.

2.2 The electronic bandstructure of carbon nanotubes from a zone-folding approach

Single-walled carbon nanotubes (CNTs) can be regarded as rolled-up, seamless graphene sheets with typical diameters in the range of 7 to 15 Å [17]. Due to the periodic boundary conditions and the reduced dimensionality of these structures, quantization effects occur, which can drastically alter the electronic and vibrational properties as compared to graphene. In fact, depending on the roll-up angle of the graphene sheet, semiconducting or metallic behavior of the CNTs can be observed [74].
The crystallographic structure of a carbon nanotube is uniquely defined by the two integer

indices (n_1, n_2), which define the so-called chiral vector $\mathbf{c}$. The chiral vector represents the circumference of the rolled-up structure and is given by [63]

$$\mathbf{c} = n_1\,\mathbf{a}_1 + n_2\,\mathbf{a}_2. \tag{2.4}$$

Since the geometry of CNTs is derived from graphene's structure, the vectors $\mathbf{a}_1$ and $\mathbf{a}_2$ refer to the unit-cell vectors of graphene. Figure 2.3 illustrates the chiral vector for the simple case of a (5,2) carbon nanotube. The structure of CNTs is further described by the translational vector, which is given by the shortest vector perpendicular to $\mathbf{c}$ that connects two equivalent points in the lattice. Both, the chiral vector and the translational vector define the unit cell of a carbon nanotube in real space. Closely related to the chiral vector is the chiral angle θ, which is the angle enclosed by $\mathbf{c}$ and $\mathbf{a}_1$. For $\theta = 0°$ or $\theta = 30°$ the CNT is called a zig-zag or an armchair tube, respectively. For all other angles in between, the tubes are referred to as chiral CNTs. Since the chiral vector reflects the circumference of a CNT, the length of $\mathbf{c}$ is directly related to the tube diameter d by [63]

$$d = \frac{|\mathbf{c}|}{\pi} = \frac{a_0}{\pi}\sqrt{n_1^2 + n_1\,n_2 + n_2^2}. \tag{2.5}$$

The experimentally observed diameter distribution of a CNT ensemble depends on the different synthesis methods and is usually in the range between 7 and 15 Å [63, 75]. For instance, CNTs produced by high-pressure CO conversion (HiPco process) usually exhibit a Gaussian diameter distribution with a mean diameter of 9.5 Å and spanning a range of approximately ±3 Å [76, 77]. The chiral angles in CNT ensembles are usually evenly distributed [63]. In contrast to their diameter, the length of a CNT is typically orders of magnitude larger. Therefore, carbon nanotubes are considered as being quasi one-dimensional.

The confinement of the graphene layer into a one-dimensional structure imposes periodic boundary conditions along the circumferential vector $\mathbf{c}$ of the CNT, leading to a quantization of the Brillouin zone. The reciprocal space of carbon nanotubes is spanned by the two vectors $\mathbf{k}_z$ and $\mathbf{k}_\perp$, which can be found by linear combination of graphene's reciprocal vectors $\mathbf{k}_1$ and $\mathbf{k}_2$. The Brillouin zone of CNTs is continuous along the vector $\mathbf{k}_z$, which can be identified with the axial direction of the nanotube. In contrast, the Brillouin zone is quantized in $\mathbf{k}_\perp$ direction (along the circumference). Thus, the Brillouin zone of CNTs contains of multiple subbands, which depend in their number, length, spacing, and direction on (n_1, n_2). Using the tight-binding zone-folding approach, these subbands can be described in a simplified model that assumes that all electronic bands originate from the bandstructure of graphene. We will point out the limitations of this model later in this chapter. For a more detailed introduction to the various CNT parameters and variables that depend on the chiral indices, as well as an introduction to zone folding in general, we refer the reader to the extensive works by Reich *et al.* and Maultzsch *et al.* [63, 78]. Here, we just want to introduce the parameter q, which is given by the number of graphene

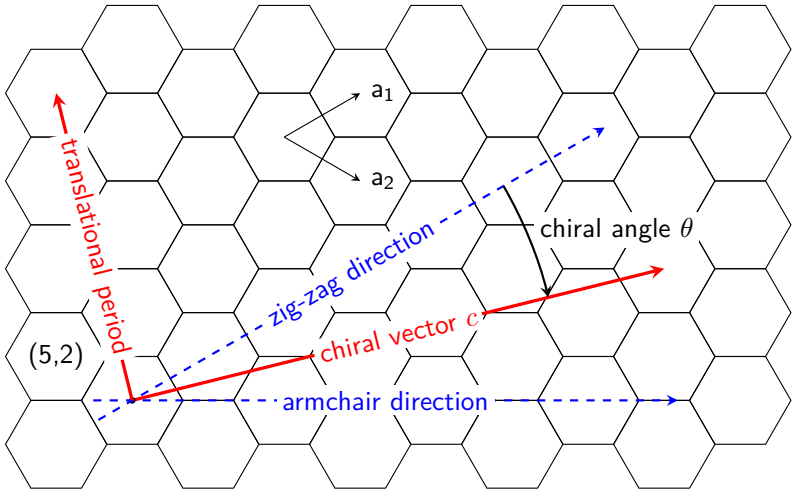

Figure 2.3: Lattice vectors for a (5,2) carbon nanotubes showing the chiral vector **c** and the translational vector perpendicular to **c**. Armchair and zig-zag directions are indicated by the blue, dashed lines.

hexagons per unit cell and also defines the number of electronic subbands. q can be written as

$$q\,(n_1, n_2) = \frac{2\,(n_1^2 + n_2^2 + n_1\,n_2)}{n(n_1, n_2)\,\mathcal{R}(n_1, n_2)},$$

where n is the greatest common divisor of n_1 and n_2; $\mathcal{R}$ has the value 3 if $(n_1 - n_2)/3n$ is integer and has the value 1 otherwise. The Brillouin zone of carbon nanotubes can be now understood as parallel cuts through the Brillouin zone of graphene, where each subband is labeled by an integer quantum number q. This representation of the Brillouin zone of a CNT is usually referred to as the linear representation. Depending on (n_1, n_2), there might be a subband that contains the **K** point of graphene's Brillouin zone. In such case, the bandgap vanishes and the carbon nanotube is said to be metallic [63]. If the subbands of a CNT do not contain the **K** point, but cut the Brillouin zone close by, the bandgap has a finite value and the tubes exhibit semiconducting behavior. Hence, according to their chiral indices, all CNTs can be classified into three different families ν, which are given by

$$\nu = (n_1 - n_2) \bmod 3. \tag{2.6}$$

If $\nu = 0$, the subbands cross the **K** point and the CNT is metallic; for $\nu = \pm 1$ the nanotubes exhibit semiconducting properties. As can be easily seen from Eq. (2.6), one-third of all carbon nanotubes are metallic. However, in reality, most metallic, non-armchair carbon nanotubes exhibit a small bandgap [79, 80]. The semiconducting CNTs are further separated into $\nu = -1$ and $\nu = +1$ tubes, depending if their closest subbands to **K** is on the $\mathbf{K} - \mathbf{M}$ or on the $\mathbf{K} - \mathbf{\Gamma}$ high-symmetry direction, respectively. This situation is shown in Fig. 2.4. Here, we plot the subbands of three different zig-zag carbon nanotubes inside the Brillouin zone of graphene, each

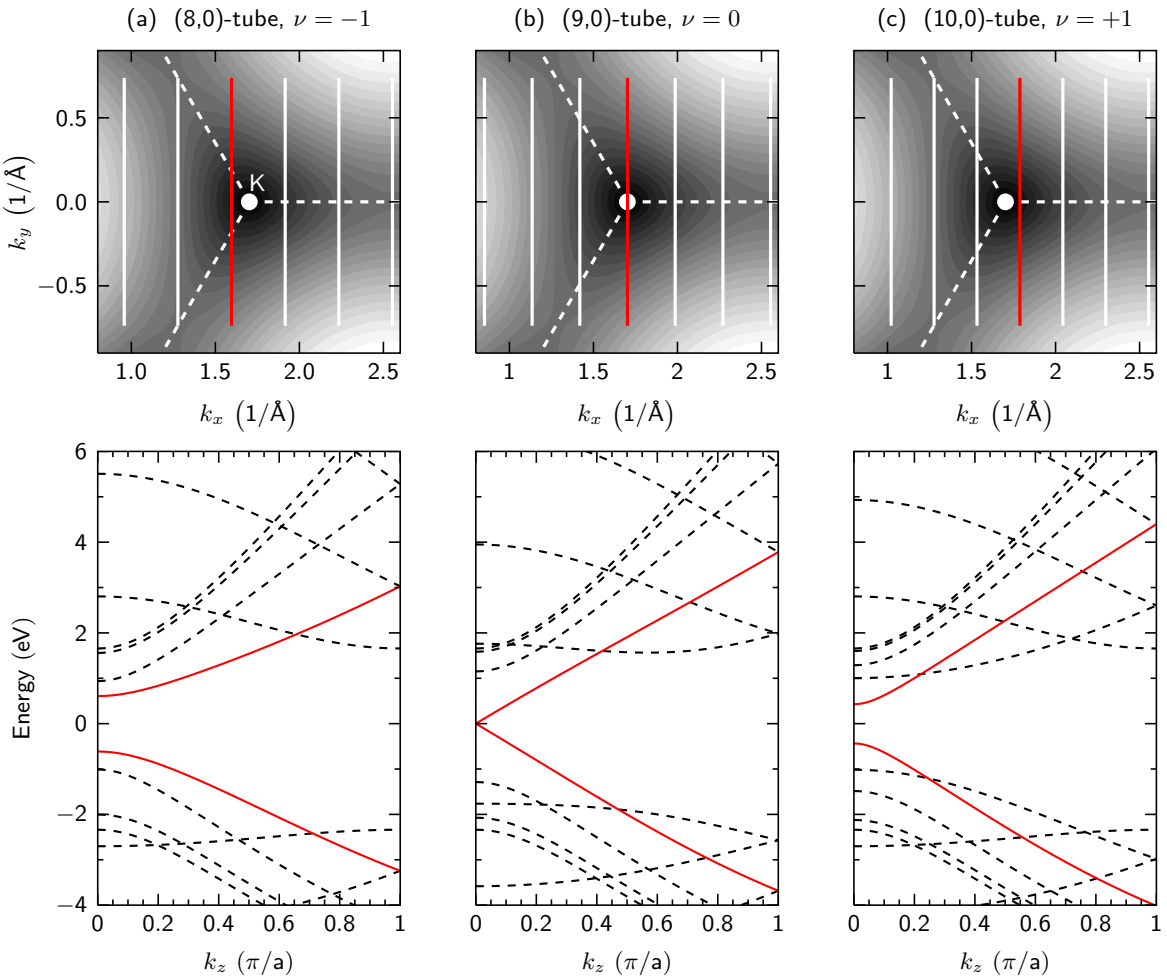

Figure 2.4: Brillouin zones (top row) and electronic band structures (bottom row) of zig-zag carbon nanotubes from different families ν. The contour plots in the top row represent the two-dimensional electron bands from single-layer graphene around the **K** point. The dashed, white lines denote the $\mathbf{K} - \mathbf{M}$ high-symmetry directions. Solid lines represent the different subbands of the CNT's reciprocal space; the red line refers to the subband that is closest to **K**. The electronic bandstructure was calculated from a third-nearest neighbor tight-binding approach. Electronic bands that refer to the red subbands from the top row are shown in red colour in the bottom row as well.

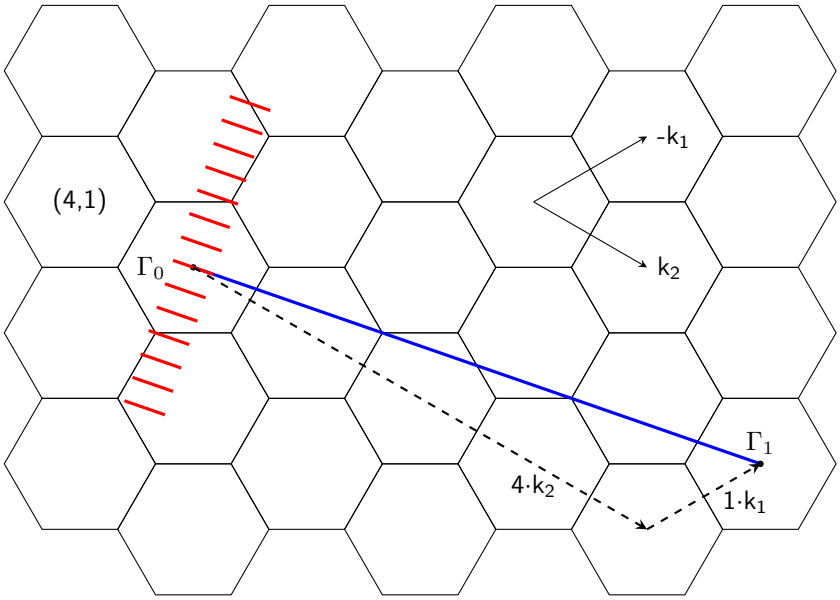

Figure 2.5: Linear and helical Brillouin zone of a (4,1)-tube. The Brillouin zone in linear representation consists of $q = 14$ bands (red lines), whereas in helical representation the Brillouin zone can be reduced to one single band (blue line). The helical band can be easily visualized by "counting" the hexagons along the reciprocal unit-cell vectors according to the chiral indices of the carbon nanotube (compare the dashed arrows).

representing a different family ν. The red-colored line in each plot represents the subband that runs closest to the **K** point. As expected, this band crosses the **K** point for the (9,0) tube, whereas it runs close by for the (8,0) and (10,0) tubes. Below these contour plots, we also show the electronic bandstructure of the corresponding carbon nanotubes along their continuous reciprocal lattice vector $\mathbf{k}_z$. Again, the red-colored electronic bands correspond to the subbands which are closest to **K**. We can clearly see the linear dispersion and the absence of a bandgap for the metallic (9,0) tube. For both semiconducting CNTs we observe a finite bandgap, as well as a parabolic dispersion of the electronic bands.

In the following, we want to introduce an alternative representation of the Brillouin zone of carbon nanotubes, which is the so-called helical representation [63, 81]. As described above, the number of subbands in linear quantum numbers corresponds to q. However, the value of q increases quadratically with the tube diameter and therefore approaches large values rapidly. For instance, the number of subbands for a (7,5) tube is $q = 218$, whereas a (9,7) has already $q = 386$ subbands. Ergo, the visualization of bandstructures or phonon dispersions in linear quantum numbers gets confusing quickly. By introducing helical quantum numbers, the q bands in linear representation are transformed to an equivalent representation of n bands in helical quantum numbers [81], typically enumerated by $\widetilde{m}$. In general, n is much smaller than q, *e.g.*, $q = 386$ but $n = 1$ for a (9,7) carbon nanotube.

In analogy to the linear representation, the electronic bandstructure in helical quantum numbers is given by the cut of the helical wave-vector $\widetilde{\mathbf{k}}_z$ with graphene's π and π^* bands along its path in

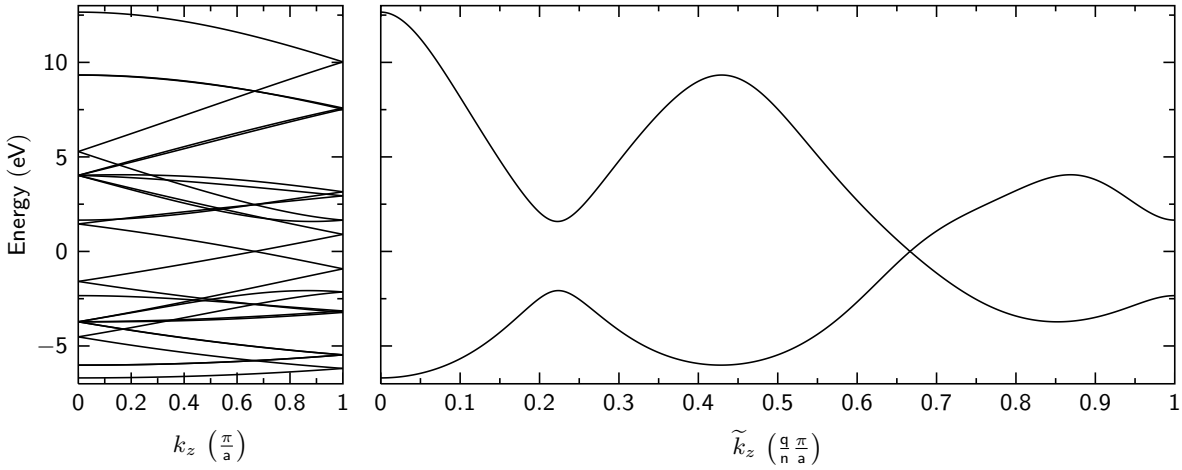

Figure 2.6: Linear and helical electronic bandstructure of a (4,1)-tube from a third-nearest-neighbor tight-binding approach.

reciprocal space. By rearranging the q linear bands to n helical bands, the domain is extended by the factor q/n and is defined in the interval $(-q\,\pi/n\,a, q\,\pi/n\,a]$, where a is the lattice constant of the CNT. Here, (and] indicate open and closed interval limits, respectively. The helical wave-vector $\widetilde{\mathbf{k}}_z$ is given by

$$\widetilde{\mathbf{k}}_z = \frac{1}{n}\,(-n_2\,\mathbf{k}_1 + n_1\,\mathbf{k}_2) + \Delta\mathbf{k}_1(n_1, n_2) + \Delta\mathbf{k}_2(n_1, n_2).$$

The $\Delta\mathbf{k}_i$ describe the shift of the different subbands and are given by

$$\Delta\mathbf{k}_1(n_1, n_2) = \frac{2\,n_1 + n_2 \cdot (1 + r(n_1, n_2) \cdot \mathcal{R}(n_1, n_2))}{\mathcal{R}(n_1, n_2) \cdot q(n_1, n_2)}$$

and

$$\Delta\mathbf{k}_2(n_1, n_2) = \frac{2\,n_2 + n_1 \cdot (1 + r(n_1, n_2) \cdot \mathcal{R}(n_1, n_2))}{\mathcal{R}(n_1, n_2) \cdot q(n_1, n_2)}.$$

The quantity r reflects the pitch of the screw axis in chiral tubes and is given by a cumbersome expression depending on n_1 and n_2, which can be looked up in Ref. [63].

In contrast to the linear representation, the prefactors of $\mathbf{k}_1$ and $\mathbf{k}_2$ in helical quantum numbers are by defintion always integers. This means that the $\widetilde{m} = 0$ band always connects two Γ points, which are given by $\Gamma = (0, 0)$ and $\Gamma_1 = (-n_2/n, n_1/n)$ in units of the reciprocal lattice vectors. All other $\widetilde{m} \neq 0$ bands can be found by a parallel translation of the zeroth band. In Figure 2.5, we show the relation between the linear and helical representation of the Brillouin zone for a (4,1) carbon nanotube. The red lines denote the $q = 14$ subbands in linear representation, whereas the blue line indicates the $n = 1$ band in helical representation. The helical wave-vector can be easily obtained by "counting" the Γ points (hexagons) along the reciprocal unit-cell vectors according

to the chiral indices of the carbon nanotube (compare the dashed arrows). In Figure 2.6, we also plot the corresponding electronic bands for the (4,1) tube in both representations. The advantage of using the helical representation for visualization of the electronic bandstructure or the phonon dispersion can be easily seen and does not need any further motivation. Moreover, also Umklapp processes can be visualized easily.
Although not explicitly shown here, the zone-folding approach can of course also be used to derive the phonon dispersion of carbon nanotubes from the phonon dispersion of single-layer graphene.

2.3 Curvature effects on the electronic bandstructure and phonon dispersion of carbon nanotubes

In the last section of this chapter, we want to comment on the limitations of the tight-binding zone-folding approach for the calculation of the electronic bandstructure and phonon dispersion of carbon nanotubes from the corresponding quantities in graphene.
The widely used zone-folding approach is based on the fundamental assumption that all angles and bond lengths in the rolled-up carbon nanotube are equivalent to the initial lattice parameters of graphene [82]. However, this approximation is certainly incorrect if the diameter of the CNT becomes too small. The exact value of 'too small' cannot be ultimately given, however, below we will discuss and compare different theoretical models that incorporate curvature effects.
As mentioned before, by deriving the electronic bands or the phonon dispersion by zone folding from graphene's properties, one will never observe curvature-related effects on these quantities. A very prominent example of curvature effects is the radial-breathing mode (RBM) in carbon nanotubes. This mode exhibits a strong diameter dependence on its frequency and is therefore commonly used for characterization and (n_1, n_2) assignment [83, 84]. However, this Raman mode is absent in single-layer graphene. In fact, the RBM-related phonon branch in carbon nanotubes originates from the acoustic ZA phonon branch in single-layer graphene, which has a frequency of $\omega_{\mathrm{ZA}} = 0\,\mathrm{cm}^{-1}$ at Γ. Zone folding will never increase this Γ point frequency and, therefore, will result in incorrect results when phonon dispersions are calculated. Nevertheless, there are different approaches beyond the tight-binding zone-folding method in order to account for curvature effects in carbon nanotubes.
The most basic approach to calculate the electronic and vibrational properties of carbon nanotubes is based on *ab-initio* density functional theory (DFT). However, as the number of carbon atoms in the CNT unit cell correspond to $2q$, these calculations will get time- and resource-intensive very quickly for larger tubes. Moreover, most DFT codes rely on periodic boundary conditions, thus, in order to avoid interaction between periodic images of the CNT unit cells, a lot of vacuum is needed between them, which further increases the calculational costs. However, small carbon nanotubes with diameters around 4 Å were successfully calculated using the SIESTA code [85]. *Ab-initio* calculations of electronic and vibrational properties of carbon nan-

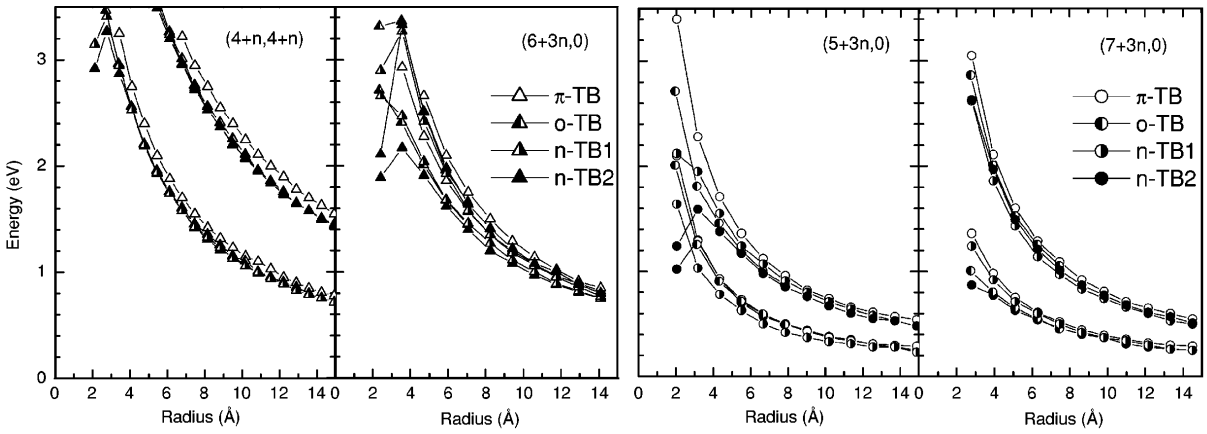

Figure 2.7: Comparison of the optical transition energies for the E_{11} and E_{22} transition as a function of CNT radius for different calculational models. The different calculational approaches are: $(\pi - TB)$ Simple zone-folding approach of the π/π^* bands of graphene, (o-TB) orthogonal tight-binding that considers all four valence electrons of graphene, and (n-TB) symmetry-adapted non-orthogonal tight-binding model that accounts for the overlap between the π and σ orbitals. Figure was taken from Ref. [80].

otubes were also demonstrated for CNTs with diameters of up to 8 Å diameter [86]. However, if the size of the unit-cell of a carbon nanotube contains more than 200 atoms, *ab-initio* approaches exceed reasonable computing times on commonly used servers [1]. Nevertheless, there are various tight-binding based approaches that allow calculations of CNT structures within reasonable computing times. These models commonly employ DFT-derived input parameters for the interaction of the π and σ orbitals and also consider the helical symmetry of carbon nanotubes, thus, reducing the eigenvalue problem for the electrons to diagonalization of 8×8 matrices [80, 87–94]. For instance, Barros *et al.* demonstrated the analysis of torsional strain and curvature-induced lattice relaxations in CNTs [93, 94]. Furthermore, Popov *et al.* presented the successful investigation of various electronic and vibrational parameters on the carbon nanotube diameter using a non-orthogonal tight-binding scheme [80, 87, 88]. Figure 2.7 compares the calculated optical transition energies of a carbon nanotube for different tight-binding models. Damnjanović and Milošević developed a symmetry-adapted modified group projector technique to calculate the properties of CNTs [89–91]. This approach is implemented in the POLSym code [95], which will be used in Chapter 5.3 for the calculation of phonon dispersions and electronic bandstructures of carbon nanotubes.

As shown by various authors, the differences in bond length and angle can be ignored for tube diameters above 10 Å [82, 87]. Moreover, Popov *et al.* demonstrated that differences of the geometric parameters between the graphene lattice and an energetically optimized carbon nanotube structure are less than 5 % for tube diameters above 6 Å [80, 87].

[1] Private communication with R. Gillen (TU Berlin)

3 Inelastic light scattering

This chapter will introduce the basic concepts of inelastic light-scattering by phonons, *i.e.*, Raman scattering and double-resonant Raman scattering. First, we will briefly introduce phonons as quasi-particles of the crystal vibrations and explain Raman scattering with phonons having wave vectors $q \approx 0$, *i.e.*, the first-order Raman spectrum. However, besides the fundamental Raman modes, in graphitic systems also $q \neq 0$ phonons can be observed. This is due to a process called double-resonant Raman scattering. The characteristics of this inelastic scattering process will be explained afterwards. Finally, we will introduce the Raman spectrum of graphene, bilayer graphene, and carbon nanotubes and discuss the characteristic Raman modes briefly.

3.1 Phonons

The quantized vibrations of atoms around their equilibrium positions in the lattice can be considered as quasi-particles and are usually referred to as phonons. These atomic vibrations are a coupled motion of the entire lattice within the potential of the atomic nuclei. The interaction between atoms in a crystal is given by an effective potential V_{eff} that depends on the different chemical or physical bonds between them, *e.g.*, covalent bonds or van-der-Waals bonds. For elongations $\mathbf{u}$ that are small compared to the interatomic distances, the potential can be expanded in a Taylor series around the atoms' equilibrium positions $\mathbf{R}^0$ [96, 97]

$$V_{\text{eff}} = V_0 + \sum_i \left(\frac{\partial V}{\partial u_i}\right)_0 \cdot u_i + \sum_{i,j} \left(\frac{\partial^2 V}{\partial u_i \, \partial u_j}\right)_0 \cdot u_i \, u_j + \dots \tag{3.1}$$

The subscript '0' indicates that these expressions are calculated at the equilibrium position of the nuclei. The first term does not vary as a function of $\mathbf{u}$ and thus can be identified with the zero-point energy of the potential. The second (linear) term reflects the forces on the atoms and is, by definition, zero, as the forces on the atoms at their equilibrium position must vanish. The harmonic approximation relies on the assumption that all terms higher than the third (quadratic) term in the Taylor series are negligible. The quadratic term

$$f_{ij} = \left(\frac{\partial^2 V}{\partial u_i \, \partial u_j}\right)_0 \tag{3.2}$$

is a symmetric ($f_{ij} = f_{ji}$), positive-definite matrix, where the f_{ij} are referred to as the (mass-weighted) interatomic force constants. Renormalization of this matrix by the atomic masses in the lattice and Fourier transformation leads to the so-called dynamical matrix $\mathbf{D}$. In a three-dimensional crystal with α atoms, this matrix has the dimension $3\alpha \times 3\alpha$. Thus, in realistic crystals with a large number of atoms, this leads to a tremendous amount of coupled differential equations. The coefficients of the dynamical matrix $\mathbf{D}$ can be described by an eigenvalue problem of the following form [96]

$$\omega^2 \nu = \sum \mathbf{D}(\mathbf{R}_0 - \mathbf{R}_0') \cdot \nu'. \tag{3.3}$$

For the sake of clarity, indices in the summation were omitted. Here, ν is the time and space-dependent amplitude of an atomic vibration with frequency ω and $(\mathbf{R}_0 - \mathbf{R}_0')$ is the relative distance of two unit cells in the crystal. By making benefit of the translational invariance of the crystal (and other mathematical operations) the eigenvalue problem can be reduced to a $3\beta \times 3\beta$ matrix, where β refers to the number of unit cell atoms. Thus, the eigenvalue equation can be written as [96]

$$\omega^2 \upsilon = \sum \mathbf{D}(\mathbf{q}) \cdot \upsilon', \tag{3.4}$$

where υ is the lattice-side independent amplitude of the vibration. In general, there are 3β eigenvalues for every wave vector $\mathbf{q}$. These eigenvalues reflect the phonon frequencies at the $\mathbf{\Gamma}$ point ($\mathbf{q} = 0$) or at any wave vector inside the Brillouin zone ($\mathbf{q} \neq 0$). In fact, the eigenvalues are grouped into different branches, so-called phonon branches, that continuously evolve inside the Brillouin zone. The dependence between the phonon frequency ω and the phonon wave-vector $\mathbf{q}$ is referred to as the phonon dispersion $\omega(\mathbf{q})$. For a crystal in d dimensions, there are always d phonon branches that satisfy $\omega(\mathbf{q} \to 0) \to 0$. These phonon branches are usually referred to as acoustic phonons, as the slope of these branches close to $\mathbf{\Gamma}$ is approximately linear and reflects the speed of sound in the crystal. Thus, in a crystal with $\beta = 1$ there are only acoustic phonons. For $\beta \geq 2$, also phonon branches with finite frequencies at the $\mathbf{\Gamma}$ point can be observed. These vibrations are referred to as optical phonons. In general, when the unit cell of a three-dimensional crystal contains β atoms, the phonon spectra consist of 3 acoustic and $3\,(\beta - 1)$ optical branches. The optical and acoustic phonons are further split into two transverse and one longitudinal mode, which may be degenerate depending on the crystal symmetry.

3.2 First-order Raman scattering

The particle-like properties of phonons become manifested by the interaction with other quasi-particles, like photons or electrons. One possibility of this interaction is Raman scattering, which is an inelastic light-scattering process of photons by phonons which is mediated by electrons

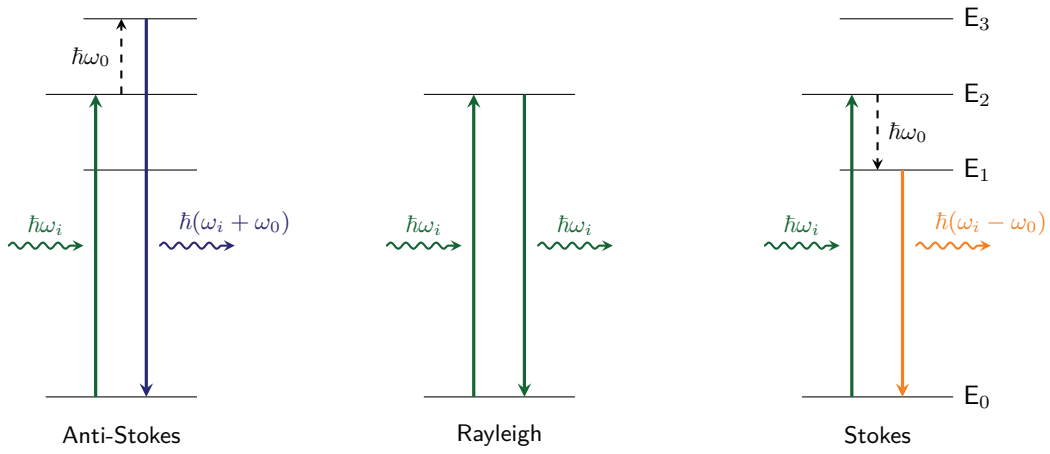

Figure 3.1: Schematic diagrams of Stokes, anti-Stokes and Rayleigh scattering. $\hbar\omega_i$ represents the energy of the incoming photon and $\hbar\omega_0$ the energy of the phonon. E_0 denotes the ground state of the system and E_i (i=1,2,3) excited states, which can be either real or virtual.

and holes. This effect was theoretically predicted in 1923 by Smekal [98] and experimentally demonstrated in 1928 by Raman [99], yielding Sir Raman the Nobel prize in physics in 1930. The Raman effect is today widely used to study the electronic and vibrational properties of all kinds of solids and gases. Due to its contactless and non-destructive nature, Raman spectroscopy has proven itself as a very versatile tool to investigate carbon systems like graphene or carbon nanotubes [31, 63]. Although Raman scattering is described as scattering of photons with phonons, the scattering process is mediated by electrons and holes. Thus, within perturbation theory, Raman scattering is a third-order process including an electron-hole pair and a phonon. The Raman process can be described from a macroscopic point of view. We assume an incoming electro-magnetic wave $\mathbf{E}(\mathbf{r}, t)$ with wave vector $\mathbf{k}$ and frequency ω_i which propagates through the material [100]

$$\mathbf{E}(\mathbf{r}, t) = \mathbf{E}_i(\mathbf{k}_i, \omega_i)\, \cos(\mathbf{k}_i\, \mathbf{r} - \omega_i\, t). \tag{3.5}$$

While traveling through the material, the radiation field causes a polarization $\mathbf{P}(\mathbf{r}, t)$ of the electron cloud around the atoms

$$\mathbf{P}(\mathbf{r}, t) = \mathbf{P}_i(\mathbf{k}_i, \omega_i)\, \cos(\mathbf{k}_i\, \mathbf{r} - \omega_i\, t). \tag{3.6}$$

The electric field and the polarization are connected via the materials susceptibility χ

$$\mathbf{P}_i(\mathbf{k}_i, \omega_i) = \chi(\mathbf{k}_i, \omega_i)\, \mathbf{E}_i(\mathbf{k}_i, \omega_i). \tag{3.7}$$

The susceptibility describes the polarizability of a material and can be altered periodically by fundamental excitations of the lattice, *i.e.*, phonons. The atomic displacements $\mathbf{Q}$ in these

vibrations can be described by

$$\mathbf{Q}(\mathbf{r},t) = \mathbf{Q}(\mathbf{q},\omega_0)\,\cos\left(\mathbf{q}\,\mathbf{r} - \omega_0\,t\right), \tag{3.8}$$

where ω_0 is the frequency of the lattice vibration. Expanding χ in a Taylor series with respect to the normal modes of the lattice vibrations yields

$$\chi(\mathbf{k}_i,\omega_i,\mathbf{Q}) = \chi_0(\mathbf{k}_i,\omega_i) + \left(\frac{\partial\chi}{\partial\mathbf{Q}}\right)_0 \mathbf{Q}(\mathbf{r},t) + \ldots \tag{3.9}$$

Here, the first term describes the susceptibility when no lattice vibrations are present. The following expressions represent vibrations of the first and higher orders. Combining Eq. (3.9) and Eq. (3.7) results in

$$\mathbf{P}(\mathbf{r},t,\mathbf{Q}) = \mathbf{P}_0(\mathbf{r},t) + \mathbf{P}_{\mathrm{ind}}(\mathbf{r},t,\mathbf{Q}), \tag{3.10}$$

where the induced polarization is given by

$$\mathbf{P}_{\mathrm{ind}}(\mathbf{r},t,\mathbf{Q}) = \left(\frac{\partial\chi}{\partial\mathbf{Q}}\right)_0 \mathbf{Q}(\mathbf{r},t)\;\mathbf{E}_i(\mathbf{k}_i,\omega_i)\,\cos\left(\mathbf{k}_i\,\mathbf{r} - \omega_i\,t\right) \tag{3.11}$$

$$= \left(\frac{\partial\chi}{\partial\mathbf{Q}}\right)_0 \mathbf{Q}(\mathbf{q},\omega_0)\,\cos\left(\mathbf{q}\,\mathbf{r} - \omega_0\,t\right)\;\mathbf{E}_i(\mathbf{k}_i,\omega_i)\,\cos\left(\mathbf{k}_i\,\mathbf{r} - \omega_i\,t\right). \tag{3.12}$$

Using addition theorems for the two cosine functions yields

$$\mathbf{P}_{\mathrm{ind}}(\mathbf{r},t,\mathbf{Q}) = \frac{1}{2}\left(\frac{\partial\chi}{\partial\mathbf{Q}}\right)_0 \mathbf{Q}(\mathbf{q},\omega_0)\;\mathbf{E}_i(\mathbf{k}_i,\omega_i) \cdot \left[\cos\left((\mathbf{k}_i+\mathbf{q})\;\mathbf{r} - (\omega_i+\omega_0)\;t\right) + \cos\left((\mathbf{k}_i-\mathbf{q})\;\mathbf{r} - (\omega_i-\omega_0)\;t\right)\right]. \tag{3.13}$$

As can be seen, the emitted light consists of three contributions. First, the Rayleigh-scattered light with frequency ω_i. In this process, no phonons were involved, thus the scattering is elastic and no energetic shift between the absorbed and scattered photons is observed. Usually, its intensity is normally orders of magnitude stronger than the Raman scattered light. Furthermore, we can identify two inelastically scattered contributions where the scattered photon exhibits energies of $\omega_i \pm \omega_0$. These contributions are the Stokes (phonon creation) and anti-Stokes (phonon annihilation) scattered photons, which contribute to the Raman signal. Ergo, a vibration is called Raman-active if the polarizability of the crystal is changed under the respective vibration of the atoms.

Equivalently, Raman scattering can be described from a microscopic viewpoint, which is schematically shown in Figure 3.1. Here, the incoming light excites an electron from the ground state E_0 to an energetically higher state. In the Stokes process, the electron inelastically scatters and excites a phonon, thus, reducing the energy of the electron. In contrast, during the anti-Stokes

process the electron annihilates phonons, leading to an increase in energy of the electron. Subsequently, the electron recombines and a photon is emitted. The outgoing photon is shifted in its energy by the energy of the created or annihilated phonon. This energy shift between the incoming and outgoing photon is called the Raman shift and is typically measured in reciprocal centimeters (cm^{-1}).
During the Raman scattering process there must be energy and momentum conservation

$$\hbar\,\omega_i = \hbar\,\omega_s + \hbar\,\omega_{\mathrm{ph}} \qquad\qquad \hbar\,\boldsymbol{k_i} = \hbar\,\boldsymbol{k_s} + \hbar\,\boldsymbol{q}$$

between the initial and the final state. Here, $\boldsymbol{q}$ is the momentum of the involved phonon, $\hbar$ the reduced Planck constant, and $\boldsymbol{k_i}$ and $\boldsymbol{k_s}$ are the momenta of the incoming and scattered photon, respectively. When the momentum of the incoming light in the visible range is compared to the dimension of the Brillouin zone, it becomes obvious that in a first-order scattering process only $\mathbf{\Gamma}$-point phonons can contribute to the Raman scattering process. The momentum of a photon with $\lambda = 500\,\mathrm{nm}$ is

$$k_i = \frac{2\,\pi\,n}{\lambda} = 0.034\,\frac{1}{\mathrm{nm}} = 0.0034\,\frac{1}{\text{Å}}$$

where the refractive index of graphene with $n = 2.7$ at $\lambda = 500\,\mathrm{nm}$ was chosen [101]. In contrast, the border of the first Brillouin zone in graphene is at $4\,\pi/(3\,a_0)$ ($\mathbf{K}$ point) and $2\,\pi/(\sqrt{3}\,a_0)$ ($\mathbf{M}$ point). In graphene, where $a_0 = 2.46\,\text{Å}$ [59], this yields $\mathbf{K} \approx 1.70\,\text{Å}^{-1}$ and $\mathbf{M} \approx 1.47\,\text{Å}^{-1}$. Thus, the photon wave-vector is more than two orders of magnitude smaller than the extension of the first Brillouin zone. Hence, only phonons from the $\mathbf{\Gamma}$ point with $\boldsymbol{q} \approx 0$ can be probed in a first order process. In a second order process the momentum conservation can also be fulfilled by two phonons with opposite wave vector or by the scattering with a defect

$$\begin{aligned}\boldsymbol{q} &= \boldsymbol{q}_1 + \boldsymbol{q}_2\\ &\approx 0\end{aligned}$$

We will discuss a very prominent second-order Raman process in graphene, *i.e.*, the so-called double-resonant Raman scattering, in the following section.

3.3 Double-resonant Raman scattering

The anomalous peak shift of certain peaks in the Raman spectrum of graphite, *e.g.*, the D and $2D$ modes, as a function of laser excitation energy has been a longstanding question in the research on graphitic carbons [102]. Although, the defect-related character of the D mode and the corresponding phonons were identified early [103], the concrete scattering mechanism remained unclear for the next 30 years. First phenomenological explanations of the observed

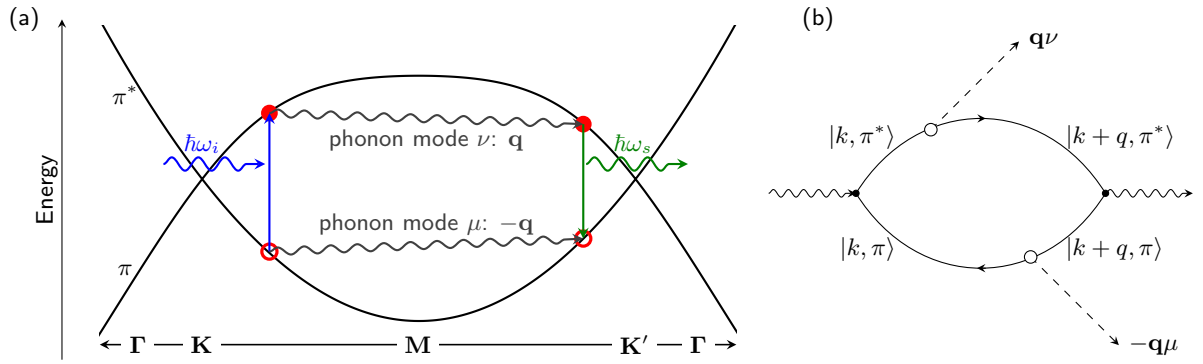

Figure 3.2: (a) Schematic illustration of a two-phonon intervalley double-resonance process in the bandstructure of single-layer graphene along the $\mathbf{\Gamma}-\mathbf{K}-\mathbf{M}-\mathbf{K}'-\mathbf{\Gamma}$ high-symmetry direction. The electron-hole pair scatters with two phonons from the ν and μ phonon branches with wave vectors $\mathbf{q}$ and $-\mathbf{q}$. (b) Goldstone diagram for a double-resonant electron-hole scattering process as depicted in (a).

effects were based on the resonant excitation of $k = q$ phonons close to the **K** point of graphite [104]. However, the correct explanation of the scattering process was given by Thomsen and Reich in 2000 [45]. In this seminal work, the concept of double-resonant Raman scattering was introduced and successfully applied to explain the different laser-energy dependent peak shifts in the Raman spectrum of graphite.

Double-resonant Raman scattering is a second-order process that involves scattering with two-phonons or a phonon and a defect [45, 47]. In contrast to the first-order Raman process as described before, double-resonant Raman scattering involves phonons with $\mathbf{q} \neq 0$. Here, momentum conservation is guaranteed by a second phonon with opposite $\mathbf{q}$ vector (two-phonon process) or by the elastic scattering with a defect (phonon-defect process). Furthermore, at least two of the intermediate electronic states have to be eigenstates, *i.e.* real states, of the investigated system. In this case, the Raman signal is resonantly enhanced and magnitudes larger than the non-resonant scattered light. Figure 3.2 shows a schematic illustration of the intervalley double-resonance process in single-layer graphene. In general, the scattering process can be divided into four steps: (i) First, the incoming photon $\hbar\omega_i$ is absorbed and resonantly excites an electron-hole pair. In graphene, this initial resonant excitation is always possible at moderate doping levels [105, 106]. (ii) The excited electron is scattered by a phonon from phonon branch ν and with wave vector $\mathbf{q}$. (iii) Likewise, the hole is scattered by a phonon from phonon branch μ and with wave vector $-\mathbf{q}$. (iv) Finally, the electron-hole pair recombines and emits a photon with energy $\hbar\omega_s$. In principle, both Stokes and anti-Stokes scattering, as well as a combination of these processes is possible in double-resonant Raman scattering [107]. Double-resonant Raman modes can be separated into either inter- or intravalley double-resonant scattering. Intervalley scattering refers to a scattering process between two inequivalent **K** points, whereas intravalley scattering describes a scattering process between electronic states at the same **K** point.

From the above explained process, the laser-energy dependent peak shifts can be directly ex-

plained. By tuning the laser excitation energy, the resonance condition for the incoming photon is satisfied by different sets of $\mathbf{k}$ vectors around the $\mathbf{K}$ point. Subsequently, the resonant scattering of the electron-hole pair is mediated by phonons with different phonon wave-vectors $\mathbf{q}$, leading to different resonantly enhanced phonon frequencies in the Raman spectrum. Depending on the electronic bandstructure and phonon dispersion, the double-resonant Raman modes may upshift or downshift with increasing laser energy. In general, double-resonant Raman scattering enables the possibility to simultaneously probe the electronic structure and phonon dispersion by tuning the laser excitation energy.

Following the notation of Venezuela *et al.* [47], the double-resonant Raman scattering cross-section for a two-phonon process can be written as

$$
\begin{aligned}
&I_{\mathbf{q}}^{\mu\nu}\left(\varepsilon_L,\gamma\right) \propto \\
&\Bigg| \sum_{\mathbf{k},e,h,\ldots} \frac{\langle \mathbf{k}+\mathbf{q},h' \left| D_{\text{out}} \right| \mathbf{k}+\mathbf{q},e' \rangle \left\langle \mathbf{k},h \left| \frac{\partial \mathcal{H}}{\partial \mathbf{u}_{-\mathbf{q}\mu}} \right| \mathbf{k}+\mathbf{q},h' \right\rangle \left\langle \mathbf{k}+\mathbf{q},e' \left| \frac{\partial \mathcal{H}}{\partial \mathbf{u}_{\mathbf{q}\nu}} \right| \mathbf{k},e \right\rangle \langle \mathbf{k},e \left| D_{\text{in}} \right| \mathbf{k},h \rangle}{(\varepsilon_L - \varepsilon_e + \varepsilon_h - i\hbar\gamma)(\varepsilon_L - \varepsilon_{e'} + \varepsilon_h - \hbar\omega_{\mathbf{q}\nu} - i\hbar\gamma)(\varepsilon_L - \varepsilon_{e'} + \varepsilon_{h'} - \hbar\omega_{\mathbf{q}\nu} - \hbar\omega_{-\mathbf{q}\mu} - i\hbar\gamma)} \\
&\quad + \frac{\langle \mathbf{k}+\mathbf{q},h' \left| D_{\text{out}} \right| \mathbf{k}+\mathbf{q},e' \rangle \left\langle \mathbf{k}+\mathbf{q},e' \left| \frac{\partial \mathcal{H}}{\partial \mathbf{u}_{\mathbf{q}\mu}} \right| \mathbf{k},e \right\rangle \left\langle \mathbf{k},h \left| \frac{\partial \mathcal{H}}{\partial \mathbf{u}_{-\mathbf{q}\nu}} \right| \mathbf{k}+\mathbf{q},h' \right\rangle \langle \mathbf{k},e \left| D_{\text{in}} \right| \mathbf{k},h \rangle}{(\varepsilon_L - \varepsilon_e + \varepsilon_h - i\hbar\gamma)(\varepsilon_L - \varepsilon_e + \varepsilon_{h'} - \hbar\omega_{-\mathbf{q}\nu} - i\hbar\gamma)(\varepsilon_L - \varepsilon_{e'} + \varepsilon_{h'} - \hbar\omega_{-\mathbf{q}\nu} - \hbar\omega_{\mathbf{q}\mu} - i\hbar\gamma)} \\
&\quad + \ldots \Bigg|^2 .
\end{aligned}
\tag{3.14}
$$

Here, μ and ν refer to the branch indices of the two contributing phonons. For every phonon wave-vector $\mathbf{q}$, the summation has to be carried out over all electron e and hole h states in $\mathbf{k}$ space. Furthermore, the summation has to consider all possibilities for electron and hole scattering, *i.e.*, an electron is scattered by two phonons (*ee* scattering), a hole is scattered by two phonons (*hh* process), or both the electron and the hole are scattered (*eh* scattering). In total, there are eight different possibilities of electron and hole scattering in a two-phonon process. In a phonon-defect process, either the hole or the electron are elastically scattered by a defect to fulfill momentum conservation. However, the number of possible processes is still eight. The ε_e and ε_h denote the energies of the electron and holes states, respectively, and depend on the wave vector $\mathbf{k}$; ε_L is the laser excitation energy. The electronic broadening γ reflects the inverse lifetime of the different electronic states and is usually assumed to be equivalent for all denominators [47]. The influence of the electronic broadening on the double-resonance process will be analyzed in Chapter 4.7. The enumerators reflect the dipole matrix elements $\mathcal{M}_{\text{e-r}}$ and the electron-phonon matrix elements $\mathcal{M}_{\text{e-p}}$ for the different electronic states $e, e', \ldots$ and $h, h', \ldots$ and phonon modes μ and ν. Using the notation of Ref. [47], the matrix elements are given by

$$
\begin{aligned}
\mathcal{M}_{\text{e-r}} &= \langle \mathbf{k},h \left| D \right| \mathbf{k},e \rangle \\
&= \frac{1}{i\varepsilon_L} \mathbf{E} \cdot \left\langle \mathbf{k},h \left| \frac{\partial \mathcal{H}}{\partial \mathbf{k}} \right| \mathbf{k},e \right\rangle
\end{aligned}
\tag{3.15}
$$

and

$$\mathcal{M}_{\text{e-p}} = \left\langle \mathbf{k}+\mathbf{q}, e' \left| \frac{\partial \mathcal{H}}{\partial \mathbf{u}_{\mathbf{q}\nu}} \right| \mathbf{k}, e \right\rangle . \tag{3.16}$$

Equation (3.15) models the interaction of the system's Hamiltonian $\mathcal{H}$ with an electromagnetic wave $\mathbf{E}$ and describes the transition of an electron between two different states at the same $\mathbf{k}$ vector by photon absorption. As the $\mathbf{E}$ field is directly connected to the polarization $\mathbf{P}$ of the electromagnetic wave, the polarization dependence of the double-resonance process is imposed by these matrix elements. In fact, the dipole matrix elements predominantly influence the angular dependence of the Raman scattering cross-section around the $\mathbf{K}$ point, as the oscillator strength, *i.e.*, the square of the transition dipole moment, is highest along the $\mathbf{K}-\mathbf{M}$ direction and lowest along the $\mathbf{K}-\mathbf{\Gamma}$ high-symmetry line [47, 108, 109].

The electron-phonon matrix elements from Eq. (3.16) describe the response of the electronic system to a phonon displacement. In the Born-Oppenheimer approximation, the motion of the atomic nuclei and the electrons is assumed to be separable and thus can be solved individually. However, to account for interactions between both systems, usually one introduces an additional Hamiltonian that describes the electron-phonon coupling. This quantity is key for the understanding of different effects such as superconductivity [110, 111] or dynamics of photo-excited charge carriers in graphene [112]. Furthermore, the electron-phonon coupling plays an import role in Raman spectroscopy on graphitic carbons. Usually, the atomic motion is screened by the motion of the electron cloud, *i.e.*, the internal electric field that results from a displacement of the ions from their equilibrium positions is screened (reduced) by the highly mobile electrons [96]. Thus, two electrons in the system at $\mathbf{k_1}$ and $\mathbf{k_2}$ do not interact via the bare Coulomb potential but 'feel' the screened potential. However, in metallic or semi-metallic systems, such as graphene, the screening can drastically change at certain high-symmetry points in the Brillouin zone and therefore can lead to an abrupt variation of phonon frequencies at certain $\mathbf{q}$ [113]. Kohn *et al.* demonstrated that electrons can lose their ability to screen the vibration of the nuclei, if the atomic displacement perturbs electrons at the Fermi surface, *i.e.*, if $\mathbf{q} = 2\,\mathbf{k}_F$, where $\mathbf{k}_F$ is the Fermi wave-vector [113]. Since graphene has to inequivalent Fermi points, *i.e.*, $\mathbf{K}$ and $\mathbf{K}'$, this reduced electronic screening may occur at $\mathbf{q} = 0$ and $\mathbf{q} = \mathbf{K}$ [40]. Ergo, the electron-phonon coupling is drastically enhanced at these points in the Brillouin zone, leading to a softening of the phonon frequency for certain phonon branches. The resulting discontinuity in the derivate of the phonon branch is usually referred to as a Kohn anomaly. The effect of the Kohn anomaly in graphene becomes manifested by the dependence of the G- and $2D$-mode positions on the doping level [34]. We will discuss the Kohn anomalies in graphene and bilayer graphene more detailed in Chapter 4 and will point out the importance of many-body corrections to the phonon dispersion and electronic bandstructure to account for this anomaly in our calculations.

A very prominent example of a double-resonant Raman mode is the $2D$ mode in graphene and graphite. This Raman mode results from an intervalley scattering process with two transverse

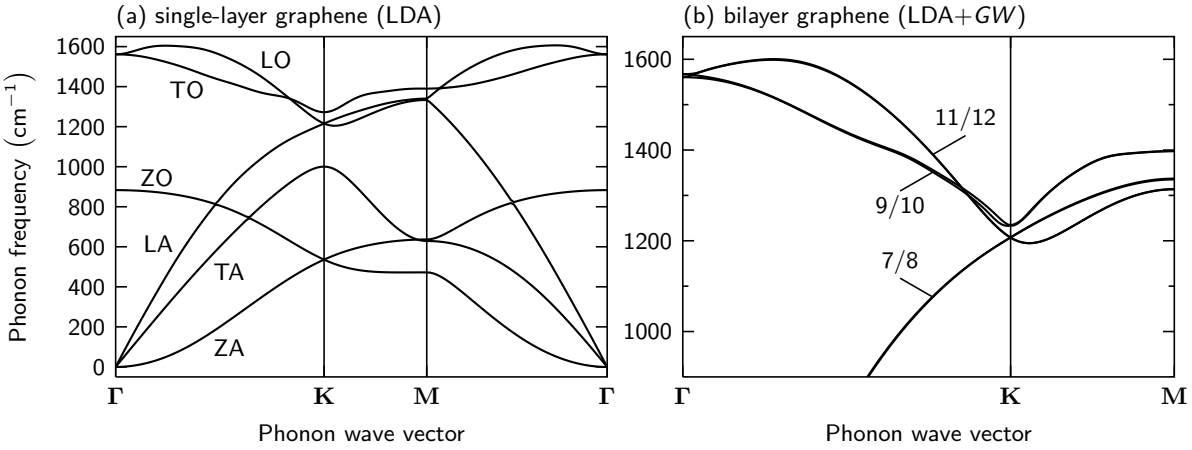

Figure 3.3: (a) Phonon dispersion of single-layer graphene along the $\mathbf{\Gamma} - \mathbf{K} - \mathbf{M} - \mathbf{\Gamma}$ high-symmetry line from an LDA calculation. The labels at each branch indicate acoustic (A) and optical (O) phonons, as well as transverse (T) and longitudinal (L) vibrations. (b) *GW*-corrected phonon dispersion of the high-energy branches in bilayer graphene along $\mathbf{\Gamma} - \mathbf{K} - \mathbf{M}$ direction. The labels refer to the phonon branch indices at the corresponding phonon wave-vector.

optical (TO) phonons close to the **K** point of the Brillouin zone. We will introduce the typical characteristic modes in the Raman spectrum of graphene in the following section.

3.4 Basic vibrational properties of graphene, bilayer graphene, and carbon nanotubes

As introduced in Chapter 2, the unit cell of graphene consists of two inequivalent atoms A and B. Thus, the phonon dispersion splits up into six branches, *i.e.*, three acoustic and three optical branches. We show the phonon dispersion of single-layer graphene along the high-symmetry directions in the first Brillouin zone in Figure 3.3 (a). The labels at each branch indicate acoustic (A) and optical (O) phonons, as well as transverse (T) and longitudinal (L) vibrations. Both high-energy optical phonon branches (LO and TO) are degenerate at $\mathbf{\Gamma}$ and exhibit E_{2g} symmetry. Away from $\mathbf{\Gamma}$, the LO phonon branch presents an overbending with frequencies up to $\approx 1620\,\mathrm{cm}^{-1}$. The third optical branch has A_{2u} symmetry and is infrared active only [114]. As briefly discussed above, the phonon dispersion of graphene presents Kohn anomalies at certain high-symmetry points in the Brillouin zone. For instance, the LO phonon branch exhibits a Kohn anomaly at the $\mathbf{\Gamma}$ point, the TO branch is affected by a Kohn anomaly at **K** [40]. Recently, different works also reported a Kohn anomaly for the ZO phonon branch at the **K** point [115, 116].

The phonon dispersion of the high-energy phonon branches in bilayer graphene is shown in Figure 3.3 (b). The labels at each branch indicate the phonon-branch index (from lowest to highest) at the corresponding **q** vector and correspond to the indices μ and ν in Eq. (3.14).

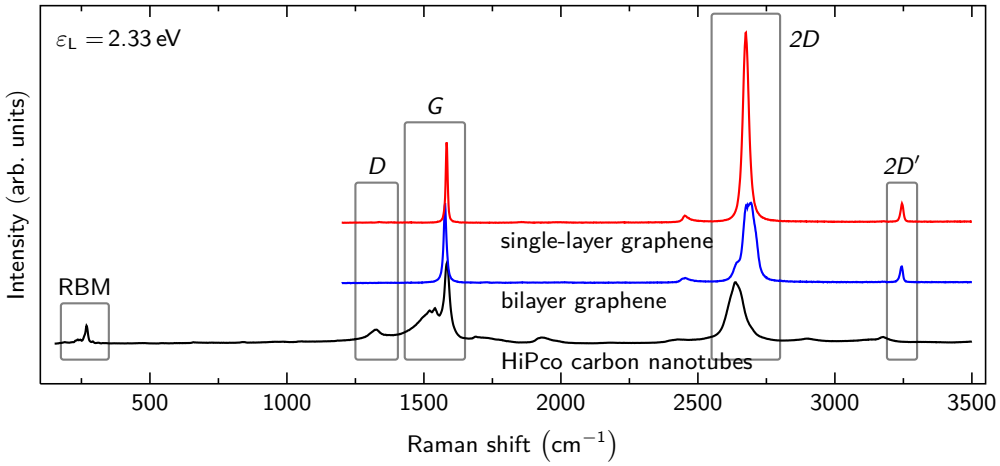

Figure 3.4: Raman spectra of graphene, bilayer graphene, and HiPco-produced carbon nanotubes. The characteristic Raman modes are indicated by gray boxes; labels are given next to the boxes. Spectra are normalized to the same G-mode intensity and offset for clarity. A laser excitation energy of 2.33 eV was used.

These labels will become important later in Chapter 4. Since bilayer graphene has twice as many atoms in the unit cell compared to single-layer graphene, the phonon spectrum of bilayer graphene consists of twelve branches. Most of these branches are degenerate throughout the Brillouin zone. However, as can be seen, the TO phonon branch exhibits a splitting along the $\mathbf{\Gamma} - \mathbf{K}$ direction. At the $\mathbf{\Gamma}$ point, the LO and TO phonon branches split up into a symmetric, Raman-active (E_g symmetry) and an anti-symmetric, infrared-active vibration (E_u symmetry). In contrast to single-layer graphene, the phonon dispersion of bilayer graphene also exhibits rigid-layer shear and out-of-plane breathing modes [107, 114, 117, 118]. These modes originate from acoustic phonons in single-layer graphene and exhibit interesting frequency dependencies in N-layer graphene.

The Raman spectra of graphene, bilayer graphene, and carbon nanotubes are composed of several characteristic peaks, which we will briefly discuss below. The spectra are shown in Figure 3.4 for an excitation energy of 2.33 eV. In all spectra, we observe Raman modes around $\sim 1580\,\text{cm}^{-1}$, which can be identified with the aforementioned degenerate LO/TO $\mathbf{\Gamma}$-point vibration. Since this peak is characteristic for all kinds of graphitic (sp^2 hybridized) carbons, it is referred to as the G mode. In carbon nanotubes, the degeneracy between the LO and TO vibration is lifted, leading to distinct peaks in the G-mode region [119, 120]. Another prominent feature of all Raman spectra is the $2D$ mode at $\sim 2650\,\text{cm}^{-1}$, which originates from a double-resonant intervalley scattering process with two TO phonons from the border of the Brillouin zone around the $\mathbf{K}$ points [45]. In single-layer graphene, this peak has a nearly single-Lorentzian lineshape with a slight asymmetry towards higher frequencies [49]. However, the lineshape changes drastically for an increasing layer number, *i.e.*, a broad peak with multiple peaks is observed for $N \geq 2$-layer graphene, reflecting the evolution of the electronic bands around the $\mathbf{K}$ points [46]. A

detailed discussion of the $2D$-mode lineshape in bilayer graphene will be given in Chapter 4. Furthermore, we also observe the $2D'$ mode in Raman spectrum of single and bilayer graphene around $\sim 3240\,\mathrm{cm}^{-1}$. This mode results from an intravalley scattering process with two LO phonons from the LO-overbending region near the $\mathbf{\Gamma}$ point. Besides the two-phonon double-resonant Raman modes, there are also Raman peaks that result from a double-resonant phonon-defect scattering process. In these processes, momentum conservation is guaranteed by the elastic scattering with a defect. Prominent examples of these defect-induced Raman modes are the D, the D', and the D'' modes at $\sim 1350\,\mathrm{cm}^{-1}$, at $\sim 1620\,\mathrm{cm}^{-1}$, and at $\sim 1100\,\mathrm{cm}^{-1}$, respectively. A very characteristic Raman mode for carbon nanotubes can observed in the spectral range between 100 and $350\,\mathrm{cm}^{-1}$ (compare Fig. 3.4). These modes can be identified with radial vibrations of the carbon nanotube and are referred to as radial breathing modes (RBMs). Comparable to the rigid-layer shear and compression modes in N-layer graphene, the RBMs exhibit frequencies that sensitively depend on the tube diameter [121]. Thus, this Raman mode is commonly used for CNT characterization and chiral index determination.

4 Analysis of the double-resonant *2D* Raman mode in bilayer graphene

Parts of this chapter were published in Ref. [122].

In this chapter, we will analyze the double-resonant $2D$-mode scattering process in bilayer graphene. Albeit intense research on this topic, the $2D$ mode in bilayer graphene has been discussed controversially by several authors in recent years. In this context, different models were proposed to explain the origin of the complex lineshape observed in experiments. However, there is still an ongoing controversy about the different contributions to the $2D$-mode scattering process and their assignment to different spectral features in the $2D$-mode spectrum.
This chapter is organized as follows: First, we will introduce the electronic and vibrational properties of bilayer graphene. Afterwards, we will describe the double-resonance process in bilayer graphene, followed by a brief introduction to the ongoing discussion about the $2D$ mode in bilayer graphene and the theories discussed so far. Finally, we analyze the different contributions and clarify the origin of the observed spectral features. We demonstrate the importance of inner processes, discuss the effect of the TO phonon splitting on the $2D$-mode Raman spectrum, and show the influence of quantum interference between different scattering processes.

4.1 Bilayer graphene: Electronic properties and phonon dispersion

Bilayer graphene consists of two vertically stacked graphene sheets in so-called Bernal-stacking. In this stacking configuration, the two graphene sublattices are horizontally shifted by the carbon-carbon bond length in the direction of the C-C bond. In other words, the A and B atoms of adjacent layers are directly on top of each other and the two remaining atoms are centered above and below the hexagons of the next layer (compare Fig. 4.1). Therefore, Bernal-stacking is often referred to as AB-stacking. Bilayer graphene has twice as many atoms in the unit cell compared to single-layer graphene, consequently, the number of π/π^* orbitals is doubled as well and give now rise to four electronic bands in the visible energy range [2]. The valence bands are referred to as π_2 and π_1, the conduction bands are denoted as π_1^*, π_2^*. The electronic bands of bilayer graphene are displayed in Fig. 4.2 (a) along the one-dimensional $\mathbf{\Gamma} - \mathbf{K} - \mathbf{M} - \mathbf{K}' - \mathbf{\Gamma}$ high-symmetry direction; Fig. 4.2 (b) shows an enlarged view of the bandstructure around the

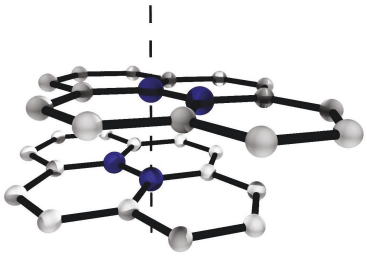

Figure 4.1: Visualization of the bilayer graphene structure in AB-stacking. The unit-cell atoms are highlighted in blue.

K point. In contrast to single-layer graphene, the electronic bandstructure of bilayer graphene is not linear around the **K** points but exhibits a parabolic energy dependence [2]. Thus, charge carriers around **K** cannot be regarded as massless Dirac fermions as in single-layer graphene. Similar to graphene, unpertubated bilayer graphene does not exhibit a bandgap. However, by breaking the inversion symmetry between both layers one can easily tune an electronic gap at **K** as large as 250 meV [72, 123–125]. The possibility of creating a band gap favors bilayer graphene for applications in field-effect transitors, which are hardly realizable using single-layer graphene.

As already mentioned, bilayer graphene consists of twice as many atoms in the unit cell compared to single-layer graphene. Thus, there are twelve phonon branches throughout the Brillouin zone, which are partially degenerated [compare Chapter 3.4]. Especially the low-frequency **Γ**-point phonons exhibit interesting layer-number dependent properties that can be used to identify the layer-number and interlayer interactions [107, 118, 126, 127]. However, in this chapter we will concentrate on the TO (transversal optical) phonon branch.

It has been shown that certain phonon branches in graphene exhibit Kohn anomalies at **Γ** and **K** [40, 59, 128], *i.e.*, the first derivate of the phonon dispersion exhibits a discontinuity at these points. The Kohn anomaly at **Γ** affects the LO phonon branch, whereas the Kohn anomaly at **K** perturbs the TO phonon branch. Kohn anomalies can occur when a phonon with wave vector **q** connects two electronic states that are both on the Fermi surface [113]. In undoped graphene, the Fermi surface consists of the two equivalent points **K** and **K′**. Consequently, Kohn anomalies may only occur for phonons with wave vectors $\mathbf{q} = \mathbf{0} = \mathbf{\Gamma}$ and $\mathbf{q} = \mathbf{K}$ [40]. At these points, the screening of atomic vibrations by electrons is strongly reduced and leads to a drastically increased electron-phonon coupling. Lazzeri *et al.* demonstrated that standard Density Functional Theory (DFT) calculations that employ the Local Density Approximation (LDA) or the Generalized Gradient Approximation (GGA) do not account for this strong coupling in single and few-layer graphene [129]. In general, DFT is a ground-state theory that does not account for many-body correlations in excited systems [130]. Furthermore, local approximations such as LDA and GGA usually do not reproduce the correct longe-range Coulomb potential [131]. However, its is precisely this long-range electron-electron interaction that enhances the electron-phonon coupling to the A_1-symmetry mode at the K point [129, 131]. Hence, standard LDA- and GGA-based DFT calculations must fail in the calculation of the electron-phonon coupling and the phonon dispersion in graphene. In order to account for the strong influence of correlation effects on the electronic and vibrational properties of graphene [2], a Green's function approach within

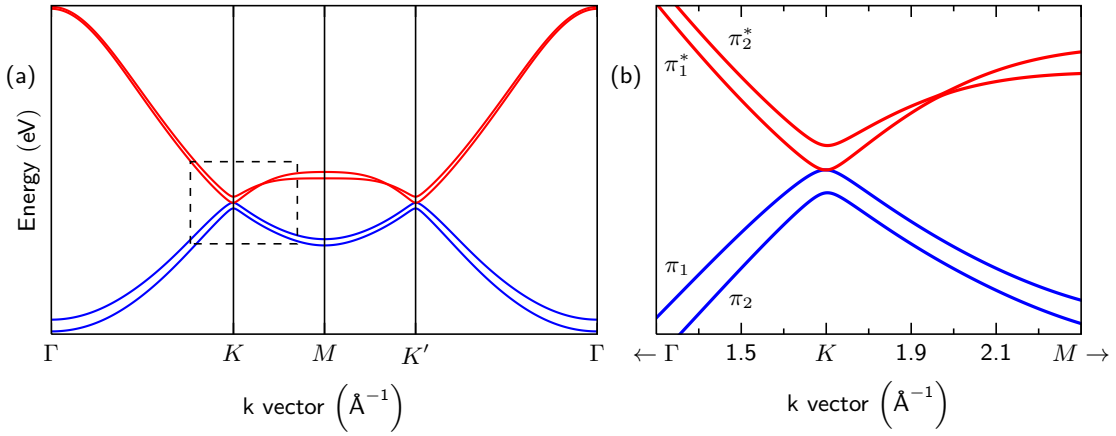

Figure 4.2: (a) Electronic bandstructure of the π/π^* orbitals in bilayer graphene along the $\mathbf{\Gamma - K - M - K' - \Gamma}$ high-symmetry direction obtained from first-principles calculations. An enlarged view of the electronic bands inside the dashed rectangle is given in (b). The electronic bands are labeled as defined in the text.

many-body theory is usually chosen. The influence of many-body effects becomes manifested in the electronic self-energy correction Σ, which can be understood as the potential on an electron due to the interaction with other quasi-particles in the system [132]. In principle, Σ can be identified with the exchange potential in Hartree-Fock calculations. A very famous and prominent method to approximate Σ is the so-called *GW* approximation [133]. Here, the self-energy correction [132]

$$\Sigma_{GW}\left(x, x', \omega\right) = \frac{i}{2\pi} \int \exp\left(i\delta\omega'\right) G\left(x, x', \omega'\right)\, W\left(r, r', \omega - \omega'\right) \mathrm{d}\omega'$$

is expanded in a Taylor series of the one-particle Green's function G and the screened Coulomb potential W and just considers the leading term [133]. In other words

$$\Sigma = i\, G_0 W_0.$$

In the equation above, x reflects the different space coordinates r plus a spin coordinate and ω is proportional to the energy of the particle. In principle, the *GW* approach can be regarded as a screened version of a Hartree-Fock calculation that more accurately includes many-body effects to the self-energy corrections. Compared to LDA- and GGA-based DFT calculations, the *GW*-derived phonon dispersion exhibits a nearly two times larger slope of the TO branch at **K** [129], in agreement with experimental data [59, 128]. Moreover, the square of the electron-phonon coupling is renormalized by almost 80 % in *GW* approximation [129]. Therefore, it is of great importance to include these corrections for a correct treatment of the double-resonance process in graphene. Although not explicitly calculated in literature, we expect qualitatively the same renormalization in bilayer graphene. Unless differently stated, all calculations presented in this

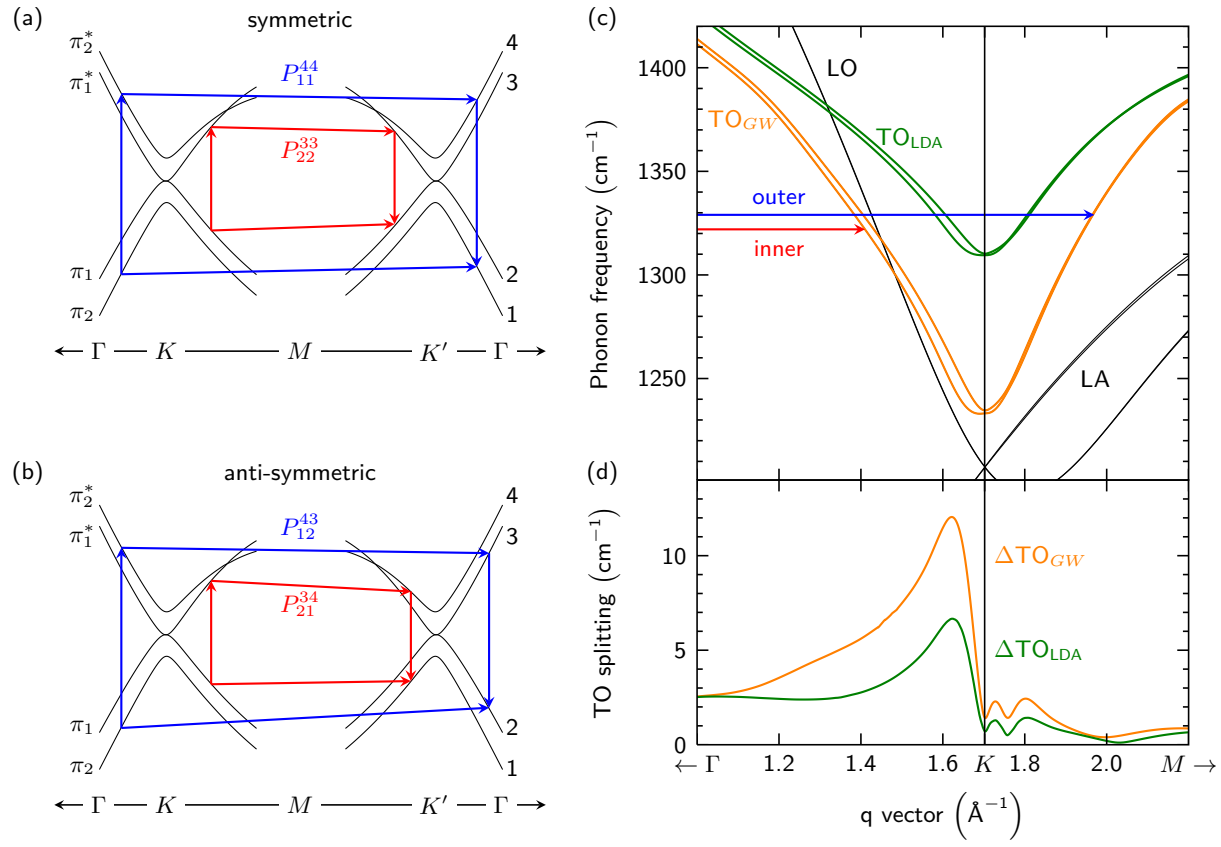

Figure 4.3: Simplified and schematized illustration of the double-resonant $2D$-mode Raman scattering processes along the $\mathbf{\Gamma} - \mathbf{K} - \mathbf{M} - \mathbf{K}' - \mathbf{\Gamma}$ high-symmetry direction for (a) symmetric scattering processes and (b) anti-symmetric scattering processes. Inner and outer processes are marked with red and blue traces, respectively. (c) Phonon dispersion of bilayer graphene close to the **K** point with and without *GW* correction. Calculations in LDA and *GW* approximation are given by green- and orange-coloured lines, respectively. (d) Splitting between the two TO phonon branches along $\mathbf{\Gamma} - \mathbf{K} - \mathbf{M}$ with and without *GW* correction. The splitting increases by a factor of almost two when *GW* corrections are considered.

chapter include electron-electron interaction at the *GW* level.

4.2 The double-resonance process in bilayer graphene

A group-theoretical analysis of the electronic bands and phonons in bilayer graphene predicts four allowed scattering processes for the double-resonant $2D$ mode [134]. Figures 4.3 (a) and (b) show a sketch of the electronic band structure of bilayer graphene along the $\mathbf{\Gamma} - \mathbf{K} - \mathbf{M} - \mathbf{K}' - \mathbf{\Gamma}$ high-symmetry line, as well as a schematized illustration of the double-resonant $2D$-mode scattering process. These scattering processes can be divided into symmetric and anti-symmetric, as well as into inner and outer processes. Symmetric processes are scattering events between equivalent electronic bands at **K** and **K′**, whereas for an anti-symmetric process

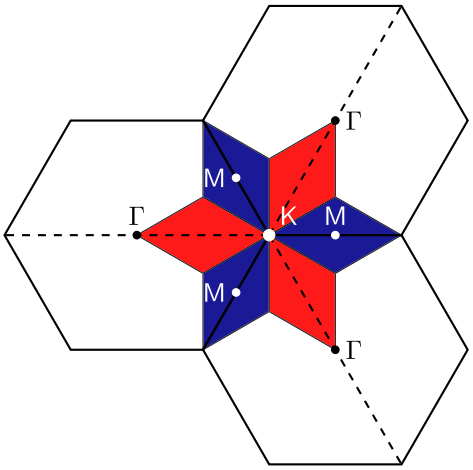

Figure 4.4: Sectors for phonon wave-vectors resulting from inner and outer double-resonant processes in the two-dimensional Brillouin zone of bilayer graphene. If the resonant phonon wave-vector in the double-resonance process stems from the red sector, it is considered as an inner process. Resonant phonon wave-vectors from the blue sector will be referred to as outer processes.

the band index is changing. So-called 'inner' or 'outer' processes can be identified by the angle and wave-vector length of the involved phonons. We refer to the term 'inner' process, if the resonant phonon wave-vector falls into a circular sector around **K** that is given by ±30° around the $\mathbf{K}-\mathbf{\Gamma}$ high-symmetry direction with respect to **K**. Consequently, phonon wave-vectors from ±30° around the $\mathbf{K}-\mathbf{M}$ direction are associated with 'outer' processes. To visualize this separation, Figure 4.4 highlights the corresponding areas for 'inner' and 'outer' phonons in red and blue color, respectively. In order to simplify the labeling of the scattering processes, we enumerate the electronic bands starting from the energetically lowest band near **K** [compare Fig. 4.3 (a) or (b)]. Every scattering process P_{mi}^{lj} is then uniquely defined by four indices that are given by the band index of the initial electron m, the band index of the excited electron l, the band index of the scattered electron j, and the band index of the scattered hole i. In principle, there are four different optical excitations between the electronic bands at **K**. However, as predicted by group theory, the incoming light couples mostly, but not exclusively, to only two ($1 \rightarrow 4$ and $2 \rightarrow 3$) of the four possible optical transitions [46, 134]. Thus, there are four different combinations of electron and hole scattering (*eh* scattering) processes in bilayer. These are the symmetric processes P_{11}^{44} and P_{22}^{33}, as well as the anti-symmetric processes P_{12}^{43} and P_{21}^{34}. These processes further split up into inner and outer contributions, resulting in eight different scattering processes.

We will now turn to an overview about the previously discussed models regarding the double-resonant $2D$-mode scattering process in single- and bilayer graphene. As mentioned in Chapter 3, the double-resonance process itself has been a long-standing question in graphite. Subsequent to the explanation of the double-resonance theory by Thomsen and Reich in 2000 [45], Ferrari *et al.* published a fundamental work on double-resonant Raman spectra of single- and few-layer graphene in 2006 [46]. In the following, this work became one of the most cited articles related to graphene research in general[1]. Ferrari *et al.* explained the double-resonance process by considering only outer processes with optical excitations along the $\mathbf{K}-\mathbf{\Gamma}$ high-symmetry direction

[1]The *Web of Science* listed 4530 citations on August 25$^{\text{th}}$ 2015.

(compare Fig. 4.5 and the peak assignments therein). However, already in 2004 Maultzsch *et al.* had pointed out that also inner processes have to be considered for a thorough analysis of the double-resonant scattering process [135]. This was further confirmed by Mohr *et al.* who showed that the observed changes in the $2D$-mode lineshape of strained single-layer graphene can be only explained when considering both inner and outer processes [38]. Related experiments on strained single-layer graphene came to the very same conclusion [136, 137]. Narula *et al.* wanted to revoke the separation of inner and outer scattering processes [138]. However, this work is based on a different interpretation of inner and outer processes and does not reflect the generally accepted definition of these terms. Furthermore, another publication by Narula *et al.* came to the conclusion that the main contribution to the double-resonant Raman scattering cross-section originates from the low-symmetry parts of graphene's Brillouin zone [139]. However, both beforementioned publications are in stark contrast to works from other groups. In fact, Venezuela *et al.* demonstrated by a complete two-dimensional calculation of the double-resonant $2D$-mode scattering cross-section in single-layer graphene that the dominant contributions indeed stem from the high-symmetry directions [47]. Furthermore, this work could show that inner processes dominate over outer ones. This result was further confirmed by experiments on freestanding single-layer graphene by Berciaud *et al.* [49]. Recently, Tyborksi *et al.* demonstrated that, by suppression of inner scattering processes using ultraviolet laser excitation energies, the Raman spectrum of graphene, graphite, and carbon nanotubes is dominated by the two-phonon density of states [140]. This work directly proves the comparatively weak contribution of outer contributions and further emphasizes the importance of inner processes in double-resonant Raman scattering. Future studies on inner and outer processes in single and bilayer graphene might investigate the $2D$-mode lineshape for laser excitation energies between 3.5 eV and 4.5 eV, *i.e.*, for energies below the M-point transition. By precisely tuning the laser energy in the ultraviolett spectral range, one can follow the different dispersions of inner and outer processes, allowing an accurate assignment of the different experimentally observed $2D$-mode subfeatures to inner and outer scattering processes.

In contrast to single-layer graphene, the $2D$ mode in bilayer graphene exhibits a complex lineshape, *i.e.*, depending on the laser excitation energy, one can usually observe three to four peaks with different relative intensities. Based on the analysis by Ferrari *et al.* [46], these peaks are usually attributed to the four allowed scattering processes, accounting for the evolution of the electronic band structure around the **K** point (compare Fig. 4.5). However, Ref. [46] did not consider the doubling of the TO branches in bilayer graphene and, as already mentioned, restricted the scattering paths to exclusively outer processes. Moreover, the four scattering processes were attributed to substantially different phonon frequencies [compare Fig. 4.5 (e)]. This interpretation of the $2D$ mode in bilayer graphene has been adapted by several other authors and was used in subsequent studies [50–54]. Although some authors discussed the possibility of inner processes in the double-resonance scattering [53, 54], all works on this topic neglected the splitting between the two TO branches. Furthermore, Mafra *et al.* investigated the relative intensities of the $2D$-mode contributions as a function of laser power by considering inner

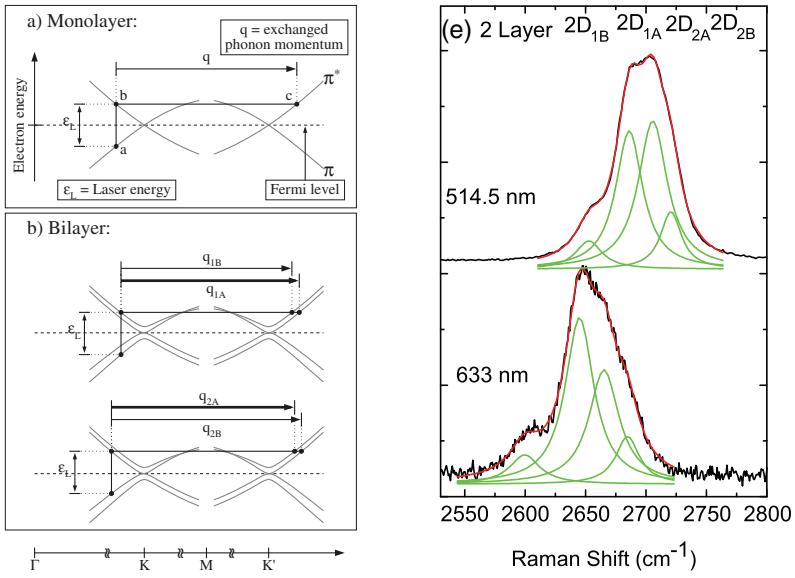

Figure 4.5: Explanation of the double-resonance Raman process in single- and bilayer graphene after Ferrari *et al.* (a) and (b) Visualization of the resonant phonon wave-vectors in the double-resonance process in the band structure of single- and bilayer graphene. (e) $2D$-mode spectrum of bilayer graphene at different laser wavelengths. The spectra are fitted with four Lorentzian profiles; each component is attributed to a different scattering process from (b), as labeled above the spectra. Figure taken from Ref. [46].

processes in their explanation [54]. However, their assignment of the scattering processes to the observed spectral features is incorrect. Finally, none of the previous works on bilayer graphene considered the effect of quantum interference in the double-resonance process. In this chapter, we will demonstrate the importance of inner processes, the TO phonon splitting, as well as quantum interference in the double-resonance process in Bernal-stacked bilayer graphene.

4.3 Calculational details

The calculations of the real and imaginary part of the single scattering processes in the double-resonant scattering cross-section were performed by Dr. Matteo Calandra, Université Pierre et Marie Curie (UPMC), Paris. In the following, these data were postprocessed by a python script to calculate the cross-sections for the different processes P_{mi}^{lj}, for inner and outer processes, for the different possibilities of electron and hole scattering, and for the analysis of the contribution from different phonon branches.

In order to calculate the dominant contributions to the $2D$-mode scattering processes, we derived the Raman scattering cross-section completely from first-principles. All calculations were performed with the DFT-code Quantum ESPRESSO [141], which relies on plane-wave basis sets and pseudopotentials. In this work, we used 'Von Barth-Car' norm-conserving pseudopotentials.

The distance between both graphene layers in the calculation was fixed to the experimental value of $c/2 = 3.35\,\text{Å}$ [59].

Due to interference effects in the double-resonance process [135, 142], the resonantly enhanced phonon wave-vectors stem from a narrow region around the K point. In order to ensure for convergence in our calculations, a fine sampling of the electron and phonon bands, as well as the matrix elements throughout the Brillouin zone is necessary. However, a standard DFT approach only allows the calculation of matrix elements on relatively coarse grids, *e.g.*, a 12×12 momentum grid. Therefore, previous works on the theoretical calculation of double-resonant Raman spectra in graphene used tight-binding derived matrix elements. In contrast, here all quantities are directly derived from first principles and we overcome the difficulties of coarse DFT sampling by using Wannier interpolation [143] of the electronic and phonon dispersions, as well as the electron-phonon and electron-photon matrix elements. This technique has been developed by Calandra *et al.* in Ref. [144]. Wannier interpolation relies on the representation of a lattice-periodic quantity, such as the electronic band structure, by Wannier orbitals. In a standard DFT calculation, each electronic band can be regarded as a superposition of contributions from different Bloch orbitals. However, in the basis of Bloch functions, these bands are not smooth and a simple linear interpolation would be insufficient, especially in the case of band crossings [145]. For this reason, one has to find an alternative way to interpolate the electron and phonon bands or the matrix elements throughout the Brillouin zone. It can be shown that the optimally smooth subspace for interpolation of these quantities can be obtained via Wannier representation[2]. Using this representation, each electronic band is described by a single Wannier orbital. Therefore, if the Wannier basis of a lattice-periodic quantity is known, one can calculate and interpolate any arbitrary point in the Brillouin zone.

We first calculate the electronic bandstructure in Local Density Approximation on a (64×64) momentum grid. Afterwards, the Fermi velocity is renormalized by 17 % in order to fit the experimentally observed slope of the electronic π/π^* bands from ARPES and magnetotransport studies of approximately $v_\text{F} = 1.1 \times 10^6\,\text{m}\,\text{s}^{-1}$ [146–148]. Phonon dispersions are calculated on a 12×12 momentum grid in LDA approximation using the linear-response scheme. Afterwards, the calculated phonon frequencies are GW-corrected, similar to what was done in Refs. [47, 129, 149] for single-layer graphene. In more detail, we define the following scheme to correct the TO phonon frequencies near the $\mathbf{K}$ point.

$$\left(\omega^{GW}_{\mathbf{q}\nu}\right)^2 = 0.5 \times \text{erfc}\left(\frac{|\mathbf{q}-\mathbf{K}_\alpha|a_0/2\pi - 0.2}{0.05}\right) \times \left[(\alpha_\mathbf{K}-1)(\omega^{\text{LDA}}_{\mathbf{q}\nu})^2 + \Delta\right] \tag{4.1}$$

Here, erfc( ) is the error function, $\nu = 1, 2$ is a label for the two TO branches, a_0 is the graphene lattice constant, and $\mathbf{K}_\alpha$ is the closest vector to $\mathbf{q}$ among those equivalent to $\mathbf{K}$. The constants $\alpha_\mathbf{K}$ and Δ are defined as $\alpha_\mathbf{K} = 1.61$ and $\Delta = 42.195\,\text{Ryd}^2$. Both TO phonon branches are degenerate at $\mathbf{K}$ and thus exhibit the same electron-phonon coupling. Therefore, they are

[2]Private communication with M. Calandra (UPMC Paris)

affected by the same renormalization, *i.e.*, the *GW* correction for both TO phonon branches is equivalent.

In contrast to previous *GW*-based calculations of the phonon dispersion in bilayer graphene, we observe a clear splitting between the two TO phonon branches along the $\mathbf{K}-\mathbf{\Gamma}$ high-symmetry direction [compare Fig. 4.3 (c) and (d)]. Ref. [150] found that the TO splitting along $\mathbf{K}-\mathbf{\Gamma}$ is negligible and similar to that along the $\mathbf{K}-\mathbf{M}$ high-symmetry line. This discrepancy to our results is explained by the coarse 6×6 phonon-momentum mesh used in Ref. [150] and the use of Fourier interpolation. In our case, this error is not present due to the use (i) of a larger phonon momentum grid and (ii) of a Wannier-interpolation scheme to obtain phonon frequencies at any electron and phonon momentum in the Brillouin zone with high accuracy [144].

The electric dipole and the electron-phonon matrix elements were first calculated on a 64×64 electron-momentum grid and a 6×6 phonon-momentum grid in LDA approximation. We then interpolate them to denser 480×480 electron-momentum grid randomly shifted from the origin and a 12288-points phonon-momentum grid, covering a sufficiently large region around the $\mathbf{K}$ point. Both quantities were *GW*-corrected afterwards, following the approach given in Ref. [47]. The electronic broadening γ in our calculations was calculated according to [47]

$$\gamma = 0.081832 \times \left(\frac{\hbar\omega_L}{2} - 0.1645\,\mathrm{eV}\right). \tag{4.2}$$

This value was chosen to be twice as large as that in Ref. [47], as this choice gives better agreement with our experimental spectra. In fact, Ref. [47] only considered the intrinsic contribution from electron-phonon scattering to the electronic broadening and neglected the contribution from electron-electron interaction. However, the analysis of Ref. [151] indicates that this contribution is not negligible and can, in fact, double the electronic broadening for high doping levels. We will discuss the effect of the electronic broadening on the $2D$-mode lineshape in Section 4.7 in more detail. Finally, the phonon broadening in our calculations is set to $8\,\mathrm{cm}^{-1}$ [152].

4.4 Experimental details

Freestanding bilayer graphene samples were obtained as described in Chapter 2. In brief, graphene samples were prepared by mechanical exfoliation of natural graphite crystals on SiO_2/Si substrates with 100 nm thick oxide layer. The silicon substrates are patterned with $8\,\mu$m deep holes with a diameter of $3\,\mu$m. These holes were etched by reactive ion etching at the Fraunhofer IZM. Bilayer graphene samples were identified by their optical contrast and cross-checked by Raman measurements of the N and $2D$ mode.

For the measurements on electrochemically-gated bilayer graphene samples, we had to produce electrical contacts to the graphene layer. Here, we followed the approach described in Ref. [153]. This method makes benefit of the low melting point and high surface tension of indium. The setup is schematically shown in Fig. 4.6 (a) and consists of a microscope, a heating plate and

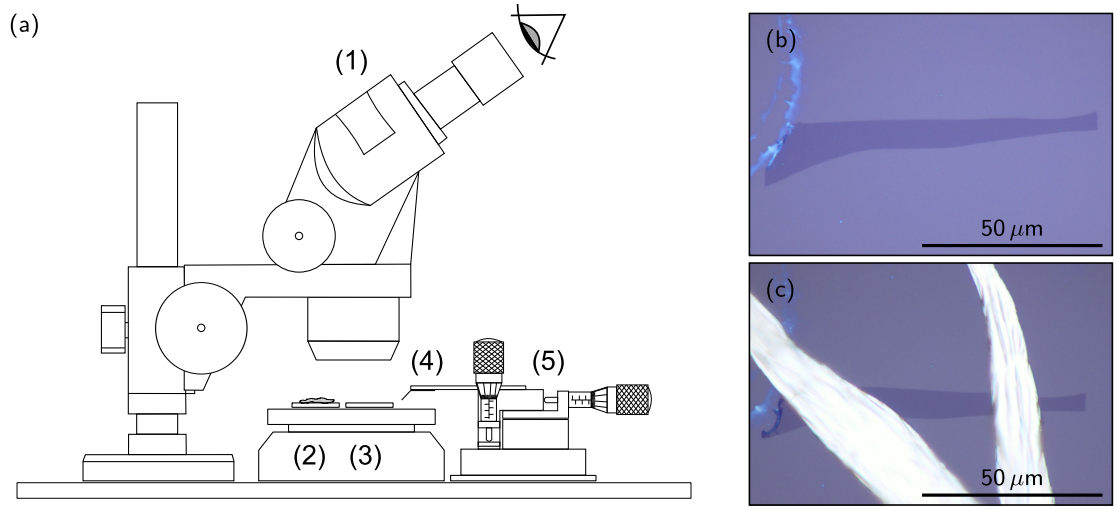

Figure 4.6: (a) Schematic illustration of the experimental setup for micro-soldering of graphene samples. The setup consist of (1) a microscope, (2) melted indium, (3) heated graphene sample, (4) a gold STM tip, and (5) an xyz micro-manipulator. Optical images of a bilayer graphene sample (b) before and (c) after contacting. Scale bares are given in the figures.

an xyz micro-manipulator. First, the solid indium is heated slightly above its melting point of $157\,°C$. In the following, a gold STM tip is pierced in the liquid indium and rapidly retracted. Thus, a thin wire of solid indium is formed at the end of the gold tip. Afterwards, the silicon substrate with the bilayer graphene sample is placed on the hotplate and heated to the same temperature as the liquid indium. Using the xyz micro-manipulator, the thin indium wire is finely positioned on the graphene layer, where it instantaneously melts and forms an electrical contact with the graphene layer. Finally, the temperature of the heating plate is reduced, the liquid indium becomes solid and can be connected to external voltage sources. Figure 4.6 (b) and (c) presents optical images of a bilayer graphene sample before and after contacting using the method described above.

The electrolyte for electrochemical gating of the graphene samples was prepared following the procedure from Ref. [154] with slight modifications. In brief, lithium perchlorate ($LiClO_4$), polyethylene oxide (PEO) with a molecular weight of 100000, and dry methanol were mixed at a weight ratio of 0.012:1:8. This mixture is then stirred for 6 hours at 45 °C under argon atmosphere until a homogeneous milky solution is obtained[3]. This solution is then filtered twice using syringe filters with a pore size of 450 μm. In the following the electrolyte is drop-casted onto the graphene sample using a micro pipette. Finally, the samples are heated to 60 °C for 30 minutes in order to remove residual solvent in the electrolyte. In order to avoid any unwanted effects from electrolyte degradation in ambient air, measurements were carried out within two days after electrolyte drop-casting. For our measurements, we used a Keithley 2400 and an Advantest R6243 DC voltage source.

[3]The electrolyte was prepared by S. Ehrmann (FU Berlin).

All spectra were measured with a Horiba HR800 spectrometer in backscattering geometry under ambient conditions. During all measurements, the laser power was kept below 0.5 mW in order to avoid damaging or heating of our samples. Spectra were calibrated using standard atomic emission lines of neon (Ne).

4.5 Analysis of the *2D* mode in bilayer graphene

Figure 4.7 shows calculated scattering cross-sections $\mathcal{I}_{\mathbf{q}}$ for the $2D$ mode in bilayer graphene for different laser excitation energies. Here, $\mathcal{I}_{\mathbf{q}}$ was calculated as

$$\mathcal{I}_{\mathbf{q}} = \sum_{\mu=9}^{12} \sum_{\nu=9}^{12} \mathcal{I}_{\mathbf{q}}^{\mu,\nu} \tag{4.3}$$

with $\mathcal{I}_{\mathbf{q}}^{\mu,\nu}$ from Eq. (3.14) and for $\omega_{\mathbf{q}}^{\mu,\nu}$ in the frequency range between $2500\,\mathrm{cm}^{-1}$ and $3000\,\mathrm{cm}^{-1}$. As can be seen, the calculated cross-sections exhibit a triangular-shaped contour around the **K** point. This shape is opposite to the electronic trigonal warping, but follows the form of the TO phonon warping around **K** [149]. In contrast to previous works [46, 50–54, 155], we find three resonances around the **K** point that contribute to the double-resonant $2D$-mode scattering cross-section. These resonances can be identified (from inside to outside) with the symmetric P_{11}^{44} process, the anti-symmetric P_{12}^{43} and P_{21}^{34} processes, and the symmetric P_{22}^{33} process. As the resonant phonon wave-vectors of the anti-symmetric processes are nearly degenerated, the resulting phonon frequencies are very similar, disproving all previous works that assigned substantially different phonon frequencies to both anti-symmetric processes [46, 50–54, 155]. Comparing our results to the assignment of Ferrari *et al.* in Fig. 4.5 from Ref. [46], we find the following correspondence:

$$\mathrm{2D_{1B}} \rightarrow P_{11}^{44} \qquad \mathrm{2D_{1A}} \rightarrow P_{12}^{43}/P_{21}^{34} \qquad \mathrm{2D_{2A}} \rightarrow \text{inner } P_{22}^{33} \qquad \mathrm{2D_{2B}} \rightarrow \text{outer } P_{22}^{33}$$

From Figure 4.7 we can further clearly observe that the maximum contribution to the $2D$-mode cross-section stems from regions along the $\mathbf{K}-\mathbf{\Gamma}$ direction. These regions can be assigned to 'inner' processes (compare Fig. 4.4) and we therefore revoke all previous explanations of the $2D$ mode that were based on 'outer' double-resonance processes.

Next, we will turn our discussion to the calculated Raman spectra of the $2D$ mode in bilayer graphene. Figure 4.8 compares our calculated $2D$-mode spectra with experimental Raman spectra from mechanically exfoliated, freestanding bilayer graphene at different laser excitation energies. As can be clearly seen, the overall agreement between the calculation and our experimental data is very good. However, we observe a slight mismatch in frequency between calculation and experiment, *i.e.*, the calculated frequencies are approximately $10\,\mathrm{cm}^{-1}$ too high. Furthermore, the calculated overall $2D$-mode linewidth is too broad. We will discuss the possible reason for both effects later in this chapter. Nevertheless, our calculations do not only reproduce the ex-

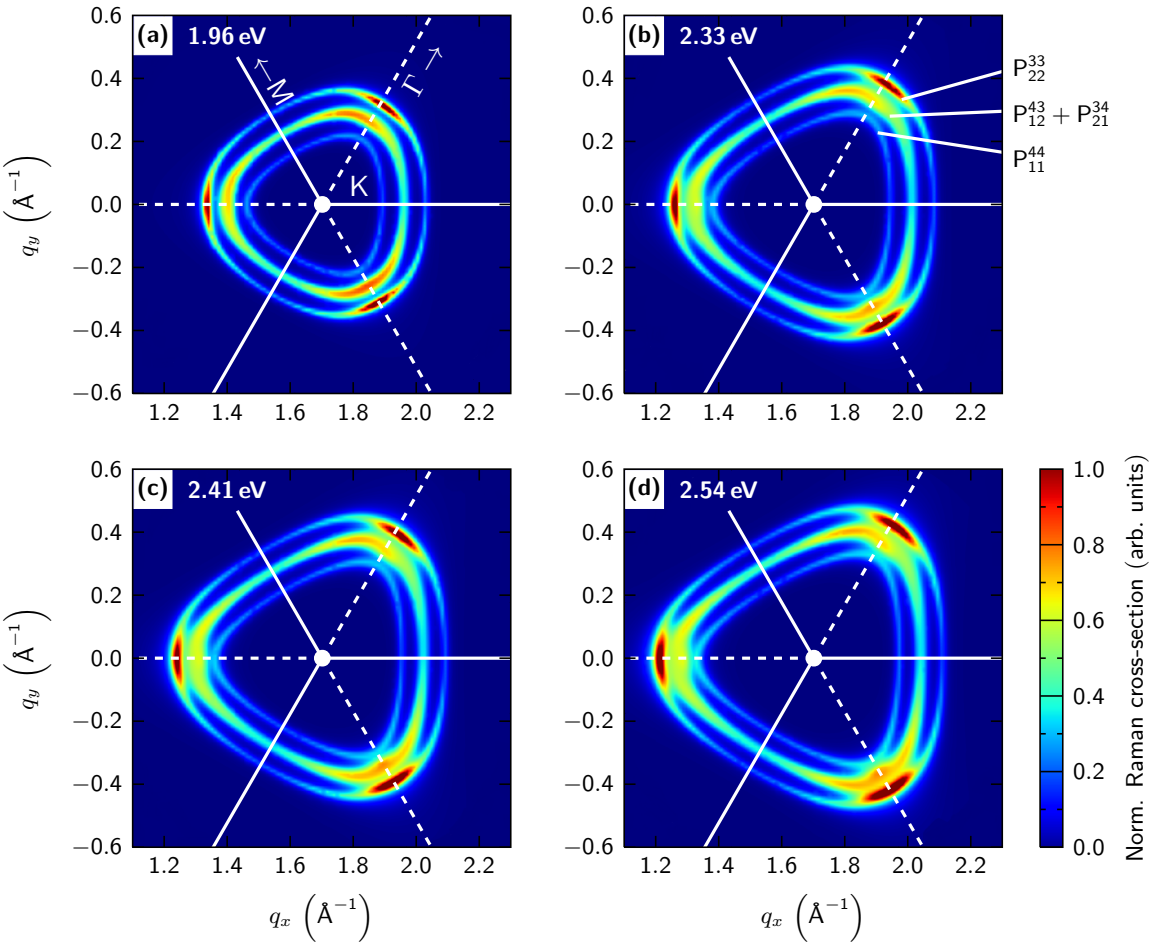

Figure 4.7: Contour plots of the normalized $2D$-mode scattering cross-section $\mathcal{I}_{\mathbf{q}}$ around the **K** point as a function of the phonon wave-vector **q** for different laser excitation energies. The solid and dashed white lines denote the $\mathbf{K}-\mathbf{M}$ and $\mathbf{K}-\mathbf{\Gamma}$ high-symmetry lines, respectively.

perimentally observed $2D$-mode phonon frequencies correctly, but also the lineshape of the $2D$ mode, *i.e.*, the relative intensities of the different contributions.

In the following, we will decompose the calculated $2D$-mode spectra into its different contributions. First, we start with the separation of the spectrum into the different scattering processes, *i.e.*, we separate between those processes where an electron *and* a hole are scattered (*eh* scattering) and those processes where two electrons *or* two holes are scattered (*ee* and *hh* scattering). Fig. 4.9 (a) shows the calculated spectrum at 1.96 eV laser excitation energy considering all scattering processes (gray curve), as well as the contribution from *eh* scattering (black curve). The latter contribution is further divided into inner and outer scattering processes following the scheme explained in Sec. 4.2 and illustrated in Fig. 4.4. We can directly see that *eh* scattering is, by far, the dominant contribution among all possible scattering paths. *eh* scattering is often referred to as a "fully resonant" or "triple resonant" process [47, 48, 156], as all three denominators in Eq. (3.14) converge to zero. However, the dominance of *eh* scattering is not due to the fact that more denominators in the double-resonant Raman scattering cross-section are close to

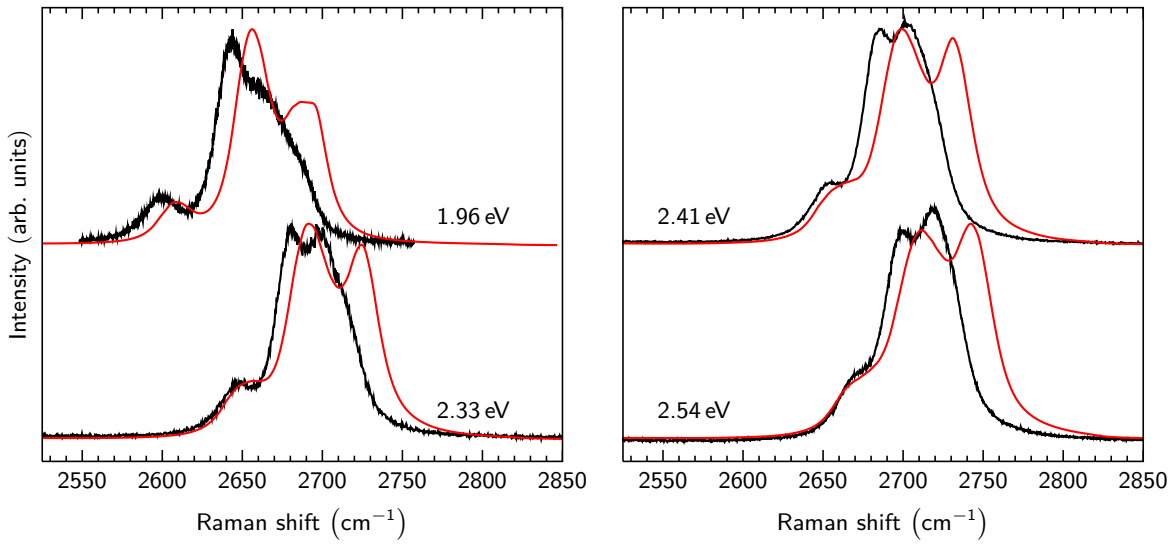

Figure 4.8: Comparison of calculated $2D$-mode spectra with Raman spectra from freestanding bilayer graphene at different laser excitation energies. Calculations and experimental data are shown as red and black curves, respectively. Spectra are normalized and vertically offset for clarity.

resonance. In fact, the large weight of *eh* processes in the scattering cross-section is due to a non-trivial interference effect in the summation of the scattering amplitudes [47]. Fig. 4.10 was adapted from Ref. [47] and shows the real and imaginary part of the scattering amplitude K_α for a double-resonant scattering process in single-layer graphene. As can be seen, the real and imaginary part of K_α for an *eh* process do not change their sign as a function of the phonon wave-vector. In contrast, $\mathrm{Im}(K_\alpha)$ and $\mathrm{Re}(K_\alpha)$ undergo change of sign for *ee* and *hh* scattering. Following Ref. [47], the double-resonant Raman intensity can written as

$$\mathcal{I}_\alpha = \left| \int_0^\infty \frac{k\,\mathrm{d}k}{2\pi} K_\alpha(k) \right|^2 . \tag{4.4}$$

Although K_α is on the same order of magnitude for the different scattering processes, the change of sign of K_α for *ee* and *hh* processes results in a destructive interference inside the integral [47]. In contrast, the K_{eh} add coherently [47]. Thus, $\mathcal{I}_{eh}$ is clearly larger than $\mathcal{I}_{ee/hh}$.

The spectrum in Figure 4.9 (a) can be further decomposed into the contributions from inner and outer scattering processes; the corresponding curves are shown in red and blue color, respectively. As it was already inferred in Figure 4.7 (a)-(d), the dominant contribution to the total Raman intensity in a double-resonant scattering process stems from inner scattering processes. This result has been already verified for single-layer graphene both experimentally and theoretically [47, 49]. There are several reasons for the dominance of inner processes in double-resonant Raman scattering. First, the oscillator strength for optical excitations along the $\mathbf{K}-\mathbf{M}$ high-symmetry line is roughly three times larger compared to the oscillator strength along the $\mathbf{K}-\mathbf{\Gamma}$ direction [109]. Second, it was noted by different authors that, due to anisotropy, the electron-

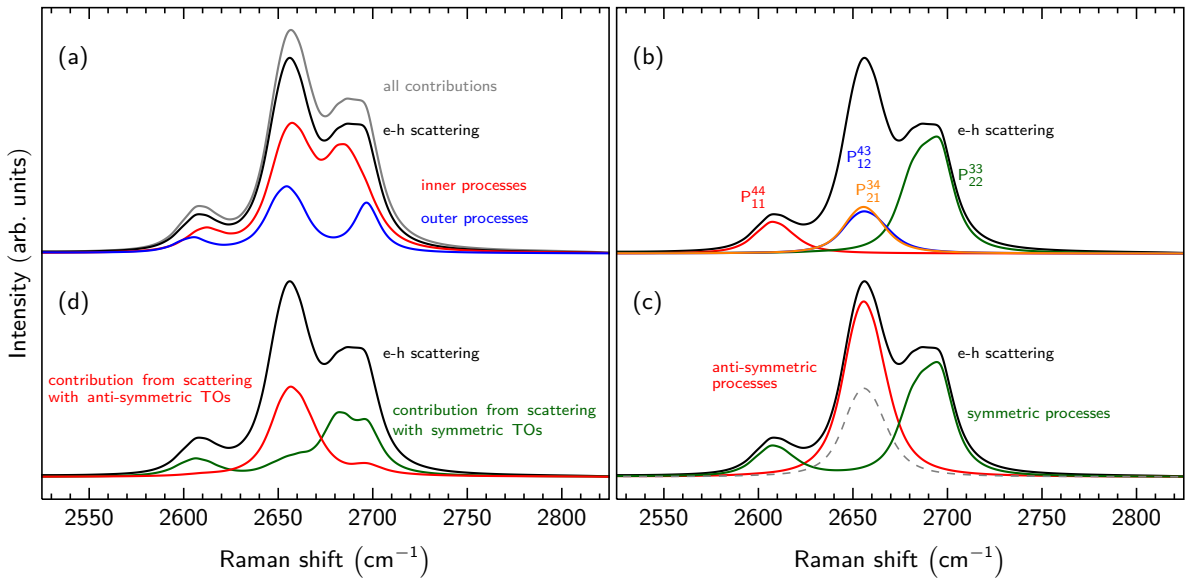

Figure 4.9: Calculated $2D$-mode Raman spectra at 1.96 eV excitation energy. In (a), the total spectrum is decomposed into *eh* scattering processes, as well as into inner and outer contributions. (b) Separation of the contributions from the four different scattering processes P_{mi}^{lj} without interference between the different processes. (c) Decomposition of the calculated spectrum into symmetric and anti-symmetric processes including interference. The dashed line in (c) represents the sum of the contributions from the single anti-symmetric processes P_{12}^{43} and P_{21}^{34} in (b). (d) Decomposition of the calculated spectrum into the contributions from scattering with symmetric and anti-symmetric TO phonons.

phonon coupling is highest for electronic states near the $\mathbf{K}-\mathbf{M}$ high-symmetry line [47, 138]. As a last point, it has been shown by Basko *et al.* [157] that excited electrons and holes around the $\mathbf{K}-\mathbf{\Gamma}$ high-symmetry direction are likely to decay into interband electron-hole pairs (carrier multiplication). Therefore, these states are suppressed in intensity in a double-resonant scattering process and, thus, electronic states along the $\mathbf{K}-\mathbf{M}$ direction are favored to contribute in the double-resonance [158]. Here, we confirm the observation of dominant inner scattering processes in single-layer graphene also for bilayer graphene. Interestingly, the contributions from outer scattering processes are equidistantly spaced in frequency, whereas the inner processes are not. As will be shown below, this is due to the splitting of both TO branches along the $\mathbf{K}-\mathbf{\Gamma}$ direction and we will present an approach to access this quantity experimentally.

In Figure 4.9 (b), we present the decomposition of the calculated $2D$-mode spectrum into the different P_{mi}^{lj} scattering processes. As could be already deduced from Figure 4.7, we find that the symmetric P_{11}^{44} and P_{22}^{33} processes are on the low- and high-frequency side of the $2D$ mode, respectively. The calculated frequencies of both anti-symmetric processes P_{12}^{43} and P_{21}^{34} are in between the symmetric contributions and are degenerate in frequency. Again, this disagrees with all previous publications on the $2D$ mode in bilayer graphene, where substantially different phonon frequencies were assigned to both anti-symmetric scattering processes [46, 50–54, 155].

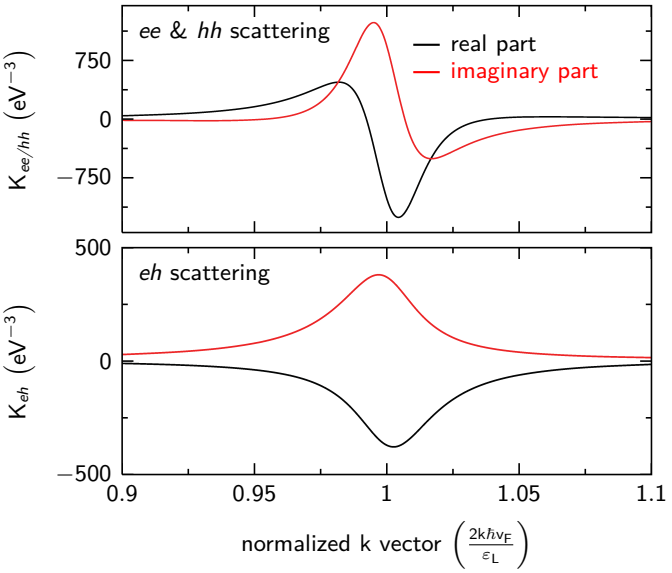

Figure 4.10: Comparison of the real and imaginary parts of the scattering amplitude K_α for ee/hh and eh processes in single-layer graphene considering conical bands. Calculations were done using $\varepsilon_L = 2.4\,\text{eV}$, $\gamma = 84\,\text{meV}$, and $\hbar v_F = 6.49\,\text{eV}\,\text{Å}$. Figure adapted from Ref. [47].

However, an interesting question arises from the presented decomposition into the different P_{mi}^{lj}: As can be seen, the decomposition into the four processes is not additive, *i.e.*, the sum of the P_{mi}^{lj} does not yield the total spectrum. We can directly attribute this effect to quantum interference between both anti-symmetric processes. In order to clarify this point closer, we have to recall the procedure how the single P_{mi}^{lj} in Figure 4.9 (b) are calculated. For every P_{mi}^{lj}, the summation in Eq. (3.14) is restricted to the given indices m, l, j, and i. In the following, the absolute square value is evaluated for each P_{mi}^{lj} separately. Therefore, interference between the four different processes is prohibited and the result can be regarded as "the sum of the absolute squares". In order to allow interference between the different scattering processes, we have to perform the summation of the single processes before the absolute square value is calculated ("the absolute square of the sum"). By decomposing the spectrum into the contributions from symmetric and anti-symmetric scattering processes, we allow interference between P_{11}^{44} and P_{22}^{33} and between P_{12}^{43} and P_{21}^{34}. The result of this calculation is shown in Figure 4.9 (c). Compared to the sum of both single anti-symmetric processes [gray, dashed curve in Figure 4.9 (c)], we can observe a drastic increase in intensity for the contribution from anti-symmetric processes by nearly a factor of two. As both P_{12}^{43} and P_{21}^{34} processes exhibit a large overlap in reciprocal space (compare Figure 4.7), they observe constructive interference. In contrast, the symmetric processes are well separated in $\mathbf{q}$-space and therefore do not show an altered intensity compared to the calculation of the single processes. As can be seen, the interference has remarkable influence on the $2D$-mode lineshape, as it enhances the intensity the anti-symmetric scattering processes drastically. The influence of interference effects on the double-resonance Raman process has been discussed by Maultzsch *et al.* in 2004 in Ref. [135]. This work could demonstrate that scattering processes with $\mathbf{q} = \mathbf{K}$ cancel out by destructive interference. However, none of the previous works on the double-resonance in graphene or graphite considered the effect of constructive interference between two different scattering processes.

As discussed above, the resonant phonon wave-vectors and thus the phonon frequencies for both

anti-symmetric processes are degenerate. Hence, one now might think of possibilities to lift the degeneracy of these scattering processes. First, we should note that the degeneracy of the anti-symmetric processes is due to the equivalence of the **K** and **K′** points in the Brillouin zone of bilayer graphene. Thus, a possible route to lift the degeneracy of P_{12}^{43} and P_{21}^{34} would aim at the breaking of the equivalence between the two carbon sublattices A and B. Sublattice-degeneracy breaking was demonstrated in single-layer graphene by preferentially doping one of the two sublattice sites, *e.g.*, by replacement of carbon atoms with nitrogen directly during the growth process [159]. However, using this approach rather small regions with spatial extents of approximately 1 nm can be produced. Moreover, this approach would not only break the sublattice degeneracy, but would also alter the electronic band structure and phonon dispersion drastically. A more promising approach might be based on a sublattice-periodic potential modulation by the substrate. This approach has been successfully demonstrated in van-der-Waals heterostructures of hexagonal boron nitride (hBN) and graphene and lead to the formation of two isolated superlattices [160]. However, laser spot diameters are usually in the range between 600 and 1000 nm, depending on the laser wavelength and the numerical aperture NA of the microscope objective. In contrast, the Moiré periodicity of the hBN/graphene structure is at most 14 nm [161]. Thus, experimentally one would average over many different Moiré patterns and the sublattice-degeneracy breaking would become indistinct. Therefore, it seems questionable that a splitting of the anti-symmetric processes in the double-resonant $2D$-mode scattering process is observable.

As a last point, we decompose the theoretically calculated $2D$-mode spectrum into the contributions from scattering with symmetric and anti-symmetric TO phonons. As discussed before, the TO branch in bilayer graphene splits up into a symmetric and an anti-symmetric vibration at the **Γ** point with E_g and E_u symmetry, respectively. The separation is performed by calculating the overlap $\alpha_{\mu,\nu}^{\mathbf{q},\mathbf{q}'}$ between the eigenvectors **e** of a phonon mode μ at a wave vector **q** with a phonon mode ν at an arbitrary point $\mathbf{q}'$ in the Brillouin zone

$$\alpha_{\mu,\nu}^{\mathbf{q},\mathbf{q}'} = \left| \sum_{i=1}^{4} \mathbf{e}_{i,\mu}^{\mathbf{q}} \cdot \overline{\mathbf{e}}_{i,\nu}^{\mathbf{q}'} \right|^2 . \tag{4.5}$$

Here, the index i labels the four atoms in the unit cell of bilayer graphene. However, only along the high-symmetry lines the vibrational character of the phonon branches is well defined. Outside these directions, the symmetric and anti-symmetric TO branches cannot be separated univocally by their vibration pattern. Therefore, we only considered the TO branches along the **Γ** − **K** − **M** high-symmetry direction in this analysis first. The reference point **q** for this calculation was chosen to be close to **K** on the **K** − **Γ** direction, because the symmetric and anti-symmetric TO branches are well separated in frequency here. This analysis yields the indices μ and ν of both TO phonon branches as a function of **q** along **Γ** − **K** − **M**. Afterwards, we can use these indices as a starting point and follow the TO phonon outside the high-symmetry directions. The result of this analysis is shown in Figure 4.11; the white circle directly at **K**

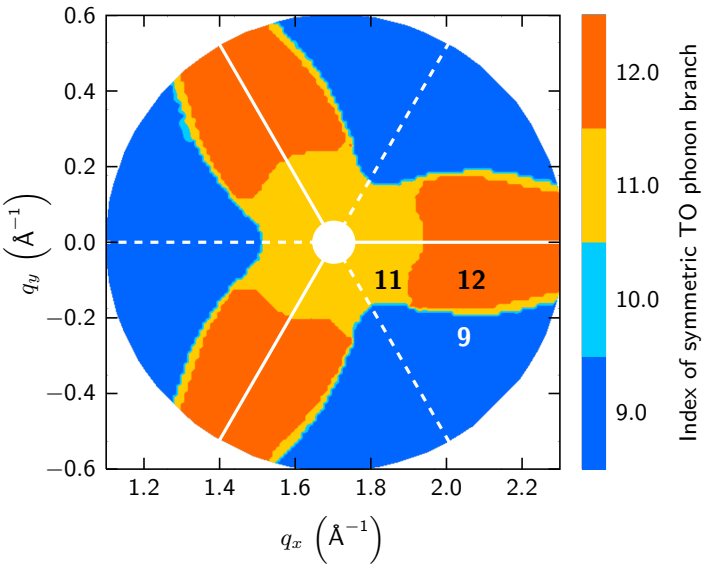

Figure 4.11: Index of the symmetric TO phonon branch around the **K** point as a function of the phonon wave-vector **q**.

was not covered in our calculations. By restricting the summation of the scattering amplitudes in Eq. (3.14) to the TO phonon indices obtained from Figure 4.11, we obtain the decomposed spectrum in Fig. 4.9 (d). As can be seen, the main contribution to the symmetric scattering processes stems from scattering with symmetric TO phonons (E_g symmetry at Γ), whereas the dominant contribution to anti-symmetric processes results from scattering with anti-symmetric TO phonons (E_u symmetry at Γ). This result is not surprising since scattering occurs between states of different symmetry in an anti-symmetric double-resonance process, thus, requiring an anti-symmetric phonon to preserve symmetry. The possibility of scattering with different TO phonons in the double-resonance process has been discussed by other authors before [134, 139]. However, as the splitting between both TO branches was not considered before, scattering with phonons of different symmetry did not led to different phonon frequencies. As will be shown later in Section 4.6, we demonstrate that the coupling of symmetric and anti-symmetric scattering processes to different phonon branches indeed affects the $2D$-mode frequencies.

Up to now, we described the $2D$-mode scattering process in terms of three dominant contributions, *i.e.*, the P_{11}^{44} process, the two degenerate processes P_{12}^{43} and P_{21}^{34}, and the P_{22}^{33} process. These three contributions should additionally split up into inner and outer processes. Thus, one would expect to observe six separate peaks in the $2D$-mode spectrum. However, this is in contrast to the experimentally observed lineshape, where usually three to four peaks can be distinguished, depending on the laser excitation energy. This discrepancy can be resolved, when we compare inner and outer contributions of the four different scattering processes in the decomposed spectrum of Fig. 4.9 (a). The inner and outer contributions for most processes are nearly degenerate in frequency, only the P_{22}^{33} process exhibits a splitting that is large enough to be detected in experiments. Thus, the number of observable peaks reduces to four. Ergo, the $2D$ mode should be fitted with four peaks, where the assignment of the peaks, from lowest to highest frequency, is P_{11}^{44}, P_{12}^{43}/P_{21}^{34}, inner P_{22}^{33} and outer P_{22}^{33}. In all previous works, the inner P_{22}^{33} contribution was erroneously assigned to an anti-symmetric scattering process, whereas the

outer contribution, *i.e.*, the small high-frequency shoulder of the $2D$ mode, was attributed to a symmetric process [46, 50–54, 155]. Here, we showed that these two peaks result from the same scattering process. Our assignment of the third and fourth $2D$-mode peaks to inner and outer P_{22}^{33} contributions is supported by an experimental work by Frank *et al.* on strained bilayer graphene [162]. Frank *et al.* argued that peak shifts and intensity variations of the third and fourth peak in strained bilayer graphene resemble the observations of inner and outer processes of the $2D$ mode in strained single-layer graphene [137]. Since inner and outer processes exhibit different dispersions with laser excitation energy [47, 49], both contributions of the P_{22}^{33} process merge with increasing laser energy. Therefore, at higher laser energies the fourth peak vanishes. Experimentally, this effect can be nicely seen in the spectrum of freestanding bilayer graphene at 2.54 eV excitation energy in Fig. 4.8. Here, the small high-frequency shoulder cannot be identified any more. At excitation energies above 2.54 eV, this effect becomes even more obvious (compare Fig. 4.19). This gives further evidence to our assignment of the different $2D$-mode contributions.

4.6 Derivation of the TO phonon and electronic splitting from *2D*-mode spectra

As explained above, the dominant contribution to symmetric and anti-symmetric processes stems from scattering with TO phonons from different phonon branches, *i.e.*, the main contribution to symmetric processes results from scattering with symmetric TO phonons and vice versa. This fact has remarkable impact on the $2D$-mode lineshape. First, we should recall that the resonant phonon wave-vectors are nearly equidistant in reciprocal space (compare Fig. 4.7). Thus, if all scattering processes would couple to the same phonon branch, we would expect that all contributions in the $2D$-mode spectrum should be equidistantly spaced in frequency. However, this is only true for outer processes, as can be seen from Fig. 4.9 (a), and is explained with the negligible TO phonon splitting along $\mathbf{K} - \mathbf{M}$ for these processes [compare Fig. 4.3 (c) and (d)]. By considering inner processes, a different situation emerges. Here, the contributions are not equidistant in frequency. This is a direct consequence of the splitting between both TO phonon branches along the $\mathbf{K} - \mathbf{\Gamma}$ direction and the coupling of the scattering processes to different phonon branches. Since the inner anti-symmetric scattering processes couple to the energetically higher phonon branch along $\mathbf{K} - \mathbf{\Gamma}$, their frequency is upshifted with respect to the center between both symmetric processes (ω_{11}^{44} and ω_{22}^{33}). This situation is shown in Fig. 4.12 (a) and (b). As the double-resonant $2D$ mode is a two-phonon process, the upshift of the anti-symmetric processes is twice the TO phonon splitting.

In the following, we want to present a method to derive the TO phonon splitting in bilayer graphene directly from experimental Raman spectra. As discussed above, the P_{22}^{33} peak splits up into an inner and outer contribution, which is clearly observable for smaller laser excitation energies. For the calculation of the TO phonon splitting we used the inner component, *i.e.*, the

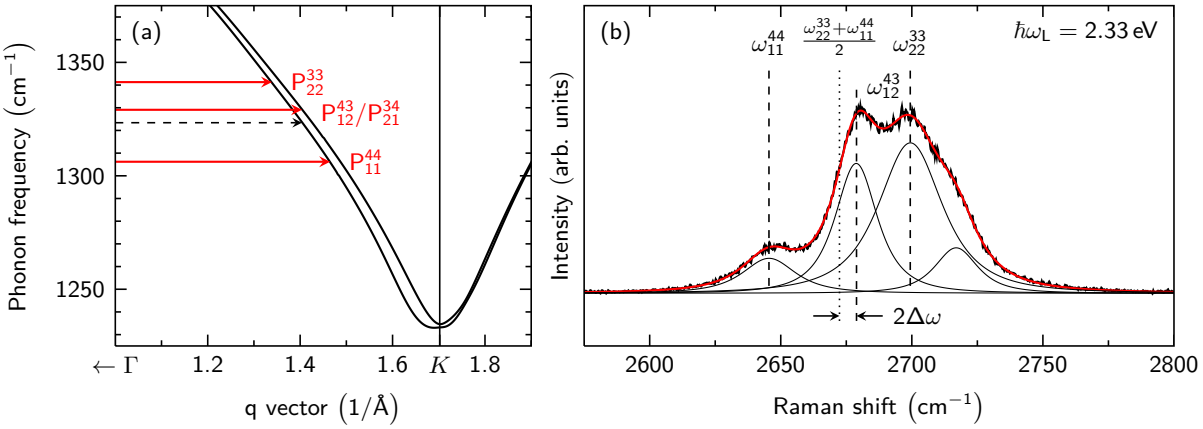

Figure 4.12: (a) *GW*-corrected TO phonon branches along the $\mathbf{\Gamma}-\mathbf{K}-\mathbf{M}$ direction for bilayer graphene. The red arrows denote the one-dimensional resonant phonon wave-vectors for the different scattering processes P^{lj}_{mi}. The dashed arrow indicates the phonon frequency of the anti-symmetric processes, if all processes would couple to the same (energetically lower) phonon branch. The frequency difference that results from the coupling of the anti-symmetric processes to the energetically higher TO branch can be clearly seen. (b) Exemplary fit of an experimental $2D$-mode spectrum from freestanding bilayer graphene at 2.33 eV laser excitation energy. The solid, red curve represents the fit to the experimental spectrum based on the model from Basko [48]. The relevant peak positions of the single peaks are marked with dashed lines, the center between the symmetric scattering processes is shown by the dotted line. The upshift of the anti-symmetric processes with respect to the center between the symmetric contributions (dotted line) is indicated.

third $2D$-mode peak [ω^{33}_{22} in Fig. 4.12 (b)], as we want to investigate the TO splitting along the $\mathbf{K}-\mathbf{\Gamma}$ direction. Figure 4.12 (b) shows an exemplary fit of a measured $2D$-mode spectrum at 2.33 eV laser energy using a fit of the form

$$f(\omega) = \sum_{i=1,4} a_i \cdot f_i\left(\omega, \omega_i, \Gamma_i\right), \tag{4.6}$$

where

$$f_i\left(\omega, \omega_i, \Gamma_i\right) = \left(\frac{\Gamma_i^2}{4\left(-1+2^{2/3}\right)(\omega-\omega_i)^2+\Gamma_i^2}\right)^{3/2} \tag{4.7}$$

is a normalized function following the model of Basko [48]. Here, a_i reflects the peak amplitude, ω_i represents the central peak frequency and Γ_i is the full width at half maximum (FWHM). During all fitting routines, no fitting parameters were shared among the different 'Baskonian' profiles, *e.g.*, the same full-width-at-half-maximum. In Figure 4.12 (b), the peak positions of the P^{44}_{11}, P^{43}_{12}, and inner P^{33}_{22} processes are marked by vertical dashed lines. Furthermore, the center

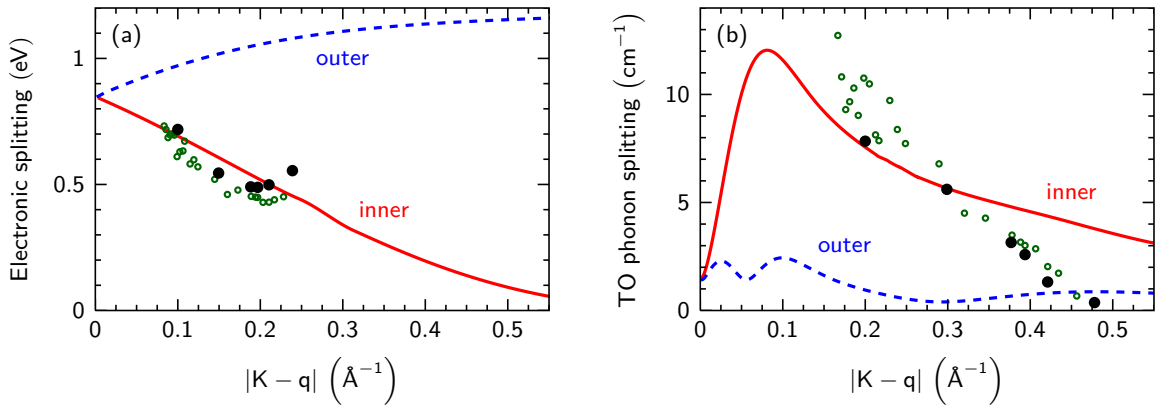

Figure 4.13: Experimentally obtained values for (a) the electronic and (b) TO phonon splitting. The solid (red) and dashed (blue) lines denote the DFT+GW calculated splittings in $\mathbf{\Gamma} - \mathbf{K}$ (inner) and $\mathbf{K} - \mathbf{M}$ (outer) direction, respectively. Open, green circles are data points taken from Ref. [52]. Filled, black circles represent data points obtained from measurements on freestanding bilayer graphene in this work.

between both symmetric processes is indicated by a dotted line. The upshift $\Delta\omega$ due to the TO phonon splitting is given by

$$\Delta\omega = \frac{1}{2}\left(\omega_{12}^{43} - \frac{\omega_{11}^{44} + \omega_{22}^{33}}{2}\right), \tag{4.8}$$

where ω_{mi}^{lj} refers to the peak positions of processes P_{mi}^{lj}. Furthermore, we can also derive the splitting between both electronic bands from the experimental $2D$-mode spectra. The electronic splitting $\Delta\varepsilon$ is given by the frequency difference between both symmetric processes divided by the dispersion of the $2D$-mode peaks with laser excitation energy. In other words,

$$\Delta\varepsilon = \frac{\omega_{22}^{33} - \omega_{11}^{44}}{\mathrm{d}\omega/\mathrm{d}\hbar\omega_L}. \tag{4.9}$$

Here, $\mathrm{d}\omega/\mathrm{d}\hbar\omega_L$ is the laser-energy dependent shift rate of the $2D$ mode. It is important to notice that the $2D$-mode dispersion is non-linear, as can be seen from Ref. [52]. We used a quadratic fit to the data points from Ref. [52] to obtain the dispersion, which has the form

$$\frac{\mathrm{d}\omega}{\mathrm{d}\hbar\omega_L} = 181\,\frac{\mathrm{cm}^{-1}}{\mathrm{eV}} - 30.5 \times \hbar\omega_L\,\frac{\mathrm{cm}^{-1}}{\mathrm{eV}^2}$$

By tuning the laser excitation energy in our experiment, we can change the resonant phonon wave-vector enhanced by the double-resonance condition and thus map the TO phonon and electronic splitting along the high-symmetry directions. Combining our own measurements with experimental data from Mafra *et al.* [52], we can plot both quantities $\Delta\varepsilon$ and $\Delta\omega$ as a function of $\mathbf{q}$. The plots are shown in Figure 4.13 (a) and (b); for simplicity and better comparison,

we plotted our data as a function of the difference between **q** and the **K** point. As can be seen, our experimental data follow the calculated curves along the inner direction. However, we observe disagreement between calculation and experiment for the TO phonon splitting. Since also phonons away from the high-symmetry direction contribute to the double resonance [142], the experimentally measured TO splitting is expected to be smaller than theoretically predicted along the $\mathbf{\Gamma} - \mathbf{K}$ direction. Thus, the theoretical curves along the inner and outer directions should represent an upper and a lower limit for the experimental values, respectively. As can be seen, for small **q** we observe a disagreement between calculation and experiment of up to 40 %. The fact that the experimental data points are significantly higher than the theoretical limit indicates that the commonly assumed *GW* correction might still underestimate the TO splitting, which is probably larger than $15\,\mathrm{cm}^{-1}$ close to **K**. The assumption of an underestimated *GW* correction is further supported by the fact that the calculated overall peak width of the $2D$ mode is larger than experimentally observed (compare Fig. 4.8). An increase of the *GW*-related correction to the TO phonons would not only increase the TO phonon splitting, but also leads to a larger slope of the TO branch. The larger slope would reduce the frequency differences between the different contributions, ergo, the overall peak width decreases. Hence, this would further increase the agreement between the calculations and our experimental Raman spectra. Yang *et al.* derived from first-principles calculations that the *GW* correction on the electronic system is qualitatively similar for single and bilayer graphene, however, the correction is not quantitatively equivalent [163]. More recently, Rösner *et al.* derived Coulomb interactions in single-layer graphene, bilayer graphene, and graphite using a Wannier function approach [164]. The differences between the Coulomb interactions in these systems can be directly understood from different dielectric environments and different screenings of the Coulomb potential. The importance of the electronic screening on electron-electron interactions in graphene was recently pointed out by Faugeras *et al.* [65]. Refs. [163] and [164] indicate that the *GW* correction on the electrons for single and bilayer graphene is slightly different in both systems. However, there are no calculations of the *GW* correction on the electron-phonon coupling in bilayer graphene. A recent work by Narula *et al.* found indications that the slope of the TO phonon branch might be 40 % larger than theoretically expected [165]. In our work, the *GW* correction for the TO phonons around the **K** point is assumed to be the same as in single-layer graphene. However, the comparison of the calculated $2D$-mode spectra with our experimental data suggest that the *GW* corrections in bilayer graphene are underestimated as compared to single-layer graphene.

4.7 Dependence of the double-resonant Raman spectra on the electronic broadening

In the following section, we want to investigate the dependence of the double-resonant $2D$-mode spectra on the electronic broadening γ. The electronic broadening, *i.e.*, the inverse lifetime of

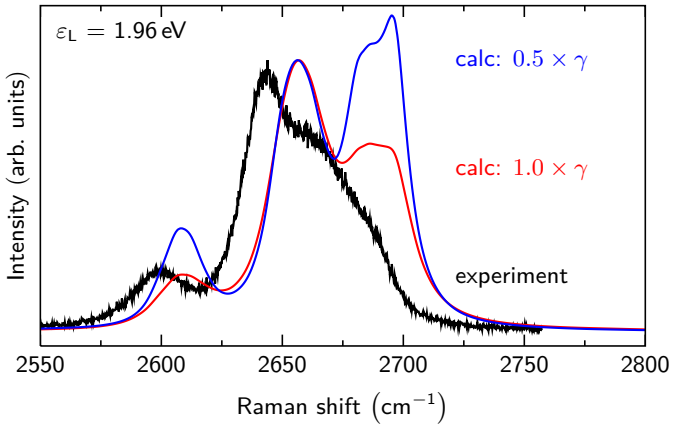

Figure 4.14: Comparison of experimental and calculated Raman spectra at 1.96 eV laser energy with different electronic broadenings. The γ was calculated according to Eq. (4.2). Spectra were normalized to the contribution from anti-symmetric scattering processes.

the electronic states, can be divided into three different contributions

$$\gamma = \gamma^{\text{e-ph}} + \gamma^{\text{D}} + \gamma^{\text{e-e}}. \tag{4.10}$$

Here, $\gamma^{\text{e-ph}}$ reflects the contribution from electron-phonon scattering, which can be further separated into the contribution from **Γ**- and **K**-point phonons. γ^{D} refers to the electron-defect scattering rate and $\gamma^{\text{e-e}}$ represents the contribution to γ from scattering between charge carriers. In principle, all three contributions can be manipulated experimentally. For instance, $\gamma^{\text{e-ph}}$ depends on the laser excitation energy [47], as well as on temperature [166, 167]. Naturally, γ^{D} depends on the amount and type of defects and is also influenced by the laser energy [47]. Finally, $\gamma^{\text{e-e}}$ can be tuned by shifting the Fermi level. In fact, Basko *et al.* calculated that $\gamma^{\text{e-e}}$ scales linearly with $|E_{\text{F}}|$ in single-layer graphene [168]. Previous studies already extensively investigated the effect of defects and doping on the double-resonant scattering process by analyzing the D/G- and $2D/G$-mode intensity ratio in single-layer graphene [32, 33, 154, 169–171]. For bilayer graphene, different studies that investigate the doping dependence of the E_{g} and E_{u} **Γ**-point vibrations were reported [35, 172–174]. However, none of the previous works analyzed the influence of the electronic broadening on the double-resonant $2D$-mode scattering process and its effect on the $2D$-mode lineshape in bilayer graphene.

Our analysis is motivated by the observation that the $2D$-mode lineshape in our calculations significantly depends on the electronic broadening, *i.e.*, we observe a strong variation between the ratio of symmetric and anti-symmetric contributions by a change in γ. Usually, in theoretical calculations of the double-resonant Raman scattering cross-section the broadening is chosen as given by Ref. [47]. However, this work only considered the contributions from electron-phonon scattering $\gamma^{\text{e-ph}}$ to the overall scattering rate γ. Figure 4.14 compares calculated $2D$-mode spectra for two different values of the electronic broadening. The blue curve ($0.5 \times \gamma$) reflects a calculation using the electronic broadenings from Ref. [47]; the red curve ($1.0 \times \gamma$) represents a calculation, where an electronic broadening twice as large as before was used. As can be seen from the comparison with the experimental data, the red curve fits our experimental $2D$-mode spectrum. The blue curve overestimates the contribution from symmetric scattering processes, or

vice versa, underestimates the contribution from anti-symmetric processes. Moreover, Ref. [175] reported a Raman study of chemically-functionalized bilayer graphene and observed a lineshape variation as a function of the doping level. However, the observed lineshape changes upon doping were not discussed. Apparently, the influence of the electronic broadening on the double-resonance process in bilayer graphene is not yet understood and needs further investigation.
In order to analyze the effect of the electronic broadening γ on the double-resonant scattering processes in bilayer graphene, we performed calculations of the Raman scattering cross-section using Eq. (3.14). For simplicity, we assumed the matrix elements $\mathcal{M}$ to be constant and restricted the integration to the $\mathbf{\Gamma} - \mathbf{K} - \mathbf{M}$ high-symmetry direction. This approach seems justified as the main contributions in the double-resonance process stem from the high-symmetry lines [47, 142, 176]. In the following, we only present the resonant phonon wave-vectors for inner processes, however, outer processes behave likewise. The results of our calculations are shown in Fig. 4.15. Figure 4.15 (a) shows the evolution of the resonant phonon wave-vectors at a constant laser excitation energy using different electronic broadenings. The correspondence between the scattering processes P_{mi}^{lj} and the different contributions is given above this plot. As can be seen, an increase of the electronic broadening γ leads to an enhancement of the anti-symmetric processes compared to the symmetric contributions. Figures 4.15 (b) and (c) show the calculated resonant phonon wave-vectors of the $2D$ mode in bilayer graphene for different laser excitation energies without and with a variation of the electronic broadening, respectively. The broadenings in Figure 4.15 (c) were calculated according to Eq. (4.2). In contrast to Figure 4.15 (a), we observe the opposite intensity variation between symmetric and anti-symmetric processes for increasing values of γ. We also want to point out the significant lineshape variations of the symmetric contributions in all calculations for an increasing value of γ, *i.e.*, we observe a strong asymmetry of P_{22}^{33} and P_{11}^{44} towards the high- and low-momentum side, respectively. Such asymmetric lineshapes are, for instance, observed in Fano resonances and are usually identified with quantum interference between different contributions. As we already discussed in Sec. 4.5, quantum interference remarkably influences the $2D$-mode lineshape, *i.e.*, we demonstrated an enhancement of the anti-symmetric contribution by a factor of two due to constructive interference between the P_{12}^{43} and P_{21}^{34} processes. Of course, this constructive interference is also present in these calculations [compare Fig. 4.15 (d)].
In order to further exploit the interference effects between symmetric and anti-symmetric scattering processes, we decompose the calculated resonant phonon wave-vectors into their real and imaginary part. This decomposition is shown in Figure 4.16 (a) and (b) for a calculation with a constant laser excitation energy and a variation of the electronic broadening. The calculated curves for the single contributions resemble the expected lineshape of the resonance of a Lorentz oscillator with finite lifetime and three denominators which are close-by in resonance energy. By comparing the real and imaginary parts in Fig. 4.16 (a) and (b), we observe changing overlaps between the different contributions as a function of γ. To emphasize this observation, we highlight the overlap in the real part of the complex scattering amplitude between the symmetric Re(sym.) and anti-symmetric Re(asym.) processes by the gray area. As can be seen,

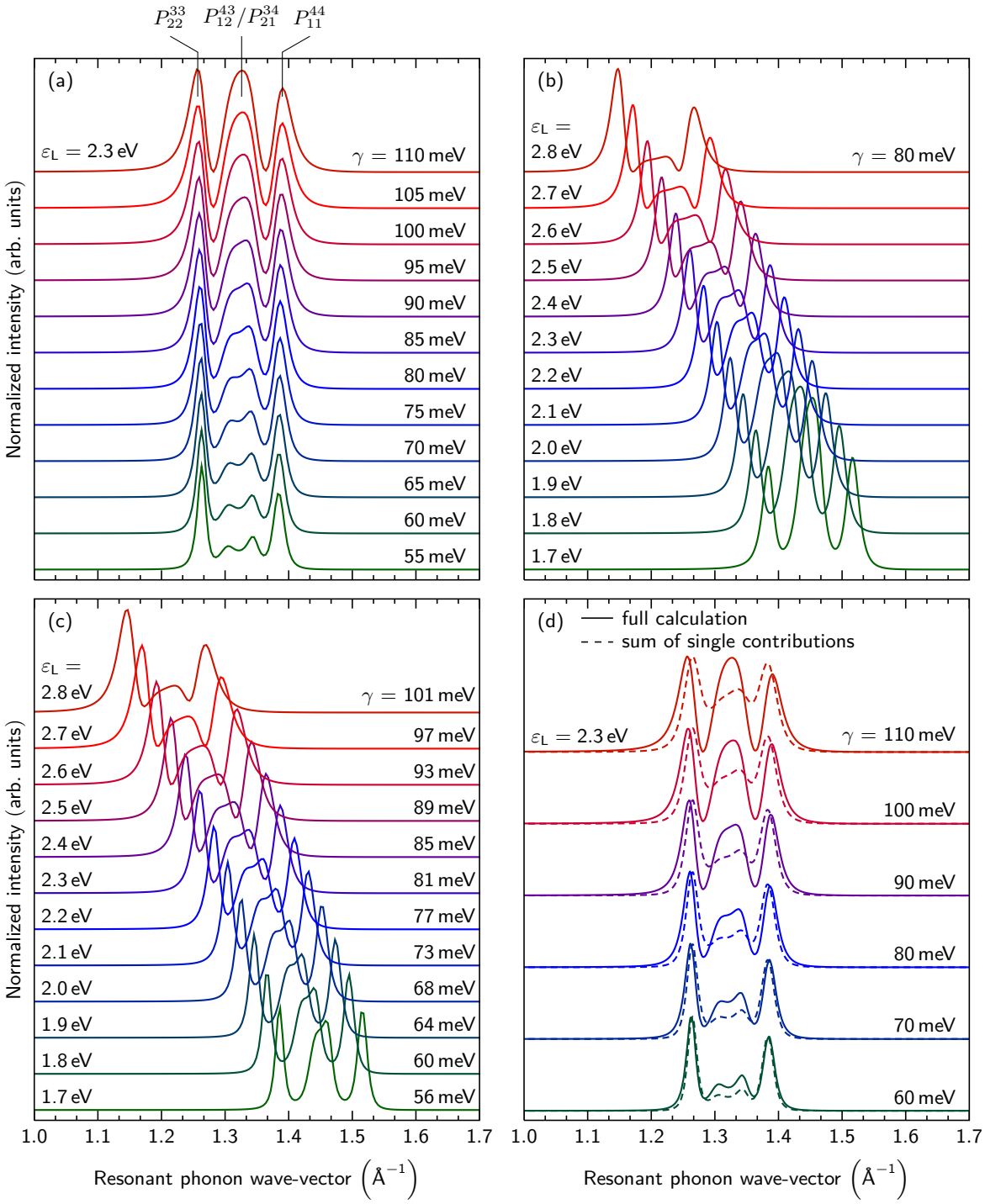

Figure 4.15: Calculated resonant phonon wave-vectors in the $2D$-mode double-resonance process of bilayer graphene using different calculational scenarios. The calculations assumed (a) a fixed laser energy ε_L and a variation of the electronic broadening γ, (b) a fixed γ and a variation of ε_L, and (c) a variation of both ε_L and γ according to Eq. (4.2). (d) Comparison of the resonant phonon wave-vectors for a full calculation considering interference between all P_{mi}^{lj} (solid line) versus the sum of the single P_{mi}^{lj} without interference (dashed line). All spectra are normalized to the P_{22}^{33} contribution and vertically offset for clarity.

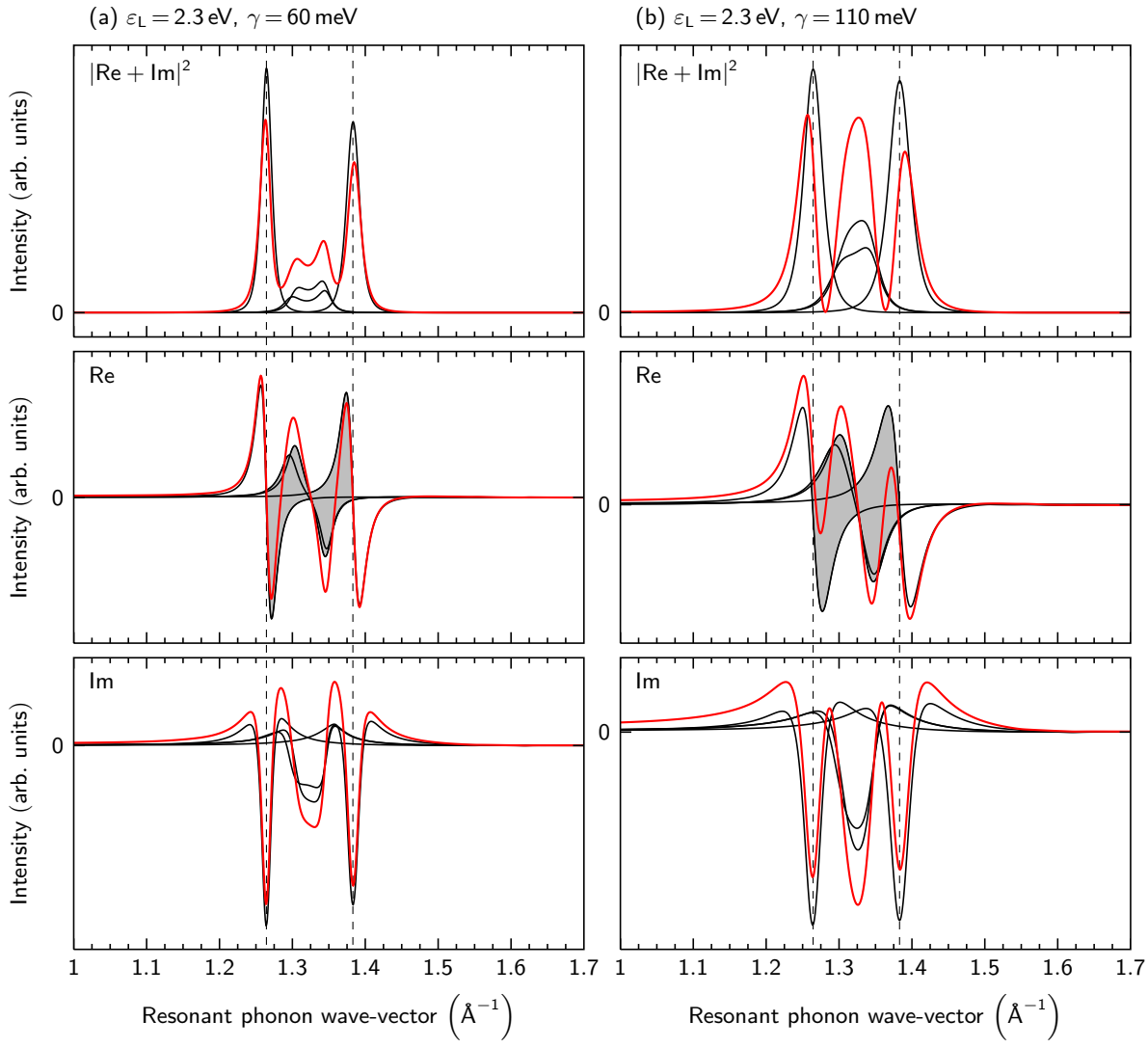

Figure 4.16: Separation into the real and imaginary part of the resonant phonon wave-vectors for a fixed laser energy and a variation of the electronic broadening. The calculational parameters are (a) $\varepsilon_L = 2.3\,\mathrm{eV}$, $\gamma = 60\,\mathrm{meV}$ and (b) $\varepsilon_L = 2.3\,\mathrm{eV}$, $\gamma = 110\,\mathrm{meV}$. The solid black lines refer to the single processes P_{mi}^{lj}, whereas the red curve is the sum of the different contributions. The overlap of the symmetric and anti-symmetric processes in the real part of the complex scattering amplitude is indicated by the gray area. The vertical dashed lines indicate the resonant phonon wave-vectors of both symmetric processes and are a guide to the eye.

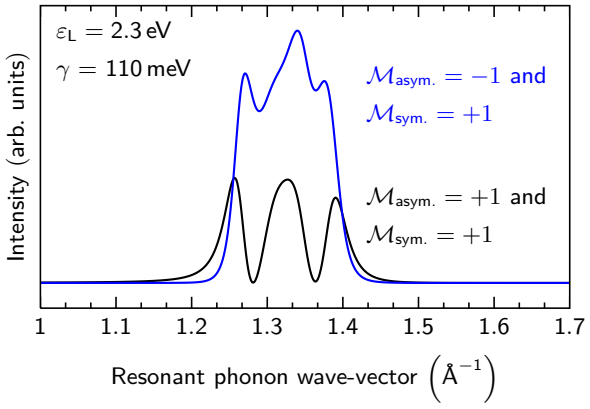

Figure 4.17: Calculation of the resonant phonon wave-vector with different signs of the matrix elements $\mathcal{M}$ for symmetric and anti-symmetric processes.

the overlap between both anti-symmetric processes depends only marginally on γ, as these processes are always degenerate. Ergo, the constructive interference between P_{12}^{43} and P_{21}^{34} cannot explain the observed variation of the ratio between symmetric and anti-symmetric processes as a function of the electronic broadening. In contrast, we identify further quantum-interference effects in our spectra, *i.e.*, both destructive and constructive interference between symmetric and anti-symmetric processes. These effects can be seen best, when we compare the sum of the real and imaginary parts [red curves in the middle and bottom panels of Fig. 4.16 (a) and (b)] with the single contributions from the scattering processes P_{mi}^{lj}. As can be seen, the resonance broadens with increasing γ and leads to a larger overlap of Re(sym.) and Re(asym.) with opposite algebraic sign. Thus, these contributions add up incoherently, leading to a destructive interference. This effect explains the asymmetric lineshape of P_{22}^{33} and P_{11}^{44} towards the high- and low-momentum side, respectively. Moreover, we observe an increasing overlap of Re(sym.) and Re(asym.) with the same algebraic sign on the low- and high-momentum side of P_{22}^{33} and P_{11}^{44}, respectively, further increasing the asymmetry of the resonant phonon wave-vectors for the symmetric contributions. By looking at the imaginary parts for symmetric and anti-symmetric processes, we can observe similar dependencies. With increasing γ, the overlap between Im(sym.) and Im(asym.) with opposite algebraic sign increases, leading to a decrease in intensity of the symmetric processes. In total, the destructive interference leads to a reduction of the intensity from symmetric processes and is also responsible for the asymmetric lineshape of the resonant phonon wave-vectors for P_{22}^{33} and P_{11}^{44}.

To support our argumentation, we performed calculations of the resonant phonon wave-vectors, where we individually adjusted the sign of the matrix elements for symmetric and anti-symmetric processes. If the above calculated $2D$-mode lineshape and the reduction in intensity of the symmetric processes is due to destructive interference, we may enable constructive interference between symmetric and anti-symmetric scattering processes by changing their relative sign. The result of this calculation is shown in Figure 4.17. As can be seen, the $2D$-mode lineshape changes drastically in our calculations when the matrix elements for symmetric and anti-symmetric processes exhibit different signs. In fact, we observe an increase in intensity for the symmetric processes, which can be identified with constructive interference. Since the sign change does

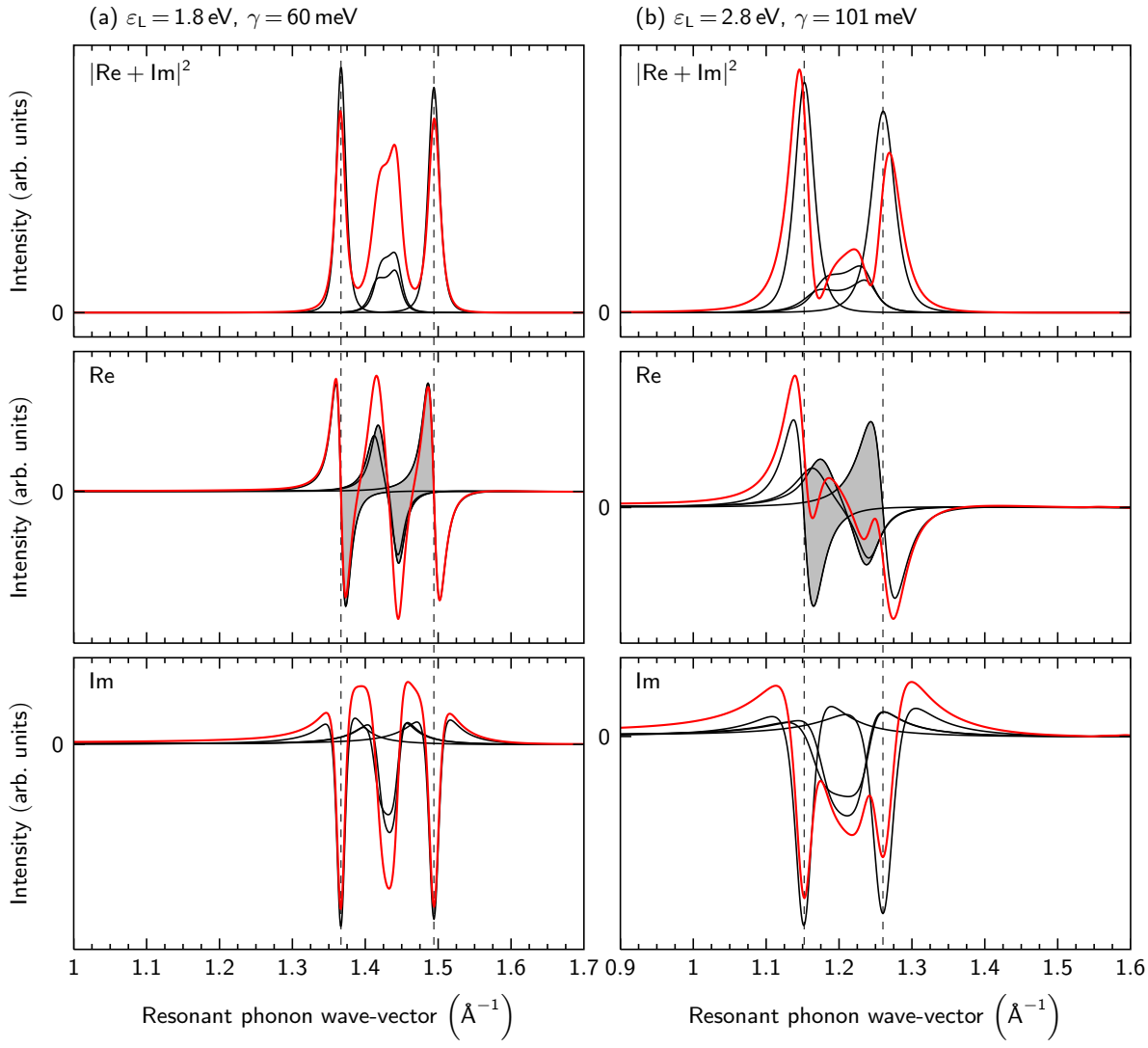

Figure 4.18: Separation into the real and imaginary part of the resonant phonon wave-vectors for a variation of both the laser energy and the electronic broadening The calculational parameters are (a) $\varepsilon_L = 1.8\,\mathrm{eV}$, $\gamma = 60\,\mathrm{meV}$ and (b) $\varepsilon_L = 2.8\,\mathrm{eV}$, $\gamma = 101\,\mathrm{meV}$. The solid black lines refer to the single processes P_{mi}^{lj}, whereas the red curve is the sum of the different contributions. The overlap of the symmetric and anti-symmetric processes in the real part of the complex scattering amplitude is indicated by the gray area. The vertical dashed lines indicate the resonant phonon wave-vectors of both symmetric processes and are a guide to the eye.

not affect the constructive interference between both anti-symmetric processes, we also observe a strong increase in intensity for these contributions. Ergo, this calculation supports our assumption of destructive interference between symmetric and anti-symmetric processes and nicely demonstrates the drastic effects that interference can have on the double-resonant phonon wave-vectors.

As mentioned before, we observe a different dependence of the ratio between symmetric and anti-symmetric scattering processes by increasing both the laser excitation energy and the electronic broadening, as compared to the above discussed situation. Also for this case, we present a decomposition into the real and imaginary parts of the scattering amplitude [see Figure 4.18 (a) and (b)]. Compared to the calculation in Fig. 4.16 (a) and (b), we do not only observe a broadening of the resonant phonon wave-vectors in this calculation, but we also notice a relative shift of the different contributions. In fact, this shift is responsible for the lineshape variations as a function of laser excitation energy. Due to the relative shift of symmetric and anti-symmetric wave-vectors, the overlap between contributions of the same algebraic sign increases, leading to an increase in intensity of symmetric processes and a decrease in intensity for the anti-symmetric processes. This effect can be observed both for the real and the imaginary part of the complex scattering amplitude. The above described intensity variations for the different resonant phonon wave-vectors as a function of the electronic broadening and the laser excitation energy, can be only understood in terms of quantum interference. Thus, by manipulating the electronic broadening by external perturbations, such as doping or defects, we can selectively tune the quantum interference in double-resonance process of bilayer graphene.

Next, we want to give an experimental verification of our calculational results from above. However, we will only discuss general dependencies of the $2D$-mode lineshape as a function of γ and will not attempt a precise quantification of the different scattering rates. Since the absolute values of the ratio between symmetric and anti-symmetric processes depend on the choice of the fitting model and the initial start parameters in the fit routine, the calculated ratios $P_{22}^{33}/P_{\text{asym.}}$ from the experimental spectra shall only represent a guide to the eye. The qualitative dependence of $P_{22}^{33}/P_{\text{asym.}}$ in our data is not affected by the different fitting models. We will start with an analysis of the lineshape variations as a function of the laser excitation energy. In Figure 4.19, we present the $2D$ mode of bilayer graphene measured at different laser energies in the range from 1.96 eV to 2.81 eV. Following Eq. (4.2), the value of $\gamma^{\text{e-ph}}$ changes from 67 meV at 1.96 eV laser excitation energy to 101 meV at 2.81 eV laser energy. The presented spectra are normalized and shifted in frequency to the contribution from the anti-symmetric processes. As can be seen, we observe a strong variation of the ratio between symmetric and anti-symmetric processes, *i.e.*, the intensity of the symmetric contributions drastically increases with respect to the intensity of the anti-symmetric processes. Since our measurements are performed on freestanding bilayer graphene, which is to a good approximation free of doping, defects, and strain, tuning the laser excitation energy should only change the contribution from electron-phonon scattering to the electronic broadening γ. Following Ref. [47], increasing the laser excitation energy will increase the contribution from $\gamma^{\text{e-ph}}$ to γ. Hence, a larger γ will lead to an increased contribution from

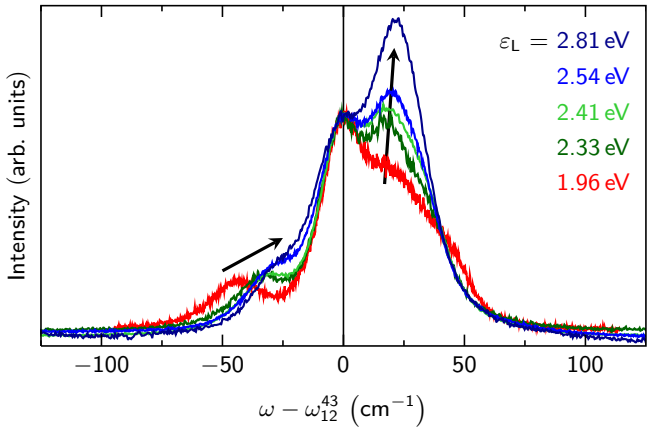

Figure 4.19: Dependence of the $2D$-mode lineshape on laser excitation energy. All spectra were normalized and shifted in frequency to the contribution of the anti-symmetric scattering process.

symmetric processes as compared to anti-symmetric scattering processes [compare Fig. 4.15 (c)]. This is in nice agreement with our experimental data presented in Fig. 4.19. Furthermore, we also observe that the P_{11}^{44} contribution shifts towards the peak from anti-symmetric scattering processes with increasing laser energy in the experimental spectra. This peak shift can be directly understood as an effect of the reduced splitting between both TO branches at larger distances from the **K** point, as demonstrated in the previous Section.

As theoretically and experimentally discussed in Refs. [47], [171] and [154], the electronic broadening does also depend on the defect concentration in the graphene sample. In general, a larger defect concentration leads to a higher electron-defect scattering rate and thus to an increased value for γ^{D}. In fact, γ^{D} should be directly proportional to n_D [47]. However, γ^{D} is usually significantly smaller than $\gamma^{\text{e-ph}}$, *e.g.*, $\gamma^{\text{e-ph}} = 50\,\mathrm{meV}$ and $\gamma^{\mathrm{D}} = 7\,\mathrm{meV}$ in defective single-layer graphene at a defect concentration of $n_D = 0.9 \times 10^{12}\,\mathrm{cm}^{-2}$ [154]. In the present study, we use ion-irradiated graphene samples that were exfoliated on standard silicon substrates with 100 nm SiO_2.[4] Ion-irradiated graphene samples allow a precise quantification of the average defect distance from the ion fluence, which is independent from geometrical parameters of the defect and more reliable than a determination from the measured D/G-mode ratio [see Chapter 5.2]. In Figure 4.20 (a), we present Raman spectra of the $2D$ mode in defective bilayer graphene with three different average defect distances L_D. We observe a dependence of the ratio between symmetric and anti-symmetric contributions on the defect concentration, *i.e.*, with increasing defect concentration (decreasing average defect distance) we observe an increase of the ratio between symmetric and anti-symmetric processes [compare Fig. 4.20 (b)]. Again, this is in nice agreement with our theoretical predictions from Fig. 4.15 (a). An increasing defect concentration leads to a larger value for the electronic broadening, which in turn results in an increase of the contribution from anti-symmetric scattering processes compared to symmetric processes.

Another approach to manipulate the electronic broadening γ experimentally is by charge-carrier doping of the graphene sample. Basko *et al.* pointed out the linear dependence between $\gamma^{\text{e-e}}$ and the Fermi-level shift $|E_{\mathrm{F}}|$ in single-layer graphene [168], which should roughly follow the

[4] Samples were provided by O. Ochedowski and M. Schleberger (AG Schleberger, Universität Duisburg-Essen).

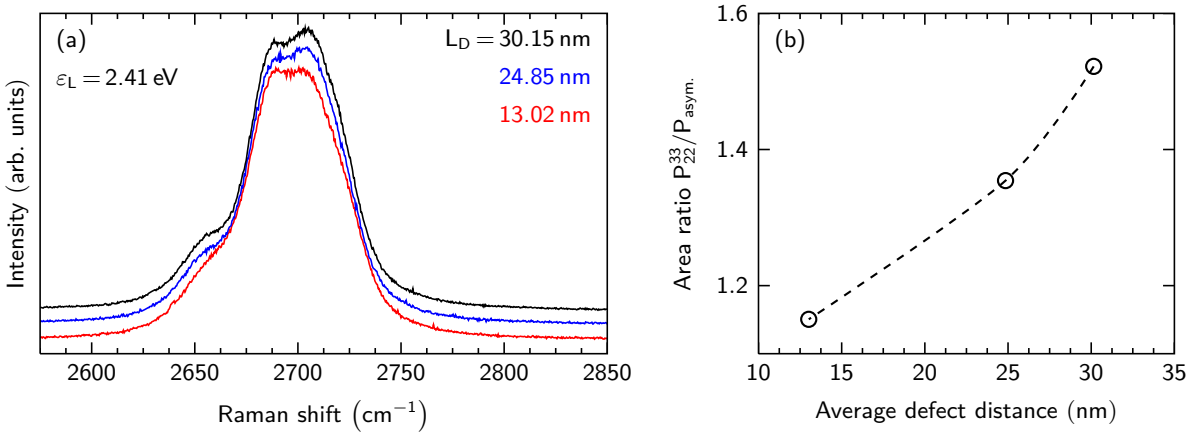

Figure 4.20: (a) Raman spectra of the $2D$ mode in ion-irradiated bilayer graphene. The average defect distances L_D for each sample are given next to the spectra. (b) Evolution of the intensity ratio between the symmetric and anti-symmetric contributions as a function of the average defect distance.

dependence

$$\gamma^{\text{e-e}} = 0.06 \times |E_{\text{F}}| \,. \tag{4.11}$$

For typical Fermi-level shifts of 300 meV, this would result in $\gamma^{\text{e-e}} = 18$ meV. However, due to different curvatures of the electronic bands in bi- and single-layer graphene, the dependence of $\gamma^{\text{e-e}}$ on the Fermi-level shift is assumed to be negligible in bilayer graphene. Following Ref. [168], this can be understood from the parabolic (convex) electronic dispersion near the **K** point, which allows electron-electron scattering even at zero doping. Thus, $\gamma^{\text{e-e}}$ is expected to observe a weaker dependence on $|E_{\text{F}}|$ as compared to single-layer graphene. As a consequence, the normalized intensity of the $2D$ mode in bilayer graphene should depend only weakly on the Fermi-level shift, as experimentally demonstrated in Ref. [35].

Experimentally, charge-carrier concentrations in single-layer graphene are commonly manipulated by two different approaches, namely, back-gated graphene on Si/SiO_2 substrates and electrochemically top-gated graphene. Combinations of both approaches are also possible of course. These methods have been successfully employed to investigate the electron-phonon coupling in graphene at different points in the Brillouin zone or to demonstrate the breakdown of the Born-Oppenheimer approximation in doped graphene [34, 154]. However, charge-carrier doping in bilayer graphene is more facile as compared to single-layer graphene. In fact, either top or back gating of bilayer graphene will not only change the charge-carrier concentration, but will also result in the formation of a finite bandgap [124, 177, 178], which can be understood from a breakdown of inversion symmetry in gated bilayer graphene. As a consequence, E_u-symmetry phonons at the **Γ** point in bilayer graphene become observable in Raman spectroscopy [179]. However, most experimental works on gated bilayer graphene do not consider this finite poten-

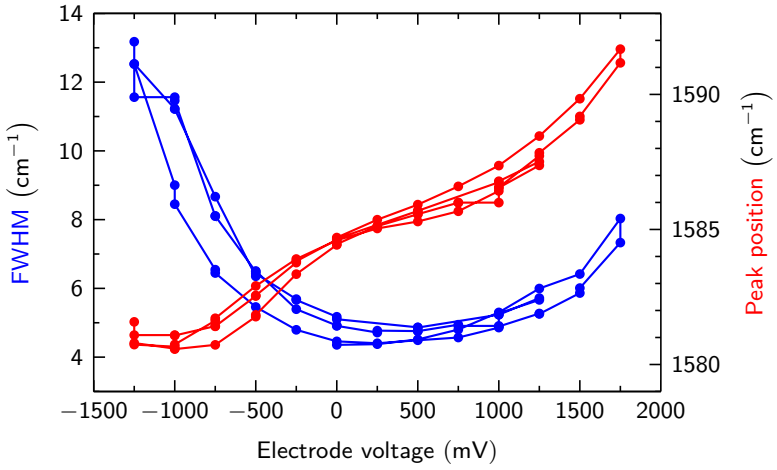

Figure 4.21: *G*-mode peak position (red) and FWHM (blue) as a function of the electrode voltage in electrochemically-gated bilayer graphene.

tial difference δV between the top and bottom layer [35, 172]. Following Ref. [35], the Fermi level in bilayer graphene as a function of the applied electrode voltage V_E can be calculated as

$$\begin{aligned} e\,V_\mathrm{E} &= \alpha\,E_\mathrm{F}^2 + (1+\alpha\gamma_1)\,E_\mathrm{F} && \text{if} \quad E_\mathrm{F} < \gamma_1 \\ e\,V_\mathrm{E} &= 2\,\alpha\,E_\mathrm{F}^2 + E_\mathrm{F} && \text{if} \quad E_\mathrm{F} > \gamma_1 \end{aligned} \tag{4.12}$$

Here, e is the elementary charge and γ_1 reflects the energy separation between the π_2 and π_2^* bands at the **K** point [compare Fig. 4.2 (b)]. The quantity α is defined as

$$\alpha = \frac{e^2}{\pi\,C_\mathrm{TG}\,(\hbar v_\mathrm{F})^2},$$

where C_TG is the top-gate capacitance and usually assumed as $C_\mathrm{TG} = 2.2 \times 10^{-6}\,\mathrm{F\,cm^{-2}}$; the splitting γ_1 is taken as 0.39 eV [35]. In general, the Fermi-level shift that is induced by a voltage V_E in bilayer graphene is less compared to single-layer graphene, which is due to the different dispersion of the electronic bands around **K** and hence different density of states. For instance, the difference between E_F for single- and bilayer graphene at an electrode voltage of $V_E = 1\,\mathrm{V}$ is more than 60 % [35].

Figure 4.21 presents measured *G*-mode positions and FWHMs in electrochemically-gated bilayer graphene during subsequent forward and backward sweeps of the electrode voltage. The observed hysteresis is negligible. As can be seen, we observe an upshift in the *G*-mode frequency with increasing voltage, in agreement with an increasing doping level [35, 172, 179, 180]. The *G*-mode FWHM shows a more complex behavior, *i.e.*, we observe an initial decrease of the FWHM from $13\,\mathrm{cm^{-1}}$ to $5\,\mathrm{cm^{-1}}$, followed by an increase to $8\,\mathrm{cm^{-1}}$ with increasing voltage. This observation is in contrast to the dependence of the *G*-mode FWHM in single-layer graphene. However, the increasing FWHM of the *G* mode in bilayer graphene can be understood from the breakdown of inversion symmetry and mixing of the Raman- and infrared-active optical phonons at **Γ** [174]. From Figure 4.21 we can also infer that our bilayer graphene sample exhibits a strong initial *p*-

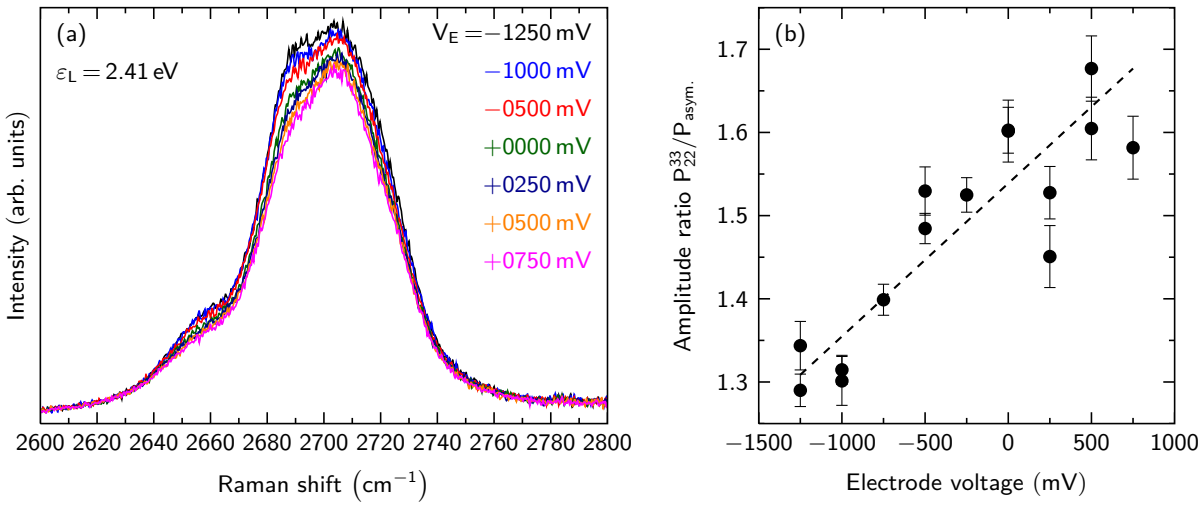

Figure 4.22: (a) Raman spectra of the $2D$ mode in electrochemically-gated bilayer graphene as a function of the electrode voltage V_E at 2.41 eV laser energy. With increasing voltage, we observe a decrease in intensity accompanied by a change in the $2D$-mode lineshape. (b) Evolution of the amplitude ratio between P_{22}^{33} and $P_{\text{asym.}}$ processes as a function of V_E. The dashed line is a linear fit and represents a guide to the eye.

type doping. This behavior is consistently observed in all of our samples and can be attributed to unintentional doping by the substrate, as well as by the electrolyte [154, 181]. In fact, the absence of the charge-neutrality point in our experimental data complicates a precise quantification of the Fermi-level shift, since E_F depends non-linear on V_E and knowledge about the zero-position is crucial. Future experiments with top- and back-gated bilayer graphene samples may overcome this drawback. The reader may notice that the applied electrode voltages extend further into the negative regime as compared to previous studies. In fact, electrode voltages below -1 V are expected to create defects in electrochemically-gated single-layer graphene [154]. However, even after multiple cycles with minimum electrode voltages of $V_E = -1.5$ V, we do not observe the evolution of a D mode in our Raman spectra. This might be understood from a reduced chemical reactivity of bilayer graphene compared to single-layer graphene [182].

Figure 4.22 (a) presents Raman spectra of the $2D$ mode in electrochemically-gated bilayer graphene at different electrode voltages. The evolution of the ratio between the P_{22}^{33} and the $P_{\text{asym.}}$ process as a function of the voltage is shown in Figure 4.22 (b). Assuming that the electronic broadening γ increases with increasing doping due to additional contributions from electron-electron scattering, we would expect a decreasing ratio between symmetric and anti-symmetric scattering processes (compare Fig. 4.15). However, our experimental data in Fig. 4.22 (b) suggests the opposite dependence, *i.e.*, the intensity of the anti-symmetric processes reduces as compared to the symmetric contributions. This observation would indicate a decreasing electronic broadening with increasing electrode voltage. In fact, not only $\gamma^{\text{e-e}}$ should depend on the charge-carrier density but also $\gamma^{\text{e-ph}}$. As discussed above, $\gamma^{\text{e-e}}$ is expected to exhibit a weak dependence on E_F in bilayer graphene. In contrast, it has been demonstrated

for single-layer graphene that the electron-phonon coupling decreases with increasing doping level [183] and it seems reasonable that bilayer graphene exhibits the same dependence. Since the electron-phonon scattering rate is proportional to the electron-phonon coupling [47], $\gamma^{\text{e-ph}}$ is expected to decrease with increasing doping level. Our experimental data in Fig. 4.22 (b) indicate that the decrease of $\gamma^{\text{e-ph}}$ exceeds the increase of $\gamma^{\text{e-e}}$, leading to an overall reduction of γ.

Besides the changing ratio between symmetric and anti-symmetric processes, we observe a slight decrease in intensity of the $2D$ mode, as well as a broadening of the single contributions with increasing electrode voltage. The observed peak shifts are less than $\pm 1\,\text{cm}^{-1}$ from the average value of each contribution, confirming the previously measured doping dependence of the $2D$-mode shifts in bilayer graphene for n-type doping [35]. Also the broadening of the different contributions with increasing doping level is in agreement with previous results [175]. This broadening might be understood from a renormalization of the Fermi velocity in doped graphene [184], *i.e.*, v_{F} reduces with increasing either n- or p-type doping. Due to the reduced slope of the electronic bands, the resonant transitions in the double-resonance process can be satisfied by a broader range of phonon wave-vectors. Ergo, the different contributions would broaden with increasing electrode voltage. The observed intensity decrease of the $2D$ mode is counterintuitive, if we keep in mind that the electronic broadening γ decreases with increasing electrode voltage. In general, a smaller electronic broadening will lead to double-resonant Raman modes with higher intensity and reduced linewidth [47]. However, the overall decrease in intensity of the $2D$ mode in gated bilayer graphene might be understood from a reduced electron-phonon coupling [183]. Since symmetric and anti-symmetric TO phonons exhibit the same electron-phonon coupling, a decrease of the electron-phonon coupling would affect symmetric and anti-symmetric scattering processes equally, explaining the overall decrease in intensity of the $2D$ mode. To sum up, our experimental data indicate that the electronic broadening in the double-resonance process decreases with increasing electrode voltage. Furthermore, we expect a renormalization of the Fermi velocity and the electron-phonon coupling. These two effects may result in a broadening of the different $2D$-mode contributions, as well as in a decrease of the overall intensity.

As a last point, we want to present an experimental situation where the lineshape variations of the $2D$ mode in bilayer graphene can be nicely observed in a simple and straight-forward measurement. In Figure 4.23 (a), we show Raman spectra of the $2D$ mode in bilayer graphene that were recorded while performing a linescan across the edge of a bilayer flake. As can be seen, we observe a strong variation of the $2D$-mode lineshape as a function of the linescan position, *i.e.*, at the edge we observe an increased ratio between symmetric and anti-symmetric scattering processes as compared to the inside of the bilayer graphene flake [compare Fig. 4.23 (b)]. Keeping in mind our above demonstrated dependence of the $2D$-mode lineshape on the electronic broadening, this lineshape variation would correspond to a larger broadening γ directly at the edge. In fact, a larger electronic broadening directly at the edge seems reasonable. For instance, the edge is an extended defect and, as demonstrated above, defects increase the broadening and result in an increased ratio between symmetric and anti-symmetric scattering processes. Further-

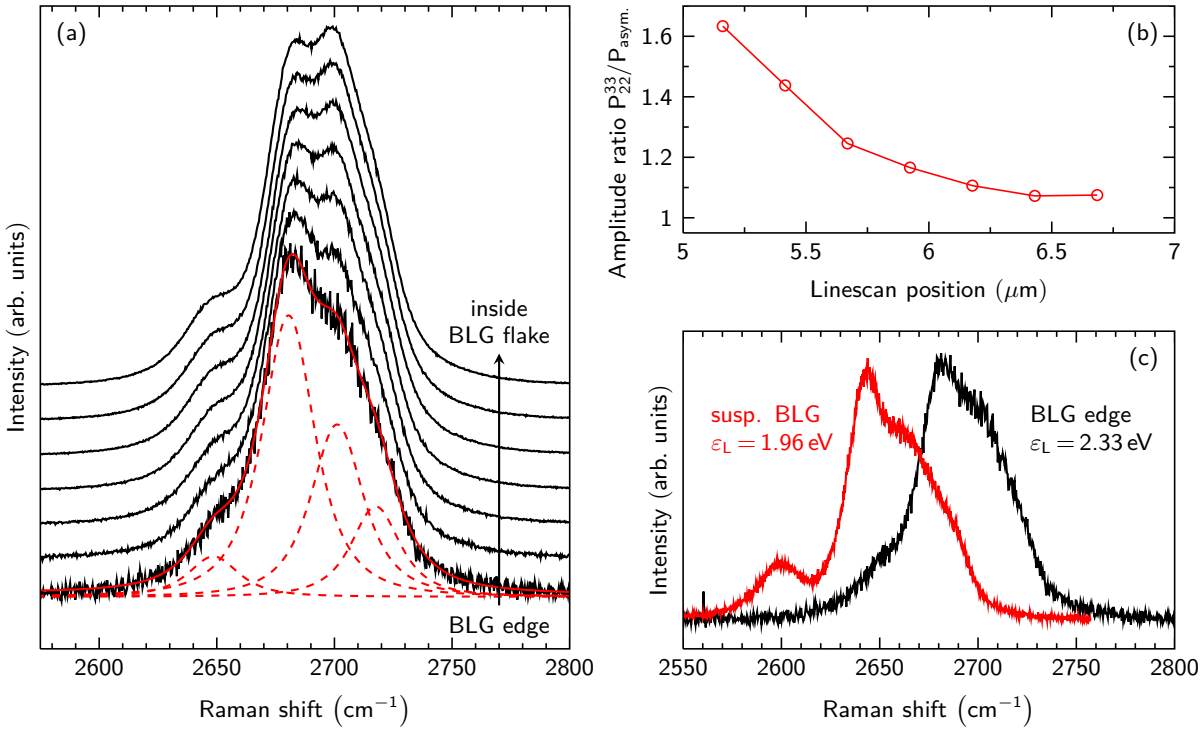

Figure 4.23: (a) Raman spectra of a linescan across a bilayer graphene edge. The lowest spectrum refers to the bilayer edge, whereas the topmost spectrum was measured inside the bilayer graphene flake. The solid red line denotes a fit with four Baskonian profiles, the dashed lines represent the single contributions. Spectra are normalized to the same $P_{\text{asym.}}$ intensity and vertically offset for clarity. (b) Evolution of the ratio between P_{22}^{33} and the contribution from anti-symmetric processes along the linescan across the bilayer graphene edge. (c) Comparison of the Raman spectrum at the bilayer graphene edge measured at 2.33 eV laser energy and a spectrum of freestanding bilayer graphene measured 1.96 eV laser excitation energy.

more, we also expect strain at the bilayer graphene edge. Figure. 4.24 presents Raman spectra of tensile-strained bilayer graphene. In fact, we observe an increasing ratio between symmetric and anti-symmetric processes with increasing tensile strain. This effect can be understood from different strain-induced intensity variations for the inner and outer contributions of the P_{22}^{33} process [162]. However, graphene edges are most likely compressively strained [185, 186], which is expected to lead to the opposite effect, in agreement with our experimental data in Figure 4.23 (a). Thus, the lineshape variations at the bilayer graphene edge might be understood from an increased electronic broadening, as well as compressive strain.

The lineshape of the $2D$ mode in bilayer graphene is often considered as unique for a certain laser excitation energy [46]. However, here we showed that the $2D$-mode lineshape is affected by various external perturbations, such as defects, strain, and doping. In fact, in extreme cases the lineshape can exhibit drastic changes. In Fig. 4.23 (c), we compare the measured $2D$-mode spectrum at the bilayer graphene edge at a laser energy of 2.33 eV with a Raman spectrum of

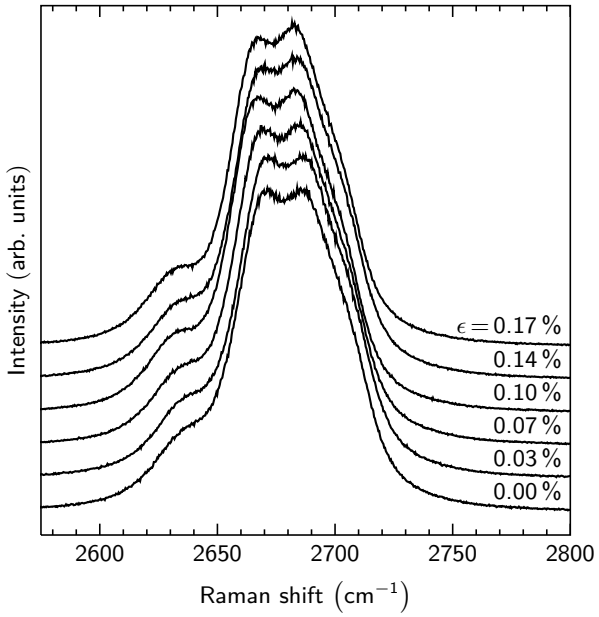

Figure 4.24: Raman spectra of tensile-strained bilayer graphene. The strain level is given next to the spectra. Spectra are normalized to the same $P_{\text{asym.}}$ intensity and vertically offset for clarity.

freestanding bilayer graphene at $\varepsilon_L = 1.96\,\text{eV}$. As can be seen, the spectrum from the bilayer edge nearly resembles the lineshape of the spectrum from freestanding bilayer graphene although the laser excitation energies are different. We want to remark that by the term lineshape, we just refer to the intensities of the different contributions. The peak positions of the $2D$ mode are, in general, more dominantly influenced by the laser energy as compared to the influence by γ. Thus, peak positions in both spectra of course do not match. Nevertheless, we demonstrated that the $2D$-mode lineshape can change drastically as a function of external parameters. In fact, knowledge about the lineshape dependence on doping, defects, and strain may add an additional tool for graphene characterization using Raman spectroscopy.

4.8 Polarization dependence of the *2D* mode in bilayer graphene

All spectra that were shown so far, were calculated for the unpolarized case. However, one might be also interested in the polarization dependence of the $2D$ mode in bilayer graphene. It has been shown that polarized Raman measurements, in combination with uniaxial strain application, enable an accurate determination of the sample orientation in single-layer graphene [36, 187]. Furthermore, those experiments gave the first experimental indications on the dominance of inner processes in double-resonant Raman scattering [38, 137]. Also Narula *et al.* demonstrated a theoretical calculation of the $2D$-mode splitting under uniaxial strain in single-layer graphene and showed that the dominant phonon wave-vectors in the double-resonance process sensitively depend on polarizer and analyzer orientation [138].

Using the notation of Venezuela *et al.* [47], the calculation of different polarizations is given by

$$\mathcal{I}_{\text{unpol}} = |\mathcal{I}_{xx}|^2 + |\mathcal{I}_{xy}|^2 + |\mathcal{I}_{yx}|^2 + |\mathcal{I}_{yy}|^2 \tag{4.13}$$

$$\mathcal{I}_{\parallel} = |\mathcal{I}_{xx}|^2 + |\mathcal{I}_{yy}|^2 \tag{4.14}$$

$$\mathcal{I}_{\perp} = |\mathcal{I}_{xy}|^2 + |\mathcal{I}_{yx}|^2 , \tag{4.15}$$

where $\mathcal{I}_{\text{unpol}}$, $\mathcal{I}_{\parallel}$, and $\mathcal{I}_{\perp}$ describe the Raman intensities for an unpolarized measurement and measurements with parallel and perpendicular polarization, respectively. The different $\mathcal{I}_{ij}$ refer to the contributions from excitation in i and emission in j direction with respect to the crystal lattice of bilayer graphene in real space.

The polarization dependence of the $2D$ mode has been extensively discussed, both experimentally and theoretically, for single-layer graphene [38, 47, 138, 188]. The observed dependence was explained by an inhomogeneous absorption and emission in the double-resonance process [189]. In principle, equivalent observations are expected for the $2D$ mode in bilayer graphene.

We will now turn our analysis to the calculated Raman spectra and contour plots of the Raman scattering cross-section. Figure 4.25 (a) presents the calculated $2D$-mode spectra for parallel polarization, crossed polarization, and for an unpolarized measurement. The different polarizations were calculated according to Eqs. (4.13)-(4.15). As can be seen, the three spectra exhibit only minor differences in their lineshape. The largest difference can be observed for the P_{22}^{33} contribution, which we magnify in Fig. 4.25 (b). Here, we see a variation of the ratio between inner and outer contributions for this scattering process. As can be seen from the calculated contour plots of the $2D$-mode scattering cross-section in Fig. 4.26, this variation is due to a partially selective suppression of inner and outer processes for the different polarizations due to inhomogeneous photon absorption around the **K** point [189]. However, due to the three-fold symmetry at the **K** point, the $2D$-mode lineshape does not change fundamentally. The partial suppression of scattering processes around the **K** point is compensated by the contribution of equivalent scattering processes. Since equivalent processes are separated by an angle of 120 ° around **K**, it is not possible to simultaneously suppress all three equivalent regions around the **K** point with parallel nor with crossed polarization. Therefore, the calculated spectra exhibit only a weak dependence on the different polarizations.

Figure 4.27 presents experimental $2D$-mode Raman spectra of freestanding bilayer graphene under parallel and perpendicular polarization for 1.96 eV and 2.33 eV laser excitation energy. In order to exclude intensity variations due to the polarization dependence of the spectrometer grating, only the incoming polarization was rotated between both measurements. As can be seen, the $2D$-mode lineshape in bilayer graphene depends only weakly on the polarization. However, we observe a non-negligible variation of the P_{22}^{33} contribution under parallel and perpendicular polarization, confirming our calculational results from Fig. 4.25. We explicitly verified that the observed effect does not depend on the crystallographic orientation of the bilayer graphene flake with respect to the laser polarization. As explained above, the intensity variation of

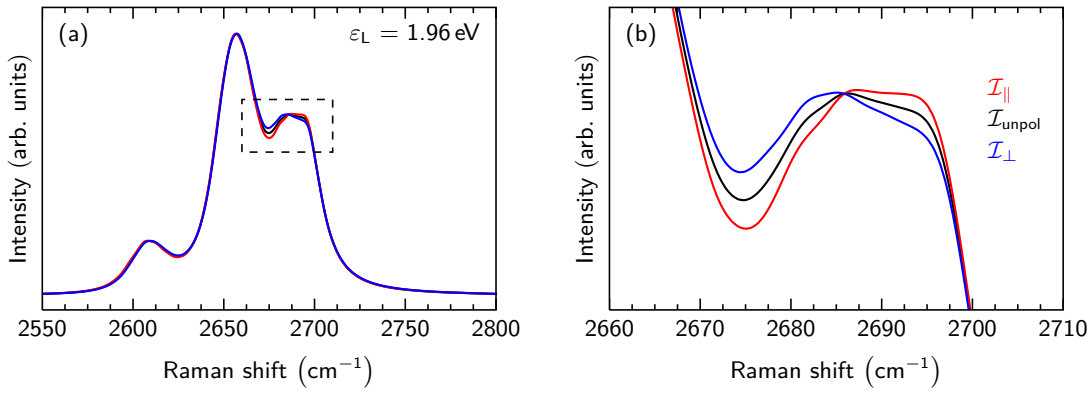

Figure 4.25: (a) Calculated $2D$-mode spectra for parallel and crossed polarization, as well as for an unpolarized measurement at 1.96 eV laser excitation energy. Spectra were normalized to the anti-symmetric contribution. (b) Magnification of the spectral range highlighted by the dashed rectangle in (a). Only minor changes due to different polarizations can be observed.

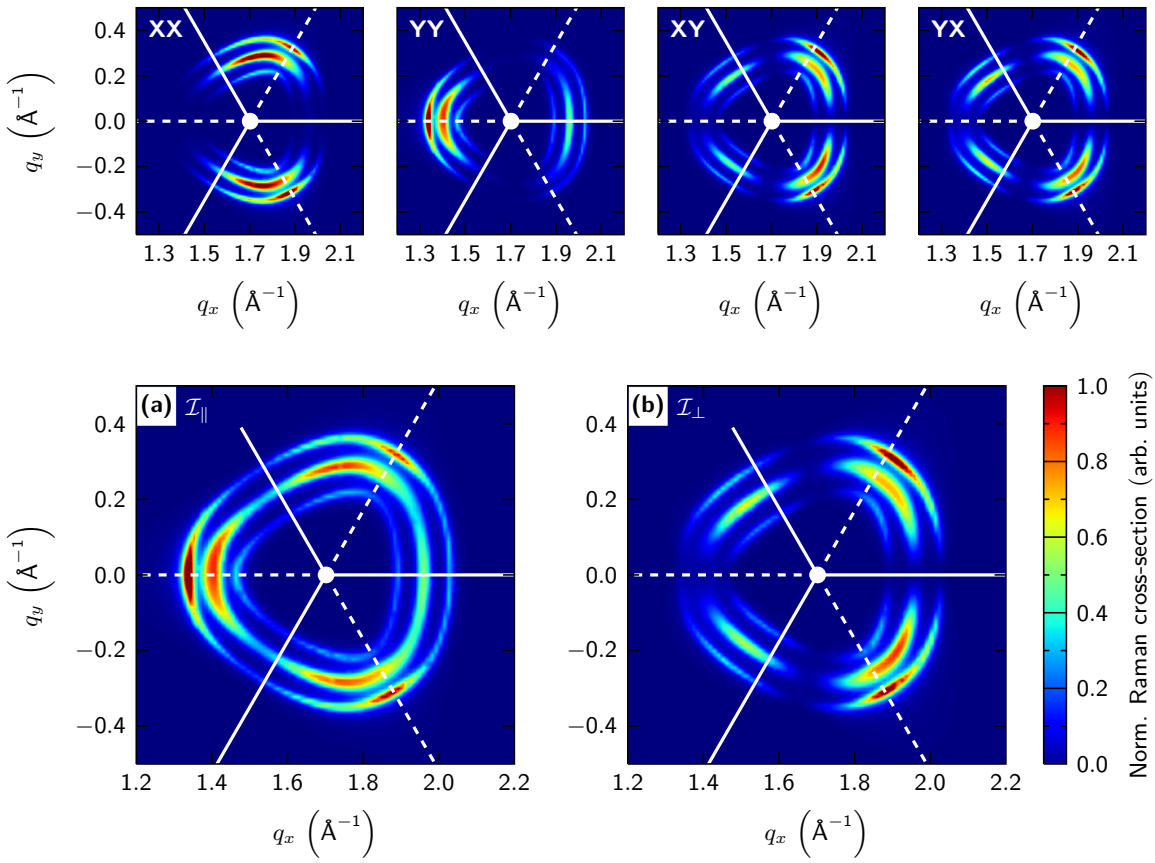

Figure 4.26: Contour plots of the normalized $2D$-mode scattering cross-section $\mathcal{I}_{\mathbf{q}}$ around the **K** point as a function of the phonon wave-vector **q** for (a) parallel and (b) crossed polarization. The upper row represents the different combinations of excitation and emission in x and y direction. The solid and dashed white lines denote the $\mathbf{K}-\mathbf{M}$ and $\mathbf{K}-\mathbf{\Gamma}$ high-symmetry lines, respectively.

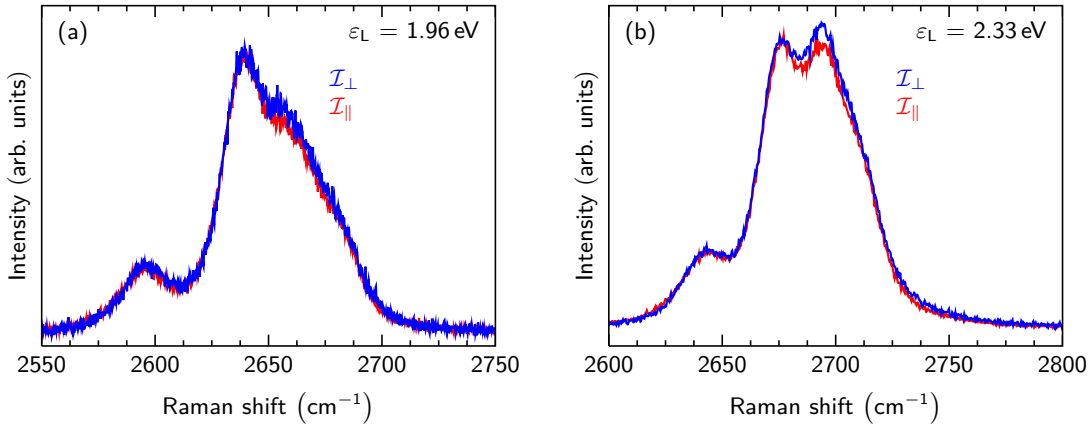

Figure 4.27: Experimental $2D$-mode spectra of freestanding bilayer graphene for different polarizations and laser excitation energies. Spectra were normalized to the contribution of the anti-symmetric scattering process.

the P_{22}^{33} contribution is due to a partially selective suppression of inner and outer processes under parallel and perpendicular polarization. The effect can be seen most clearest for the P_{22}^{33} contribution, since only this contribution exhibits a frequency difference between inner and outer processes [compare Fig. 4.9 (a)]. As the frequency difference between the inner and outer P_{22}^{33} contributions decrease with increasing laser excitation energy, we expect that the polarization-dependent lineshape variation also reduces for higher ε_L. This effect can be seen in the calculated spectra in Figure 4.28. Figure 4.27 compares the measured spectra for parallel and crossed polarization for two different laser excitation energies, *i.e.*, $\varepsilon_L = 1.96\,\mathrm{eV}$ and $\varepsilon_L = 2.33\,\mathrm{eV}$. As can be seen, for both laser energies we observe an intensity variation of the P_{22}^{33} contribution under parallel and perpendicular polarization compared to the contribution from anti-symmetric scattering processes. By fitting the different spectra with Baskonian profiles and comparing the intensity of the P_{22}^{33} contribution between the different polarizations, we find an intensity difference of $\mathcal{I}_\parallel/\mathcal{I}_\perp = 0.91$ at $1.96\,\mathrm{eV}$ laser energy and $\mathcal{I}_\parallel/\mathcal{I}_\perp = 0.96$ at $2.33\,\mathrm{eV}$. Thus, we can confirm the decreasing differences between parallel and crossed polarization decreases with increasing laser energy.

Previous polarization-dependent Raman measurements of the $2D$ mode in bilayer graphene showed the same systematics as described here [190–192]. However, the lineshape variations were obviously to small to be recognized by the different authors. Thus, the authors only discussed the angular dependence of the overall intensity variation. Variations of the lineshape were neglected. In contrast, here, we demonstrated both theoretically and experimentally that the $2D$-mode lineshape does depend on the laser polarization.

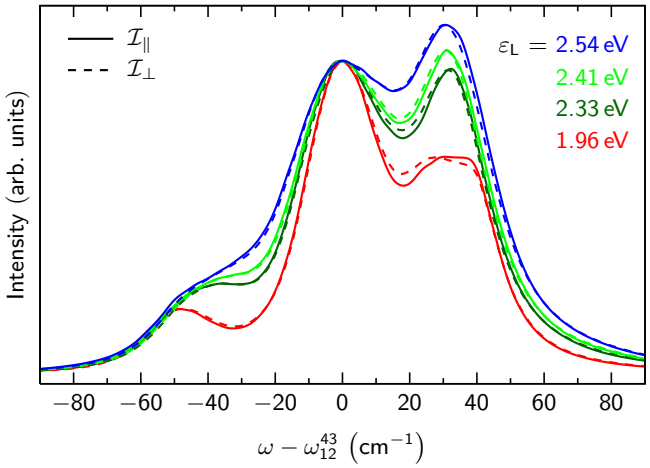

Figure 4.28: Calculated $2D$-mode spectra for parallel and perpendicular polarization for different laser excitation energies. Spectra were normalized to the contribution of the anti-symmetric scattering process.

4.9 Summary

In summary, we presented a detailed and conclusive analysis of the double-resonant $2D$-mode Raman scattering process in Bernal-stacked bilayer graphene. We proved that the $2D$ mode in bilayer graphene is composed of three dominant contributions, contradicting all previous works on this topic. In detail, we attribute the dominant contributions to symmetric P_{11}^{44}/P_{22}^{33} and degenerate anti-symmetric P_{12}^{43}/P_{21}^{34} processes. We showed that the dominant contribution to the Raman scattering cross-section stems from so-called inner processes, as in single-layer graphene. We furthermore demonstrated that quantum interference between both anti-symmetric processes strongly affects the $2D$-mode lineshape in bilayer graphene. In fact, it drastically increases these contributions to the $2D$ mode spectrum. Moreover, we also showed that the splitting between both TO phonon branches in bilayer graphene along $\mathbf{K} - \mathbf{\Gamma}$ is of great importance for a correct analysis of the $2D$-mode lineshape. Relying on the fact that the dominant contribution to symmetric and anti-symmetric processes stems from scattering with different TO phonons, we presented an approach to directly extract the TO phonon splitting from experimental Raman spectra. Furthermore, we also showed that the splitting of the electronic bands can be also measured using the presented analysis.

Our experimental data indicate that the GW correction in bilayer graphene might be larger as commonly assumed. We proved that the $2D$-mode lineshape in bilayer graphene sensitively depends on the electronic broadening γ, which can be manipulated experimentally in various ways. Our calculated dependencies could be verified experimentally. We also discussed the polarization dependence of the $2D$-mode lineshape and showed that inner and outer contributions for the P_{22}^{33} process depend on polarization. Finally, we should note that all of our results for the $2D$ mode in bilayer graphene are also valid for the D mode. Our results highlight the key role of inner processes and finally clarify the origin of the complex $2D$-mode lineshape in bilayer

graphene.
The presented results may lead to a more profound understanding of the different phonon scattering mechanisms in bilayer graphene and might enable a more detailed analysis of the $2D$-mode lineshape in the future. For instance, the ratio between symmetric and anti-symmetric processes can be used to investigate electron-phonon and electron-defect scattering rates, adding an additional parameter for the analysis of experimental data.

5 Defect-induced double-resonant Raman modes in graphene and carbon nanotubes

Parts of this chapter were published in Refs. [176, 193, 194].

This chapter is devoted to the analysis of defect-induced double-resonant Raman scattering in graphene and carbon nanotubes. First, we will introduce the different possible defects in the crystallographic structure of graphene. Afterwards, we will review the current literature on Raman spectroscopy of defect-related Raman modes. In the following, we will introduce a simple geometric approach to model the D-mode scattering process in arbitrary carbon nanotubes. We derive the systematic dependence of the D-mode frequency on the chiral index of the carbon nanotube and discuss the family behavior and diameter dependence of this Raman mode. Subsequently, we will present an analysis of the D'' mode in single and few-layer graphene, as well as in carbon nanotubes. We investigate the layer-number and excitation-energy dependence of this mode in graphene and further analyze its diameter-dependence in carbon nanotubes. Our discussion on defect-related Raman modes in graphene is finalized by an *in-situ* study of laser-induced oxidation in graphene.

5.1 Defects in graphene

In general, a defect is a local or extended variation of the crystallographic lattice that breaks the translational invariance of the system. According to the Noether theorem, momentum conservation is not given in defective, inhomogeneous systems [96]. The presence of defects and disorder in real crystalline systems can be understood not only from shortcomings in crystal-growth processes, but also from fundamental physical concepts [195]. Referring to the second law of thermodynamics, the entropy S of isolated, adiabatic systems will never decrease; in other words

$$\partial_t S \geq 0.$$

Thus, a certain amount of disorder in crystals is favored by thermodynamics. Although defects and imperfections in crystals are commonly thought to decrease material properties, intentionally

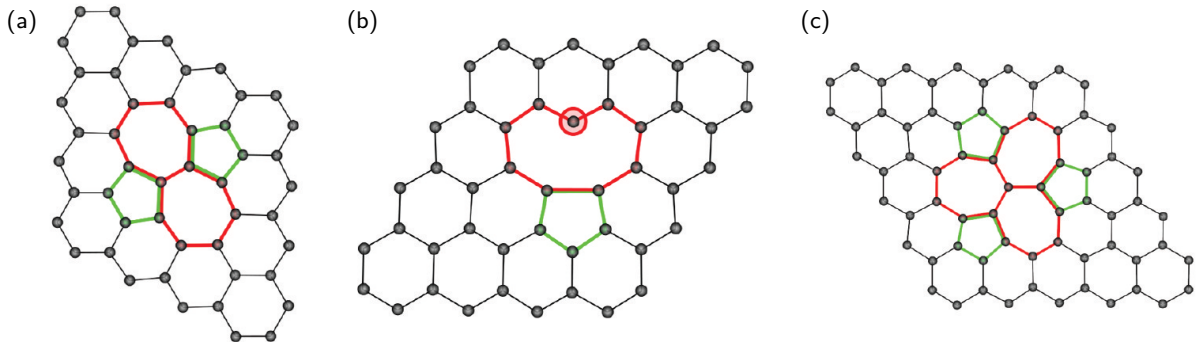

Figure 5.1: Schematic visualization of different defects in the crystal lattice of graphene. (a) Stone-Wales defect, (b) single-vacancy defect, and (c) reconstructed double-vacancy defect. Figure is taken from Ref. [195].

created defects can also manipulate electrical and optical material characteristics as preferred. For instance, dopant atoms in semiconductors are usually weakly-bound charge carrier close to the band edges and thus provide free charge carriers and increased electrical conductivity at moderate thermal energies [96].

Defects in graphene can be generally divided into intrinsic and extrinsic defects. Intrinsic defects refer to structural defects that locally alter the carbon-carbon bond lengths and angles in the system, but not introduce new atom species to the crystal. A prominent example for these defects is the so-called Stone-Wales defect that consists of two seven-membered and two five-membered carbon rings [196]. In this case, no atoms are removed or introduced to the lattice, Furthermore, single- and double-vacancy defects can be present in graphene [195]. A schematic visualization of these defects is shown in Figure 5.1. In contrast to these point-like defects, the lattice of graphene can be of course also distorted on larger scales. This may include line defects and grain boundaries, which can extend to length larger than several tenth of μm [195]. The reconstruction of the crystal lattice due to a defect is usually not limited to in-plane variations of C-C bond length and angles, as shown in Fig. 5.1. In fact, out-of-plane deformations are also possible and very likely in the case of extrinsic defects, as will be discussed in the next paragraph.

The term extrinsic defects is usually identified with foreign adatoms or foreign substitutional atoms in the lattice of graphene. In general, these additional atoms can be summarized as dopants or 'chemical' defects. The effect of foreign adatoms on graphene's properties strongly depends on the chemical bonds that form between the adsorbate and graphene. Weak interaction leads to van-der-Waals dipol-dipol bonds and physisorbtion of the adsorbate. However, if the interaction between the adatom and graphene is strong, covalent bonds may form which lead to chemisorbtion. These bonds usually account for out-of-plane deformations of the graphene lattice. In general, adatoms on graphene are mobile and their migration along the graphene surface can be even monitored by high-resolution transmission electron microscopy [195]. A

more stable chemical defect in graphene is introduced by direct substitution of a carbon atom with a foreign atom. Here, boron or nitrogen is commonly used [195], as the number of electrons compared to the carbon atom differs by one. In principle, the substitution of carbon by boron or nitrogen allows the manipulation of the Fermi level, as well as engineering the electronic bandstructure of graphene.

In a realistic graphene sheet, it most likely not possible to strictly differentiate between intrinsic and extrinsic defects. For instance, vacancies in graphene, *i.e.*, intrinsic defects, are preferred reaction sides for adsorbates and molecules from the air, *i.e.*, extrinsic defects. Thus, both defects may coexist at the same time. Finally, we want to recall that the most likely defect in a system is always the surface/edge of a crystal, as these defects are always present in real systems.

5.2 Raman spectroscopy of defects in graphene

As already shown and discussed in previous chapters of this work, Raman spectroscopy has been proven to be a versatile technique to study fundamental properties of graphene. Among the various other parameters that can be accessed by Raman scattering, we can analyze the average defect concentration n_D in a graphene sample by the occurrence and intensity of defect-induced Raman modes. The analysis of the defect-induced D mode goes back to the early works by Tuinstra and Koenig [103], who pointed out the dependence between the D/G-mode ratio and the inverse crystallite size in graphite samples. In the following years, many different works reported on the defect-related origin of the D and D' modes in the Raman spectrum of graphite and attempted a quantitative analysis of the average crystallite sizes, the sp^2/sp^3 content, and different defect species [197–201]. It has been also noted that the experimentally determined D/G-mode ratio in defective graphite not only depends on the crystallite size, but also on the laser excitation energy [202–204]. In fact, Cançado *et al.* demonstrated a strong ε_L^{-4} dependence of the D/G-mode ratio in nanocrystalline graphite [203, 204], which can be understood from the different scattering mechanisms for both Raman modes. However, problems in the quantitative analysis of the D/G-mode ratio in graphite samples arise when defects extend over several layers in z direction. The influence of the defect geometry was not understood and different authors pointed out the inaccuracy of Raman measurements for defect characterization in graphite with errors of up to 100 % [200]. Thus, the successful isolation of single-layer graphene in 2004 has enabled a more precise and more quantitative analysis of defects in this material.

In graphene, bombardment with heavy ions is commonly used to artificially introduce defects into the crystallographic lattice. Here, most works rely on the bombardment with low energy argon ions (Ar^+) with kinetic energies of 90 eV and at angles of 45° with respect to the graphene plane. The first quantitative analysis of the D/G-mode ratio in graphene is based on a work by Lucchese *et al.* [32], introducing the so-called 'local activation model'. Following this model, a defect creates a structurally-disordered region with radius r_S. Around this region, the lattice

is not distorted, however, the close proximity to the defect locally breaks the translational invariance of the lattice and enables defect scattering. This second region is characterized by a radius r_A around the defect, thus, the annulus between r_S and r_A contributes to the D mode intensity. Consequently, the D/G-mode intensity ratio as a function of the average distance between defects L_D can be modeled as [32]

$$\begin{aligned}\frac{I_D}{I_G}(L_D) &= C_A\, f_A(L_D) + C_S\, f_S(L_D) \\ &= C_A\, \frac{r_A^2 - r_S^2}{r_A^2 - 2\,r_S^2}\, \left[\exp\left(-\frac{\pi\, r_S^2}{L_D^2}\right) - \exp\left(-\frac{\pi\, (r_A^2 - r_S^2)}{L_D^2}\right)\right] \\ &+ C_S \left[1 - \exp\left(-\frac{\pi\, r_S^2}{L_D^2}\right)\right]. \end{aligned} \tag{5.1}$$

Here, f_A and f_S represent the fractions of the corresponding A and S areas in the graphene lattice; the prefactors C_A and C_S characterize the relative contribution of the respective areas to the overall D-mode intensity. Since the lattice is strongly distorted for radii smaller than r_S, a complete breakdown of the lattice structure in this region is expected and, consequently, this region will contribute less to the D-mode intensity. In fact, the ratio between C_A and C_S was estimated to be larger than five [32]. As a consequence, the second term in Eq. (5.1) is usually omitted. In the following, Cançado *et al.* pointed out that the prefactor C_A should depend on the laser excitation energy ε_L and reflects the scattering efficiency of optical phonons at **K** and **Γ** [33]. Using Ar^+-created defects as described above, typical defect dimensions are $r_S = 1.0\,\mathrm{nm}$ and $r_A = 3.1\,\mathrm{nm}$ [32]. By using these values and setting $C_A = (160 \pm 48)\,\varepsilon_L^{-4}\,\mathrm{eV}^4$, Eq. (5.1) is commonly simplified to [33]

$$\frac{I_D}{I_G}(L_D) = \frac{(4.3 \pm 1.3) \times 10^3\ \mathrm{nm}^2\,\mathrm{eV}^4}{L_D^2\,\varepsilon_L^4}. \tag{5.2}$$

In fact, this formula has been used widely throughout literature for defect analysis in graphene [31]. However, defect-density characterization by this formula can be misleading or incorrect in certain cases. The influence of the defect dimensions is commonly neglected, however, these parameters can significantly influence the measured D/G ratio. For instance, the irradiation with 91 MeV Xe ions creates significantly smaller defects compared to low-energy argon-created defects, *i.e.*, $r_S = 0.35\,\mathrm{nm}$ and $r_A = 2.11\,\mathrm{nm}$ [1]. Thus, one would observe a reduced D/G-mode ratio at the same L_D compared to Ref. [33]. The influence of the defect size on the measured D/G-mode ratio is demonstrated in Figure 5.2. As can be seen, for defect distances larger than 3 nm the calculated D/G-mode ratio for Xe-irradiated graphene (red curve) is significantly smaller than for Ar-induced defects in graphene (blue curve); for L_D smaller than 3 nm this relation is inversed. Hence, it is crucial to verify if the experimental conditions from Refs. [32] and [33] apply before researchers may use Eq. (5.2) for defect characterization in graphene. Only

[1] Private communication with O. Ochedowski (Universität Duisburg-Essen)

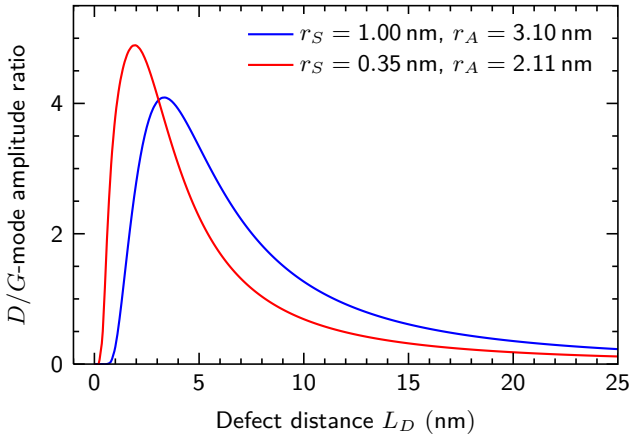

Figure 5.2: Calculated D/G-mode amplitude ratio in single-layer graphene for different defect sizes at 2.33 eV laser excitation energy following Eq. (5.1) and Ref. [33]. The blue curve represents Argon-induced defects in graphene, whereas the red curve is calculated for smaller defect sizes that result from irradiation with high-energy Xe ions.

very recently, Pollard *et al.* published a systematic study on the dependence of the D/G ratio on the defect size in ion-irradiated graphene [205]. The influence of r_S and r_A on the D/G ratio could be nicely demonstrated.

The D/G-mode ratio does not only depend on the defect dimensions, but also on the number of graphene layers, as demonstrated in Ref. [206]. In general, the D/G ratio decreases with increasing layer number at the same defect concentration. On the one hand, this can be understood from an approximately doubled G-mode intensity in bilayer graphene as compared to single-layer graphene [207]. On the other hand, the intensity of double-resonant Raman modes in few-layer graphene is reduced compared to single-layer graphene, as can be easily seen for the $2D$ mode (compare Fig. 3.4). The reduced intensity of double-resonant Raman modes in few-layer graphene may be understood from a larger electronic screening, which would lead to less coupling of electrons and phonons.

A major disadvantage of Raman spectroscopy for defect analysis is the fact that different defect species cannot be separated univocally. Venezuela *et al.* demonstrated theoretically that the intensity ratio of the D and D' modes should depend on the defect type [47]. In this work, defects were categorized into on-site defects, hopping defects, and Coulomb defects. For instance, on-site defects may represent chemisorbed atoms on the graphene sheet, whereas Coulomb defects refer to physisorbed charges over the graphene layer that interact with graphene via a Coulomb potential. Hopping defects can be identified with lattice distortions that alter the carbon-carbon bonds in graphene. In principle, these defects are described by different matrix elements that each depend differently on $\mathbf{q}$, $\mathbf{k}$, and ε_L [47]. Thus, inter- and intravalley defect modes should be affected differently by the different defect types. Ergo, the D/D'-mode ratio should show a dependence on the defect species. For instance, hopping defects should exhibit the highest D/D' ratio, whereas on-site defects are expected to exhibit a D/D' ratio of approximately one [47]. In contrast, the simulation of Coulomb defects lead to a negligible small contribution to the D mode and a small contribution to the D' mode. Besides these theoretical considerations of the influence of the defect type on the intensity of defect-induced Raman modes, there are also experimental works that attempted to characterize defects species in defective graphene by Raman spectroscopy [169, 170]. However, the observed dependence of the D/D'-mode ratio on

the defect type could not be verified by other researchers [2]. In fact, the D/D'-mode ratio does not only depend on the defect species, but also on the defect concentration n_D [206], making defect characterization by this approach unfeasible.

As a last point, we want to comment on the doping dependence of the D- and G-mode intensity. It has been experimentally demonstrated by Bruna *et al.* [171] and Froehlicher *et al.* [154] that the D/G-mode ratio depends strongly on the doping level in single-layer graphene. This observation results from two different effects. First, doping leads to an increase of the electron-electron scattering rate and thus $\gamma^{\text{e-e}}$ increases. An increased electronic broadening γ in the D-mode double-resonance process results in a decreased intensity of the double-resonant Raman modes [47, 168]. Second, for high doping levels, the G-mode intensity increases with either n- or p-type doping [105, 106], which can be understood from a partial cancellation of destructive interference contributions in the G-mode scattering process. Hence, both effects lead to a reduction of the measured D/G-mode ratio in doped graphene.

From the above reviewed results, we can conclude that a precise and quantitative characterization of defects in graphene is still challenging. Although Raman spectroscopy is routinely used to characterize CVD- or MBE-grown graphene samples [31], the validity of a single measurement of the D/G-mode ratio to analyze the quality of graphene samples should be questioned. In contrast, a more elaborate characterization of the D/G mode ratio as a function of the doping level, as presented in Refs. [171] and [154], should be envisaged.

[2] Private communication with F. Kampmann (TU Berlin) and M. Bruna (University of Cambridge)

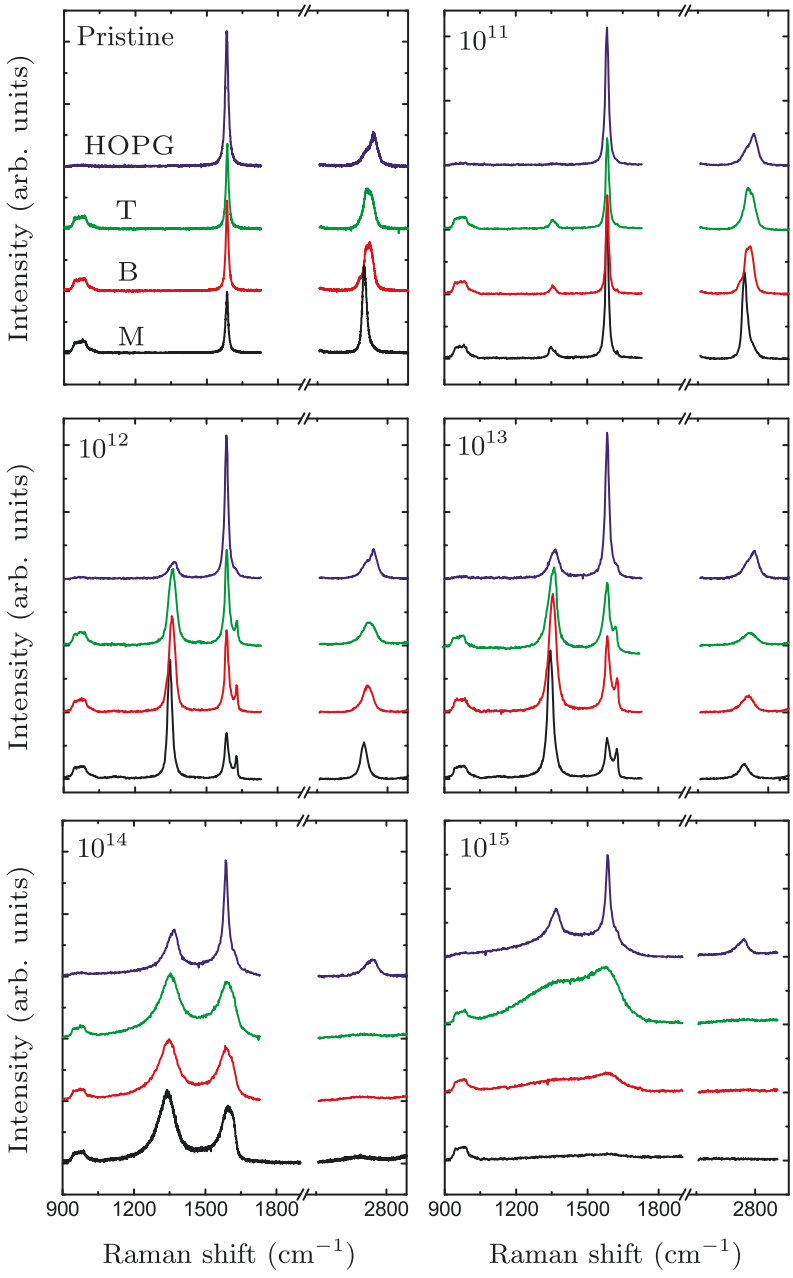

Figure 5.3: Dependence of the Raman spectrum in (M) single-layer graphene, (B) bilayer graphene, (T) trilayer graphene, and (HOPG) bulk graphite on the defect density. A laser excitation energy of 2.41 eV was used; the ion-irradiation doses are given as labels in the top-left corner of each plot. Figure taken from Ref. [206].

5.3 The *D* mode in carbon nanotubes

In this part of the chapter, we will analyze the D mode in carbon nanotubes. The dependence of the D-mode frequency on the chiral indices (n_1, n_2), the tube diameter d, and the energy of the optical transition E_{ii} was discussed widely in literature in the last decade [55–58, 208, 209]. Different dependencies were suggested and controversially discussed. However, the fundamental mechanism that determines the D-mode frequency in carbon nanotubes as a function of the mentioned parameters remained unclear. Moreover, Maultzsch *et al.* argued that only certain metallic carbon nanotubes should exhibit a D mode in their Raman spectrum due to symmetry-based arguments [210].

Here, we will show that double-resonant Raman scattering in carbon nanotubes can be reduced to a simple geometrical model. Our approach is based on the symmetry of the hexagonal lattice and inherently does not include any restrictions on the tube chiral index. We will apply this model for the analysis of the D mode in carbon nanotubes and demonstrate that, in principle, the D-mode scattering process should be possible in any carbon nanotube. We will discuss the dependencies of the D-mode frequency as a function of (n_1, n_2) and compare our results with recent experimental data.

5.3.1 Introduction

Besides the fact that the D and $2D$ Raman modes in graphene and graphite have been explained already in 2000 by Thomsen and Reich [45], there is an ongoing controversy about the D-mode scattering process in carbon nanotubes [55–57]. In fact, it has been questioned if all carbon nanotubes could exhibit a D mode in their Raman spectrum [210]. Due to symmetry-based arguments, Maultzsch *et al.* suggested that only tubes where $(n_1 - n_2)/(3n)$ is integer should contribute to the D-mode spectrum, *i.e.*, carbon nanotubes with $\mathcal{R} = 3$ [63, 211]. This relation is particularly true for armchair carbon nanotubes and some other metallic CNTs. In contrast, semiconducting carbon nanotubes should never exhibit a D mode with the same systematic energy dependence of its frequency [210]. The argumentation of Maultzsch *et al.* is based on the idea that the D-mode scattering process in carbon nanotubes should be only possible if the conduction (valence) band exhibits a minimum (maximum) at $2\,\pi/(3\,a)$ of the Brillouin zone [210]. However, recent experiments on carbon nanotube samples enriched with single chiral indices demonstrated the existence of a D mode in semiconducting CNTs that do not satisfy the aforementioned restriction [212].

Furthermore, there is an ongoing discussion about the dependence of the D-mode frequency in CNTs on the tube diameter and the transition energy. During the past decade many different explanations were postulated and discussed. For instance, in 2001 Souza Filho *et al.* proposed that the D-mode frequency is proportional to the inverse diameter of the CNT [55]. Interestingly, the same authors claimed the opposite dependence, *i.e.*, the D-mode frequency should be proportional to the CNT diameter, in a work published later in the same year [56]. Subsequent

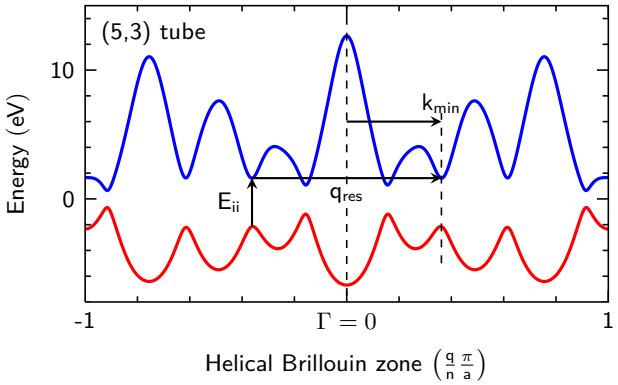

Figure 5.4: Illustration of the enhanced double-resonant scattering process between two energetically equivalent minima in the helical bandstructure of a (5,3) tube. The transition energy is labeled as E_{ii}, the position of the electronic minimum as k_{min}, and the resonant phonon wave-vector as q_{res}.

to this work, Souza Filho *et al.* published another article, presenting experimental data to support their results of a D-mode frequency proportional to the tube diameter [57]. In contrast, Laudenbach *et al.* demonstrated that in principle two different dependencies of the D-mode frequency on the tube diameter can be obtained in a Raman measurement, depending on the experimental conditions [58, 208, 209]. However, the underlying theoretical systematic of the D-mode scattering process is not yet fully understood and thus needs clarification.

5.3.2 Simplification of the double-resonance process in carbon nanotubes

The Raman spectrum of carbon nanotubes has been intensively studied by various groups [213–215]. Many authors demonstrated that certain first-order Raman modes, *e.g.*, the RBM or the G mode, are resonantly enhanced when the laser excitation energy is close to an excitonic transition of the carbon nanotube [83, 84, 119, 216–220]. This fact has been used extensively to determine transition energies and chiral indices in carbon nanotube samples experimentally. Recently, Laudenbach *et al.* showed that this is also valid for the D mode [212]. In contrast to graphene, where electron-hole excitations are always resonant, the D mode in carbon nanotubes is resonantly enhanced when the laser excitation energy is close to an optical transition [221]. Thus, the D mode in carbon nanotubes can be regarded as distinctive contributions from different CNTs coming in resonance by tuning the laser energy. Consequently, we restrict our calculations to only those processes, where the laser excitation energy is in resonance with an optical transition of the carbon nanotube. Furthermore, Laudenbach *et al.* demonstrated that the main contribution to the D-mode process stems from scattering between equivalent minima in the electronic bandstructure [58], *i.e.*, scattering between two E_{ij} transitions with $i = j$. This situation is schematically shown in Figure 5.4 for a double-resonance process in the electronic bandstructure of the (5,3) carbon nanotube. The laser excitation energy (black, vertical arrow) is in resonance with the E_{ii} transition, which can be found at k_{min} in the electronic bandstructure. Following the resonant excitation, the electron and hole are scattered by a TO phonon and a defect with wave vectors $q_{\mathrm{res}} = 2\,k_{\mathrm{min}}$ to the equivalent minimum E_{ii} across the $\mathbf{\Gamma}$ point. This approach directly implies the $q \approx 2\,k$ approximation. Furthermore, we only consider the incoming resonance in our simulations, as it was shown that the incoming resonance is usually

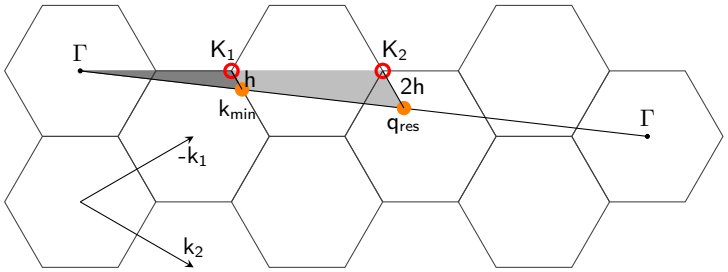

Figure 5.5: Illustration of the dependence between the electronic transition and the resonant phonon wave-vector for a coprime tube. The black solid line denotes the helical vector of a $(3, 2)$ tube, the full orange circles mark a minimum in the electronic band structure (k_{min}) and the corresponding resonant phonon wave-vector length (q_{res}), which is twice k_{min}. The open red circles denote the closest **K** points to k_{min} and q_{res}, respectively. As can be seen easily, the distance $\mathbf{K}_1$-k_{min} is always half the distance $\mathbf{K}_2$-q_{res}.

more dominant compared to the outgoing resonance [58, 220, 221]. This directly means that phonon energies are neglected in our approach.

Using the abovementioned assumptions, we will now derive a systematic dependence between the resonant phonon wave-vector in the double-resonance process and the energy E_{ii} of the optical transition. Before, we want to briefly recall that the D mode results from scattering with a TO phonon and a defect [222]. In general, the dispersion of the TO phonon branch has the same systematic behavior as the electronic bandstructure, *i.e.*, the highest frequencies are observed at the zone center **Γ** and the lowest can be found at the **K** points. In contrast to the electronic bands, the TO dispersion is nearly isotropic around the **K** point with only a slight trigonal warping, which is opposite in direction to the electronic trigonal warping [149]. The distance of a phonon vector from a **K** point can be therefore directly related to a TO phonon frequency.

In Figure 5.5, we show the D-mode scattering process in helical representation for a (3,2)-tube, however, this concept is of course valid for all other tubes. Without loss of generality, we assume that the minimum in the bandstructure of a CNT occurs at the position where the helical vector crosses a $\mathbf{K}-\mathbf{M}-\mathbf{K}'$ high-symmetry line. The minimum shall have the **k**-vector k_{min} (measured from the **Γ** point) and is indicated by a filled orange circle. Hence, the resonant phonon wave-vector in the D-mode scattering process has the length $q_{\mathrm{res}} = 2\,k_{\mathrm{min}}$, given by the second orange circle. We label the closest **K** point to the electronic minimum as $\mathbf{K_1}$ and refer to their distance as h. In general, the distance h is a measure for the transition energy, *i.e.*, a smaller value for h directly translates into a lower transition energy. The three points **Γ**, k_{min}, and $\mathbf{K_1}$ form a triangle, which is indicated by the dark-gray area in Figure 5.5. In the next step all sides of this triangle are doubled, which results in the light-gray triangle formed by the points **Γ**, q_{res}, and $\mathbf{K_2}$. This mathematical operation is known as a similarity transformation. It is an intrinsic property of the hexagonal lattice that twice the distance between **Γ** and a **K** point, is again a **K** point ($\mathbf{K_2}$). If $\mathbf{K_1}$ is the closest **K** point to k_{min}, it directly follows that $\mathbf{K_2}$ is the closest

$\mathbf{K}$ point to q_{res}. Since all sides of the larger triangle were doubled, the distance $\mathbf{K_2} - q_{\mathrm{res}}$ is now twice the distance h. Ergo, an electronic transition with a distance h from $\mathbf{K_1}$ results in a resonant phonon vector with a distance $2h$ from $\mathbf{K_2}$. It is important to notice that k_{min} and q_{res} form the same angle with the closest $\mathbf{K}$ point.

From the above presented model, we can directly extract that a resonant electronic transition between a minimum and a maximum in the electronic bandstructure always leads to a resonantly enhanced phonon wave-vector that originates close from a $\mathbf{K}$ point in the Brillouin zone of graphene. As can be seen, there are no restrictions on the tube chiral index, thus, this scattering process is possible in all carbon nanotubes, in contrast to previous results [210]. Since h and $2h$ are indicative for the energy of the transition and the D-mode frequency, respectively, we can deduce two important results: First, tubes with large diameters and thus lower transition energies exhibit a systematically lower D-mode frequency for the resonantly enhanced transition compared to small-diameter tubes. Second, different transitions in a CNT also exhibit different D-mode frequencies. Although these results seem trivial at a first glance, they enable a deeper understanding of the D mode in CNTs.

If we now also consider trigonal warping effects on the electronic band structure, the electronic minimum may not be exactly on the $\mathbf{K} - \mathbf{M} - \mathbf{K}'$ high-symmetry direction, but slightly shifted away. This would lead to a slightly different distance h and angle between k_{min} and $\mathbf{K}_1$. Nevertheless, the distance between the resonant phonon wave-vector q_{res} and $\mathbf{K}_2$ is again $2h$. Furthermore, as pointed out above, the angle is also conserved. Hence, this relation is independent from the exact position of the electronic minimum, which may differ depending on the band structure model that is used.

We now want to extend our geometrical model to non-coprime tubes, *i.e.*, carbon nanotubes where $n > 1$. These tubes have more than only one subband and thus scattering between different subbands needs to be considered. The situation is shown in Fig. 5.6 for a $(15, 3)$ tube, which has $n = 3$ subbands ($\widetilde{m} = -1, 0, +1$). Due to the scattering between energetically equivalent minima and the point symmetry at the $\mathbf{\Gamma}$ point, the scattering process can always be represented by a scattering across the $\mathbf{\Gamma}$ point at $(0, 0)$. The process can be also represented as symmetric scattering across the $\mathbf{M}$ point, however, for convenience we use the representation across the $\mathbf{\Gamma}$ point. Let us now assume that an electron is scattered between a minimum on the $\widetilde{m} = +1$ band to a minimum on the $\widetilde{m} = -1$ band, *i.e.*, the electron is scattered between $-k_{\mathrm{min}}$ and k_{min}. Again, the resonant phonon wave-vector is given by $q_{\mathrm{res}} = 2\,k_{\mathrm{min}}$. We can now introduce the same triangles with the same edge points to our plot as in Figure 5.5 for coprime tubes. Hence, exactly the same systematics as before apply (see above). Furthermore, our geometrical approach instrinsically assigns the phonons from the correct subband, *i.e.*, with the correct quantum number $\widetilde{m}$. In our example, the electrons are scattered between the $\widetilde{m} = +1$ and $\widetilde{m} = -1$ band, which results in a change of the helical quantum number by $\Delta\widetilde{m} = -2$. Therefore, the phonons must stem from the $\widetilde{m} = -2$ band, which is equivalent to the $\widetilde{m} = +1$ band (compare Fig. 5.6). Since the $\widetilde{m}$ bands are equidistantly spaced in the reciprocal lattice, this result is naturally produced in our model and can be seen very nicely.

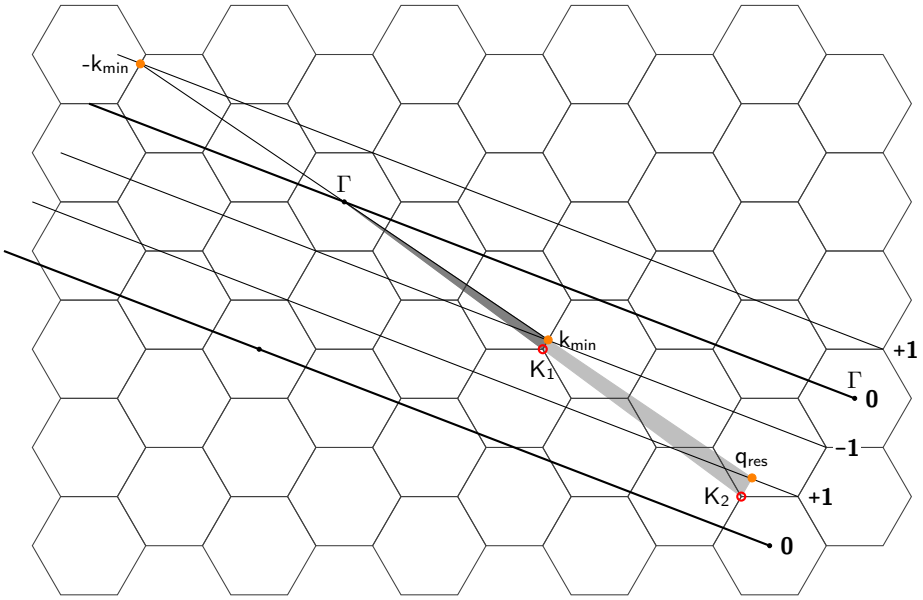

Figure 5.6: Illustration of the geometrical model for non-coprime tubes, *i.e.*, for carbon nantoubes with $n > 1$. In this example, we used the helical bands of a (15,3) tube. The numbers -1, 0, and $+1$ refer to the helical quantum number $\widetilde{m}$ of each subband. Due to the scattering between two equivalent minima and the point symmetry at the $\mathbf{\Gamma}$ point, the resonant phonon wave-vector is always twice the distance $\mathbf{\Gamma} - k_{\mathrm{min}}$.

Up to now, we did not made any assumptions concerning the concrete model that is used to describe the dispersion for the electrons or the phonons. Thus, these results are universally valid as long as zone-folding is an appropriate model to describe the properties of CNTs. In the following, we want to derive a quantitative dependence of the D-mode frequency on the tube diameter and the transition energy using the presented geometrical approach.

5.3.3 Calculational details

As motivated above, our calculations only consider resonant scattering processes between energetically equivalent van-Hove singularities in the electronic bandstructure of carbon nanotubes. Furthermore, only the incoming resonance was considered.

The calculation of electronic bandstructures and phonon dispersions was performed using the POLSym code in sixth-nearest neighbor approximation [95]. As briefly described in Chapter 2.3, this package uses the modified group projectors technique and includes curvature effects on the band energies and phonon frequencies. Electronic bands and phonon dispersions are calculated for all 274 chiral tubes with diameters between 5 and 25 Å. A major shortcoming of the POLSym code is the incorrect treatment of the Kohn anomaly of the A_1-symmetry phonons at the **K** point. In fact, the Kohn anomaly is absent in all calculated carbon nanotube phonon dispersions. Therefore, we additionally used an experimental graphite TO phonon dispersion from Ref. [149] for an alternative calculation of the D-mode frequencies and for comparison with

the POLSym-derived frequencies. Diameter- or chiral-index-dependent excitonic effects on the optical transition energies are not considered in the POLSym code.

5.3.4 Dependence of the *D*-mode frequency in carbon nanotubes on tube diameter and transition energy

Using the model described above, we can derive the diameter and transition-energy dependent D-mode frequencies in carbon nanotubes. As already pointed out by Kataura *et al.* [74], the energy of an optical transition E_{ii} is inversely proportional to the CNT diameter d. This can be easily understood, as the number of subbands, their spacing, and their length depend on d. In general, this means that the subbands of the carbon nanotube are closer to the **K** points in the Brillouin zone of graphene with increasing tube diameter d, leading to a reduction of the transition energy. Keeping in mind the systematics of the presented geometrical model, an optical transition that is closer to a **K** point results in a lower, resonantly enhanced D-mode frequency. This result is summarized in Figure 5.7 (a) for all chiral carbon nanotubes with diameters between 5 Å and 25 Å. Here, we show the evolution of the distance between the resonant phonon wave-vector and the closest **K** point, previously introduced as $2h$, as a function of the tube diameter d. As can be seen, the distance $2h$ decreases with a $1/d$-dependence. Furthermore, energetically higher transitions have a larger distance $2h$ for the same tube diameter. Since the distance $2h$ directly depends on the energy of the optical transition of a carbon nanotube, we observe a close correspondence between the dependence shown in Figure 5.7 (a) and the so-called Kataura Plot [74].

We now translate the distance $2h$ into a TO phonon frequency using our calculated phonon dispersions and replot the result from Figure 5.7 (a). The dependence between the D-mode frequency and the tube diameter is shown in Figure 5.7 (b). Since the distance $2h$ is an approximate measure for the TO phonon frequency, *i.e.*, a larger value for $2h$ reflects a larger D-mode frequency and vice versa, the systematic of this plot again resembles the Kataura plot. We observe a decreasing D-mode frequency with increasing tube diameter. Furthermore, energetically higher optical transitions exhibit a higher D-mode position. Interestingly, we also observe that each transition E_{ii} splits up into different branches that evolve below and above the average $1/d$ dependence [not seen in Figure 5.7 (a) for the same optical transitions]. This splitting can be directly attributed to the different tube families ν. Although the distance of subbands to the **K** point in graphene's Brillouin zone might be the same for tubes with similar diameter [compare Figure 5.7 (a)], there are differences in the corresponding D-mode frequencies due to a non-isotropic TO dispersion around **K** [compare Figure 5.7 (b)]. We will discuss this observation later in more detail.

By plotting the calculated D-mode frequencies as a function of the optical transition energy (see Fig. 5.8), we observe another interesting feature in the D-mode dispersion. The dispersion of the branches is not continuous, in contrast, we observe a small jump in frequency between different optical transitions. This frequency jump has been reported recently in enriched carbon

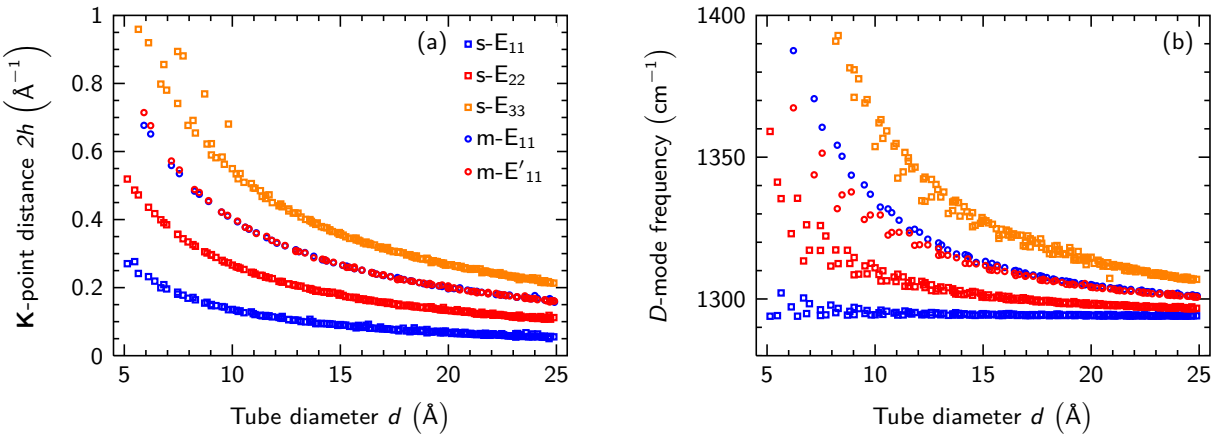

Figure 5.7: (a) Distance between the resonant phonon wave-vector and the closest **K** point as a function of the tube diameter d for the resonantly enhanced scattering process obtained from a sixth-nearest neighbor tight-binding model. (b) Calculated D-mode frequency ω_{D} as a function of the tube diameter. ω_{D} decreases with increasing tube diameter following a $1/d$ dependence.

nanotube samples and in HiPco-produced carbon nanotubes ensembles [58, 208, 209]. The observed discontinuity is a direct consequence of curvature effects on the phonon frequencies and thus cannot be explained in a simple zone-folding approach, as will be shown below.

Considering a zone-folding tight-binding model without any curvature effects, only the helical vector would depend on n_1 and n_2, but not the electronic bands nor the phonon dispersion. Let us now assume that two different carbon nanotubes with different diameters exhibit, by chance, the same energy for different optical transitions, *e.g.*, the E_{11} transition of the $(6,5)$ and the E_{22} transition of the $(12,10)$ tube. Thus, the distance h of the optical transition to the closest **K** point would be the same for both CNTs, leading to same distance $2h$ for the resonantly enhanced phonon wave-vector[3]. Hence, two different tubes with different diameters but the same transition energy would exhibit the same D-mode frequency. Ergo, by neglecting curvature effects, the experimentally observed frequency jump between different optical transitions cannot be explained. However, it is well-known that phonons in carbon nanotubes show a strong dependence on the tube diameter due to curvature effects and rehybridization of σ and π orbitals. For instance, in semiconducting carbon nanotubes the **Γ**-point TO phonon (G^- mode) decreases with decreasing tube diameter [120]. Assuming an analogous diameter dependence for the TO phonons around the **K** point, the same distance $2h$ would result in different D-mode frequencies, *i.e.*, the smaller CNT would exhibit a lower D-mode peak position. This directly opens a gap in the otherwise continuous D-mode dispersion between different optical transitions. In our calculations this jump is smaller than the experimentally observed discontinuity. For instance, we calculate a frequency jump of $2\,\mathrm{cm}^{-1}$ between the second semiconducting and

[3]This example considers the E_{11} and E_{22} transitions of two semiconducting tubes from different families ν, resulting in optical transitions on the same side of the **K** point. However, for optical transitions on opposite sides of **K**, the argumentation is analogous and leads to the same conclusion.

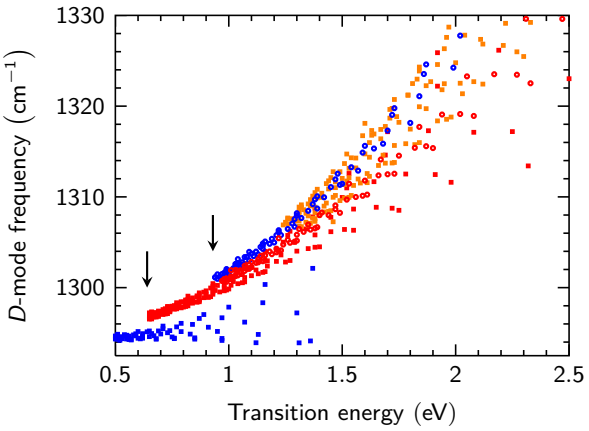

Figure 5.8: Calculated D-mode frequencies as a function of the optical transition energy. The experimentally observed jumps between the different transitions are indicated.

the first metallic transition. In contrast, the experimentally observed discontinuity is as large as $15\,\mathrm{cm}^{-1}$ [208, 209]. Furthermore, D modes from the E_{11}^S transition show nearly no dispersion with transition energy in our calculations. We attribute these discrepancies to the fact that the Kohn anomaly and the region around the **K** point in the TO phonon dispersion is not well approximated by the POLSym code. This can be also inferred from the too high D-mode frequencies in our calculations compared to experimental data [208]. In fact, our calculated values are approximately $20\,\mathrm{cm}^{-1}$ too high. Since the resonantly enhanced phonons from the E_{11}^S transition stem from a region close to the **K** point, small deviations in the phonon dispersion directly influence our result and in our case lead to an overestimated D-mode frequency with nearly no dispersion. We expect a larger jump and a better correspondence to experimental data for calculations using a non-orthogonal tight-binding model or an *ab-initio* approach. Nevertheless, the jump can be reproduced in our simulations, as seen between E_{11}^S and E_{22}^S. We want to emphasize that the systematics of the resonant phonon wave-vector in the double-resonance process do not depend on the choice of the calculational model and are therefore universally valid.

Next, we want to investigate the diameter distribution along a given transition E_{ii}. It is well known that the energy of an optical transition in CNTs is inversely proportional to the tube diameter [74]. Thus, the same transition, *e.g.*, the E_{22} transition in semiconducting tubes, has a smaller energy in tubes with a larger diameter. Ergo, along the D-mode branches in Fig. 5.8 the diameter decreases with increasing energy. Therefore, tubes with a small diameter can be always found on the higher-energy side of such branches, exhibiting a higher D-mode frequency (see Figure 5.8).

The above presented results finally harmonize the different conclusions from various previous works where a decreasing D-mode frequency for a decreasing tube diameter was claimed [56, 57] or vice versa [55]. It is very important to point out that, depending on the experimental conditions, one can generally observe two different D-mode dispersions with laser excitation

energy. By measuring the same optical transition for all tubes in an ensemble, *e.g.*, the E_{22} transition, a $\propto 1/d$-dependence will be observed due to the mentioned diameter distribution along the different E_{ii} branches [55]. This would correspond to an experimental setup, where the laser energy is tuned to measure every tube always at its resonance energy. In Figure 5.8, we would follow a single E_{ii} branch in this experimental situation. By using only a single or just very few laser energies, a different behavior is observed [56, 57]. This experimental condition corresponds to a vertical cut through the dispersion relation shown in Figure 5.8. Along such a cut, a higher D-mode frequency corresponds to a higher tube diameter and a dependence proportional to d is observed. Both cases are distinctly different and must be separated carefully. Recently, Laudenbach *et al.* presented a careful analysis of the different dispersions in HiPco-produced carbon nanotubes samples and experimentally observed the same dependence as theoretically derived here [208, 209].

5.3.5 *D*-mode families

The family behavior of Raman modes in carbon nanotubes is already known for the radial-breathing modes [84, 121] or the G^- mode in semiconducting carbon nanotubes [120], where each branch is given by the relation

$$\nu = (n_1 - n_2) \bmod 3 = \pm 1 \quad \text{and} \quad \mu = 2\,n_1 + n_2 = \text{const.}$$

Here, we will show that the D mode follows a similar behavior and that the D-mode frequencies arrange in a 'Kataura Plot'-like pattern. Figure 5.9 shows the calculated D-mode frequencies for the E_{22} transition of semiconducting tubes (same data as in Figure 5.8). As can be seen easily, we observe a fan-like structure around the average dispersion. D-mode frequencies that are found above the mean value can be identified with double-resonance processes in carbon nanotubes from the $\nu = -1$ family, whereas D modes below the average dispersion result from CNTs of the $\nu = +1$ family. The labels at the calculated D-mode frequencies refer to the chiral indices of the outmost carbon nanotubes of each branch μ. These tubes exhibit a chiral angle close to 0° (zig-zag like carbon nanotubes), whereas the helical vector of the innermost tubes is close to the armchair direction (chiral angle of 30°). Compared to the RBM families, the positions of the D-mode branches are flipped, *i.e.*, the $\nu = -1$ families are on the upper side of the E_{22}^S branch and the $\nu = +1$ families on the lower side. This behavior can be understood by reducing our geometrical model to just a single **K** point.

If the optical transition occurs at a distance h and an angle φ near a **K** point, the resonantly enhanced phonons stem from the distance $2h$ and an angle φ from a $\mathbf{K}'$ point (see Figure 5.5). Since **K** and $\mathbf{K}'$ are equivalent but rotated by 180° with respect to each other, a phonon with distance $2h$ and angle φ at $\mathbf{K}'$ can be represented by a phonon with the same distance but angle $(\varphi + \pi)$ at **K**. Thus, we can project the electronic transition and the corresponding resonant phonons onto a single **K** point, where the electronic transition and the resonantly enhanced

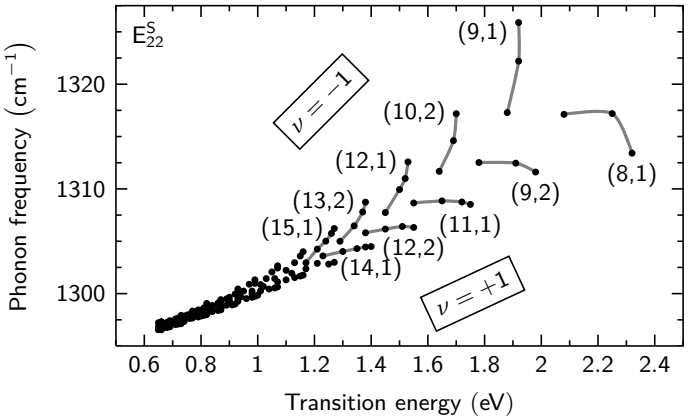

Figure 5.9: Family behavior of the D-mode frequencies for the E_{22}^S transition. The labels refer to the chiral indices of the outmost tube of each branch.

phonon stem from opposite sides. Figure 5.10(a) shows the schematics of the reduced model.

As discussed above, the optical transitions in carbon nanotubes split up into different branches with $\nu = \pm 1$ families. Thus, also the resonant phonon wave-vectors in the D-mode scattering process split up accordingly. This can be seen in Figure 5.10(b), where we plot the resonant phonon wave-vectors for the E_{22}^S transition of all carbon nanotubes in our calculation. As can be seen, the phonons are arranged in branches forming a spiral that evolves into the **K** point with increasing tube diameter. Thus, tubes with small diameters can be found at larger distances to **K**, directly translating into a higher D-mode frequency. If we now want to understand the family behavior of the D mode, we have to keep in mind that we plot the resonantly enhanced phonons, which are on the **K**-point side opposite to the electronic transition. Thus, the D-mode phonon frequencies behave contrary to the families of the electronic transitions or the RBMs. Since the TO phonon branch exhibits a weaker diameter-dependent frequency shift compared to the RBMs (ZA phonon branch in graphene) [208], the splitting between the D-mode peak positions is not as pronounced as for the RBM families.

Finally, we want to comment on expected Raman-intensity variations between D modes from different branches. For the RBM families, it is well-known that the $\nu = -1$ family of the E_{22} transition gives a much larger Raman signal compared to the $\nu = +1$ family [223]. This behavior is due to a higher oscillator strength of the optical transition and a higher electron-phonon coupling for these tubes [224]. Although the electron-phonon coupling might be different for the TO phonon, the oscillator strength should be the same for the RBM and the D-mode scattering process, as the optical transitions are nearly equivalent. Moreover, the oscillator strength usually dominates the double-resonant scattering cross-section, as it enters to the power of four in the calculation in Eq. (3.14). Thus, a similar behavior regarding the intensities of the RBM and D-mode families can be expected. If we keep in mind that the RBM and D-mode families are on different sides of the E_{ii} transitions, this would mean that the upper family of a D-mode branch is predominantly observed in experiments and the lower family is weaker in signal. Although

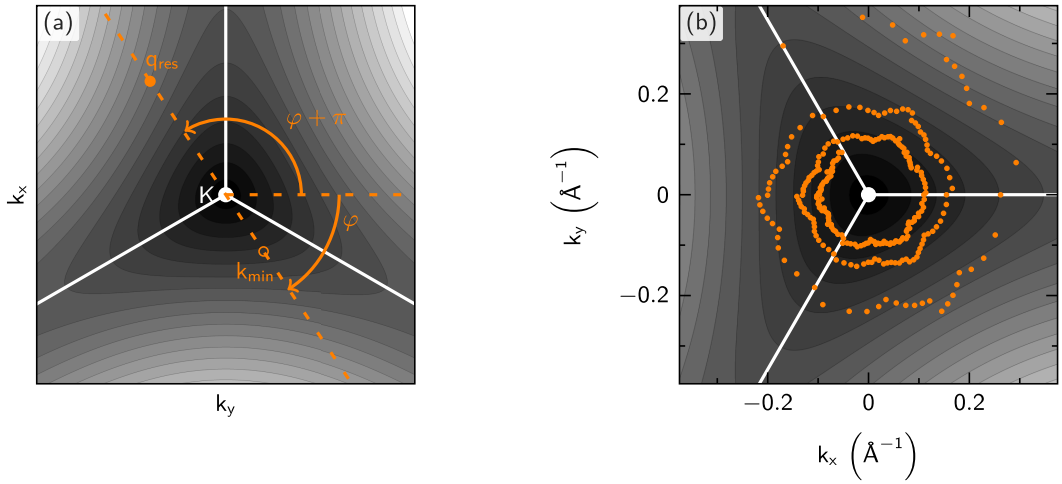

Figure 5.10: (a) Reduced scheme of the geometric model to a single **K** point. k_{min} and q_{res} label the positions at which the electronic transition occurs and the resonant phonons stem from, respectively. The solid white lines denote the $\mathbf{K}-\mathbf{M}$ high-symmetry directions. (b) Calculated resonant phonon wave-vectors for the E_{22}^S transition projected on a single **K** point at (0,0). The positions of the resonant phonon wave-vectors evolve along a spiral into the **K** point for increasing tube diameter.

an experimental validation of this prediction appears to be difficult, recent experimental works hint in this directions [209].

5.3.6 Diameter correction of the *D*-mode frequencies

To finalize our results, we want to investigate the influence of diameter-corrections on the *D*-mode dispersion in carbon nanotubes. In a first approximation, the diameter-dependent frequency shift of the TO phonons in CNTs can be found by comparison of the *D*-mode frequencies in carbon nanotubes with the *D*-mode dispersion in graphene and graphite. In Figure 5.11 (a) we show a schematized, experimental *D*-mode dispersion of HiPco-produced carbon nanotubes and single-tube measurements from Refs. [208, 209]. Additionally, we also plot the experimentally known dispersion of the *D* mode in graphene and graphite [31, 102]. Since the *D* mode in graphene and graphite does not include any curvature effects, the difference between both dispersions is a direct measurement of the diameter-dependent correction of the *D*-mode frequency. From the difference of both dispersions, we can derive the frequency downshift of the TO phonons in CNTs as a function of the tube diameter. The result of this analysis is shown in Figure 5.11 (b). As expected, the frequency difference is always negative and decreases for increasing carbon nanotube diameters. By using a classical mechanical approach, the diameter

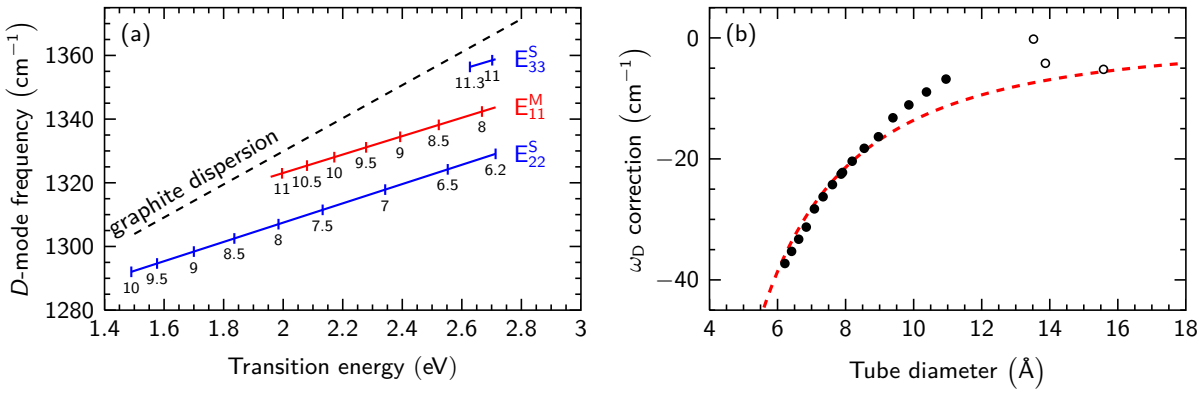

Figure 5.11: (a) Schematized experimental dispersion of the D mode in carbon nanotubes (after Ref. [208]). The solids lines denote fits to the experimental data for each transition; the numbers at each line correspond to the diameter of the tubes. The dashed line indicates the D-mode dispersion in graphite [31], where no diameter dependence is expected. (b) D-mode frequency correction as a function of the tube diameter. The red, dashed line reflects a square-root fit to the data points. Solid symbols were obtained from (a), open symbols are single-tube measurements from Ref. [208].

dependence of the TO phonon can be modeled as [208]:

$$\Delta\omega_D(d) = A\left[\sqrt{1-\left(\frac{2.13\,\text{Å}}{d}\right)^2}-1\right]. \tag{5.3}$$

Here, d is the tube diameter and A is a fit parameter. From a least-squares fit of the data points, we find $A = 593\,\text{cm}^{-1}$. The resulting curve is indicated by the dashed line in Figure 5.11 (b).

Using the above result, we can now analyze the influence of diameter effects on the D-mode dispersion. In detail, we want to investigate if the experimentally observed jump of the D mode dispersion can be reproduced by artificially introducing curvature effects. Therefore, we use the calculated resonant phonon wave-vectors from our sixth-nearest-neighbor tight-binding model [95] and obtain the resonant phonon frequencies from an experimentally measured TO phonon dispersion of graphite by Grüneis *et al.* from Ref. [149]. Subsequently, we apply the curvature correction using the above formula Eq. (5.3). The diameters of the carbon nanotubes in this calculation were chosen to fit the experimentally measured nanotubes from Ref. [208], *i.e.*, tubes with diameters between 6 Å and 14 Å were considered. The result of this calculation is shown in Figure 5.12. Without curvature corrections, the D mode shows a continuous dispersion as for graphene or graphite (gray data points). However, by artificially introducing curvature effects, we observe the emergence of a frequency jump between the different optical transitions. This can be easily understood from the D-mode dispersion in Figure 5.8 or Figure 5.11: There are always carbon nanotubes with different diameters from different optical transitions E_{ii} that exhibit very similar transition energies. If no curvature effects are present, this would result in an overlap of

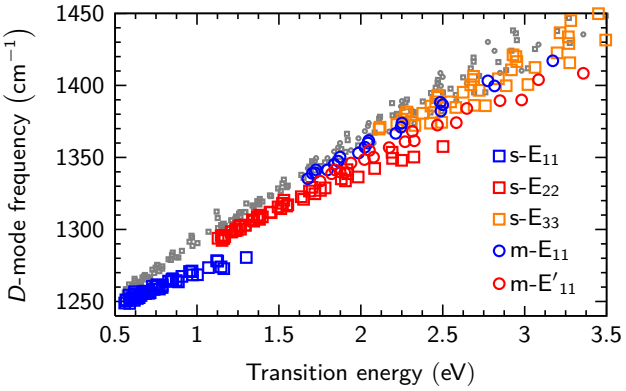

Figure 5.12: Artificially curvature-corrected D-mode dispersion of carbon nanotubes. The curvature correction was performed using the relation given in Eq. (5.3) and phonon frequencies obtained from Ref. [149]. Electronic band structures were obtained from a sixth-nearest-neighbor tight-binding model. The experimentally observed discontinuities could be reproduced. Gray data points reflect calculated D-mode frequencies without curvature corrections.

these sets of transitions and thus in very similar D-mode frequencies (compare gray data points in Figure 5.12). However, by introducing a diameter-dependent frequency correction according to Eq. (5.3), CNTs with smaller diameter observe a larger frequency downshift compared to nanotubes with large diameters. Keeping in mind the diameter distribution along the different transition branches E_{ii}, D modes from the high-energy side of the different E_{ii} transitions are more affected by the frequency downshift compared to the low-energy side. Ergo, the slope of the D-mode branches is reduced compared to the D mode dispersion in graphite, in agreement with experimental data [208, 209]. As a result, a discontinuity opens between different transitions. In our curvature-corrected D-mode frequencies in Figure 5.12 this discontinuity can be seen again most clearest between E_{11}^S and E_{22}^S (approx. $15\,\mathrm{cm}^{-1}$). For energetically higher transition the frequency jump decreases, *e.g.*, the difference between E_{22}^S and E_{11}^M is approx. $9\,\mathrm{cm}^{-1}$. Both theoretically calculated frequency jumps are in reasonable agreement with experimental data and are shown to be a consequence of the diameter dependence of phonon frequencies in carbon nanotubes.

5.3.7 Summary

In summary, we derived a geometrical model to describe the diameter dependence of the resonant phonon wave-vector in the double-resonance process in carbon nanotubes. The presented approach is independent of the specific model used for the electronic bandstructure or phonon dispersion and is therefore universally valid. We applied our model to investigate the defect-induced D mode in chiral carbon nanotubes at their resonant optical transitions. First, we demonstrated that, in principle, there is no restriction of the D-mode scattering process to specific carbon nanotubes. Moreover, we could show that small-diameter tubes exhibit a higher

D-mode frequency in general and that higher resonant optical transitions exhibit a systematically higher D-mode frequency. Furthermore, we proved that the experimentally observed discontinuity between different transition branches is due to curvature effects that alter the TO phonon dispersion around the **K** point. In analogy to other Raman modes in carbon nanotubes, *e.g.*, the RBM or the G mode, we showed that the D-mode frequencies are arranged in branches and families.

The presented results finally harmonize the different experimental observations regarding the diameter dependence of the D mode in carbon nanotubes and are equally valid for the behavior of the $2D$ mode. The observed diameter dependence can be seen as a superposition of D modes from different CNTs coming in resonance after each other. Finally, we want to point out that our geometrical model can be easily expanded to other intervalley Raman modes in carbon nanotubes, as will be shown in the next section.

5.4 The D'' mode in graphene and carbon nanotubes

In this part of the chapter, we will investigate the double-resonant D'' Raman mode in graphene and carbon nanotubes and its dependence on laser excitation energy, on the number of graphene layers, and on the carbon nanotube diameter.

5.4.1 Introduction

The Raman spectrum of graphene and carbon nanotubes is dominated by Raman modes that are related to optical phonons, such as the well-known D, D', and $2D$ modes, or the first-order G band in graphene and the RBM in carbon nanotubes [32, 34, 36, 38, 84, 120, 121, 201, 207]. Their observation can be easily understood from fundamental selection rules of the Raman process and the strong electron-phonon coupling of optical phonons compared to acoustic phonons [40, 167]. However, beside these aforementioned modes, there are various other Raman-active vibrations that result from double-resonant two-phonon scattering processes or from phonon-defect scattering [47]. In this part of the chapter, we focus on the defect-induced D'' mode in graphene and carbon nanotubes that results from double-resonant scattering of longitudinal acoustic (LA) phonons with defects. Acoustic phonons strongly affect charge carrier mobilities and thermal transport properties and are thus very important for the performance of electronic devices [10, 225]. However, first-order Raman scattering does not allow to probe these phonons due to momentum conservation in the Raman process. Therefore, the LA phonon was often observed in combination with other phonons in double-resonant Raman scattering processes [142, 226]. Especially in bi- and few-layer graphene, combination modes containing the LA phonon can be observed in the frequency range between the G and the $2D$ mode [227–229]. For instance, at $\approx$1950 cm^{-1} and $\approx$2050 cm^{-1} double-resonant intravalley LA+TO and LA+LO combination modes can be observed. Furthermore, the double-resonant intervalley scattering of TO and LA phonons can be observed at $\approx$2450 cm^{-1} in the Raman spectrum of single-layer graphene. However, none of the previous works analyzed the LA phonon itself. Here, we demonstrate that acoustic phonons can indeed be directly studied by optical spectroscopy, namely double-resonant Raman scattering.

5.4.2 Experimental details

Measurements presented in this chapter were carried out on mechanically exfoliated graphene samples that were prepared on silicon substrates with an 100 nm thick silicon dioxide layer. The samples were then transferred into a vacuum chamber and irradiated with swift heavy ions (Xe^{26+}, 91 MeV) using a fluence of approximately 65.000 ions/μm^2 at normal incidence. The irradiated graphene samples were provided by Oliver Ochedowski from the Universität Duisburg-Essen. Under grazing-incidence, irradiation swift heavy ions would cause extended modifications in the crystal lattice of graphene, such as splits and folds with lengths up to 100 nm [230, 231]. On the contrary, at normal incidence, point-like defects are created [232]. Due to their high

energy, the interaction of swift heavy ions with matter is exclusively by inelastic scattering. As the penetration depth of 91 MeV Xe ions is about 10 μm [233], defects are not introduced exclusively in single-layer but in bi- and tri-layer graphene as well. This enables us to investigate the layer-number dependence of the D'' mode in few-layer graphene.

As already discussed in the second section of this chapter, Raman spectroscopy is frequently used for defect characterization in graphene. However, several problems arise, when the common formula

$$\frac{I_D}{I_G} = \frac{(4.3 \pm 1.3) \times 10^3 \text{ nm}^2\,\text{eV}^4}{L_D^2\,\varepsilon_L^4}$$

is used to determine the average defect distance L_D from the experimentally measured D/G-mode ratio. Especially in the present case, where defects were created by irradiation with swift heavy ions, defect sizes differ significantly from the original work in Ref. [33]. To overcome this problem, we rely on the calculation of L_D from the Xe fluence per area. Assuming that defects are homogenously created in the graphene layer, we deduce an average distance between defects of approximately 4 nm.

For the measurements on carbon nanotubes, we used buckypaper CNTs produced by the HiPco process [234]. The investigated CNT ensemble had a diameter distribution of (10±2) Å [76, 235], which was verified by resonance profiles of the RBM. Measurements on carbon nanotubes were carried out by Christoph Tyborski (TU Berlin) and are shown here only for completeness.

Raman measurements were performed with a Horiba HR800 and a Dilor XY spectrometer, equipped with solid-state lasers, as well as dye and gas lasers. Raman spectra were recorded in back-scattering geometry under ambient conditions using a 1800 lines/mm grating and an 100× objective, yielding a spectral resolution of approximately 1 cm^{-1}. Since the D'' mode and the second-order Raman modes of silicon are close in frequency, it was necessary to perform a background subtraction for graphene measured on silicon substrates. For this purpose, we used the same experimental conditions as for the Raman measurements on graphene, *i.e.*, the same laser power and integration time, and recorded the silicon background at a spot adjacent to the investigated graphene flake. During all measurements the laser power was kept below 1 mW in order to avoid sample heating, laser-induced doping or the creation of additional unwanted defects.

The calculation of phonon dispersions and bandstructures of single-layer graphene in this chapter were carried out with the SIESTA code in Local Density Approximation (LDA) [236]. The lattice parameters were fixed to the experimentally observed values [59]. The phonon dispersion was calculated using a 3×3 supercell approach. For the determination of the resonant phonon wave-vectors in the double-resonance process, we used a GW-corrected bandstructure of graphene, *i.e.*, the Fermi velocity of the LDA-calculated bandstructure was renormalized by 17 % [146].

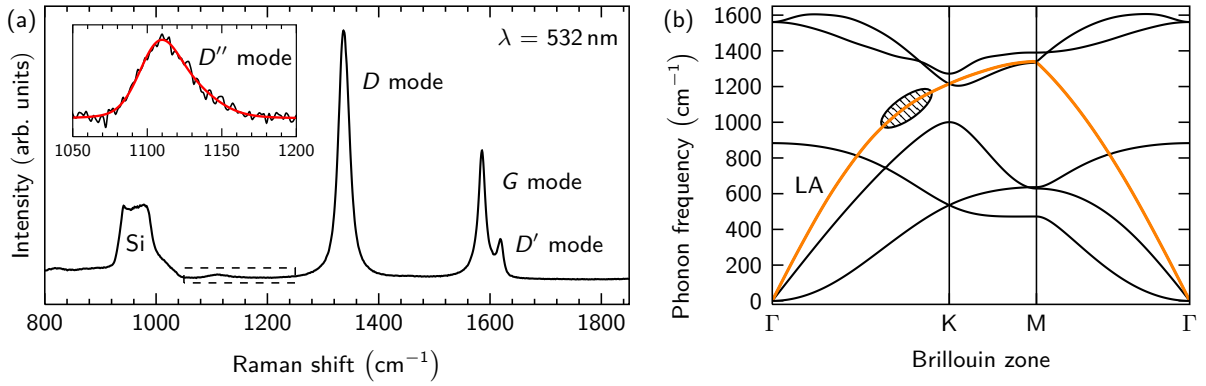

Figure 5.13: (a) Raman spectrum of defective single-layer graphene at 532 nm laser excitation wavelength. The spectral range, where the D'' mode can be observed, is enlarged in the inset. The solid red line denotes a fit composed of two Lorentzian contributions. (b) DFT-calculated phonon dispersion of single-layer graphene. The LA phonon branch is highlighted in orange, the k-space region where the resonant phonons stem from is marked with the hatched ellipse.

5.4.3 Analysis of the D'' mode in graphene

Figure 5.13 (a) presents a Raman spectrum of defective single-layer graphene, the prominent Raman modes are labeled next to the peaks. The inset shows an enlarged view of the spectral range between the second-order Raman signal of the silicon substrate and the D mode, as indicated by the dashed rectangle. In this region, an asymmetric Raman mode can be observed that is absent in defectless graphene. Despite the large D/G-mode intensity ratio of approximately 2.0, this new Raman mode can be barely observed and is approximately 50 to 100 times weaker in intensity than the D mode. We explicitly verified that this Raman mode cannot be observed at arbitrary edges of exfoliated graphene, indicating that a larger number of defects is needed to result in a measurable Raman signal. Following the notation of Venezuela *et al.* in Ref. [47], we will refer to this new Raman mode as the D'' mode.

Figure 5.14 (a) presents Raman spectra of the D'' mode in single-layer graphene at four different laser excitation energies. Each spectrum was fitted with two Lorentzian profiles, accounting for the observed asymmetric lineshape. We will discuss the asymmetry of the D'' mode later. We can observe a simultaneous downshift of both contributions to this Raman mode by increasing the laser excitation energy [see Figure 5.14 (c)]. The laser-energy dependent peak shift indicates that this Raman mode results from a double-resonance process. However, the observed downshift of approximately $-80\,\mathrm{cm}^{-1}/\mathrm{eV}$ is opposite to the well-known behavior of the D and $2D$ mode in graphene. This can be understood from the dispersion of the phonon branch that is involved in the scattering process. The D'' mode is assigned to a double-resonant intervalley scattering process that involves an LA phonon and a defect, as theoretically predicted in Ref. [47]. The DFT-calculated phonon dispersion of single-layer graphene is shown in Figure 5.13 (b), the LA branch is highlighted in orange. Since this Raman mode results from an intervalley scattering process, the dominant contributions stem from phonons along the $\mathbf{\Gamma} - \mathbf{K} - \mathbf{M}$ high-symmetry

direction. However, only between **Γ** and **K** the measured D''-mode frequencies match the calculated LA dispersion. Therefore, the D'' mode must be an inner process. The dispersion of the LA phonon branch is monotonously increasing along $\mathbf{\Gamma} - \mathbf{K}$ and since an increasing laser excitation energy leads to shorter phonon wave vectors in intervalley double-resonant scattering, the D'' mode downshifts with larger laser energies [compare Fig. 5.14 (c)]. Venezuela *et al.* demonstrated that also double-resonant intravalley processes of LA phonons and defects shall be observable in the Raman spectrum of graphene [47]. The calculated frequency of this process is approximately $450\,\mathrm{cm}^{-1}$ at 2.4 eV laser excitation energy. However, the intensity of this mode is roughly five to ten times smaller than the intensity of the D'' mode and could not be observed in our study. The intensity of a double-resonant Raman mode mainly depends on the electron-phonon coupling of the specific phonon that is involved in the scattering process. As shown by Piscanec *et al.* [40], both optical phonon branches present a Kohn anomaly at specific points in the Brillouin zone of graphene. Namely, the TO and LO phonon branches exhibit Kohn anomalies at **K** and **Γ**, respectively. Due to these Kohn anomalies, the electronic screening of lattice vibrations is drastically reduced, leading to an increased electron-phonon coupling for the TO and LO-derived phonon branches at the mentioned **k**-space points. In contrast, the electron-phonon coupling for all other phonon modes is much smaller throughout the Brillouin zone [40, 47], explaining the small intensity of the D''-mode and other double-resonant Raman modes, such as the LO±ZO′ combination mode [107, 126].

Since double-resonant Raman spectroscopy enables to probe the phonon dispersion as well as the electronic bandstructure, we can now map the LA phonon branch along the **Γ**−**K** high-symmetry direction by tuning the laser excitation energy. Figure 5.14 (b) compares the experimentally obtained D''-mode frequencies with the calculated LA phonon branch dispersion along **Γ**−**K**−**M**. The resonant phonon wave vectors for each laser excitation energy were obtained from the resonance condition on the incoming and scattered photon in the double-resonance process. Here, only inner processes are considered. The experimental values match the theoretical curve along $\mathbf{\Gamma} - \mathbf{K}$ within an error of less than $10\,\mathrm{cm}^{-1}$. By tuning the laser excitation energy, one can now follow the LA phonon branch along the high-symmetry line. However, the **q**-space range that is accessible by this scattering process is limited to $0.5 - 0.9 \times \mathbf{\Gamma} - \mathbf{K}$ for laser excitation energies between 4.0 and 1.2 eV [47]. In order to obtain the LA dispersion outside these limits, *e.g.*, close to **Γ** where acoustic phonons dominate heat transfer, we fitted the experimentally obtained values by a sine function of the following form

$$\omega(q) = A \cdot \sin\left(\pi * \frac{q}{w}\right). \tag{5.4}$$

Here, A is the amplitude and w refers to the period. A fit with $A = 1170.7\,\mathrm{cm}^{-1}$ and $w = 3.3\,\mathrm{Å}^{-1}$ yielded the best approximation to our data. The resulting fit, the *ab-initio* calculated LA branch, and the experimental data points are shown together in Fig. 5.15. Although fit and calculation differ for **q** vectors close to **K**, the overall agreement is very good with a deviation of less than

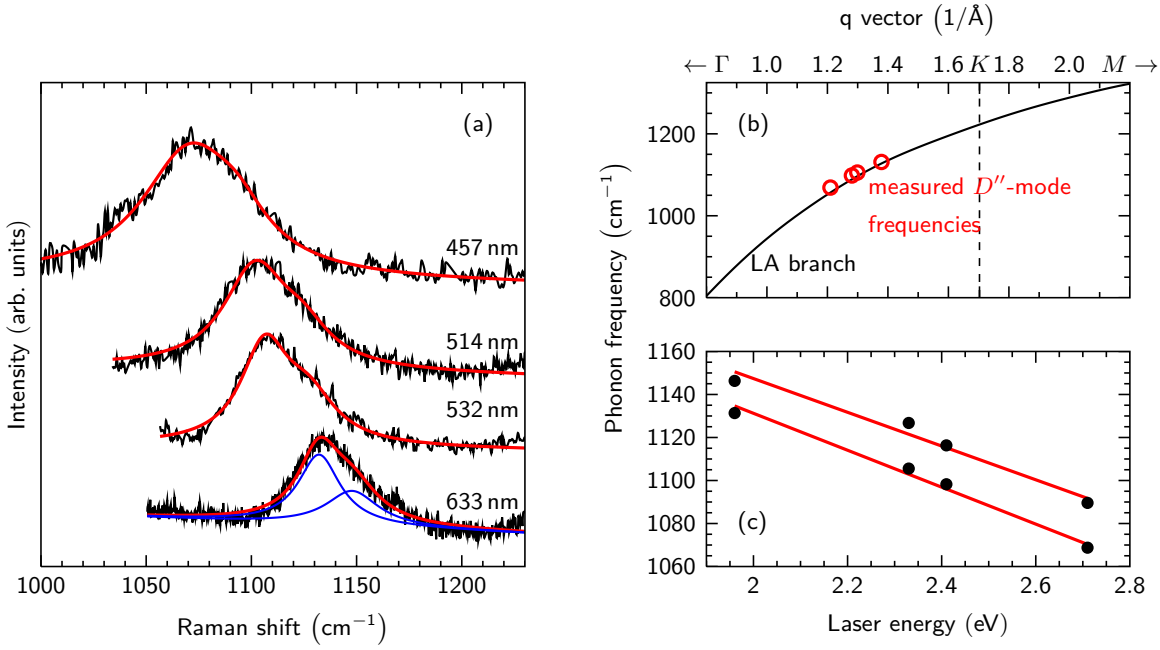

Figure 5.14: (a) Raman spectra of the D'' mode in single-layer graphene for different laser excitation energies. The thick solid lines denote fits to the measured spectra. For the spectra recorded at 633 nm laser wavelength, we additionally show both Lorentzian contributions of the D'' mode. (b) Comparison of the measured D''-mode frequencies and the LA phonon dispersion along $\mathbf{\Gamma}-\mathbf{K}-\mathbf{M}$. (c) Dispersion of the two D''-mode contributions with laser excitation energy. The solid line denotes a linear fit to the data points with a slope of approximately $-80\,\mathrm{cm}^{-1}/\mathrm{eV}$.

5 % along $\mathbf{\Gamma}-\mathbf{K}$. Especially close to $\mathbf{\Gamma}$, the slope of the LA phonon branch is reproduced very accurately. Since phonons around $\mathbf{\Gamma}$ influence heat dissipation and electron transfer most, a reliable extrapolation in this region is of high interest.

We will now turn our discussion to the lineshape of the D'' mode in Fig. 5.14 (a). Here, we can notice two things. First, the D'' mode shows a pronounced asymmetry towards higher frequencies and second, the FWHM of the D'' mode increases by increasing the laser excitation energy. The asymmetric tail can be seen in all spectra very clearly. This asymmetry of the D'' mode is explained with the two-dimensional phonon dispersion of the LA branch around the $\mathbf{K}$ point. As can be seen in Fig. 5.16, the LA phonon branch shows a non-constant angular frequency dependence around the $\mathbf{K}$ point, *i.e.*, the lowest frequencies can be found along $\mathbf{K}-\mathbf{\Gamma}$ and the highest along $\mathbf{K}-\mathbf{M}$ [142]. The triangular-shaped contour in Fig. 5.16 marks the region of the resonant phonon wave vectors in the double-resonance process at approximately 2.3 eV laser excitation energy. We can now directly see that the main contributions to the D'' mode must stem from phonons along the $\mathbf{\Gamma}-\mathbf{K}$ line. The asymmetric tail can be assigned to phonons next to this high-symmetry direction in the Brillouin zone, following the analysis of May *et al.* [142]. Phonons next to the high-symmetry direction contribute significantly less to

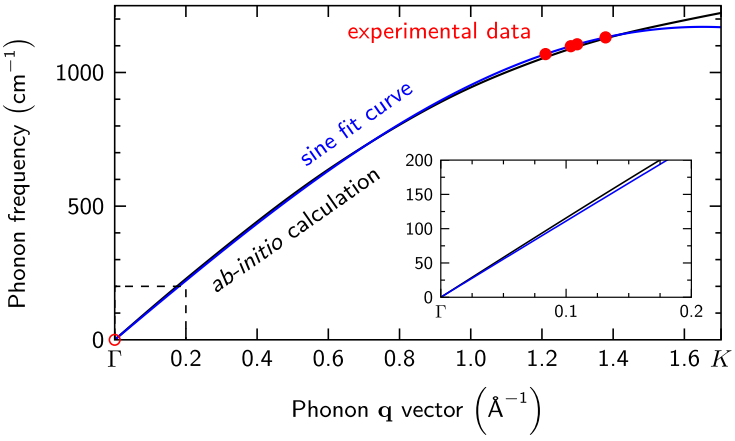

Figure 5.15: Comparison of the *ab-initio* calculated LA branch (black curve) and the sine fit (blue curve) together with the experimental data (red points).

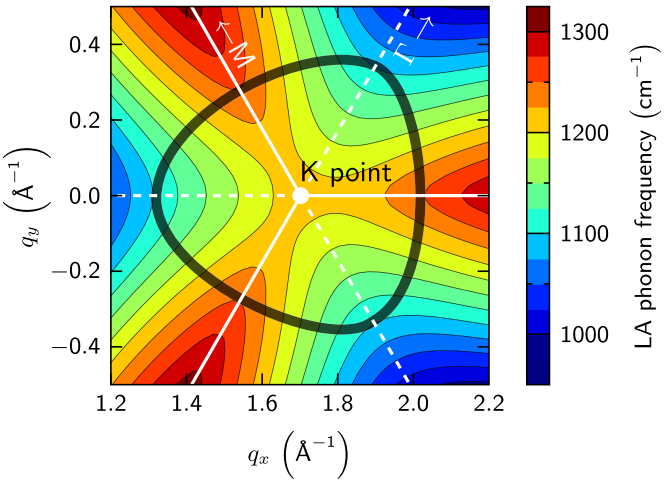

Figure 5.16: Two-dimensional phonon dispersion of the LA branch in graphene around the **K** point. Solid and dashed lines label the $\mathbf{K}-\mathbf{M}$ and $\mathbf{K}-\mathbf{\Gamma}$ directions, respectively. The triangular-shaped contour highlights the region, where the resonantly enhanced phonons stem from in a double-resonance process at approximately 2.3 eV laser excitation energy. Data was provided by P. Venezuela.

the D'' mode than phonons directly on the $\mathbf{\Gamma}-\mathbf{K}$ line. This can be understood from the strong angular dependence of the electron-phonon coupling for the LA phonon branch and the optical matrix elements around the **K** point [142, 190]. Both quantities show an angular dependence so that inner processes, with optical excitations along $\mathbf{K}-\mathbf{M}$ and resonant phonons from $\mathbf{K}-\mathbf{\Gamma}$, are favored. The same holds, for example, for the D and $2D$ mode, however, the involved TO phonon branch does not exhibit a comparable angular frequency dependence as the LA branch. The second thing to notice is the broadening of the lineshape at larger excitation energies. This effect can be easily explained by considering the slope of the LA branch along $\mathbf{K}-\mathbf{\Gamma}$, which observes a steeper dispersion at larger distances from **K** [see Fig. 5.13 (b)]. Therefore, at shorter resonant phonon wave-vectors, *i.e.*, for larger excitation energies, a larger frequency range can be accessed, leading to a broadening of this Raman mode. Furthermore, the electronic broadening in the double-resonance process increases with increasing laser energy, resulting in a further broadening of the resonance (compare Chapter 4.7). Similar observations, both theoretically and experimentally, were made for the $D+D''$ mode at approximately 2450 cm^{-1} in the Raman spectrum of single-layer graphene [142].

The comparison of our measured D''-mode spectra with calculations from Venezuela *et al.* (compare Ref. [47], Fig. 11) shows very good agreement, both qualitatively and quantitatively. The

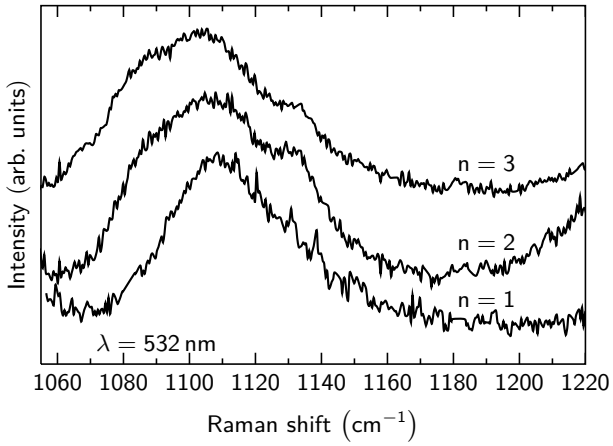

Figure 5.17: D''-mode spectra at 532 nm laser wavelenghts for single-, bi-, and trilayer graphene. The broadening of the D'' mode in bi- and trilayer graphene can be clearly seen.

prediction of an asymmetric high-frequency tail was confirmed by our measurements. Also the absolute frequencies match with the experimentally observed.

Figure 5.17 shows D''-mode spectra at 2.33 eV laser excitation energy for different numbers of graphene layers. As can be seen very clearly, the lineshape significantly broadens when going from single- to bilayer graphene. This broadening can be directly attributed to the evolution of the electronic bandstructure around the **K** point. Since bilayer graphene has two valence and conduction bands, the number of resonant scattering processes is quadrupled compared to single-layer graphene (compare Chapter 4 of this thesis). The increased number of resonant phonon wave vectors leads to an increased number of resonantly enhanced phonons, thus, resulting in a broadening of the Raman mode. This effect can be also observed for the $D + D''$ mode in bilayer graphene [142], as well as for the $2D$ mode [46, 122]. By further increasing the layer number, the lineshape does not show any noticeable changes in linewidth or by the appearance of additional peaks. This can be again identified with the shape of the electronic bands around **K**. The bandstructure of trilayer graphene can be regarded as a superposition of the electronic bands of single and bilayer graphene [73]. Thus, also the resonant phonon wave-vectors in the double-resonance process are very similar to the ones from single and bilayer graphene. Therefore, the D''-mode lineshape in trilayer graphene does not differ from the peak observed in bilayer graphene. One could also argue that the evolution of the phonon dispersion in fewlayer graphene accounts for the broadening of the D'' mode. However, the LA phonon branches in bi- and trilayer graphene are still degenerate [150] and thus, would not result in a broadened D''-mode lineshape.

5.4.4 Analysis of the D'' mode in carbon nanotubes

Similar to graphene, only a few publications have reported double-resonant Raman modes in carbon nanotubes that involve LA phonons [237–240]. Besides intravalley scattering with LO and LA derived phonons, also intervalley combinational modes of TO and LA derived phonons were reported [238–241]. However, double-resonance processes containing both a defect and an LA phonon have not been reported so far in carbon nanotubes.

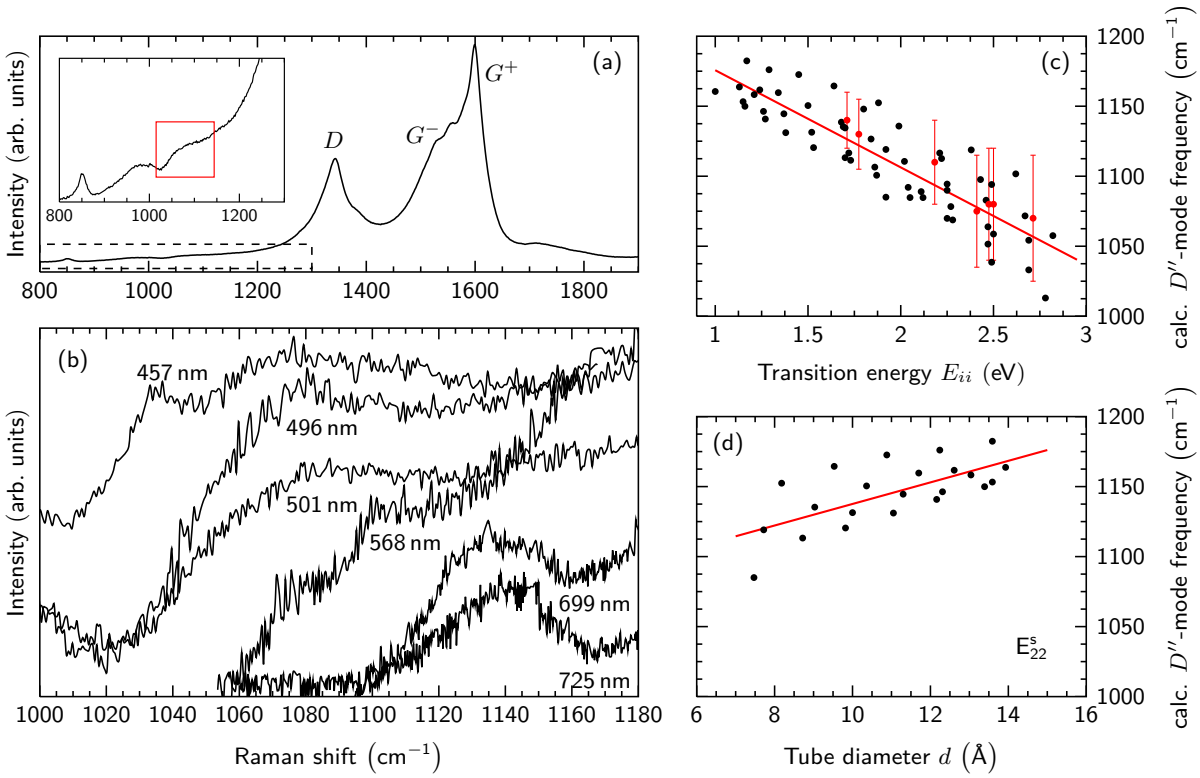

Figure 5.18: (a) Overview Raman spectrum of HiPco carbon nanotubes at 514 nm laser wavelength. The inset shows an enlarged view of the D''-mode region; the D'' mode is marked with the red rectangle. (b) Raman spectra of the D'' mode in carbon nanotubes for different laser excitation energies. Spectra are vertically offset for clarity. (c) Calculated D''-mode frequencies for carbon nanotubes in the diameter range between 7 Å and 14 Å. The red data points correspond to experimentally obtained D''-mode frequencies from (a); the error bars indicate the approximate peak width. (d) Calculated frequencies as a function of the tube diameter for the semiconducting E_{22} transition. The solid, red lines in (c) and (d) represent linear fits to the calculated data points. Raman spectra were measured by Christoph Tyborski (TU Berlin).

Figure 5.18 (b) presents Raman spectra of the D'' mode in carbon nanotubes at six different laser excitation energies. As discussed in Chapter 5.3, the D mode in carbon nanotubes exhibits a broader lineshape compared to graphene [58]. Therefore, the D'' mode can only be observed as a low-frequency shoulder to the D mode [compare Fig. 5.18 (a)]. From the experimental spectra we estimate a downshift of the D'' mode of approximately $-75\,\mathrm{cm}^{-1}/\mathrm{eV}$ with higher laser excitation energies. In contrast to graphene, we do not observe an asymmetric lineshape but rather a complex peak structure with many different contributions. This can be understood by keeping in mind that the Raman spectrum of carbon nanotubes results from many tubes in or close to resonance with the excitation laser. The analyzed HiPco sample contains a large variety of carbon nanotubes with diameters around 10 Å. Therefore, the D''-mode lineshape is broadened by the different contributions of carbon nanotubes in or close to resonance. However,

an assignment of the different features in the D'' band to distinct carbon nanotubes is not possible because of two reasons: the large number of different carbon nanotubes analyzed and the very low intensity of the D'' band.

In order to derive a systematic analysis, we present calculated D''-mode frequencies for all carbon nanotubes in the diameter range between 7 Å and 14 Å, comparable to the diameter distribution in our sample. The calculation is based on a sixth-nearest neighbor tight-binding model with symmetry-imposed modifications for carbon nanotubes using the POLSym code [95]. The calculated LA phonon branch is scaled in frequency by 5.1 %, such that the LA phonon frequency in CNTs with large diameters ($d \approx 25$ Å) fit the experimentally observed value at the **K** point for graphite [149]. The resonant phonon wave vectors in the double-resonance process were obtained by the approach presented in Chapter 5.3. Similar to graphene, the oscillator strength for optical transitions in carbon nanotubes is highest along the wavevectors derived from the $\mathbf{K} - \mathbf{M}$ direction in the graphene Brillouin zone [223, 242]. Therefore, the Raman spectrum is dominated by carbon nanotubes, where these transitions are probed, *e.g.*, the $\nu = -1$ family for the semiconducting E_{22} transition. Thus, we restrict our calculations to those transitions. The calculated D''-mode frequencies in Fig. 5.18 (c) reproduce the experimentally observed peak positions and peak shift very well. The calculated shift rate of $-70\,\mathrm{cm}^{-1}/\mathrm{eV}$ is in reasonable agreement with the experiments. As can be seen in Fig. 5.18 (c), the calculated D''-mode frequencies at each laser energy cover a large frequency range of approximately $40\,\mathrm{cm}^{-1}$, in accordance with the experimentally observed broad lineshape of the D'' mode in carbon nanotubes [compare with experimental data in Fig. 5.18 (c)]. As explained before, this broad lineshape is due to different carbon nanotubes in or close to resonance with the laser excitation energy. Fig. 5.18 (d) shows the calculated D''-mode frequencies as a function of the tube diameter for the semiconducting E_{22} transition (all other transitions show the same behavior). We observe an upshift of approximately $7\,\mathrm{cm}^{-1}/\text{Å}$ with increasing tube diameter. Since the LA phonon branch itself shows nearly no dependence on the tube diameter [95, 222], the observed diameter dependence basically reflects the diameter dependence of the optical transition energies.

5.4.5 Summary

In summary, we presented experimental Raman spectra of the D'' mode in graphene and carbon nanotubes at different laser excitation energies. We showed that this mode results from double-resonant intervalley scattering of LA phonons with defects and has a dispersion of $-80\,\mathrm{cm}^{-1}/\mathrm{eV}$ in single-layer graphene. We demonstrated that the D'' must stem from inner scattering processes with additional contributions from phonons next to the $\mathbf{\Gamma} - \mathbf{K}$ direction, explaining the observed high-frequency tail of this Raman mode. We further showed that the lineshape in graphene depends on the layer number, reflecting the evolution of the electronic bands around **K**. In carbon nanotubes, the lineshape of the D'' mode is significantly broadened due to contributions from different tubes in or close to resonance with the excitation laser. Our theoretical calculations of this Raman mode in carbon nanotubes showed very good agreement with the ex-

perimental data. Our analysis shows that acoustic phonons can indeed be studied by an optical method, namely double-resonant Raman spectroscopy.

5.5 *In-situ* Raman study of laser-induced graphene oxidation

This last part of the chapter will report on an *in-situ* study of high-power laser irradiation on exfoliated single-layer graphene and the subsequent observation of graphene oxidation.

5.5.1 Introduction

As already pointed out many times in this thesis, graphene and related two-dimensional materials, such as transition metal dichalcogenides, have experienced increasing scientific interest during the last decade [2–4]. However, despite graphene's extraordinary high charge-carrier mobility [1], the lack of an intrinsic bandgap prevents this material from integration in transistors and logic devices. A possible route to overcome this limitation is the precise and controllable modification of graphene's electronic properties using, for instance, oxidation or hydrogenation [243–252]. Selective functionalization may also offer the possibility to design artificial graphene structures with tailored properties. In fact, it has been demonstrated that oxidation of graphene may open a bandgap [253]. Furthermore, methods that are based on optical manipulation of graphene's properties have presented themselves as a versatile technique [245, 246, 253, 254]. However, the precise temporal evolution of graphene photo-oxidation has not been reported so far and thus prevents a deeper understanding of this process.
In this last part of the chapter, we present an *in-situ* Raman study of the oxidation process in mechanically exfoliated single-layer graphene. We demonstrate that the oxidation process can be selectively initiated by high-power laser irradiation. Subsequently, we observe the temporal dependence of the G- and $2D$-mode peak position and identify two different processes during laser irradiation, namely, tensile strain due to laser-induced heating and subsequent p-type doping due to oxidation. During oxidation, we observe a strong variation of the D/G-mode ratio and the background intensity. Both observations can be consistently explained within the presented model. Finally, we discuss AFM measurements of the irradiated single-layer graphene and demonstrate the possibility of sub-μm patterning in graphene.

5.5.2 Experimental details

Single-layer graphene samples were prepared by mechanical exfoliation of natural graphite crystals onto silicon substrates with an 100 nm thick oxide layer. Raman measurements were carried out using a Horiba HR800 spectrometer equipped with a Nd:YAG laser with 532 nm emission wavelength. The *in-situ* measurements were performed in ambient conditions with a time resolution of approximately 1 s over a period of more than 2000 s. We used a 600 lines/mm grating in order to record all important Raman modes within the same spectral window at each time frame. The laser power was chosen to be 40 mW on the sample. Raman maps with low laser power after irradiation were obtained by a motorized xyz stage with a minimum step size of 250 nm and using a laser power of less than 1 mW in order to avoid sample heating or additional structure modifications of the graphene layer.

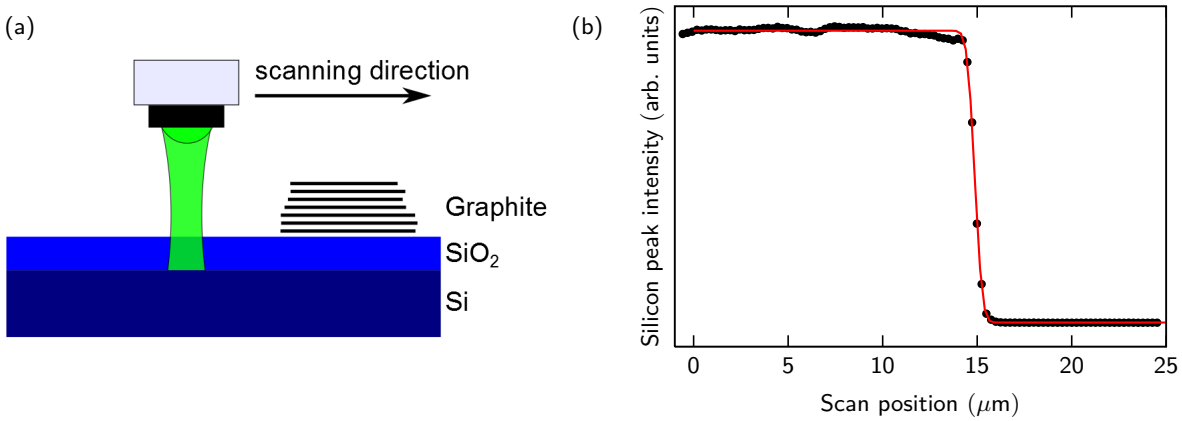

Figure 5.19: (a) Illustration of the experimental approach to estimate the laser spot size by a linescan across a thick graphite flake. (b) Intensity of the silicon peak at 520 cm^{-1} as function of the linescan position. The red, solid line reflects a least-square fit according to Eq. (5.5).

The laser-spot diameter (full width at half maximum - FWHM) in our studies was estimated from a simple, straight-forward measurement. We performed a linescan across the edge of a thick graphite flake on a SiO_2/Si substrate and recorded the intensity of the silicon Raman signal [compare Fig. 5.19 (a)]. The decrease of the silicon signal at the graphite edge gives a good estimate of the laser spot size. The spatially varying silicon signal was fitted by a cumulative distribution function, *i.e.*, the convolution of a Gaussian curve and a Theta function:

$$f(x, \mu, \sigma, I) = y_0 + \frac{I}{2} \times \left[1 - \mathrm{erf}\left(\frac{x-\mu}{\sqrt{2\,\sigma^2}}\right)\right]. \tag{5.5}$$

Here, y_0 is a constant offset, I is the maximum intensity, μ reflects the graphite edge position, and σ^2 is usually referred to as the variance of the distribution function. The laser-spot size d and σ are connected via

$$d = 2\sqrt{2\,\ln 2}\,\sigma.$$

At 532 nm laser wavelength with a power of 40 mW and using a 100x objective (NA = 0.90), we determine a FWHM of the laser spot size of approximately 750 nm.
Atomic force microscopy (AFM) images were recorded in true non-contact mode using a Park Systems XE 100 AFM. All measurements were performed in ambient conditions and at room temperature. AFM images were processed using the WSxM software [255].

5.5.3 Results and discussion

Figure 5.20 presents two Raman spectra measured at different times during laser irradiation with 40 mW laser power. We want to explicitly point out that the spectra are not scaled nor vertically offset in intensity. As can be seen, the spectrum at $t = 65$ s only exhibits the well-

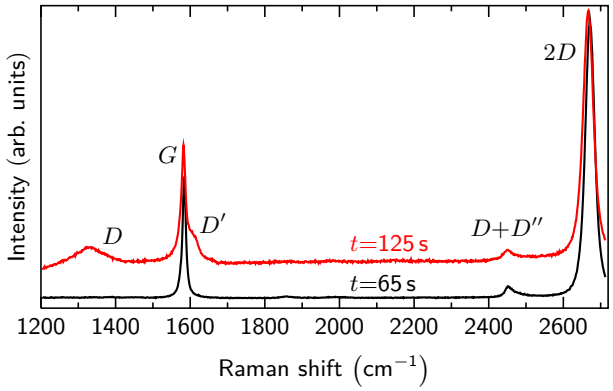

Figure 5.20: Raman spectra of exfoliated single-layer graphene under high-power laser irradiation at different times as given next to the spectra. The main characteristic Raman modes are labeled next to their positions. Spectra are not scaled nor vertically offset.

known Raman modes in exfoliated single-layer graphene, *i.e.*, the first-order G mode, as well as the double-resonant $D+D''$ (iTOLA) and $2D$ modes. Spectra that were recorded for irradiation times $t < 65\,\mathrm{s}$ did not showed significant differences compared to the spectrum at $t = 65\,\mathrm{s}$. However, for measurement times larger than 65 s we observe a strong increase of the background intensity, as can be seen for the spectrum at 125 s. Furthermore, we observe the occurrence of the defect-induced double-resonant D and D' Raman modes at $\sim 1345\,\mathrm{cm}^{-1}$ and $\sim 1615\,\mathrm{cm}^{-1}$, respectively. In contrast to most previous works, we will not limit our measurements on single or very few Raman measurements to assess and analyze spectral changes during the oxidation process. In fact, single measurements may only enable a snap shot of the different effects and thus prevent a thorough analysis of the oxidation process. The careful analysis of spectral changes as a function of irradiation time allows to extract even more information about the oxidation process from the measured Raman spectra, as will be shown below.

In Figure 5.21 (a), we present the evolution of the D/G-mode amplitude ratio in single-layer graphene with increasing time under high-power laser irradiation of 40 mW. As can be seen, until $t_1 = 65\,\mathrm{s}$ this ratio does not change. Afterwards, we observe an abrupt increase to a maximum value of approximately 0.27 at $t_2 = 300\,\mathrm{s}$, followed by a nearly linear decrease with increasing irradiation time. An enlarged view of the inital sharp increase is given in Fig. 5.21 (b). For irradiation times larger than $t_4 \approx 1000\,\mathrm{s}$, the Raman spectrum of the graphene layer inside the laser spot nearly resembles the initial Raman spectrum at $t_0 = 0\,\mathrm{s}$, *i.e.*, the D/G-mode ratio drops to values of less than 0.01. The main difference between the spectra at t_0 and t_4 is a significantly reduced $2D/G$-mode ratio of approximately 1.5 at t_4 and a downshifted $2D$-mode position, which will be discussed later in this section. The broadening and downshift of the $D + D''$ mode follows the evolution of the $2D$ mode. The corresponding spectra for each time t_i from Fig. 5.21 (a) are given in Figs. 5.21 (c) and (d) for the G- and $2D$-mode spectral range, respectively. Again, we want to explicitly point out that the spectra are not scaled in intensity nor vertically offset.

As already pointed out before, we also observe a strong variation of the background intensity during the oxidation process. The differences can be seen best by comparing the black spectrum at t_1 and the blue spectrum at t_2 in Fig. 5.21 (c). In Figure 5.21 (a), we also plot the background intensity as a function of the irradiation time. Qualitatively, the same behavior as for the D/G-

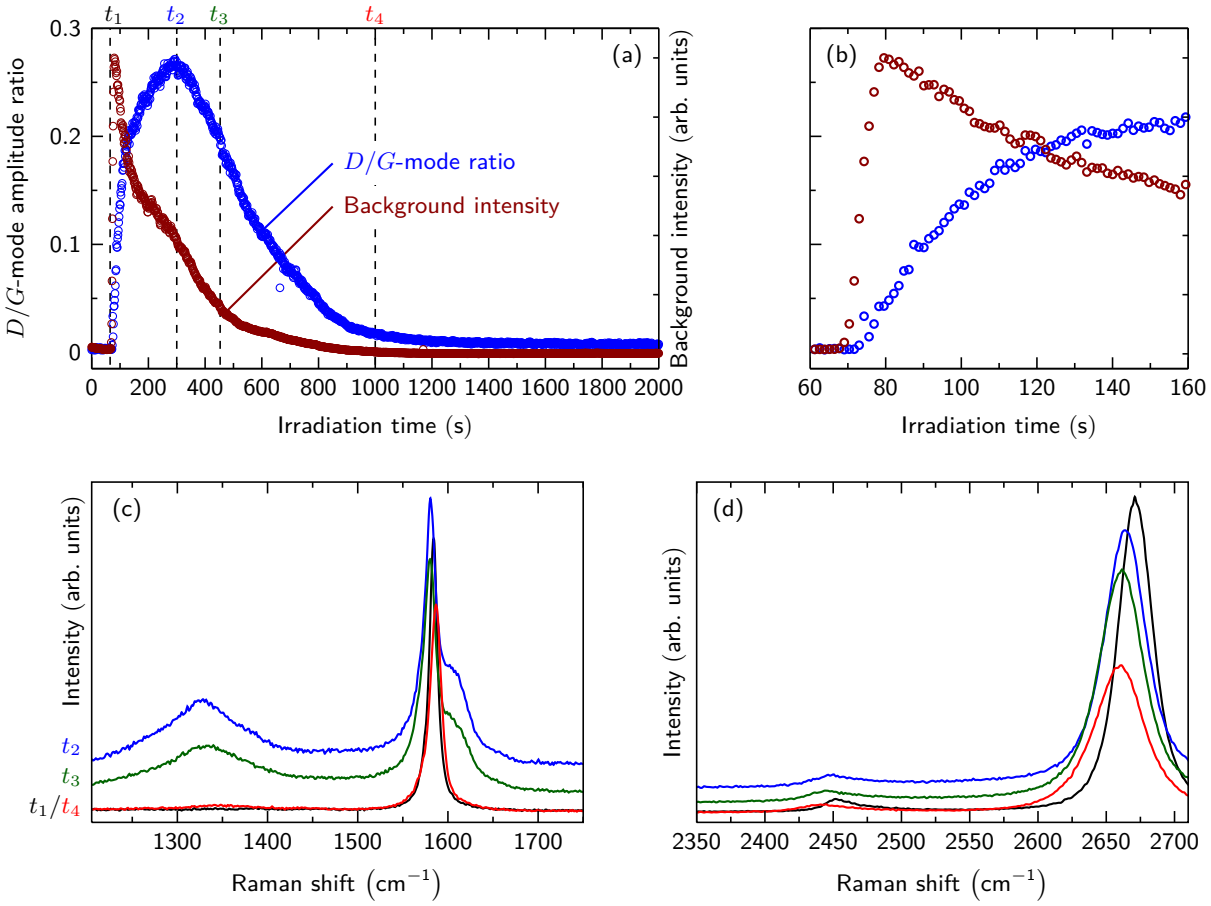

Figure 5.21: (a) Evolution of the D/G-mode amplitude ratio (blue circles) and the background intensity (red circles) in single-layer graphene with increasing irradiation time using high-power laser irradiation of 40 mW. (b) Enlarged view of the initial sharp increase in background intensity and D/G-mode ratio; same y-axis scales as in (a). (c),(d) Raman spectra in the G- and $2D$-mode spectral range for different irradiation times t_i as defined in (a). Spectra are not scaled in intensity nor vertically offset.

mode ratio is observed, *i.e.*, a first sharp increase in intensity followed by a continuous decrease back to the initial level. However, the background intensity rises and drops more abruptly than the D/G-mode ratio. Furthermore, we observe the increase in background intensity slightly before the D/G ratio starts rising. In fact, the inflection point of the background-intensity curve, *i.e.*, the point where the slope has reached the maximum value and starts decreasing, coincides with the point where we observe the initial increase of the D/G-mode ratio [compare Fig. 5.21 (b)]. This may indicate that the origin of these effects are two competing processes. We attribute the strong and spectrally broad background in our spectra to luminescence from recombination of thermalized electron-hole pairs [256, 257]. By starting the laser irradiation of our single-layer graphene sample, we effectively start heating the graphene layer. Furthermore, we also start heating the silicon substrate underneath. However, the graphene layer and the silicon substrate are separated by 100 nm of silicon dioxide. Since SiO_2 is an amorphous, wide-bandgap

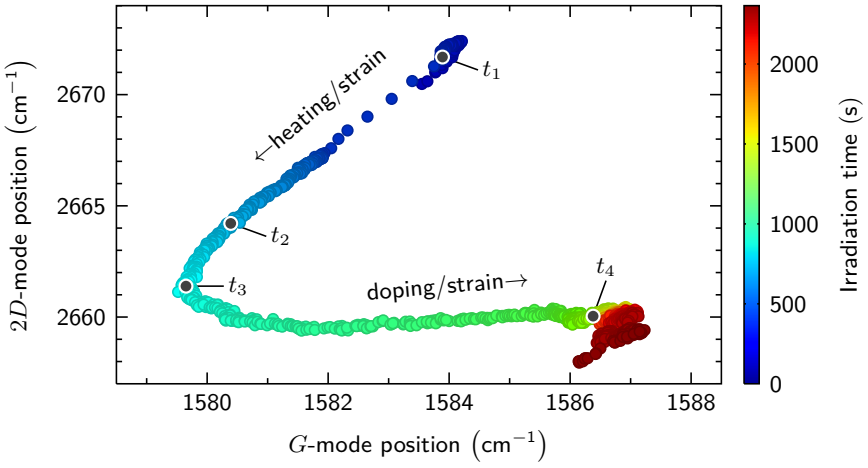

Figure 5.22: Time evolution of the $2D$-mode position as a function of the G-mode position. Characteristic times from Fig. 5.21 (a) are marked with gray, filled circles and labeled with t_i.

insulator with a low thermal conductivity of approximately 1 W/(m·K) [258], the graphene layer is shielded from the heat of the silicon substrate at short irradiation times. However, at a certain time t the heat from the Si substrate will reach the SiO_2 surface and additionally heat the graphene layer. The exact value of t differed in our measurements and ranged from less than 10 s to more than 60 s. Obviously, the value of t does not only depend on the SiO_2 thickness, but might be also influenced by a precise laser focus on the graphene layer and/or the initial conformation of the graphene layer on the SiO_2/Si substrate. Nevertheless, as the heat from the silicon substrate reaches the SiO_2 surface, this will introduce short-range distortions and buckling in the graphene layer [247]. Thus, the local curvature of the graphene layer will increase, which drastically enhances the hot-carrier emission efficiency [257]. For instance, Chen *et al.* demonstrated that graphene nanospheres with diameters of approximately 300 nm show an increase in hot-carrier luminescence by more than one order of magnitude compared to flat graphene [257]. Therefore, the first sharp increase in background intensity is given by the time, when the heat from the silicon substrate reaches the SiO_2 surface and graphene straining and buckling begins. In the following, the background intensity drops, while the D/G-mode ratio increases, *i.e.*, defects are created. The decreasing background can be understood from the fact that the contribution from carrier-defect scattering increases and thus reduces the number of excited charge carriers. Furthermore, the creation of defects leads to a reduction of the local curvature of the graphene layer and therefore lowers the hot-luminescence emission efficiency. For $t > 700$ s, the background intensity has dropped below 5 % of its maximum value.

We will now turn to a discussion of the G- and $2D$-mode positions. Figure 5.22 plots the peak positions of both Raman modes for all data points with $t \leq 2365$ s; the time order of the data is indicated by the different colors of the points. For times larger than t_4, we observe only minor peak shifts that can be attributed to further increasing tensile strain. As can be seen, for irradiation times between t_1 and t_3 both the G- and $2D$-mode frequencies decrease linearly with

a slope of approximately $\Delta\omega(2D)/\Delta\omega(G) = 2.2$. A slope with this value is commonly identified with uniaxial or biaxial tensile strain [36, 37, 259, 260]. However, keeping in mind that strain in our experiment is introduced by the laser beam itself, biaxial or radial strain is most likely to occur. Using a strain-induced G-mode shift rate of $-50\,\mathrm{cm}^{-1}/\%$ [260, 261], we calculate a strain difference of $\Delta\epsilon \approx 0.1\,\%$ between t_1 and t_3. The linear decrease of the Raman modes between t_1 and t_3 due to tensile strain can be attributed to laser-induced heating of the graphene flake and the silicon substrate underneath [262–264]. Assuming that the observed G-mode shift is due to temperature and using the thermal-expansion coefficient of graphene on SiO_2/Si of $-0.016\,\mathrm{cm}^{-1}/^{\circ}\mathrm{C}$ [262], we estimate a temperature increase of approximately 250 K inside the laser spot during irradiation at t_3. For irradiation times larger than t_3, the G mode upshifts again, whereas the $2D$ mode shows a nearly constant peak position with only slight increase. The slope of these data points exhibits a value of approximately $\Delta\omega(2D)/\Delta\omega(G) = 0.1$. Since this slope does not fit to either purely n-type or purely p-type doping [154, 259, 265], we suggest that the measured slope is a superposition of doping and strain effects. In fact, it is very reasonable that the tensile strain further increases from t_3 to t_4. This assumption is supported by the evolution of the $2D$- and G-mode positions for times larger than t_4, which indicate additional tensile strain. Thus, the observed evolution of the G- and $2D$-mode positions between t_3 and t_4 is most likely a superposition of tensile strain and doping effects. Ergo, without additional tensile strain, the slope of the data points between t_3 and t_4 would be larger. Since the experiments were performed in ambient conditions, functionalization by oxygen is very likely to occur. This would lead to p-type doping [247]. Similar observations were reported in previous works on laser-induced doping effects [266]. Graphene doping due to oxidation is further confirmed by the temporal evolution of the FWHM of the G mode. As can be seen in Fig. 5.23, the FWHM initially rises to a maximum value of approximately $19\,\mathrm{cm}^{-1}$. We expect that this first initial increase in FWHM is caused by the creation of defects. The time at which the maximum value occurs roughly coincides with t_3, *i.e.*, the time when the onset of doping can be observed. For increasing irradiation times between t_3 and t_4, we observe a decrease of the FWHM of the G mode, in accordance with doping [34]. For $t > t_4$, no significant changes in the FWHM of the G mode can be observed, indicating that the doping level has saturated to a maximum level. From the G-mode shift, we estimate a difference in carrier concentration between t_3 and t_4 of $\Delta n = 6 \times 10^{12}\,\mathrm{cm}^{-2}$ [259].

As discussed in Ref. [247], thermal annealing of graphene supported on SiO_2/Si substrates introduces short-range distortions to the graphene lattice and therefore facilitates oxygen binding. Oxygen functionalization is further catalyzed by the likely presence of a partial water layer between graphene and the substrate, as well as a water adlayer on top of graphene [248]. Following Refs. [247] and [248], the initially observed tensile strain results from a conformation of graphene to the SiO_2/Si substrate, leading to the creation of ripples. These surface ripples reduce the activation energy for oxygen binding [248]. Therefore, oxidation does not occur directly, but apparently needs a certain amount of strain to weaken the bonds and increase chemical reactivity [247]. Both effects can be clearly seen in Figure 5.22.

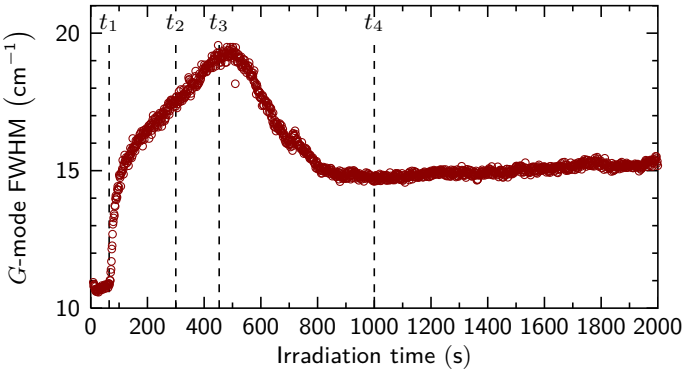

Figure 5.23: Time evolution of the G-mode FWHM during oxidation. Characteristic times t_i are marked with vertical dashed lines.

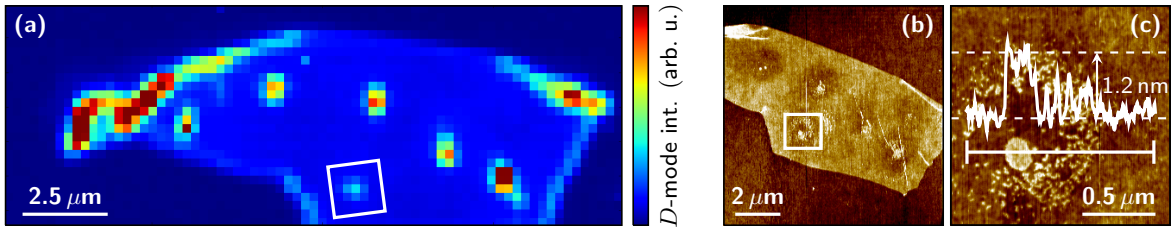

Figure 5.24: (a) Raman mapping of the D-mode intensity on a single-layer graphene flake that was treated by high-power laser irradiation. The irradiated regions can be identified as small circular spots. (b) Atomic-force microscopy image of the same flake as in (a). Again, the irradiated regions can be clearly identified as circular spots. (c) Enlarged view of the region that is marked in (a) and (b) by the white rectangle. The height profile has been recorded along the white, horizontal line. The height difference between graphene and the adsorbates is approximately 1.2 nm, which corresponds to the height of single-layer graphene oxide.

Finally, we want to comment on the unexpected decrease of the D/G-mode ratio with increasing irradiation time [see Fig. 5.21 (a)]. In principle, one would expect increasing defect-related Raman modes due to adsorption of molecules from the air and the progressing oxygen binding to the basal plane of graphene. However, we identify two processes that antagonize this expectation. First, laser-induced annealing inside the laser spot and, second, the doping dependence of the D/G-mode ratio. It has been reported by many different works that annealing of graphene and/or carbon nanotubes leads to a reduction of physisorbed adsorbates and thus a decrease of the D-mode intensity [248, 267, 268]. Since average temperatures inside our laser spot reach values of approximately 550 K, annealing and self-healing seems likely to occur [269]. Moreover, it has been experimentally demonstrated by Bruna *et al.* [171] and Froehlicher *et al.* [154] that the D/G-mode ratio depends strongly on the doping level in single-layer graphene, as already discussed in the introduction of this chapter. This effect can be understood from an increased electronic broadening in the D-mode double-resonance Raman process, resulting in a decrease in intensity [47, 168]. Moreover, for high doping levels, the G-mode intensity increases with either n- or p-type doping [105, 106]. Both effects lead to a reduction of the measured D/G-mode ratio in doped graphene. As we have undoubtedly demonstrated in Figure 5.22, we observe an

increasing doping level in our graphene layer with increasing irradiation time due to chemisorbed oxygen. Thus, a doping-related decrease of the D/G-mode ratio is reasonable. In total, these two effects, *i.e.*, annealing of physisorbed adsorbates and doping by chemisorbed oxygen, lead to a reduction of the D/G-mode ratio with increasing irradiation time although oxidation continues and probably creates further defects.

In Figure 5.24 (a), (b), and (c), we present a Raman map (1 mW laser power) of the D-mode intensity and AFM images of the same graphene flake that has been irradiated at different spatial positions. The AFM measurements were performed by E. Poliani and R. Mirzayev. The Raman map is composed of 1898 individual Raman spectra with a point-to-point distance of 250 nm. Inside the graphene flake, we can identify several regions that exhibit a significantly increased D-mode intensity compared to the surrounding regions. These regions correlate with the spatial positions, where we oxidized the graphene layer by high-power laser irradiation. The increased D-mode intensities at the left edge and at the top right corner correspond to regions of folded graphene [compare Fig. 5.24 (b)] and are not related to laser irradiation. Interestingly, we also observe a variation of the D-mode intensity at the different edges of the graphene flake, which can be understood from selective D-mode scattering at zig-zag and armchair edges [270]. However, we wont discuss this effect in more detail. In Figure 5.24 (b) we present an AFM image of the same graphene flake. We observe a close correspondence between the regions with high D-mode intensity and the structurally modified regions in the AFM image, *i.e.*, the laser-modified regions can be again identified as circular regions. The diameter of these regions is approximately 970 nm and in reasonable agreement with the experimentally determined laser spot size of 750 nm. Inside these regions, we observe small spots of laser-deposited material that show a drastically increased height compared to the surrounding area [see Figure 5.24 (c)]. The height of the laser-deposited material inside the laser spot is approximately 1.2 nm, which nicely coincides with the height of graphene oxide reported in literature [271]. This gives further evidence to laser-induced oxidation of our graphene samples on the sub-μm scale. Thus, by scanning the laser spot across the graphene flake, spatially controlled functionalization of graphene can be achieved. In principle, arbitrary structures can be realized, as demonstrated in similar experiments [246, 249, 250, 253].

We performed the same experiments on exfoliated bilayer graphene on SiO_2/Si substrates. However, only in a very limited number of measurements, *i.e.*, in less than 33 % of our experiments, we observed the same temporal evolution of the Raman modes as described above for single-layer graphene. Apparently, the bilayer graphene flake is more stable under high-power laser irradiation and less reactive to oxidation compared to the single-layer graphene flake. Similar observations were made in plasma-treated single and bilayer graphene [272, 273]. The reduced chemical reactivity of bilayer graphene can be understood from an increased van-der-Waals interaction in these systems [182]. In fact, a second graphene layer stabilizes the bilayer graphene and hinders an out-of-plane deformation and in-plane strains of the top graphene layer when oxidation occurs. Thus, bilayer graphene is stabilized by the internal van-der-Waals forces between the layers and is therefore chemically less reactive than single-layer graphene, in nice agreement with our experimental observations.

As a very last point, we want to give an outlook on future experiments regarding the laser-induced oxidation of graphene. To undoubtedly prove the oxidation of graphene, the presented experiments should be repeated in a controlled atmosphere of nitrogen or argon gas. Those experiments were already started, however, due to drawbacks of the experimental setup, laser powers were too low on the graphene sample to observe laser-induced oxidation even in normal air. Furthermore, measurements should be repeated with different substrates underneath the graphene, *e.g.*, silicon substrates with a thicker oxide layer or graphene on hexagonal boron nitride. Laser irradiation of graphene on silicon substrates with different oxide thicknesses is currently performed by R. Mirzayev at the University of Vienna. Preliminary results indicate that graphene on 300 nm SiO_2 requires a higher laser power on the sample to initiate the oxidation process compared to graphene on 90 nm SiO_2.

5.5.4 Summary

In summary, we demonstrated an *in-situ* analysis of the oxidation process in single-layer graphene. We showed that high-power laser irradiation in ambient conditions can be separated into two different stages; tensile strain due to laser-induced heating and subsequent p-type doping due to oxidation. The observed temporal decrease of the D/G-mode ratio with increasing irradiation time can be explained with laser-induced annealing and the doping dependence of the double-resonant D-mode scattering process. Our results provide a deeper understanding of basal-plane oxidation in graphene and demonstrate the possibility of tailoring graphene's properties selectively at the sub-μm scale using a fully optical method.

6 Conclusion

In this work, we analyzed both experimentally and theoretically double-resonant two-phonon and phonon-defect Raman modes in graphene, few-layer graphene and carbon nanotubes. Although the concept of double-resonant Raman scattering has been introduced more than a decade ago, the precise scattering processes of certain Raman modes were still controversially discussed. Here, we demonstrated a detailed analysis of various aspects of double-resonant Raman scattering in graphitic carbons and finally resolved fundamental questions concerning the different scattering processes.

The first part of this thesis was devoted to the analysis of the $2D$ mode in Bernal-stacked bilayer graphene. The characteristic and complex lineshape of the $2D$ mode in bilayer graphene was subject of different works that attempted an explanation of the different scattering processes. However, none of the presented models could reproduce or explain the correct lineshape of the $2D$ mode. Starting from a complete first-principles based calculation of the double-resonant Raman scattering cross-section, we provided a consistent explanation of the different processes and unraveled the dominant contributions to the peak structure. We proved that the $2D$ mode in bilayer graphene is composed of three dominant contributions, contradicting all previous works on this topic. We showed that the dominant contribution to the Raman scattering cross-section stems from so-called inner processes, as in single-layer graphene. We furthermore demonstrated that quantum interference between both anti-symmetric processes strongly affects the $2D$-mode lineshape in bilayer graphene, *i.e.*, the intensity of these contributions is drastically enhanced due to constructive interference. In fact, quantum interference is also key for the understanding of the lineshape variations as a function of the electronic broadening. We theoretically calculated and experimentally demonstrated that the characteristic lineshape of the $2D$ mode in bilayer graphene strongly depends on the electronic broadening. By tuning the laser excitation energy, the doping level, or the defect concentration, we showed that the $2D$-mode lineshape can be easily manipulated, reflecting the quantum mechanical character of double-resonant Raman scattering. Moreover, we also showed that the splitting between both TO phonon branches in bilayer graphene along $\mathbf{K} - \mathbf{\Gamma}$ is of great importance for a correct analysis of the $2D$-mode lineshape. We presented an approach to directly extract the TO phonon splitting from experimental Raman spectra. Furthermore, we showed that the splitting of the electronic bands can be also measured using the presented analysis. Finally, we discussed the polarization dependence

of the $2D$ mode and demonstrated that inner and outer processes can be partially selectively suppressed. Our results finally clarified the origin of the complex $2D$-mode lineshape in bilayer graphene and its dependencies on external perturbations.

The second part of this thesis was devoted to the analysis of double-resonant phonon-defect Raman modes. We started with an analysis of the D mode in carbon nanotubes. The diameter dependence of this Raman mode was discussed by various authors and different dependencies were experimentally demonstrated. Here, we attempted a harmonization all previous experimental results. First, we presented a geometrical model to describe the diameter and energy dependence of the resonant phonon wave-vector in the double-resonance process in carbon nanotubes. The presented approach is independent of the specific model used for the electronic bandstructure or phonon dispersion and is therefore universally valid. In the following, we applied our model to investigate the defect-induced D mode in chiral carbon nanotubes and calculate the D-mode frequency at their resonant optical transitions. We could show that small-diameter tubes exhibit a higher D-mode frequency in general and that higher resonant optical transitions exhibit a systematically higher D-mode frequency. Furthermore, we proved that the experimentally observed discontinuity between different transition branches is due to curvature effects that alter the dispersion of A_1-symmetry phonon branch around the $\mathbf{K}$ point. In analogy to other Raman modes in carbon nanotubes, *e.g.*, the RBM or the G mode, we showed that the D-mode frequencies are arranged in branches and families. The experimentally observed dispersion of the D mode can be understood as a superposition of D modes from different carbon nanotubes that come into resonance after each other. Our results finally harmonized the different previous experimental observations regarding the diameter dependence of the D mode in carbon nanotubes.

In the following, we analyzed the defect-induced D'' mode in graphene, few-layer graphene, and carbon nanotubes. We showed that this mode results from a double-resonant intervalley scattering process of longitudinal acoustic phonons with defects and has a dispersion of $-80\,\mathrm{cm}^{-1}/\mathrm{eV}$ in single-layer graphene. The characteristic asymmetric lineshape with a high-frequency tail is explained by the dominant contributions from inner scattering processes from the $\mathbf{\Gamma} - \mathbf{K}$ direction with additional contributions from phonons next to this high-symmetry direction. We further showed that the lineshape in graphene depends on the layer number, reflecting the evolution of the electronic bands around $\mathbf{K}$. In carbon nanotubes, the lineshape of the D'' mode is significantly broadened due to contributions from different tubes in or close to resonance with the laser excitation energy. Using our previously developed model for the analysis of the double-resonance process in carbon nanotubes, we observed very good agreement between our experimental data and the theoretically predicted D''-mode frequencies.

The last part of this thesis presented an *in-situ* analysis of the laser-induced oxidation process in single-layer graphene. We demonstrated that the oxidation process can be selectively initiated by high-power laser irradiation of graphene. By a careful analysis of the temporal evolution of the D, G and $2D$ modes, we showed that the laser-induced oxidation of graphene can be separated into two different stages, namely, tensile strain due to laser-induced heating and

subsequent p-type doping due to oxygen binding. The unexpected observation of a decreasing D/G-mode ratio with increasing irradiation time and progressing oxidation could be explained with laser-induced annealing, as well as by the doping dependence of the double-resonant D-mode scattering process. Our results provided a deeper understanding of basal-plane oxidation in graphene and demonstrated the possibility of tailoring graphene's properties selectively at the sub-μm scale using a fully optical method.

To finalize, we presented various aspects of double-resonant Raman scattering in graphene, few-layer graphene and carbon nanotubes. Our results emphasize the significance of inner processes and, even more important, demonstrate the quantum mechanical character of this second-order process, which becomes manifested by the interference between different scattering processes. The presented results have led to a fundamental understanding of the double-resonance process in graphene and carbon nanotubes and thus enable a precise analysis of other double-resonant Raman modes in these materials. Besides the various fundamental results that were demonstrated here, we also want to point out the pratical benefits that result from this work. We established a method to derive basic material parameters such as the TO phonon splitting or the electronic splitting in bilayer graphene from experimental data. Furthermore, also the dependence of the $2D$-mode lineshape on γ can be used in practical terms and adds another parameter for the interpretation of experimental Raman spectra. Finally, we presented an approach to selectively pattern graphene, which can be helpful for the engineering of artificial graphene structures in future industrial applications.

Future works on the double-resonance process in graphene may use the results presented in this work as a starting point for ongoing studies. For instance, it would be tempting to perform a detailed analysis of the double-resonance process in bulk graphite. Bilayer graphene and bulk graphite belong to the same symmetry group, however, the $2D$-mode lineshape of both materials looks completely different. In fact, bulk graphite exhibits an out-of-plane dispersion along the $\mathbf{\Gamma} - \mathbf{H}$ high-symmetry direction, which has to be considered for a careful analysis of double-resonant scattering processes in this material. Moreover, it would be interesting to further exploit the double-resonance process directly at the edge of graphene. In this context, bilayer graphene might be favored over single-layer graphene, since the Raman modes of bilayer graphene contain more information about fundamental material parameters, as demonstrated in our analysis of the $2D$ mode at the bilayer graphene edge. Related to these experiments, one might also investigate Raman processes at edges of freestanding graphene. Preliminary measurements have been already performed and reveal as significant difference in the D/G-mode ratio at the edges between suspended and supported graphene. Finally, one might be interested in further analyzing the influence of laser irradiation on graphene. Here, it would be reasonable to design an experimental setup with two laser paths, in order to separate both actions of manipulating and probing graphene's properties. Furthermore, this setup would also allow to investigate the spatial extents of the laser-induced changes around the laser focus.

List of Figures

Bibliography

[1] K. S. Novoselov, A. K. Geim, S. V. Morozov, D. Jiang, Y. Zhang, *et al.*, "Electric field effect in atomically thin carbon films", Science **306**, 666–669 (2004).

[2] A. H. Castro Neto, F. Guinea, N. M. R. Peres, K. S. Novoselov, and A. K. Geim, "The electronic properties of graphene", Rev. Mod. Phys. **81**, 109–162 (2009).

[3] A. K. Geim, "Graphene: Status and prospects", Science **324**, 1530–1534 (2009).

[4] Q. H. Wang, K. Kalantar-Zadeh, A. Kis, J. N. Coleman, and M. S. Strano, "Electronics and optoelectronics of two-dimensional transition metal dichalcogenides", Nature Nanotechnology **7**, 699–712 (2012).

[5] F. H. L. Koppens, T. Mueller, P. Avouris, A. C. Ferrari, M. S. Vitiello, and M. Polini, "Photodetectors based on graphene, other two-dimensional materials and hybrid systems", Nature Nanotechnology **9**, 780–793 (2014).

[6] G. Fiori, F. Bonaccorso, G. Iannaccone, T. Palacios, D. Neumaier, *et al.*, "Electronics based on two-dimensional materials", Nature Nanotechnology **9**, 768–779 (2014).

[7] K. I. Bolotin, K. J. Sikes, Z. Jiang, M. Klima, G. Fudenberg, *et al.*, "Ultrahigh electron mobility in suspended graphene", Solid State Communications **146**, 351–355 (2008).

[8] L. Banszerus, M. Schmitz, S. Engels, J. Dauber, M. Oellers, *et al.*, "Ultrahigh-mobility graphene devices from chemical vapor deposition on reusable copper", Science Advances **1** (2015).

[9] C. Lee, X. Wei, J. W. Kysar, and J. Hone, "Measurement of the elastic properties and intrinsic strength of monolayer graphene", Science **321**, 385–388 (2008).

[10] A. A. Balandin, S. Ghosh, W. Bao, I. Calizo, D. Teweldebrhan, F. Miao, and C. N. Lau, "Superior thermal conductivity of single-layer graphene", Nano Letters **8**, 902–907 (2008).

[11] Nobelprize.org, "The Nobel Prize in Physics 2010", `http://www.nobelprize.org/nobel_prizes/physics/laureates/2010/` (23. July 2015).

[12] L. D. Landau, "Zur Theorie der Phasenumwandlungen II", Physikalische Zeitung der Sowjetunion **11**, 26–35 (1937).

[13] N. D. Mermin, "Crystalline order in two dimensions", Phys. Rev. **176**, 250–254 (1968).

[14] N. D. Mermin and H. Wagner, "Absence of ferromagnetism or antiferromagnetism in one- or two-dimensional isotropic Heisenberg models", Phys. Rev. Lett. **17**, 1133–1136 (1966).

[15] J. C. Meyer, A. K. Geim, M. I. Katsnelson, K. S. Novoselov, T. J. Booth, and S. Roth, "The structure of suspended graphene sheets", Nature **446**, 60–63 (2007).

[16] H. W. Kroto, J. R. Heath, S. C. O'Brien, R. F. Curl, and R. E. Smalley, "C60: Buckminsterfullerene", Nature **318**, 162–163 (1985).

[17] S. Iijima, "Helical microtubules of graphitic carbon", Nature **354**, 56–58 (1991).

[18] A. K. Geim and K. S. Novoselov, "The rise of graphene", Nature Materials **6**, 183–191 (2007).

[19] K. S. Novoselov, A. K. Geim, S. V. Morozov, D. Jiang, M. I. Katsnelson, *et al.*, "Two-dimensional gas of massless Dirac fermions in graphene", Nature **438**, 197–200 (2005).

[20] E. Hill, A. Vijayaragahvan, and K. Novoselov, "Graphene sensors", Sensors Journal IEEE **11**, 3161–3170 (2011).

[21] Y. Shao, J. Wang, H. Wu, J. Liu, I. Aksay, and Y. Lin, "Graphene based electrochemical sensors and biosensors: A review", Electroanalysis **22**, 1027–1036 (2010).

[22] Y.-M. Lin, K. A. Jenkins, A. Valdes-Garcia, J. P. Small, D. B. Farmer, and P. Avouris, "Operation of graphene transistors at gigahertz frequencies", Nano Letters **9**, 422–426 (2009).

[23] Y.-M. Lin, C. Dimitrakopoulos, K. A. Jenkins, D. B. Farmer, H.-Y. Chiu, A. Grill, and P. Avouris, "100-GHz transistors from wafer-scale epitaxial graphene", Science **327**, 662 (2010).

[24] E. Yoo, J. Kim, E. Hosono, H.-s. Zhou, T. Kudo, and I. Honma, "Large reversible Li storage of graphene nanosheet families for use in rechargeable Lithium ion batteries", Nano Letters **8**, 2277–2282 (2008).

[25] K. S. Novoselov, V. I. Fal'ko, L. Colombo, P. R. Gellert, M. G. Schwab, and K. Kim, "A roadmap for graphene", Nature **490**, 192–200 (2012).

[26] F. Schedin, A. K. Geim, S. V. Morozov, E. W. Hill, P. Blake, M. I. Katsnelson, and K. S. Novoselov, "Detection of individual gas molecules adsorbed on graphene", Nature Materials **6**, 652–655 (2007).

[27] W. Yuan and G. Shi, "Graphene-based gas sensors", J. Mater. Chem. A **1**, 10 078–10 091 (2013).

[28] W. J. Yu, Y. Liu, H. Zhou, A. Yin, Z. Li, Y. Huang, and X. Duan, "Highly efficient gate-tunable photocurrent generation in vertical heterostructures of layered materials", Nature Nanotechnology **8**, 952–958 (2013).

[29] K. F. Mak, C. Lee, J. Hone, J. Shan, and T. F. Heinz, "Atomically thin MoS_2: A new direct-gap semiconductor", Phys. Rev. Lett. **105**, 136 805 (2010).

[30] C. R. Dean, L. Wang, P. Maher, C. Forsythe, F. Ghahari, *et al.*, "Hofstadter's butterfly and the fractal quantum Hall effect in moiré superlattices", Nature **497**, 598–602 (2013).

[31] A. C. Ferrari and D. M. Basko, "Raman spectroscopy as a versatile tool for studying the properties of graphene", Nat. Nanotechnol. **8**, 235–246 (2013).

[32] M. Lucchese, F. Stavale, E. M. Ferreira, C. Vilani, M. Moutinho, *et al.*, "Quantifying ion-induced defects and Raman relaxation length in graphene", Carbon **48**, 1592 – 1597 (2010).

[33] L. G. Cançado, A. Jorio, E. H. M. Ferreira, F. Stavale, C. A. Achete, *et al.*, "Quantifying defects in graphene via Raman spectroscopy at different excitation energies", Nano Letters **11**, 3190–3196 (2011).

[34] S. Pisana, M. Lazzeri, C. Casiraghi, K. S. Novoselov, A. K. Geim, A. C. Ferrari, and F. Mauri, "Breakdown of the adiabatic Born-Oppenheimer approximation in graphene", Nature Materials **6**, 198 – 201 (2007).

[35] A. Das, B. Chakraborty, S. Piscanec, S. Pisana, A. K. Sood, and A. C. Ferrari, "Phonon renormalization in doped bilayer graphene", Phys. Rev. B **79**, 155 417 (2009).

[36] T. M. G. Mohiuddin, A. Lombardo, R. R. Nair, A. Bonetti, G. Savini, *et al.*, "Uniaxial strain in graphene by Raman spectroscopy: G peak splitting, Grüneisen parameters, and sample orientation", Phys. Rev. B **79**, 205 433 (2009).

[37] M. Mohr, K. Papagelis, J. Maultzsch, and C. Thomsen, "Two-dimensional electronic and vibrational band structure of uniaxially strained graphene from *ab initio* calculations", Phys. Rev. B **80**, 205 410 (2009).

[38] M. Mohr, J. Maultzsch, and C. Thomsen, "Splitting of the Raman 2D band of graphene subjected to strain", Phys. Rev. B **82**, 201 409 (2010).

[39] Y. Y. Wang, Z. H. Ni, T. Yu, Z. X. Shen, H. M. Wang, *et al.*, "Raman studies of monolayer graphene: The substrate effect", J. Phys. Chem. C **112**, 10 637–10 640 (2008).

[40] S. Piscanec, M. Lazzeri, F. Mauri, A. C. Ferrari, and J. Robertson, "Kohn anomalies and electron-phonon interactions in graphite", Phys. Rev. Lett. **93**, 185 503 (2004).

[41] J. Yan, Y. Zhang, P. Kim, and A. Pinczuk, "Electric field effect tuning of electron-phonon coupling in graphene", Phys. Rev. Lett. **98**, 166 802 (2007).

[42] C.-H. Park, F. Giustino, M. L. Cohen, and S. G. Louie, "Electron-phonon interactions in graphene, bilayer graphene, and graphite", Nano Letters **8**, 4229–4233 (2008).

[43] A. H. Castro Neto and F. Guinea, "Electron-phonon coupling and Raman spectroscopy in graphene", Phys. Rev. B **75**, 045 404 (2007).

[44] J.-U. Lee, D. Yoon, and H. Cheong, "Estimation of Young's modulus of graphene by Raman spectroscopy", Nano Letters **12**, 4444–4448 (2012).

[45] C. Thomsen and S. Reich, "Double resonant Raman scattering in graphite", Phys. Rev. Lett. **85**, 5214–5217 (2000).

[46] A. C. Ferrari, J. C. Meyer, V. Scardaci, C. Casiraghi, M. Lazzeri, *et al.*, "Raman spectrum of graphene and graphene layers", Phys. Rev. Lett. **97**, 187 401 (2006).

[47] P. Venezuela, M. Lazzeri, and F. Mauri, "Theory of double-resonant Raman spectra in graphene: Intensity and line shape of defect-induced and two-phonon bands", Phys. Rev. B **84**, 035 433 (2011).

[48] D. M. Basko, "Theory of resonant multiphonon Raman scattering in graphene", Phys. Rev. B **78**, 125 418 (2008).

[49] S. Berciaud, X. Li, H. Htoon, L. E. Brus, S. K. Doorn, and T. F. Heinz, "Intrinsic line shape of the Raman 2D-mode in freestanding graphene monolayers", Nano Letters **13**, 3517–3523 (2013).

[50] L. M. Malard, J. Nilsson, D. C. Elias, J. C. Brant, F. Plentz, *et al.*, "Probing the electronic structure of bilayer graphene by Raman scattering", Phys. Rev. B **76**, 201 401 (2007).

[51] L. G. Cançado, A. Reina, J. Kong, and M. S. Dresselhaus, "Geometrical approach for the study of G' band in the Raman spectrum of monolayer graphene, bilayer graphene, and bulk graphite", Phys. Rev. B **77**, 245 408 (2008).

[52] D. L. Mafra, L. M. Malard, S. K. Doorn, H. Htoon, J. Nilsson, A. H. Castro Neto, and M. A. Pimenta, "Observation of the Kohn anomaly near the K point of bilayer graphene", Phys. Rev. B **80**, 241 414 (2009).

[53] D. L. Mafra, E. A. Moujaes, S. K. Doorn, H. Htoon, R. W. Nunes, and M. A. Pimenta, "A study of inner process double-resonance Raman scattering in bilayer graphene", Carbon **49**, 1511 – 1515 (2011).

[54] D. L. Mafra, J. Kong, K. Sato, R. Saito, M. S. Dresselhaus, and P. T. Araujo, "Using the G' Raman cross-section to understand the phonon dynamics in bilayer graphene systems", Nano Letters **12**, 2883–2887 (2012).

[55] A. G. Souza Filho, A. Jorio, G. Dresselhaus, M. S. Dresselhaus, R. Saito, *et al.*, "Effect of quantized electronic states on the dispersive Raman features in individual single-wall carbon nanotubes", Phys. Rev. B **65**, 035 404 (2001).

[56] M. A. Pimenta, A. Jorio, S. D. M. Brown, A. G. Souza Filho, G. Dresselhaus, *et al.*, "Diameter dependence of the Raman D-band in isolated single-wall carbon nanotubes", Phys. Rev. B **64**, 041 401 (2001).

[57] A. G. Souza Filho, A. Jorio, G. G. Samsonidze, G. Dresselhaus, M. A. Pimenta, *et al.*, "Competing spring constant versus double resonance effects on the properties of dispersive modes in isolated single-wall carbon nanotubes", Phys. Rev. B **67**, 035 427 (2003).

[58] J. Laudenbach, F. Hennrich, M. Kappes, and J. Maultzsch, "Resonance behavior of defect-induced modes in metallic and semiconducting single-walled carbon nanotubes", physica status solidi (b) **249**, 2460–2464 (2012).

[59] M. Mohr, J. Maultzsch, E. Dobardžić, S. Reich, I. Milošević, *et al.*, "Phonon dispersion of graphite by inelastic x-ray scattering", Phys. Rev. B **76**, 035 439 (2007).

[60] D. Yoon, H. Moon, Y.-W. Son, J. S. Choi, B. H. Park, *et al.*, "Interference effect on Raman spectrum of graphene on SiO_2/Si", Phys. Rev. B **80**, 125 422 (2009).

[61] P. R. Wallace, "The band theory of graphite", Phys. Rev. **71**, 622 (1947).

[62] S. Reich, J. Maultzsch, C. Thomsen, and P. Ordejón, "Tight-binding description of graphene", Phys. Rev. B **66**, 035 412 (2002).

[63] S. Reich, C. Thomsen, and J. Maultzsch, *Carbon Nanotubes: Basic Concepts and Physical Properties* (Wiley-VCH, Weinheim, 2004).

[64] D. C. Elias, R. V. Gorbachev, A. S. Mayorov, S. V. Morozov, A. A. Zhukov, *et al.*, "Dirac cones reshaped by interaction effects in suspended graphene", Nature Physics **7**, 701–704 (2011).

[65] C. Faugeras, S. Berciaud, P. Leszczynski, Y. Henni, K. Nogajewski, *et al.*, "Landau level spectroscopy of electron-electron interactions in graphene", Phys. Rev. Lett. **114**, 126 804 (2015).

[66] D. N. Basov, M. M. Fogler, A. Lanzara, F. Wang, and Y. Zhang, "*Colloquium*: Graphene spectroscopy", Rev. Mod. Phys. **86**, 959–994 (2014).

[67] K. Novoselov, Z. Jiang, Y. Zhang, S. Morozov, H. Stormer, *et al.*, "Room-temperature Quantum Hall effect in graphene", Science **315**, 1379 (2007).

[68] F. J. Morin and J. P. Maita, "Electrical properties of silicon containing arsenic and boron", Phys. Rev. **96**, 28–35 (1954).

[69] J. O. Sofo, A. S. Chaudhari, and G. D. Barber, "Graphane: A two-dimensional hydrocarbon", Phys. Rev. B **75**, 153 401 (2007).

[70] R. Balog, B. Jorgensen, L. Nilsson, M. Andersen, E. Rienks, *et al.*, "Bandgap opening in graphene induced by patterned hydrogen adsorption", Nature Materials **9**, 315–319 (2010).

[71] M. Dvorak, W. Oswald, and Z. Wu, "Bandgap opening by patterning graphene", Scientific Reports **3**, 2289 (2013).

[72] Y. Zhang, T.-T. Tang, C. Girit, Z. Hao, M. C. Martin, *et al.*, "Direct observation of a widely tunable bandgap in bilayer graphene", Nature Materials **459**, 820–823 (2009).

[73] K. F. Mak, M. Y. Sfeir, J. A. Misewich, and T. F. Heinz, "The evolution of electronic structure in few-layer graphene revealed by optical spectroscopy", PNAS **107**, 14 999 (2010).

[74] H. Kataura, Y. Kumazawa, Y. Maniwa, I. Umezu, S. Suzuki, Y. Ohtsuka, and Y. Achiba, "Optical properties of single-wall carbon nanotubes", Synthetic Metals **103**, 2555–2558 (1999).

[75] C. Journet and P. Bernier, "Production of carbon nanotubes", Applied Physics A **67**, 1–9 (1998).

[76] M. J. Bronikowski, P. A. Willis, D. T. Colbert, K. A. Smith, and R. E. Smalley, "Gas-phase production of carbon single-walled nanotubes from carbon monoxide via the HiPco process: A parametric study", Journal of Vacuum Science & Technology A **19**, 1800–1805 (2001).

[77] S. M. Bachilo, M. S. Strano, C. Kittrell, R. H. Hauge, R. E. Smalley, and R. B. Weisman, "Structure-assigned optical spectra of single-walled carbon nanotubes", Science **298**, 2361–2366 (2002).

[78] J. Maultzsch, *Vibrational properties of carbon nanotubes and graphite*, Ph.D. thesis, TU Berlin (2004), URN: urn:nbn:de:kobv:83-opus-8674.

[79] M. Ouyang, J.-L. Huang, C. L. Cheung, and C. M. Lieber, "Energy gaps in "metallic" single-walled carbon nanotubes", Science **292**, 702–705 (2001).

[80] V. N. Popov and L. Henrard, "Comparative study of the optical properties of single-walled carbon nanotubes within orthogonal and nonorthogonal tight-binding models", Phys. Rev. B **70**, 115 407 (2004).

[81] M. Damnjanović, I. Milosević, T. Vuković, and J. Maultzsch, "Quantum numbers and band topology of nanotubes", Journal of Physics A: Mathematical and General **36**, 5707 (2003).

[82] B. J. Cox and J. M. Hill, "Exact and approximate geometric parameters for carbon nanotubes incorporating curvature", Carbon **45**, 1453–1462 (2007).

[83] A. Jorio, R. Saito, J. H. Hafner, C. M. Lieber, M. Hunter, *et al.*, "Structural (n,m) determination of isolated single-wall carbon nanotubes by resonant Raman scattering", Phys. Rev. Lett. **86**, 1118–1121 (2001).

[84] J. Maultzsch, H. Telg, S. Reich, and C. Thomsen, "Radial breathing mode of single-walled carbon nanotubes: Optical transition energies and chiral-index assignment", Phys. Rev. B **72**, 205 438 (2005).

[85] M. Machón, S. Reich, C. Thomsen, D. Sánchez-Portal, and P. Ordejón, "*Ab initio* calculations of the optical properties of 4-Å-diameter single-walled nanotubes", Phys. Rev. B **66**, 155 410 (2002).

[86] S. Reich, C. Thomsen, and P. Ordejón, "Electronic band structure of isolated and bundled carbon nanotubes", Phys. Rev. B **65**, 155 411 (2002).

[87] V. N. Popov, "Curvature effects on the structural, electronic and optical properties of isolated single-walled carbon nanotubes within a symmetry-adapted non-orthogonal tight-binding model", New Journal of Physics **6**, 17 (2004).

[88] V. N. Popov and P. Lambin, "Radius and chirality dependence of the radial breathing mode and the G-band phonon modes of single-walled carbon nanotubes", Phys. Rev. B **73**, 085 407 (2006).

[89] M. Damnjanović and I. Milošević, "Modified group-projector technique: subgroups and generators", Journal of Physics A: Mathematical and General **27**, 4859 (1994).

[90] M. Damnjanović, T. Vuković, and I. Milosević, "Modified group projectors: tight-binding method", Journal of Physics A: Mathematical and General **33**, 6561 (2000).

[91] I. Milošević, T. Vuković, S. Dmitrović, and M. Damnjanović, "Polarized optical absorption in carbon nanotubes: A symmetry-based approach", Phys. Rev. B **67**, 165 418 (2003).

[92] E. B. Barros, A. Jorio, G. G. Samsonidze, R. B. Capaz, A. G. S. Filho, *et al.*, "Review on the symmetry-related properties of carbon nanotubes", Physics Reports **431**, 261 – 302 (2006).

[93] D. G. Vercosa, E. B. Barros, A. G. Souza Filho, J. Mendes Filho, G. G. Samsonidze, R. Saito, and M. S. Dresselhaus, "Torsional instability of chiral carbon nanotubes", Phys. Rev. B **81**, 165 430 (2010).

[94] B. G. M. Vieira, E. B. Barros, D. G. Vercosa, G. Samsonidze, A. G. S. Filho, and M. S. Dresselhaus, "Fermi-energy-dependent structural deformation of chiral single-wall carbon nanotubes", Phys. Rev. Applied **2**, 014 006 (2014).

[95] I. Milošević, A. Damjanović, and M. Damnjanović, "Symmetry-oriented research of polymers PC program POLSym and DNA", in *Quantum Mechanical Simulation Methods in Studying Biological Systems*, edited by D. Bicout and M. Field (Springer, Berlin, 1996).

[96] G. Czycholl, *Theoretische Festkörperphysik: Von den klassischen Modellen zu modernen Forschungsthemen* (Springer-Verlag Berlin Heidelberg, 2008), 3. edn.

[97] E. B. Wilson, J. C. Decius, and P. C. Cross, *Molecular vibrations: The theory of infrared and Raman vibrational spectra* (Dover Publications, New York, 2001), revised edn.

[98] A. Smekal, "Zur Quantentheorie der Dispersion", Naturwissenschaften **11**, 873–875 (1923).

[99] C. V. Raman and K. S. Krishnan, "A new type of secondary radiation", Nature **121**, 501 (1928).

[100] H. Kuzmany, *Solid-State Spectroscopy: An Introduction* (Springer-Verlag Berlin Heidelberg, 2009), 2. edn.

[101] J. W. Weber, V. E. Calado, and M. C. M. van de Sanden, "Optical constants of graphene measured by spectroscopic ellipsometry", Applied Physics Letters **97**, 091 904 (2010).

[102] S. Reich and C. Thomsen, "Raman spectroscopy of graphite", Phil. Trans. R. Soc. Lond. A **362**, 2271–2288 (2004).

[103] F. Tuinstra and J. L. Koenig, "Raman spectrum of graphite", The Journal of Chemical Physics **53**, 1126–1130 (1970).

[104] M. Matthews, M. Pimenta, G. Dresselhaus, M. Dresselhaus, and M. Endo, "Origin of dispersive effects of the Raman D band in carbon materials", Phys. Rev. B **59**, R6585–R6588 (1999).

[105] M. Kalbac, A. Reina-Cecco, H. Farhat, J. Kong, L. Kavan, and M. S. Dresselhaus, "The influence of strong electron and hole doping on the Raman intensity of chemical vapor-deposition graphene", ACS Nano **4**, 6055–6063 (2010).

[106] C.-F. Chen, C.-H. Park, B. W. Boudouris, J. Horng, B. Geng, *et al.*, "Controlling inelastic light scattering quantum pathways in graphene", Nature **471**, 617–620 (2011).

[107] F. Herziger, P. May, and J. Maultzsch, "Layer-number determination in graphene by out-of-plane phonons", Phys. Rev. B **85**, 235 447 (2012).

[108] E. Malic, T. Winzer, E. Bobkin, and A. Knorr, "Microscopic theory of absorption and ultrafast many-particle kinetics in graphene", Phys. Rev. B **84**, 205 406 (2011).

[109] F. Kadi and E. Malic, "Optical properties of Bernal-stacked bilayer graphene: A theoretical study", Phys. Rev. B **89**, 045 419 (2014).

[110] H. Fröhlich, "Theory of the superconducting state. I. The ground state at the absolute zero of temperature", Phys. Rev. **79**, 845–856 (1950).

[111] J. Bardeen, L. N. Cooper, and J. R. Schrieffer, "Theory of superconductivity", Phys. Rev. **108**, 1175–1204 (1957).

[112] E. Malic, T. Winzer, and A. Knorr, "Efficient orientational carrier relaxation in optically excited graphene", Applied Physics Letters **101**, 213 110 (2012).

[113] W. Kohn, "Image of the Fermi surface in the vibration spectrum of a metal", Phys. Rev. Lett. **2**, 393–394 (1959).

[114] S. K. Saha, U. V. Waghmare, H. R. Krishnamurthy, and A. K. Sood, "Phonons in few-layer graphene and interplanar interaction: A first-principles study", Phys. Rev. B **78**, 165 421 (2008).

[115] A. Politano, F. de Juan, G. Chiarello, and H. A. Fertig, "Emergence of an out-of-plane optical phonon (ZO) Kohn anomaly in quasifreestanding epitaxial graphene", Phys. Rev. Lett. **115**, 075 504 (2015).

[116] S. Tanaka, M. Matsunami, and S. Kimura, "An investigation of electron-phonon coupling via phonon dispersion measurements in graphite using angle-resolved photoelectron spectroscopy", Scientific Reports **3**, 3031 (2013).

[117] P. H. Tan, W. P. Han, W. J. Zhao, Z. H. Wu, K. Chang, *et al.*, "The shear mode of multilayer graphene", Nature Materials **11**, 294–300 (2012).

[118] C. H. Lui and T. F. Heinz, "Measurement of layer breathing mode vibrations in few-layer graphene", Phys. Rev. B **87**, 121 404 (2013).

[119] H. Telg, M. Fouquet, J. Maultzsch, Y. Wu, B. Chandra, *et al.*, "G^- and G^+ in the Raman spectrum of isolated nanotube: a study on resonance conditions and lineshape", physica status solidi (b) **245**, 2189–2192 (2008).

[120] H. Telg, J. G. Duque, M. Staiger, X. Tu, F. Hennrich, *et al.*, "Chiral index dependence of the G^+ and G^- Raman modes in semiconducting carbon nanotubes", ACS Nano **6**, 904–911 (2012).

[121] H. Telg, J. Maultzsch, S. Reich, F. Hennrich, and C. Thomsen, "Chirality distribution and transition energies of carbon nanotubes", Phys. Rev. Lett. **93**, 177 401 (2004).

[122] F. Herziger, M. Calandra, P. Gava, P. May, M. Lazzeri, F. Mauri, and J. Maultzsch, "Two-dimensional analysis of the double-resonant 2D Raman mode in bilayer graphene", Phys. Rev. Lett. **113**, 187 401 (2014).

[123] T. Ohta, A. Bostwick, T. Seyller, K. Horn, and E. Rotenberg, "Controlling the electronic structure of bilayer graphene", Science **313**, 951–954 (2006).

[124] E. V. Castro, K. S. Novoselov, S. V. Morozov, N. M. R. Peres, J. M. B. L. dos Santos, *et al.*, "Biased bilayer graphene: Semiconductor with a gap tunable by the electric field effect", Phys. Rev. Lett. **99**, 216 802 (2007).

[125] K. F. Mak, C. H. Lui, J. Shan, and T. F. Heinz, "Observation of an electric-field-induced band gap in bilayer graphene by infrared spectroscopy", Phys. Rev. Lett. **102**, 256 405 (2009).

[126] C. H. Lui, L. M. Malard, S. Kim, G. Lantz, F. E. Laverge, R. Saito, and T. F. Heinz, "Observation of layer-breathing mode vibrations in few-layer graphene through combination Raman scattering", Nano Letters **12**, 5539–5544 (2012).

[127] C. H. Lui, Z. Ye, C. Keiser, X. Xiao, and R. He, "Temperature-activated layer-breathing vibrations in few-layer graphene", Nano Letters **14**, 4615–4621 (2014).

[128] J. Maultzsch, S. Reich, C. Thomsen, H. Requardt, and P. Ordejón, "Phonon dispersion in graphite", Phys. Rev. Lett. **92**, 075 501 (2004).

[129] M. Lazzeri, C. Attaccalite, L. Wirtz, and F. Mauri, "Impact of the electron-electron correlation on phonon dispersion: Failure of LDA and GGA DFT functionals in graphene and graphite", Phys. Rev. B **78**, 081 406 (2008).

[130] N. Argaman and G. Makov, "Density functional theory: An introduction", American Journal of Physics **68**, 69–79 (2000).

[131] D. M. Basko and I. L. Aleiner, "Interplay of Coulomb and electron-phonon interactions in graphene", Phys. Rev. B **77**, 041 409 (2008).

[132] L. Hedin, "On correlation effects in electron spectroscopies and the GW approximation", Journal of Physics: Condensed Matter **11**, R489 (1999).

[133] L. Hedin, "New method for calculating the one-particle Green's function with application to the electron-gas problem", Phys. Rev. **139**, A796–A823 (1965).

[134] L. M. Malard, M. H. D. Guimarães, D. L. Mafra, M. S. C. Mazzoni, and A. Jorio, "Group-theory analysis of electrons and phonons in n-layer graphene systems", Phys. Rev. B **79**, 125 426 (2009).

[135] J. Maultzsch, S. Reich, and C. Thomsen, "Double-resonant Raman scattering in graphite: Interference effects, selection rules, and phonon dispersion", Phys. Rev. B **70**, 155 403 (2004).

[136] D. Yoon, Y.-W. Son, and H. Cheong, "Strain-dependent splitting of the double-resonance Raman scattering band in graphene", Phys. Rev. Lett. **106**, 155 502 (2011).

[137] O. Frank, M. Mohr, J. Maultzsch, C. Thomsen, I. Riaz, *et al.*, "Raman 2D-band splitting in graphene: Theory and experiment", ACS Nano **5**, 2231–2239 (2011).

[138] R. Narula, N. Bonini, N. Marzari, and S. Reich, "Dominant phonon wave vectors and strain-induced splitting of the $2D$ Raman mode of graphene", Phys. Rev. B **85**, 115 451 (2012).

[139] R. Narula and S. Reich, "Double resonant Raman spectra in graphene and graphite: A two-dimensional explanation of the Raman amplitude", Phys. Rev. B **78**, 165 422 (2008).

[140] C. Tyborski, F. Herziger, R. Gillen, and J. Maultzsch, "Beyond double-resonant Raman scattering: Ultraviolet Raman spectroscopy on graphene, graphite, and carbon nanotubes", Phys. Rev. B **92**, 041 401 (2015).

[141] P. Giannozzi, S. Baroni, N. Bonini, M. Calandra, R. Car, *et al.*, "Quantum ESPRESSO: a modular and open-source software project for quantum simulations of materials", J. Phys.: Condens. Matter **21**, 395 502 (2009).

[142] P. May, M. Lazzeri, P. Venezuela, F. Herziger, G. Callsen, *et al.*, "Signature of the two-dimensional phonon dispersion in graphene probed by double-resonant Raman scattering", Phys. Rev. B **87**, 075 402 (2013).

[143] A. A. Mostofi, J. R. Yates, Y.-S. Lee, I. Souza, D. Vanderbilt, and N. Marzari, "wannier90: A tool for obtaining maximally-localised Wannier functions", Comput. Phys. Commun. **178**, 685 – 699 (2008).

[144] M. Calandra, G. Profeta, and F. Mauri, "Adiabatic and nonadiabatic phonon dispersion in a Wannier function approach", Phys. Rev. B **82**, 165 111 (2010).

[145] N. Marzari, A. A. Mostofi, J. R. Yates, I. Souza, and D. Vanderbilt, "Maximally localized Wannier functions: Theory and applications", Rev. Mod. Phys. **84**, 1419–1475 (2012).

[146] A. Grüneis, C. Attaccalite, T. Pichler, V. Zabolotnyy, H. Shiozawa, *et al.*, "Electron-electron correlation in graphite: A combined angle-resolved photoemission and first-principles study", Phys. Rev. Lett. **100**, 037 601 (2008).

[147] P. E. Trevisanutto, C. Giorgetti, L. Reining, M. Ladisa, and V. Olevano, "*Ab initio GW* many-body effects in graphene", Phys. Rev. Lett. **101**, 226 405 (2008).

[148] Y. Zhang, Y.-W. Tan, H. L. Stormer, and P. Kim, "Experimental observation of the quantum Hall effect and Berry's phase in graphene", Nature **438**, 201–204 (2005).

[149] A. Grüneis, J. Serrano, A. Bosak, M. Lazzeri, S. L. Molodtsov, *et al.*, "Phonon surface mapping of graphite: Disentangling quasi-degenerate phonon dispersions", Phys. Rev. B **80**, 085 423 (2009).

[150] J.-A. Yan, W. Y. Ruan, and M. Y. Chou, "Phonon dispersions and vibrational properties of monolayer, bilayer, and trilayer graphene: Density-functional perturbation theory", Phys. Rev. B **77**, 125 401 (2008).

[151] K. F. Mak, F. H. da Jornada, K. He, J. Deslippe, N. Petrone, *et al.*, "Tuning many-body interactions in graphene: The effects of doping on excitons and carrier lifetimes", Phys. Rev. Lett. **112**, 207 401 (2014).

[152] L. Paulatto, F. Mauri, and M. Lazzeri, "Anharmonic properties from a generalized third-order *ab initio* approach: Theory and applications to graphite and graphene", Phys. Rev. B **87**, 214 303 (2013).

[153] C. Girit and A. Zettl, "Soldering to a single atomic layer", Applied Physics Letters **91**, 193 512 (2007).

[154] G. Froehlicher and S. Berciaud, "Raman spectroscopy of electrochemically gated graphene transistors: Geometrical capacitance, electron-phonon, electron-electron, and electron-defect scattering", Phys. Rev. B **91**, 205 413 (2015).

[155] H. Wang, J. You, L. Wang, M. Feng, and Y. Wang, "Theory of the evolution of $2D$ band in the Raman spectra of monolayer and bilayer graphene with laser excitation energy", J. Raman Spectrosc. **41**, 125–129 (2010).

[156] I. Kupčić, "Triple-resonant two-phonon Raman scattering in graphene", J. Raman Spectrosc. **43**, 1–5 (2012).

[157] D. M. Basko, "Effect of anisotropic band curvature on carrier multiplication in graphene", Phys. Rev. B **87**, 165 437 (2013).

[158] D. M. Basko, "Effect of inelastic collisions on multiphonon Raman scattering in graphene", Phys. Rev. B **76**, 081 405 (2007).

[159] A. Zabet-Khosousi, L. Zhao, L. Pálová, M. S. Hybertsen, D. R. Reichman, A. N. Pasupathy, and G. W. Flynn, "Segregation of sublattice domains in Nitrogen-doped graphene", Journal of the American Chemical Society **136**, 1391–1397 (2014).

[160] B. Hunt, J. D. Sanchez-Yamagishi, A. F. Young, M. Yankowitz, B. J. LeRoy, *et al.*, "Massive Dirac fermions and Hofstadter butterfly in a van der Waals heterostructure", Science **340**, 1427–1430 (2013).

[161] M. Yankowitz, J. Xue, D. Cormode, J. D. Sanchez-Yamagishi, K. Watanabe, *et al.*, "Emergence of superlattice Dirac points in graphene on hexagonal boron nitride", Nature physics **8**, 382–386 (2012).

[162] O. Frank, M. Bouša, I. Riaz, R. Jalil, K. S. Novoselov, *et al.*, "Phonon and structural changes in deformed Bernal-stacked bilayer graphene", Nano Letters **12**, 687–693 (2012).

[163] L. Yang, J. Deslippe, C.-H. Park, M. L. Cohen, and S. G. Louie, "Excitonic effects on the optical response of graphene and bilayer graphene", Phys. Rev. Lett. **103**, 186 802 (2009).

[164] M. Rösner, E. Şaşıoğlu, C. Friedrich, S. Blügel, and T. O. Wehling, "Wannier function approach to realistic Coulomb interactions in layered materials and heterostructures", Phys. Rev. B **92**, 085 102 (2015).

[165] R. Narula and S. Reich, "Graphene band structure and its 2D Raman mode", Phys. Rev. B **90**, 085 407 (2014).

[166] C.-H. Park, N. Bonini, T. Sohier, G. Samsonidze, B. Kozinsky, *et al.*, "Electron-phonon interactions and the intrinsic electrical resistivity of graphene", Nano Letters **14**, 1113–1119 (2014).

[167] T. Sohier, M. Calandra, C.-H. Park, N. Bonini, N. Marzari, and F. Mauri, "Phonon-limited resistivity of graphene by first-principles calculations: Electron-phonon interactions, strain-induced gauge field, and Boltzmann equation", Phys. Rev. B **90**, 125 414 (2014).

[168] D. M. Basko, S. Piscanec, and A. C. Ferrari, "Electron-electron interactions and doping dependence of the two-phonon Raman intensity in graphene", Phys. Rev. B **80**, 165 413 (2009).

[169] A. Eckmann, A. Felten, I. Verzhbitskiy, R. Davey, and C. Casiraghi, "Raman study on defective graphene: Effect of the excitation energy, type, and amount of defects", Phys. Rev. B **88**, 035 426 (2013).

[170] A. Eckmann, A. Felten, A. Mishchenko, L. Britnell, R. Krupke, K. S. Novoselov, and C. Casiraghi, "Probing the nature of defects in graphene by Raman spectroscopy", Nano Letters **12**, 3925–3930 (2012).

[171] M. Bruna, A. K. Ott, M. Ijäs, D. Yoon, U. Sassi, and A. C. Ferrari, "Doping dependence of the Raman spectrum of defected graphene", ACS Nano **8**, 7432–7441 (2014).

[172] J. Yan, E. A. Henriksen, P. Kim, and A. Pinczuk, "Observation of anomalous phonon softening in bilayer graphene", Phys. Rev. Lett. **101**, 136 804 (2008).

[173] P. Gava, M. Lazzeri, A. M. Saitta, and F. Mauri, "Probing the electrostatic environment of bilayer graphene using Raman spectra", Phys. Rev. B **80**, 155 422 (2009).

[174] J. Yan, T. Villarson, E. A. Henriksen, P. Kim, and A. Pinczuk, "Optical phonon mixing in bilayer graphene with a broken inversion symmetry", Phys. Rev. B **80**, 241 417 (2009).

[175] Q. H. Wang, C.-J. Shih, G. L. C. Paulus, and M. S. Strano, "Evolution of physical and electronic structures of bilayer graphene upon chemical functionalization", Journal of the American Chemical Society **135**, 18 866–18 875 (2013).

[176] F. Herziger, C. Tyborski, O. Ochedowski, M. Schleberger, and J. Maultzsch, "Double-resonant LA phonon scattering in defective graphene and carbon nanotubes", Phys. Rev. B **90**, 245 431 (2014).

[177] E. A. Henriksen and J. P. Eisenstein, "Measurement of the electronic compressibility of bilayer graphene", Phys. Rev. B **82**, 041 412 (2010).

[178] E. McCann and M. Koshino, "The electronic properties of bilayer graphene", Reports on Progress in Physics **76**, 056 503 (2013).

[179] L. M. Malard, D. C. Elias, E. S. Alves, and M. A. Pimenta, "Observation of distinct electron-phonon couplings in gated bilayer graphene", Phys. Rev. Lett. **101**, 257 401 (2008).

[180] T. Ando, "Anomaly of optical phonons in bilayer graphene", Journal of the Physical Society of Japan **76**, 104 711 (2007).

[181] A. Das, S. Pisana, B. Chakraborty, S. Piscanec, S. K. Saha, *et al.*, "Monitoring dopants by Raman scattering in an electrochemically top-gated graphene transistor", Nature Nanotechnology **3**, 210–215 (2008).

[182] J. H. Lee, A. Avsar, J. Jung, J. Y. Tan, K. Watanabe, *et al.*, "van der Waals force: A dominant factor for reactivity of graphene", Nano Letters **15**, 319–325 (2015).

[183] C. Attaccalite, L. Wirtz, M. Lazzeri, F. Mauri, and A. Rubio, "Doped graphene as tunable electron-phonon coupling material", Nano Letters **10**, 1172–1176 (2010).

[184] C. Attaccalite and A. Rubio, "Fermi velocity renormalization in doped graphene", physica status solidi (b) **246**, 2523–2526 (2009).

[185] B. Huang, M. Liu, N. Su, J. Wu, W. Duan, B.-l. Gu, and F. Liu, "Quantum manifestations of graphene edge stress and edge instability: A first-principles study", Phys. Rev. Lett. **102**, 166 404 (2009).

[186] V. B. Shenoy, C. D. Reddy, A. Ramasubramaniam, and Y. W. Zhang, "Edge-stress-induced warping of graphene sheets and nanoribbons", Phys. Rev. Lett. **101**, 245 501 (2008).

[187] M. Huang, H. Yan, C. Chen, D. Chen, T. F. Heinz, and J. Hone, "Phonon softening and crystallographic orientation of strained graphene studied by Raman spectroscopy", Proceedings of the National Academy of Sciences **106**, 7304–7308 (2009).

[188] D. Yoon, H. Moon, Y.-W. Son, G. Samsonidze, B. H. Park, *et al.*, "Strong polarization dependence of double-resonant Raman intensities in graphene", Nano Letters **8**, 4270–4274 (2008).

[189] A. Grüneis, R. Saito, G. G. Samsonidze, T. Kimura, M. A. Pimenta, *et al.*, "Inhomogeneous optical absorption around the K point in graphite and carbon nanotubes", Phys. Rev. B **67**, 165 402 (2003).

[190] P. May, *Electronic and vibrational properties of low-dimensional carbon systems*, Ph.D. thesis, TU Berlin (2012), URN: urn:nbn:de:kobv:83-opus-35280.

[191] S. Sahoo, R. Palai, and R. S. Katiyar, "Polarized Raman scattering in monolayer, bilayer, and suspended bilayer graphene", Journal of Applied Physics **110**, 044 320 (2011).

[192] J.-U. Lee, N. M. Seck, D. Yoon, S.-M. Choi, Y.-W. Son, and H. Cheong, "Polarization dependence of double resonant Raman scattering band in bilayer graphene", Carbon **72**, 257–263 (2014).

[193] F. Herziger, A. Vierck, J. Laudenbach, and J. Maultzsch, "Understanding double-resonant Raman scattering in chiral carbon nanotubes: Diameter and energy dependence of the D mode", (2015), accepted for publication in Phys. Rev. B, arXiv:1508.03456.

[194] F. Herziger, R. Mirzayev, E. Poliani, and J. Maultzsch, "*In-situ* Raman study of laser-induced graphene oxidation", physica status solidi (b) **252**, 2551–2557 (2015).

[195] F. Banhart, J. Kotakoski, and A. V. Krasheninnikov, "Structural defects in graphene", ACS Nano **5**, 26–41 (2011).

[196] A. Stone and D. Wales, "Theoretical studies of icosahedral C60 and some related species", Chemical Physics Letters **128**, 501–503 (1986).

[197] R. Vidano and D. B. Fischbach, "New lines in the Raman spectra of carbons and graphite", Journal of the American Ceramic Society **61**, 13–17 (1978).

[198] R. J. Nemanich and S. A. Solin, "First- and second-order Raman scattering from finite-size crystals of graphite", Phys. Rev. B **20**, 392–401 (1979).

[199] I. Pócsik, M. Hundhausen, M. Koós, and L. Ley, "Origin of the D peak in the Raman spectrum of microcrystalline graphite", Journal of Non-Crystalline Solids **227-230**, 1083–1086 (1998).

[200] A. Cuesta, P. Dhamelincourt, J. Laureyns, A. Martinez-Alonso, and J. M. D. Tascon, "Comparative performance of X-ray diffraction and Raman microprobe techniques for the study of carbon materials", J. Mater. Chem. **8**, 2875–2879 (1998).

[201] A. C. Ferrari and J. Robertson, "Interpretation of Raman spectra of disordered and amorphous carbon", Phys. Rev. B **61**, 14 095–14 107 (2000).

[202] K. Sinha and J. Menéndez, "First- and second-order resonant Raman scattering in graphite", Phys. Rev. B **41**, 10 845–10 847 (1990).

[203] L. G. Cançado, K. Takai, T. Enoki, M. Endo, Y. A. Kim, *et al.*, "General equation for the determination of the crystallite size L_a of nanographite by Raman spectroscopy", Applied Physics Letters **88**, 163 106 (2006).

[204] L. G. Cançado, A. Jorio, and M. A. Pimenta, "Measuring the absolute Raman cross section of nanographites as a function of laser energy and crystallite size", Phys. Rev. B **76**, 064 304 (2007).

[205] A. J. Pollard, B. Brennan, H. Stec, B. J. Tyler, M. P. Seah, I. S. Gilmore, and D. Roy, "Quantitative characterization of defect size in graphene using Raman spectroscopy", Applied Physics Letters **105**, 253 107 (2014).

[206] E. H. Martins Ferreira, M. V. O. Moutinho, F. Stavale, M. M. Lucchese, R. B. Capaz, C. A. Achete, and A. Jorio, "Evolution of the Raman spectra from single-, few-, and many-layer graphene with increasing disorder", Phys. Rev. B **82**, 125 429 (2010).

[207] D. Graf, F. Molitor, K. Ensslin, C. Stampfer, A. Jungen, C. Hierold, and L. Wirtz, "Spatially resolved Raman spectroscopy of single- and few-layer graphene", Nano Letters **7**, 238–242 (2007).

[208] J. Laudenbach, *Raman spectroscopy of single-walled carbon nanotubes: Resonance behavior of the defect-induced Raman modes*, Ph.D. thesis, TU Berlin (2014), URN: urn:nbn:de:kobv:83-opus4-46019.

[209] J. Laudenbach, D. Schmid, F. Herziger, F. Hennrich, M. Kappes, *et al.*, "Diameter dependence of the defect-induced Raman modes in functionalized carbon nanotubes", (2015), in preparation.

[210] J. Maultzsch, S. Reich, and C. Thomsen, "Chirality-selective Raman scattering of the D mode in carbon nanotubes", Phys. Rev. B **64**, 121 407 (2001).

[211] M. Damnjanović, I. Milošević, T. Vuković, and R. Sredanović, "Full symmetry, optical activity, and potentials of single-wall and multiwall nanotubes", Phys. Rev. B **60**, 2728–2739 (1999).

[212] J. Laudenbach, F. Hennrich, H. Telg, M. Kappes, and J. Maultzsch, "Resonance behavior of the defect-induced Raman mode of single-chirality enriched carbon nanotubes", Phys. Rev. B **87**, 165 423 (2013).

[213] C. Thomsen, S. Reich, and J. Maultzsch, "Resonant Raman spectroscopy of nanotubes", Phil. Trans. R. Soc. Lond. A **362**, 2337–2359 (2004).

[214] C. Thomsen and S. Reich, "Raman scattering in carbon nanotubes", in *Light Scattering in Solid IX*, edited by M. Cardona and R. Merlin (Springer Berlin Heidelberg, 2007), vol. 108 of *Topics in Applied Physics*, pp. 115–234.

[215] M. Dresselhaus, G. Dresselhaus, R. Saito, and A. Jorio, "Raman spectroscopy of carbon nanotubes", Physics Reports **409**, 47 – 99 (2005).

[216] M. A. Pimenta, A. Marucci, S. A. Empedocles, M. G. Bawendi, E. B. Hanlon, *et al.*, "Raman modes of metallic carbon nanotubes", Phys. Rev. B **58**, 16 016(R) (1998).

[217] P. Araujo, P. Pesce, M. Dresselhaus, K. Sato, R. Saito, and A. Jorio, "Resonance Raman spectroscopy of the radial breathing modes in carbon nanotubes", Physica E: Low-dimensional Systems and Nanostructures **42**, 1251–1261 (2010).

[218] H. Telg, C. Thomsen, and J. Maultzsch, "Raman intensities of the radial-breathing mode in carbon nanotubes: the exciton-phonon coupling as a function of (n_1, n_2)", Journal of Nanophotonics **4**, 041 660 (2010).

[219] C. Thomsen, H. Telg, J. Maultzsch, and S. Reich, "Chirality assignments in carbon nanotubes based on resonant Raman scattering", physica status solidi (b) **242**, 1802–1806 (2005).

[220] E. H. Hároz, J. G. Duque, E. B. Barros, H. Telg, J. R. Simpson, *et al.*, "Asymmetric excitation profiles in the resonance Raman response of armchair carbon nanotubes", Phys. Rev. B **91**, 205 446 (2015).

[221] J. Kürti, V. Zólyomi, A. Grüneis, and H. Kuzmany, "Double resonant Raman phenomena enhanced by van Hove singularities in single-wall carbon nanotubes", Phys. Rev. B **65**, 165 433 (2002).

[222] S. Piscanec, M. Lazzeri, J. Robertson, A. C. Ferrari, and F. Mauri, "Optical phonons in carbon nanotubes: Kohn anomalies, Peierls distortions, and dynamic effects", Phys. Rev. B **75**, 035 427 (2007).

[223] H. Telg, J. Maultzsch, S. Reich, and C. Thomsen, "Resonant-Raman intensities and transition energies of the E_{11} transition in carbon nanotubes", Phys. Rev. B **74**, 115 415 (2006).

[224] M. Machón, S. Reich, H. Telg, J. Maultzsch, P. Ordejón, and C. Thomsen, "Strength of radial breathing mode in single-walled carbon nanotubes", Phys. Rev. B **71**, 035 416 (2005).

[225] A. V. Savin, B. Hu, and Y. S. Kivshar, "Thermal conductivity of single-walled carbon nanotubes", Phys. Rev. B **80**, 195 423 (2009).

[226] R. Ferone, J. R. Wallbank, V. Zólyomi, E. McCann, and V. I. Fal'ko, "Manifestation of LO-LA phonons in Raman scattering in graphene", Solid State Communications **151**, 1071 – 1074 (2011).

[227] K. Sato, J. S. Park, R. Saito, C. Cong, T. Yu, *et al.*, "Raman spectra of out-of-plane phonons in bilayer graphene", Phys. Rev. B **84**, 035 419 (2011).

[228] R. Rao, R. Podila, R. Tsuchikawa, J. Katoch, D. Tishler, A. M. Rao, and M. Ishigami, "Effects of layer stacking on the combination Raman modes in graphene", ACS Nano **5**, 1594–1599 (2011).

[229] C. Cong, T. Yu, R. Saito, G. F. Dresselhaus, and M. S. Dresselhaus, "Second-order overtone and combination Raman modes of graphene layers in the range of 1690-2150 cm^{-1}", ACS Nano **5**, 1600–1605 (2011).

[230] S. Akcöltekin, H. Bukowska, T. Peters, O. Osmani, I. Monnet, *et al.*, "Unzipping and folding of graphene by swift heavy ions", Applied Physics Letters **98**, 103 103 (2011).

[231] O. Ochedowski, B. Kleine Bussmann, B. Ban-d'Etat, H. Lebius, and M. Schleberger, "Manipulation of the graphene surface potential by ion irradiation", Applied Physics Letters **102**, 153 103 (2013).

[232] O. Ochedowski, K. Marinov, G. Wilbs, G. Keller, N. Scheuschner, *et al.*, "Radiation hardness of graphene and MoS_2 field effect devices against swift heavy ion irradiation", Journal of Applied Physics **113**, 214 306 (2013).

[233] J. F. Ziegler, M. Ziegler, and J. Biersack, "SRIM - the stopping and range of ions in matter", Nucl. Instrum. Methods B **268**, 1818–1823 (2010).

[234] P. Nikolaev, M. J. Bronikowski, R. K. Bradley, F. Rohmund, D. T. Colbert, K. A. Smith, and R. E. Smalley, "Gas-phase catalytic growth of single-walled carbon nanotubes from carbon monoxide", Chemical Physics Letters **313**, 91–97 (1999).

[235] I. W. Chiang, B. E. Brinson, A. Y. Huang, P. A. Willis, M. J. Bronikowski, *et al.*, "Purification and characterization of single-wall carbon nanotubes (SWNTs) obtained from the gas-phase decomposition of CO (HiPco process)", The Journal of Physical Chemistry B **105**, 8297–8301 (2001).

[236] J. M. Soler, E. Artacho, J. D. Gale, A. Garcia, J. Junquera, P. Ordejon, and D. Sanchez-Portal, "The SIESTA method for ab-initio order-N materials simulation", J. Phys: Condens. Matter **14**, 2745–2779 (2002).

[237] P. Tan, L. An, L. Liu, Z. Guo, R. Czerw, *et al.*, "Probing the phonon dispersion relations of graphite from the double-resonance process of Stokes and anti-Stokes Raman scatterings in multiwalled carbon nanotubes", Phys. Rev. B **66**, 245 410 (2002).

[238] V. W. Brar, G. G. Samsonidze, M. S. Dresselhaus, G. Dresselhaus, R. Saito, *et al.*, "Second-order harmonic and combination modes in graphite, single-wall carbon nanotube bundles, and isolated single-wall carbon nanotubes", Phys. Rev. B **66**, 155 418 (2002).

[239] C. Fantini, M. A. Pimenta, and M. S. Strano, "Two-phonon combination Raman modes in covalently functionalized single-wall carbon nanotubes", J. Phys. Chem. C **112**, 13 150–13 155 (2008).

[240] A. V. Ellis, "Second-order overtone and combination modes in the LOLA region of acid treated double-walled carbon nanotubes", Journal of Chemical Physics **125**, 121 103 (2006).

[241] T. Shimada, T. Sugai, C. Fantini, M. Souza, L. G. Cançado, *et al.*, "Origin of the 2450 cm^{-1} Raman bands in HOPG, single-wall and double-wall carbon nanotubes", Carbon **43**, 1049–1054 (2005).

[242] E. Malic, M. Hirtschulz, F. Milde, A. Knorr, and S. Reich, "Analytical approach to optical absorption in carbon nanotubes", Phys. Rev. B **74**, 195 431 (2006).

[243] D. C. Elias, R. R. Nair, T. M. G. Mohiuddin, S. V. Morozov, P. Blake, *et al.*, "Control of graphene's properties by reversible hydrogenation: Evidence for graphane", Science **323**, 610–613 (2009).

[244] L. Liu, S. Ryu, M. R. Tomasik, E. Stolyarova, N. Jung, *et al.*, "Graphene oxidation: Thickness-dependent etching and strong chemical doping", Nano Letters **8**, 1965–1970 (2008).

[245] H. Liu, S. Ryu, Z. Chen, M. L. Steigerwald, C. Nuckolls, and L. E. Brus, "Photochemical reactivity of graphene", Journal of the American Chemical Society **131**, 17 099–17 101 (2009).

[246] R. J. Stöhr, R. Kolesov, K. Xia, and J. Wrachtrup, "All-optical high-resolution nanopatterning and 3D suspending of graphene", ACS Nano **5**, 5141–5150 (2011).

[247] S. Ryu, L. Liu, S. Berciaud, Y.-J. Yu, H. Liu, *et al.*, "Atmospheric oxygen binding and hole doping in deformed graphene on a SiO_2 substrate", Nano Letters **10**, 4944–4951 (2010).

[248] N. Mitoma, R. Nouchi, and K. Tanigaki, "Photo-oxidation of graphene in the presence of water", The Journal of Physical Chemistry C **117**, 1453–1456 (2013).

[249] W. Xiong, Y. S. Zhou, W. J. Hou, L. J. Jiang, Y. Gao, *et al.*, "Direct writing of graphene patterns on insulating substrates under ambient conditions", Scientific Reports **4**, 4892 (2014).

[250] B. H. Seo, J. Youn, and M. Shim, "Direct laser writing of air-stable p-n junctions in graphene", ACS Nano **8**, 8831–8836 (2014).

[251] P. Nemes-Incze, G. Magda, K. Kamaras, and L. P. Biro, "Crystallographically selective nanopatterning of graphene on SiO_2", Nano Research **3**, 110–116 (2010).

[252] T. Gokus, R. R. Nair, A. Bonetti, M. Böhmler, A. Lombardo, *et al.*, "Making graphene luminescent by oxygen plasma treatment", ACS Nano **3**, 3963–3968 (2009).

[253] J. Aumanen, A. Johansson, J. Koivistoinen, P. Myllyperkio, and M. Pettersson, "Patterning and tuning of electrical and optical properties of graphene by laser induced two-photon oxidation", Nanoscale **7**, 2851–2855 (2015).

[254] J. Aumanen, A. Johansson, O. Herranen, P. Myllyperkio, and M. Pettersson, "Local photo-oxidation of individual single walled carbon nanotubes probed by femtosecond four wave mixing imaging", Phys. Chem. Chem. Phys. **17**, 209–216 (2015).

[255] I. Horcas, R. Fernandez, J. Gomez-Rodriguez, J. Colchero, J. Gomez-Herrero, and A. M. Baro, "WSXM: A software for scanning probe microscopy and a tool for nanotechnology", Rev. Sci. Instrum. **78**, 013 705 (2007).

[256] R. J. Stöhr, R. Kolesov, J. Pflaum, and J. Wrachtrup, "Fluorescence of laser-created electron-hole plasma in graphene", Phys. Rev. B **82**, 121 408 (2010).

[257] Q. Chen, C. Zhang, F. Xue, Y. Zhou, W. Li, *et al.*, "Enhanced hot-carrier luminescence in multilayer reduced graphene oxide nanospheres", Scientific Reports **3**, 2315 (2013).

[258] D. G. Cahill, M. Katiyar, and J. R. Abelson, "Thermal conductivity of *a*-Si:h thin films", Phys. Rev. B **50**, 6077–6081 (1994).

[259] J. E. Lee, G. Ahn, J. Shim, Y. S. Lee, and S. Ryu, "Optical separation of mechanical strain from charge doping in graphene", Nature Communications **3**, 1024 (2012).

[260] D. Metten, F. Federspiel, M. Romeo, and S. Berciaud, "All-optical blister test of suspended graphene using micro-Raman spectroscopy", Phys. Rev. Applied **2**, 054 008 (2014).

[261] J. Zabel, R. R. Nair, A. Ott, T. Georgiou, A. K. Geim, K. S. Novoselov, and C. Casiraghi, "Raman spectroscopy of graphene and bilayer under biaxial strain: Bubbles and balloons", Nano Letters **12**, 617–621 (2012).

[262] I. Calizo, A. A. Balandin, W. Bao, F. Miao, and C. N. Lau, "Temperature dependence of the Raman spectra of graphene and graphene multilayers", Nano Letters **7**, 2645–2649 (2007).

[263] D. Yoon, Y.-W. Son, and H. Cheong, "Negative thermal expansion coefficient of graphene measured by Raman spectroscopy", Nano Letters **11**, 3227–3231 (2011).

[264] S. Linas, Y. Magnin, B. Poinsot, O. Boisron, G. D. Förster, *et al.*, "Interplay between Raman shift and thermal expansion in graphene: Temperature-dependent measurements and analysis of substrate corrections", Phys. Rev. B **91**, 075 426 (2015).

[265] F. Fromm, P. Wehrfritz, M. Hundhausen, and T. Seyller, "Looking behind the scenes: Raman spectroscopy of top-gated epitaxial graphene through the substrate", New Journal of Physics **15**, 113 006 (2013).

[266] A. Tiberj, M. Rubio-Roy, M. Paillet, J. R. Huntzinger, P. Landois, *et al.*, "Reversible optical doping of graphene", Scientific Reports **3**, 2355 (2013).

[267] Z. H. Ni, H. M. Wang, Y. Ma, J. Kasim, Y. H. Wu, and Z. X. Shen, "Tunable stress and controlled thickness modification in graphene by annealing", ACS Nano **2**, 1033–1039 (2008).

[268] S. Pei and H.-M. Cheng, "The reduction of graphene oxide", Carbon **50**, 3210–3228 (2012).

[269] F. Ding, K. Jiao, Y. Lin, and B. I. Yakobson, "How evaporating carbon nanotubes retain their perfection?", Nano Letters **7**, 681–684 (2007).

[270] C. Casiraghi, A. Hartschuh, H. Qian, S. Piscanec, C. Georgi, *et al.*, "Raman spectroscopy of graphene edges", Nano Letters **9**, 1433–1441 (2009).

[271] S. Park and R. S. Ruoff, "Chemical methods for the production of graphenes", Nature Nanotechnology **4**, 217–224 (2009).

[272] A. Felten, B. S. Flavel, L. Britnell, A. Eckmann, P. Louette, *et al.*, "Single- and double-sided chemical functionalization of bilayer graphene", Small **9**, 631–639 (2013).

[273] A. Felten, A. Eckmann, J. J. Pireaux, R. Krupke, and C. Casiraghi, "Controlled modification of mono- and bilayer graphene in O_2 , H_2 and CF_4 plasmas", Nanotechnology **24**, 355 705 (2013).

Acknowledgement

I would like to thank everyone who contributed to this work, especially

my supervisor Janina Maultzsch for the possibility to work on various interesting topics during the last years, for her sincere interest in this work, her continuous support and the literally always "open door" to her office. I really enjoyed the time in her group!

Prof. Dr. Stéphane Berciaud for reviewing this thesis.

Prof. Dr. Thomas Möller for being the chairman of my thesis committee.

Patrick May for "introducing" me to the wonderful world of graphene and graphitic carbons and for laying the foundation of this thesis.

Matteo Calandra and Francesco Mauri for the kind hospitality during my stays in Paris and the very interesting and fruitful collaboration on double-resonant Raman scattering in bilayer graphene.

Gunther Lippert for the nice collaboration on MBE-grown graphene.

Ivanka Milošević for interesting discussions about CNT symmetries and kind support regarding problems with the POLSym code.

Oswin Ehrmann and the Fraunhofer IZM for a continuous supply with silicon substrates.

Oliver Ochedowski for the ion-irradiated graphene samples.

Christoph Tyborski for so many funny and enjoyable moments during the last years, for eye-opening discussions about Raman spectroscopy in general, and for the interesting projects we did together. Also thanks to Chris and Aurélie for proofreading this thesis.

the "08:30 coffee group" and the "11:15 lunch group" for always a nice start into the day and many amusing lunch breaks in the Mensa.

Jan Laudenbach and Asmus Vierck for interesting and sometimes confusing discussions about the D mode in carbon nanotubes.

the whole group for the nice atmosphere and support during the last years, especially Sevak Khachadorian, Felix Kampmann, Roland Gillen, Felix Nippert, Harald Scheel, Dirk Heinrich, and Michael Mayer.

Anja Sandersfeld for all her support in surviving the bureaucracy.

my master and bachelor students: Daniel Meza, Rasim Mirzayev, Pascal Röder, and Markus Schleuning.

my parents and my sister for all their support and guidance.

last and most importantly Svenja for all her love, for always encouraging me during sometimes frustrating moments and situations, and for enriching my life every single day.